Finanziato dall'Unione europea NextGenerationEU
Ministero dell'Università e della Ricerca
Italiadomani PIANO NAZIONALE DI RIPRESA E RESILIENZA
UNIVERSITÀ DEGLI STUDI FIRENZE

PhD COURSE IN

EARTH AND PLANETARY SCIENCES

XXXVIII Cycle - ex DM 351

Geomechanical analysis for heritage conservation: development and application of a novel point cloud-based methodology for rockfall susceptibility and stability

GSD:

GEOS-03/B

Candidate

Eugenio Segabinazzi

Supervisor

Prof. Emanuele Intrieri

Co-Supervisor

Prof. Giovanni Gigli

Coordinator

Prof. Sandro Conticelli

A Fiamma, Luciano, Flora e Musa

ABSTRACT

Historic stone buildings increasingly face material detachment risks from weathering and discontinuity evolution. Traditional conservation practices lack systematic approaches for assessing detachment risk and visitor safety. This research develops a novel diagnostic methodology adapting geomechanical principles from rock slope stability analysis to architectural heritage conservation. The methodology treats architectural stone elements as rock masses characterized by geological parameters, that can be used to perform kinematic and dynamic analysis of different failure mechanisms. Central to this methodology is RoDiAn (Rock Discontinuity Analyzer), a custom software developed to overcome fundamental limitations of commercial slope stability tools when applied to finite architectural elements. Unlike conventional software that assumes semi-infinite slope geometries and defines discontinuities solely through angular parameters, RoDiAn incorporates spatial positioning of planes within three-dimensional space, needed for accurate identification of wedge formations and facade interactions specific to individual building blocks. To provide a quantitative prioritization criteria for conservation interventions, the research uses a Kinematic Susceptibility Index (KSI) adapted from rock mass classification systems. The dynamic analysis functions of RoDiAn can calculate block volumes, sliding areas, and safety factors, to support engineering design of stabilization systems. The methodology was applied to three Florentine monuments: Palazzo Pitti, Palazzo Medici Riccardi, and Palazzo Zuccari, and shows the ability to adapt to different case studies and architectural contexts.

PUBLICATIONS

Salvatici, T., Centauro, I., Calandra, S., **Segabinazzi, E.**, Intrieri, E., Garzonio, C.A. (2023). Non-destructive methods applied for in situ mechanical diagnosis: Florentine historical buildings in Pietra Serena. Heritage Science, 11, 116. https://doi.org/10.1186/s40494-023-00959-8

Segabinazzi, E., Salvatici, T., Calandra, S., Centauro, I., Garzonio, C.A. (2023). Sonic test for decay assessment of historical stone coat of arms. XII Congresso Nazionale AIAr, Messina, Italy, 19–21 April 2023.

Salvatici, T., Centauro, I., **Segabinazzi, E.**, Calandra, S., Intrieri, E., Garzonio, C.A. (2023). Multi-analytical methodology to investigate the Pietraforte sandstone risk assessment. EGU General Assembly 2023, Vienna, Austria, 24–28 April 2023. EGU23-14744.
https://doi.org/10.5194/egusphere-egu23-14744

Segabinazzi, E., Salvatici, T., Centauro, I., Calandra, S., Garzonio, C.A. (2023). Assessing weathering damage in Arenitic Rock using Non-Destructive Testing: the case study of the stone coats of arms of Palazzo Ricasoli in Florence. EGU General Assembly 2023, Vienna, Austria, 24–28 April 2023. EGU23-13699.
https://doi.org/10.5194/egusphere-egu23-13699

Segabinazzi, E., Salvatici, T., Centauro, I., Intrieri, E., Calandra, S., Garzonio, C.A. (2024). Applying a geomechanical approach to mitigate rockfall risk from stone heritage buildings. In R. Tomás, M. Cano, A. Riquelme, J.L. Pastor, D. Benavente S. Ordóñez (Eds.), New Challenges in Rock Mechanics and Rock Engineering (1st ed.). CRC Press. https://doi.org/10.1201/9781003429234

Salvatici, T., Centauro, I., **Segabinazzi, E.**, Calandra, S., Pilati, F., Garzonio, C.A., Intrieri, E. (2024). An integrated methodology of NDTs for the characterization of stone pillars and columns. Restauro Archeologico, 32(2, Part 2), 200. ISSN: 2465-2377.

Salvatici, T., **Segabinazzi, E.**, Calandra, S., Centauro, I., Azil, C., Garzonio, C.A., Intrieri, E. (2025). Diagnostic investigations on corbels of

Pietra Serena sandstone. XIV Congresso Nazionale AIAr, Messina, Italy, 14 February 2025.

Segabinazzi, E., Centauro, I., Salvatici, T., Calandra, S., Intrieri, E., Garzonio, C.A. (2025). Architectural Heritage Monitoring: Implementing Data-Driven Preservation for Stone Corbels with Low-Code App Tools and Reporting. In The Future of Heritage Science and Technologies II (Florence Heri-Tech 2024), Lecture Notes in Mechanical Engineering, pp. 355–368.

Salvatici, T., Vieri de Mitri, M., Centauro, I., Calandra, S., **Segabinazzi, E.**, Curatella, G., Garzonio, C.A., Santo, A.P. (2025). A Conservation Study of Sandstone: The Church of Orsanmichele in Florence (Italy). In The Future of Heritage Science and Technologies II (Florence Heri-Tech 2024), Lecture Notes in Mechanical Engineering, pp. 93–104.

Scelza, H., Bracciali, S., Papaleo, M., Angellotto, D., Calandra, S., Centauro, I., Garzonio, C.A., Intrieri, E., Pilati, F., Ricci, M., Salomone, S., Salvatici, T., **Segabinazzi, E.** (2025). Il restauro della facciata dello studio di Federico Zuccari a Firenze. In Tutela e Restauro 2022 (pp. 233–246). All'Insegna del Giglio.

Scelza, H., Bracciali, S., Papaleo, M., Angellotto, D., Calandra, S., Centauro, I., Garzonio, C.A., Intrieri, E., Pilati, F., Ricci, M., Salomone, S., Salvatici, T., **Segabinazzi, E.** (2025). Il restauro della facciata dello studio di Federico Zuccari a Firenze. In Tutela e Restauro 2022 (pp. 233–246). All'Insegna del Giglio.

ACKNOWLEDGMENTS

My sincere thanks go first to my supervisor, Professor Emanuele Intrieri, and my co-supervisor, Professor Giovanni Gigli, for their constant support and guidance throughout this journey, making this research possible. I would also like to give an heartful thank Professor Carlo Alberto Garzonio for introducing me to this field with passion and trust. A special thanks goes to Professor Adrian J. Riquelme Guill for his generous hospitality at the University of Alicante and for the valuable insights he shared during my stay. I am also grateful to those who made me feel at home even when I was far away: Domenico, Antonio, Mariangela, Enea, Melissa, Giulia, Serena, and Giampiero. I would also like to express my sincere appreciation to Tommaso Beni and Francesco Di Meo for their valuable assistance during the data collection phase. Finally, I wish to thank my colleagues and fellow adventurers at the LAM laboratory, that helped me for years and with whom I shared so many wonderful moments: Teresa, Irene, Sara, Cheima, and Francesco.

CONTENTS

List of Figures xv
1 Introduction 1
1.1 Research background, motivation and objectives 1
1.2 Methodology overview 5
2 State of the Art 7
2.1 Stone conservation and degradation 7
2.2 Current conservation practices and regulatory frameworks 10
2.3 Risk assessment in cultural heritage 11
2.4 Florentine Sandstones: Failure Modes 12
2.5 Geomechanical approaches in rock engineering 19
2.5.1 Kinematic analysis 20
2.5.2 Limit equilibrium methods 21
2.6 Knowledge gap in geomechanical methods for heritage materials 22
3 Methodology 27
3.1 Applying geomechanical methodologies to architectural elements 27
3.2 Proposed workflow 28
3.3 3D Data acquisition 32
3.4 Discontinuities extraction (CloudCompare) 33
3.5 Geomechanical parameters needed for Dynamic Analysis in RoDiAn 37
3.6 JRC calculation using EZ_2JRC 38
3.6.1 EZ_2JRC processing 41
3.7 RoDiAn processing 44
3.7.1 Input Files 45
3.7.2 Data Visualization 47
3.7.3 Kinematic Analysis 51
3.7.4 Dynamic Analysis 63
4 Software Development: RoDiAn 85
4.1 Introduction 85
4.2 Main Functions 86
4.2.1 View Planes 86
4.2.2 View Wedges 92
4.2.3 Planar/Freefall 108

4.2.4 Wedge/Freefall . . . 117
4.2.5 Compute Planar KSI . . . 122
4.2.6 Compute Wedge KSI . . . 132
4.2.7 Planar volume Side 1/Side 2 - Wedge Volume . . . 137
4.2.8 Planar and Wedge Area . . . 143
4.2.9 Compute safety factor (planar and wedge) . . . 149
4.3 Validation and Testing . . . 152
4.3.1 Geometrical Validation . . . 152
4.3.2 Kinematic Analysis validation . . . 164
4.3.3 Sensitivity and uncertainty analysis of geomechanical assumptions . . . 169
4.3.4 Historical failures validation . . . 173
5 Software Development: EZ_2JRC 181
5.1 Introduction . . . 181
5.2 Main Functions . . . 181
5.2.1 Load Point Cloud . . . 181
5.2.2 PCA Detrending . . . 185
5.2.3 Calculate JRC . . . 190
5.3 Validation and Testing . . . 194
5.3.1 Synthetic data validation . . . 194
5.3.2 Field data validation . . . 197
6 Case Studies 209
6.1 Palazzo Pitti . . . 209
6.2 Palazzo Medici Riccardi . . . 214
6.3 Palazzo Zuccari . . . 217
7 Results and discussion 221
7.1 Palazzo Pitti . . . 221
7.1.1 Test Area 1 . . . 222
7.1.2 Test Area 2 . . . 233
7.1.3 Test Area 3 . . . 240
7.2 Palazzo Medici Riccardi . . . 243
7.2.1 Rusticated block of the facade . . . 246
7.2.2 Dentils of the cornice . . . 262
7.2.3 Summit Cornice . . . 268
7.3 Palazzo Zuccari . . . 271
7.4 Discussion . . . 275
8 Conclusions and future developments 281
8.1 Key Findings and Practical Applications in Conservation . 281
8.2 Current Limitations and Critical Considerations . . . 282
8.3 Future Developments . . . 284

8.4 Concluding Remarks 284
Bibliography 287
9 Appendix 303

LIST OF FIGURES

Figure 1 Warning sign for "falling fragments" posted outside of Palazzo Pitti, Florence 2

Figure 2 Examples of rock failure phenomena observed on the facades of historic buildings in Florence. A–B: Palazzo Pitti; C: Fortezza da Basso; D: Chiesa di San Firenze; E: Palazzo Medici Riccardi. 4

Figure 3 Examples of extensive natural rock facades in Florence. A: Palazzo Pitti; B: Palazzo Medici Riccardi 5

Figure 4 Examples of detachment phenomena on stone elements. A-B-C: Examples from the ICOMOS-ISCS GLOSSARY [136] of Fracture, Exfoliation and Delaminatoin; D-E Detachement phenomana observed is situ during the research campaign 9

Figure 5 Florence main buildings made in Pietraforte. 1 Arco dei Peruzzi, 2 Bargello, 3 Bourbon del Monte, 4 Casa Altoviti, 5 Casa Buondelmonti, 6 Casa del Garbo, 7 Casa Guidacci, 8 Casa Marignolli, 9 Casa-torre dei Foresi, 10 Loggia del Mercato Nuovo, 11 Orsanmichele, 12 Palagio di Parte Guelfa, 13 Palazzo Alamanni, 14 Palazzo Alberti, 15 Palazzo Bartolini-Salimbeni, 16 Palazzo Bezzoli, 17 Palazzo Biliotti, 18 Palazzo Boni-Antinori, 19 Palazzo Borgherini, 20 Palazzo Buondelmenti, 21 Palazzo Cambi del Nero, 22 Palazzo Cavalcanti, 23 Palazzo Corsi-Horne, 24 Palazzo Corsini Suarez, 25 Palazzo Coverelli, 26 Palazzo da Uzzano, 27 Palazzo Davanzati, 28 Palazzo de' Cerchi, 29 Palazzo degli Altoviti, 30 Palazzo dei Mozzi, 31 Palazzo del Gran Siniscalco, 32 Palazzo Del Nero, 33 Palazzo dell'arte dei mercatanti, 34 Palazzo dell'Arte della Lana, 35 Palazzo della Condotta, 36 Palazzo della Mercatanzia, 37 Palazzo dello Strozzino, 38 Palazzo di Benedetto degli Alberti, 39 Palazzo Davanzati, 40 Palazzo Giandonati, 41 Palazzo Gianfigliazzi, 42 Palazzo Ginori, 43 Palazzo Giugni, 44 Palazzo Gondi, 45 Palazzo Guadagni, 46 Palazzo Lotteringhi della Stufa, 47 Palazzo Manetti, 48 Palazzo Medici, 49 Palazzo Minerbetti, 50 Palazzo Niccolini, 51 Palazzo Pazzi Quaratesi, 52 Palazzo Peruzzi-Lotti, 53 Palazzo Pitti, 54 Palazzo Ricasoli, 55 Palazzo Ridolfi, 56 Palazzo Rinuccini, 57 Palazzo Rucellai, 58 Palazzo Salviati, 59 Palazzo Soldani, 60 Palazzo Spini, 61 Palazzo Strozzi, 62 Palazzo Uguccioni, 63 Palazzo Vecchio, 64 Residenza dell'arte dei Galigai, 65 Torre de' Baldovinetti, 66 Torre de' Buondelmonti, 67 Torre de' Cerchi, 68 Torre de' Visdomini, 69 Torre degli Alepri, 70 Torre dei Donati, 71 Torre dei Ghiberti, 72 Torre dei Giuochi, 73 Torre dei Peruzzi, 74 Torre dei Pierozzi, 75 Torre del Vescovo, 76 Torre della Castagna, 77 Torre di Casa Ciacchi, 78 Torre Galigai, 79, 80 Torre degli Adimari.Some of the most famous buildings made in Pietraforte until the XVI century. (From [30]) 13

Figure 6 Example of detachment via gravitational failure in a Pietraforte facade element on the facade of the Fortezza da Basso, Florence 15
Figure 7 Example of detachment via gravitational failure in a Pietraforte facade element on the facade of the Fortezza da Basso, Florence 16
Figure 8 Example of a planar-like failure on a block on the facade of Palazzo Pitti, Florence 17
Figure 9 Example of a wedge-like failure on a block on the facade of Palazzo Pitti, Florence 18
Figure 10 Example of a freefall-like failure on a block on the facade of Palazzo Pitti, Florence 19
Figure 11 Methodology flowchart. 29
Figure 12 Logic flowchart of the methodology. 30
Figure 13 Example Block P3-B3, Palazzo Pitti 33
Figure 14 Manual discontinuity tracing in CloudCompare. Points are laid of the trace of the discontinuity (left red square) and a new cloud is created containing the selected points of the trace 34
Figure 15 Plane fitting in CloudCompare via the 'Fit -> Plane' tool 35
Figure 16 Planes info export in CloudCompare via the 'Batch Export -> Export Plane Info' tool 36
Figure 17 A simple, "good enough" workflow for the calculation of JRC, from [83] 40
Figure 18 Point cloud loading in EZ_2JRC via the 'Load Point Cloud' button 41
Figure 19 3D visualization windows that opens in EZ_2JRC upon the point cloud loading 42
Figure 20 Point cloud detrendinf in EZ_2JRC via the 'PCA Detrending' button 42
Figure 21 Direction selection in EZ_2JRC via the 'Direction Picking' button 43
Figure 22 Number of profiles and JRC computation prompt in EZ_2JRC via the 'Number of profiles' and 'Compute JRC' buttons 43
Figure 23 Logical diagram of RoDiAn functionalities 44
Figure 24 Point cloud and plane info files loading in RoDiAn via the 'Load TXT' and 'Load CSV' buttons 46

Figure 25 Point cloud and planes visualization in RoDiAn via the 'View Cloud' and 'View Planes' buttons . . 48
Figure 26 Point cloud (A) and planes (B) visualization in RoDiAn's 3D visualization window 49
Figure 27 Table of planes attribute in RoDiAN. Each row of the table corresponds to a plane, and the columns show each plane name (Plane ID), its Dip value (Dip) and Dip Direction (Dip Direction) 50
Figure 28 3D views (A-B different camera position) of the graphical results of the 'Wiew Wedges' button. For each pair of planes that form an interesection inside of the block (a wedge), the function plots the intersection line (plunge line of the wedge) 51
Figure 29 Table of wedges attribute in RoDiAN. Each row of the table corresponds to a wedge, and the columns show each of the planes that form the inserction name (Plane 1-2 ID), the wedge Dip value (Wedge Dip) and Dip Direction (Wedge Dip Direction) . . 52
Figure 30 Interactive fields in the GUI of RoDiAn to enter the dip of the facade ("Facade Dip"), the dip direction ("Facade Dip Dir"), and the friction angle ("Friction Angle") 53
Figure 31 Planar and Freefall kinematic test in RoDiAn via te 'Planar/Freefall' button 54
Figure 32 Planar and Freefall kinematic results table (in red). Sample block that illustrates possible results of the planar/freefal kinematic test 56
Figure 33 Planar and Freefall kinematic results table (in red). Sample block that illustrates possible results of the planar/freefal kinematic test 56
Figure 34 Planar and Freefall kinematic results table (in red). Sample block that illustrates possible results of the planar/freefal kinematic test 57
Figure 35 Wedge and Freefall kinematic results table (in red). Sample block that illustrates possible results of the wedge/freefal kinematic test 59
Figure 36 Wedge and Freefall kinematic results table (in red). Sample block that illustrates possible results of the wedge/freefal kinematic test 59
Figure 37 RoDiAn susceptibilty legend of KSI classes 60

Figure 38 Examples of susceptibility output of RoDiAn. A-B: Block with no susceptible planes and one susceptible wedge; C-D: Block with a non-intersecting sliding plane and one non-intersecting sliding wedge; E-F: Block with one plane susceptible to freefall failure and two suscpetibile wedges, one to freefaal failure, one to sliding with no facade interesection; G-F: Block with a plane susceptibile to planar failure and multiple susceptibile wedges. 61
Figure 39 Example of numerical results of the 'Compute Planar KSI' and 'Compute Wedge KSI' in RoDiAn, populating the corrisponding table (in red) 62
Figure 40 Position of the 'Planar FS' 'Wedges FS' tabs in the RoDiAn GUI, to access the dynamic analysis pages 63
Figure 41 Visualization tools in the dynamic analysis tab of RoDiAn. 'The button View Cloud and Planes' (left) prompts the 3D visualization of the 3DPC and planes (right). The information of the planes populate the two tables, upper and lower 64
Figure 42 Input field to select to plane to be analyzed 65
Figure 43 Volume calculation of the potentially unstable block in RoDiAn via the 'Planar Volume Side 1' and 'Planar Volume Side 2' buttons 66
Figure 44 Example of the graphical output of the volume calculation in RoDiAn. A-B: the two complementary volumes calculated via the Side 1 or Side 2 buttons; C: The two volumes overlaid to show how they form the whole block 67
Figure 45 Numerical output of the 'Planar Volume' functions in RoDiAn. The results appear in the dedicated table (in red) 68
Figure 46 Volume grid step slider in RoDiAn, to modify the intensity of the downsampling of the mesh used in the volume calculation 69
Figure 47 Calculation of the sliding area of the potentially unstable block in RoDiAn via the 'Planar Area' button. The numerical results populate the corresponding table. It is possible to adjust the volume of the space within which the 3DPC points are projected onto the plane using the 'Area Point Density' 70

Figure 48 Example of the graphical output of the area calculation in RoDiAn 71
Figure 49 Input box for the physical and geomechanical parameters needed in the dynamic analysis in RoDiAn 72
Figure 50 Example of numerical results of the dynamic analysis of a sliding block. The results populate the corresponding field (in red) 74
Figure 51 Visualization tools in the dynamic analysis tab for wedegs in RoDiAn. The button 'Cloud and Wedges' (left) prompts the 3D visualization of the 3DPC with the convex hull overlaid used for wedge filtering on top. The plunge lines of the wedges are also plotted (in white). The information of the wedges populate the two tables, upper and lower 75
Figure 52 Wedge selection and volume calculation via the 'Wedge Number' edit field and 'Wedge Volume' button 76
Figure 53 Sample block for explaining how to select the correct wedge volume. The wedge considered in the exmaple is the one formed by Plane 2 and 3 (in red) 77
Figure 54 The planes forming the wedge divide the block in four different spatial regions (A-B-C-D) 78
Figure 55 The four different spatial regions (Top A-B-C-D) correspond to four parts of the block. Only one portion correspond to the wedge volume (C in this example) 80
Figure 56 Wedge sliding area calculation in RoDiAn via the 'Wedge Area' button. The numerical output populates the corresponding table (in red). The 'Area Point Density' slider defines the spatial volume within which the 3DPC is projected onto the reference plane 81
Figure 57 Example of the graphical output of the wedge sliding area calculation in RoDiAn 82
Figure 58 Input box for the physical and geomechanical parameters needed for wedge dynamic analysis in RoDiAn 83
Figure 59 RoDiAn's user graphical interface 86

Figure 60 Construction of a planar surface in 3D space using center point (C) and normal vector (red) extracted from the .csv data. The orthonormal basis (u, blue; v, green) is derived via cross products with a reference vector (black) 90
Figure 61 Block that contains four discontinuity planes (1-2-3-4). Only the intesections between the planes 1–2 and 1–3 acrutally create wedges in the block . . . 93
Figure 62 Wedge sliding output from RocScience Dips for the example block. All the intersections between the planes are considered as revelant, regardless of theu actual position in the space 94
Figure 63 Visualization of the example block model showing all computed intersection lines between discontinuity planes, highlighted in red. As illustrated, several plane intersections extend beyond the block's geometry, occurring in spatial regions not relevant to the analysis 95
Figure 64 Geometric interpretation of the cross product between vectors **A** and **B**. Vectors **A** and **B** define two distinct families of parallel planes, each representing a directional discontinuity set. Their cross product, $\mathbf{A} \times \mathbf{B}$, yields a vector orthogonal to both inputs, corresponding to the lines of intersection between the two plane families. 97
Figure 65 Two planes defined by point coordinates ($C_1 = (x_1, y_1, z_1)$ and $C_2 = (x_2, y_2, z_2)$) and normal vectors ($\vec{N}_1 = (a_1, b_1, c_1)$ and $\vec{N}_2 = (a_2, b_2, c_2)$) 99
Figure 66 Determination of the intersection line between two planes in three-dimensional space. The direction vector $\vec{d} = \vec{N}_1 \times \vec{N}_2$ defines the orientation of the intersection line, obtained as the cross product of the normal vectors of the two planes. The coordinates of a point on the intersection are computed by solving the linear system defined by the two plane equations 101

Figure 67 Comparison between convex hull and alpha shape representations of point cloud. The alpha shape captures concave features with greater fidelity but assumes that point clouds with an 'hollow' side have concave features 104
Figure 68 Possible interaction scenarios between discontinuities and the facade. Plane 1 does not intersects the wall, Plane 2 does 110
Figure 69 Projection of sample points onto a plane for intersection testing. A grid of sample points is generated and tested for intersection by verifying horizontal/vertical bounds and crossing relative to the facade 113
Figure 70 Planes with geometries susceptible to planar sliding and lacking contact with the facade are considered more critical and are categorized separately and plotted in dark purple 125
Figure 71 Planes with geometries susceptible to freefall failure are plotted in bright purple 126
Figure 72 Parallelism (A) between discontinuity and slope strikes for planar failure (left). Parallelism (A) between the plunge direction of the line of intersection of two discontinuities (α_i) and the slope dip direction (α_s) for wedge failure (right). Adapted from Pastor et al. (2018) 128
Figure 73 Planes with geometries susceptible to planar sliding and that contact the facade are categorized using the KSIp and color coded accordingly 129
Figure 74 Wedges with geometries susceptible to planar sliding and lacking contact with the facade are considered more critical and are categorized separately and plotted in dark purple 134
Figure 75 Wedges with geometries susceptible to free fall are plotted in bright purple 135
Figure 76 Wedges with geometries susceptible to planar sliding and that contact the facade are categorized using the KSIw and color coded accordingly . . . 136

Figure 77 Illustration of the volume calculation logic in RoDiAn. The plane separates the downsampled point cloud into two sides based on the dot product between the plane's normal vector $\vec{n}$ and the vector from the plane center P_0 to each point P_i. Points with non-negative dot products ($\vec{n} \cdot (P_i - P_0) > 0$) are assigned to Side 1, while points with negative dot products ($\vec{n} \cdot (P_i - P_0) < 0$) are assigned to Side 2. Points lying on the plane satisfy $\vec{n} \cdot (P_i - P_0) = 0$. 139

Figure 78 Point cloud classification and separation by a discontinuity plane. Left: Original 3DPC (3D Point Cloud). Center: Plane intersecting the point cloud. Right: Separated sub-clouds with points classified into Side 1 (red) and Side 2 (blue) based on their position relative to the plane. 140

Figure 79 Distance calculation from each point in the 3DPC to the user-selected discontinuity plane. Points are color-coded based on their perpendicular distance d from the plane, with the color scale ranging from blue (farthest) to red (closest). The spatial coordinates of the discontinuity plane are provided by RoDiAn's input data structure 143

Figure 80 Threshold-based selection of points belonging to the discontinuity plane. Left: Point cloud colored by distance from the plane. Center: User-adjustable threshold slider with values (0.5 and 1 shown as examples). Right: Resulting point selections showing how different threshold values affect the identification of points considered to belong to the plane. 145

Figure 81 Convex hull computation and area calculation of the discontinuity plane. Top: 3D visualization showing the sliding area (blue) within the point cloud (red) from two perspectives. Bottom: 2D projections of the convex hull onto the plane with computed areas ranging from 0.1859 m^2 to 0.2189 m^2, demonstrating how the threshold selection affects the calculated sliding contact area. The plotted convex hull allows visual validation of whether it reasonably covers the sliding contact region. . . . 148

Figure 82 Synthetic 3D point clouds designed for validation. The clouds replicate characteristics of laser scanning or photogrammetric surveys of historical building facades: (left) a rectangular parallelepiped with 1×1 m base and 2×1 m sides, (center) a square-based pyramid with 1 m base, and (right) a hemisphere with 1 m diameter. All geometries have an empty backface (the side in contact with the facade), dimensions on the order of one meter, and are vertically oriented. 153
Figure 83 Validation of volume and area calculation functions on the parallepiped point cloud. Top: Configuration showing the planes applied. Bottom: Visual representation of the four planes applied to the parallelepiped along with their 2D 'slice' projections. 154
Figure 84 Validation of volume and area calculation functions on the pyramid point cloud. Top: Configuration showing the planes applied. Bottom: Visual representation of the four planes applied to the pyramid along with their 2D 'slice' projections. . 156
Figure 85 Validation of volume and area calculation functions on the hemisphere point cloud. Top: Configuration showing the planes applied. Bottom: Visual representation of the four planes applied to the hemisphere along with their 2D 'slice' projections. 158
Figure 86 Validation of wedge volume calculation on the parallelepiped point cloud. Top: Configuration showing the planes applied. Bottom: Visual representation of the fours sectors obtained by the wedge intersection. 160
Figure 87 Validation of wedge volume calculation on the pyramid point cloud. Top: Configuration showing the planes applied. Bottom: Visual representation of the fours sectors obtained by the wedge intersection. 161

Figure 88 Validation of wedge volume calculation on the hemisphere point cloud. Top: Configuration showing the planes applied. Bottom: Visual representation of the fours sectors obtained by the wedge intersection. 162
Figure 89 Example block for Kinematic analysis validation. Left: Original point cloud of the block. Right: Three discontinuity planes (labeled 1, 2, and 3) identified within the block for kinematic analysis. 165
Figure 90 RoDiAn Kinematic analysis results for the example block. 166
Figure 91 RoDiAn (top) and RocScience Dips (bottom) planar sliding Kinematic analysis results for the example block. 167
Figure 92 RoDiAn (top) and RocScience Dips (bottom) wedge sliding Kinematic analysis results for the example block. 168
Figure 93 Block P1B16. Example of a case with a discontinuity susceptible to planar slide with an intersection with the facade. Top left: planar susceptibilty; Top right: Wedge susceptibility; Bottom: dynamic analysis results. 170
Figure 94 Block P2B11. Example of a case with a wedge susceptible to planar slide. Top left: planar susceptibilty; Top right: Wedge susceptibility; Bottom: dynamic analysis results. 171
Figure 95 Block P1B17. Example of a case with a discontinuity susceptible to planar slide without an intersection with the facade. Top left: planar susceptibilty; Top right: Wedge susceptibility; Bottom: dynamic analysis results. 172
Figure 96 Planar Sliding historical failure. A-B: current post-failure morphology of the selected block, shown in frontal and top views; C-D reconstructed pre-failure morphology based on adjacent intact blocks and architectural stylistic features, shown in the same views. 174

Figure 97 Kinematic and dynamic analysis of the planar sliding case performed in RoDiAn. A-B: results of kinematic analysis in RoDiAn shown in frontal and top views; C-D: potential volume of detachment shown in frontal and top views; E: results of the dynamic analysis in RoDiAn. 175
Figure 98 Free Fall historical failure. A-B: current post-failure morphology of the selected block, shown in frontal and top views; C-D reconstructed pre-failure morphology based on adjacent intact blocks and architectural stylistic features, shown in the same views. 176
Figure 99 Kinematic and dynamic analysis of the Free Fall case performed in RoDiAn. A-B: results of kinematic analysis in RoDiAn shown in frontal and top views; C-D: potential volume of detachment shown in frontal and top views; E: results of the dynamic analysis in RoDiAn. 177
Figure 100 Wedge Sliding historical failure. A-B: current post-failure morphology of the selected block, shown in frontal and top views; C-D reconstructed pre-failure morphology based on adjacent intact blocks and architectural stylistic features, shown in the same views. 178
Figure 101 Kinematic and dynamic analysis of the wedge sliding case performed in RoDiAn. A-B: results of kinematic analysis in RoDiAn shown in frontal and top views; C-D: potential volume of detachment shown in frontal and top views; E: results of the dynamic analysis in RoDiAn. 179
Figure 102 EZ_2JRC graphical user interface. The GUI includes: (1) Load Point Cloud button for importing XYZ or XYZ-RGB format data, (2) PCA Detrending, (3) Direction Picking via interactive point cloud selection, (4) profile number selection dropdown, and (5) Compute JRC button. A dialog window on the right provides step-by-step user instructions and displays results. All visualization panels are interactive 3D fields. 182

Figure 103 PCA detrending process in EZ^{2}JRC. Visualization of the detrending process showing Step 1 (original 3D points) and Step 2 (centered points around the origin) before rotation and flattening. 186
Figure 104 PCA eigenvector analysis and point cloud alignment. Step 3 (top left): PCA eigenvectors overlaid on the centered point cloud, where the eigenvector with the smallest eigenvalue (black arrow) represents the normal vector to the best-fit plane with least variation. Step 4 (top right): Best-fit plane visualization that shows the alignment of its normal vector with the relative Z-axis. Step 5 (bottom): Rotation vector in green, used to make the current normal (black arrow) and target normal (red arrow) coincide. 187
Figure 105 Final flattened point cloud after PCA rotation (Step 6). Left: 3D view showing the rotated points (red) aligned with the XY plane (green), with original points (blue) shown for reference. Right: Side view demonstrating that the rotated points now lie approximately on the XY plane ($Z \approx 0$). 188
Figure 106 Profile selection and extraction for JRC calculation. (A) Flattened point cloud on the XY plane with user-selected direction line traced across the surface. (B) 3D view showing the points selected for the profile extraction. (C) 2D representation of the extracted profiles. 190
Figure 107 Synthetic point clouds generated for JRC validation. Each cloud corresponds to one JRC class. The surfaces are shown flattened for visualization purposes, while in the actual dataset each cloud has a random inclination with respect to the Z axis. . . . 196
Figure 108 Examples of real rock surface models acquired through photogrammetry. The selected lithotypes exhibit varying degrees of apparent roughness, and were used to validate the app's performance on natural samples. 198

Figure 109 Example of the EZ_2JRC workflow applied to a real rock surface model. A: Loaded point cloud; B: Detrended point cloud after PCA alignment; C: Custom direction selection for profile extraction; D: Generated profiles used for JRC estimation and comparison with Barton's standard charts. 199
Figure 110 Example of the EZ_2JRC workflow applied to a real rock surface model. Results of Sample 1. A: Loaded point cloud; B: Detrended point cloud after PCA alignment; C: Custom direction selected for profile extraction. 200
Figure 111 Example profiles from Sample 1 extracted to show the comparison with Barton standard profiles chart. 201
Figure 112 Example of the EZ_2JRC workflow applied to a real rock surface model. Results of Sample 2. A: Loaded point cloud; B: Detrended point cloud after PCA alignment; C: Custom direction selected for profile extraction. 202
Figure 113 Example profiles from Sample 2 extracted to show the comparison with Barton standard profiles chart. 203
Figure 114 Example of the EZ_2JRC workflow applied to a real rock surface model. Results of Sample 3. A: Loaded point cloud; B: Detrended point cloud after PCA alignment; C: Custom direction selected for profile extraction. 204
Figure 115 Example profiles from Sample 3 extracted to show the comparison with Barton standard profiles chart. 205
Figure 116 Example of the EZ_2JRC workflow applied to a real rock surface model. Results of Sample 4. A: Loaded point cloud; B: Detrended point cloud after PCA alignment; C: Custom direction selected for profile extraction. 206
Figure 117 Example profiles from Sample 4 extracted to show the comparison with Barton standard profiles chart. 207
Figure 118 Map of the three buildings selected for methodological application: Palazzo Pitti, Palazzo Medici Riccardi, Palazzo Zuccari 210
Figure 119 Palazzo Pitti main facade 211

Figure 120 Documentation of facade survey using MLS and photogrammetric techniques: left, operator with Microgeo GeoSLAM device (Mobile Laser Scanner); right, operator with tripod-mounted camera for photogrammetric acquisition. 212
Figure 121 Ground control point location for the MLS acquisition. 212
Figure 122 Outputs from the survey of ground-accessible facade sectors. A-C: progressive detail levels from Mobile Laser Scanner (MLS) acquisition using the Microgeo GeoSLAM device; D: high-density point cloud generated via photogrammetry using Agisoft Metashape Pro. 213
Figure 123 Palazzo Medici Riccardi main facade 215
Figure 124 Outputs from the 2019–2021 investigation campaign conducted by LAM laboratory using the Saturn Mini drone (DST-UNIFI): left, full 3D model of the palace facade along Via Cavour; right, detailed view of the portion of rusticated blocks studied in this research 215
Figure 125 Dentils of the first level cornice of Palazzo Medici Riccardi along Via Gori 216
Figure 126 Summit cornice of Palazzo Medici Riccardi along via Gori and Via Ginori 217
Figure 127 Palazzo Zuccari facade 218
Figure 128 Stone coat of arms on the facade of Palazzo Zuccari 219
Figure 129 Test areas on Palazzo Pitti 222
Figure 130 Summary of kinematic mechanisms identified in individual blocks at Palazzo Pitti. Each row corresponds to a sample ID, with binary indicators for four kinematic mechanisms: Planar slide (PSLIDE), Planar FreeFall (P.FFALL), Wedge slide (WSLIDE), Wede FreeFall (W.FFALL). Cells marked in blue denote presence of the respective mechanism. . . . 223
Figure 131 Distribution of kinematic mechanisms per sample at Palazzo Pitti. 224
Figure 132 Pie chart illustrating the relative frequency of failure modes at Palazzo Pitti: Planar slide (PSLIDE), Planar FreeFall (P.FFALL), Wedge slide (WSLIDE), Wede FreeFall (W.FFALL) 224

Figure 133 Planar susceptibility map on Area Test 1 - Palazzo Pitti. The blocks are color coded using RoDiAn KSI legend (Figure 37) 225
Figure 134 Wedge susceptibility map on Area Test 1 - Palazzo Pitti. The blocks are color coded using RoDiAn KSI legend (Figure 37) 225
Figure 135 Planar (bottom left of each block) and Wedge (top right of each block) susceptibility map on Area Test 1 - Palazzo Pitti. The blocks are color coded using RoDiAn KSI legend (Figure 37) 226
Figure 136 Map of total number of discontinuities that exhibit susceptibility to any kinematic mechanism on Area Test 1 - Palazzo Pitti 227
Figure 137 Block P1B2. Example of cases with null susceptibility due to the absence of visibile discontinuities. 228
Figure 138 Block P1B13. Example of cases with discontinuities oriented in stable configurations 229
Figure 139 Block P1B3. Example of cases with free fall susceptibile discontinuities. Top left: planar susceptibilty; Top right: Wedge susceptibility; Bottom: dynamic analysis results. 230
Figure 140 Block P1B5. Example of cases with multiple possible kinematic mechanisms. Top left: planar susceptibilty; Top right: Wedge susceptibility; Bottom: dynamic analysis results. 231
Figure 141 Block P1B15. Example of cases with all possible kinematic mechanisms identified. Top left: planar susceptibilty; Top right: Wedge susceptibility; Bottom: dynamic analysis results. 232
Figure 142 Planar susceptibility map on Area Test 2- Palazzo Pitti. The blocks are color coded using RoDiAn KSI legend (Figure 37) 233
Figure 143 Wedge susceptibility map on Area Test 2- Palazzo Pitti. The blocks are color coded using RoDiAn KSI legend (Figure 37) 234
Figure 144 Planar (bottom left of each block) and Wedge (top right of each block) susceptibility map on Area Test 2- Palazzo Pitti. The blocks are color coded using RoDiAn KSI legend (Figure 37) 234

Figure 145 Map of total number of discontinuities that exhibit susceptibility to any kinematic mechanism on Area Test 2 - Palazzo Pitti 235
Figure 146 Block P2B21. Example of cases with no visibile discontinuities. 236
Figure 147 Block P2B04. Example of cases with discontinuities oriented in stable configurations that form stable wedges. 237
Figure 148 Block P2B14. Example of cases with discontinuities oriented in stable configurations that form stable wedges. 237
Figure 149 Block P2B11. Example of cases with discontinuities oriented in stable configurations relative to planar sliding that form unstable wedges. 238
Figure 150 Block P2B15. Example of cases with discontinuities oriented in stable configurations relative to planar sliding that form unstable wedges. 239
Figure 151 Planar susceptibility map on Area Test 3- Palazzo Pitti. The blocks are color coded using RoDiAn KSI legend (Figure 37) 240
Figure 152 Wedge susceptibility map on Area Test 3- Palazzo Pitti. The blocks are color coded using RoDiAn KSI legend (Figure 37) 241
Figure 153 Planar (bottom left of each block) and Wedge (top right of each block) susceptibility map on Area Test 3- Palazzo Pitti. The blocks are color coded using RoDiAn KSI legend (Figure 37) 241
Figure 154 Map of total number of discontinuities that exhibit susceptibility to any kinematic mechanism on Area Test 3 - Palazzo Pitti 242
Figure 155 Block P3B06. Example of cases with discontinuities oriented in stable configurations. 243
Figure 156 Block P3B09. Example of cases that exhibit susceptibility many kinematic mechanism. 244
Figure 157 Block P3B03. Example of a block that was installed rotated by 90° compared to other blocks on the facade and shows a distinctive susceptibility to planar sliding 245
Figure 158 Test area selected for this research on the facade of Palazzo Medici Riccardi 247

Figure 159 Map of the selected block (in red) for the analysis 248
Figure 160 Summary of kinematic mechanisms identified in individual blocks at Palazzo Medici Riccardi. Each row corresponds to a sample ID, with binary indicators for four kinematic mechanisms: Planar slide (PSLIDE), Planar FreeFall (P.FFALL), Wedge slide (WSLIDE), Wede FreeFall (W.FFALL). Cells marked in blue denote presence of the respective mechanism. 249
Figure 161 Distribution of kinematic mechanisms per sample at Palazzo Medici Riccardi 250
Figure 162 Pie chart illustrating the relative frequency of failure modes at Palazzo Medici Riccardi: Planar slide (PSLIDE), Planar FreeFall (P.FFALL), Wedge slide (WSLIDE), Wede FreeFall (W.FFALL) 251
Figure 163 Planar susceptibility map on Palazzo Medici Riccardi. The blocks are color coded using RoDiAn KSI legend (Figure 37) 251
Figure 164 Wedge susceptibility map on Palazzo Medici Riccardi. The blocks are color coded using RoDiAn KSI legend (Figure 37) 252
Figure 165 Planar (bottom left of each block) and Wedge (top right of each block) susceptibility map on APalazzo Medici Riccardi. The blocks are color coded using RoDiAn KSI legend (Figure 37) 252
Figure 166 Map of total number of discontinuities that exhibit susceptibility to any kinematic mechanism on Palazzo Medici Riccardi 253
Figure 167 Block CL1-12. Example of cases with discontinuities oriented in stable configurations due to their dip direction 253
Figure 168 Block CL1-39. Example of cases with discontinuities oriented in stable configurations due to their dip direction 254
Figure 169 Block CL2-20. Example of discontinuities susceptible to planar sliding with no facade intersection . 255
Figure 170 Block CL2-33. Example of discontinuities susceptible to planar sliding with no facade intersection . 256
Figure 171 Block CL1-13. Example of cases with discontinuities susceptible to free fall failure 257

Figure 172 Block CL2-20. Example of discontinuities not susceptible to planar sliding that form wedges which could fail. . . . 258
Figure 173 Block CL2-33. Example of discontinuities not susceptible to planar sliding that form wedges which could fail. . . . 259
Figure 174 Block CL1-13. Example of discontinuities not susceptible to planar sliding that form wedges which could fail via free fall. . . . 260
Figure 175 Example of discontinuities not susceptible to planar sliding that form wedges which could fail via free fall. . . . 261
Figure 176 Dentil of the cornice at Palazzo Medici Riccardi that detached along two calcite veins in February 2025. . . . 262
Figure 177 Blocks that form the portion of the cornice analyzed at Palazzo Medici Riccardi. . . . 263
Figure 178 Block 1 of the cornice at Palazzo Medici Riccardi. RoDiaN susceptibility results for planar (top) and wedge (bottom) kinematic. . . . 264
Figure 179 Block 1 of the cornice at Palazzo Medici Riccardi. RoDiaN susceptibility results for planar (top) and wedge (bottom) kinematic. . . . 265
Figure 180 Block 1 of the cornice at Palazzo Medici Riccardi. RoDiaN susceptibility results for planar (top) and wedge (bottom) kinematic. . . . 266
Figure 181 Block 1 of the cornice at Palazzo Medici Riccardi. RoDiaN susceptibility results for planar (top) and wedge (bottom) kinematic. . . . 267
Figure 182 Portion of the summit cornice at Palazzo Medici Riccardi analyzed in this research . . . 268
Figure 183 Portion of the summit cornice at Palazzo Medici Riccardi analyzed in this research . . . 269
Figure 184 RoDiAn results for the summit cornice at Palazzo Medici Riccardi. The computed mass and volume values can help decide the dimensioning of stabilization devices based on driving force. . . . 270
Figure 185 Stone coat of arms of Palazzo Zuccari (left) showing three discontinuities in the rock matrix. . . . 271

Figure 186 Stone coat of arms of Palazzo Zuccari. RoDiaN susceptibility results for planar (left) and wedge (right) kinematic. 272
Figure 187 Stone coat of arms of Palazzo Zuccari, RoDiaN dynamic analysis results for planar sliding (A, B) and sliding area (C) 273
Figure 188 Stone coat of arms of Palazzo Zuccari, RoDiaN dynamic analysis results for wedge sliding (A, B) and sliding area (C) 274
Figure 189 Example of error arising from the analysis in Block P3-B04: the intersection between Plane 1 and Plane 3 generates a wedge that is not physically valid due to the block's elongated morphology. 277
Figure 190 Example of boundary case error in RoDiAn analysis: the convex hull used for wedge computation slightly exceeds the actual point cloud, leading to identification of a wedge that does not physically form within the block. This conservative false positive is recognizable by the wedge line appearing on the surface of the point cloud. 278

1

INTRODUCTION

1.1 RESEARCH BACKGROUND, MOTIVATION AND OBJECTIVES

In the field of cultural heritage conservation, a “stone” is a rock that has been quarried, shaped and utilized for building or decorative purposes. These stone materials experience deterioration processes linked to their inherent geological properties and the environmental conditions they endure. In urban contexts, additional degradation occurs due to exposure to various atmospheric pollutants [21]. Physical deterioration of these materials can result in material separation and loss. This process, commonly defined as "detachment" in cultural heritage contexts, can be characterized from a geomechanical standpoint as a rockfall event, representing both heritage damage and a potential safety hazard for visitors and residents. Heritage conservation practices rarely, if ever, incorporate visitor safety considerations and tend to focus on the protection of historical materials. On the contrary, slope stability and rockfall risk assessment approaches reverse these priorities, as championed by the United Nations Office for Disaster Risk Reduction (UNDRR) that fosters a people-centered approach to landslide risk reduction [60]. The present research aims to connect heritage conservation practices with methods used in rock slope stability, to develop a new methodology based on geomechanical principles, adapted to a different context, with its own specific features and goals. To demonstrate and validate this approach, Florence’s historic city center, recognized as a UNESCO World Heritage Site since 1982, will serve as our study site. The city center is known world-wide for its numerous heritage buildings constructed from two principal local sandstone varieties, Pietra Serena and Pietraforte, which have consistently served as construction and ornamental materials in significant structures, continuing their use into the early 20th century [109] [11] [81] [94] [42]. These materials are particularly affected by degradation phenomena, with urban pollutants exacerbating deterioration processes

[116] [23]. In recent years, there have been numerous cases of detachment of sandstone elements that have put citizens and visitors of Florence at risk, having occurred on accessible public ground. In addition to these "near misses" documented in recent times, numerous instances of missing material from stone elements throughout the city have been reported which, from an analysis of the morphology and detachment surface, highlight the degradation evolution and subsequent detachment of material. As tragic proof of the danger of these detachment phenomena, it is finally appropriate to mention the 2017 case at the Basilica of Santa Croce in which a Spanish tourist, Daniel Testor, lost his life after being struck by a sandstone fragment that had detached from the internal decorative facings. The phenomenon of fragments detachment has recently become a safety issue that also involves the communicative management of the problem: at Palazzo Pitti, warning signs about falling fragments have recently been posted (Figure 1).



Figure 1: Warning sign for "falling fragments" posted outside of Palazzo Pitti, Florence

The detachments observed in recent years are mainly of two types:

- Detachments occurring along newly-formed discontinuities, i.e., discontinuities that develop after the installation of the element. These are caused not only by loads for which the architectural elements were not designed, but also by severe degradation (such as water infiltration), damage from accidents, construction work, earthquakes, or improperly installed safety systems (nets, metallic rods and pins). An example is the corbel detachment at Santa Croce mentioned above.

- Detachments occurring along pre-existing discontinuities, i.e., joints already present in the quarry stone, which evolve under gravitational forces in elements whose morphology allows it.

It should be noted that Pietraforte inherently presents more discontinuities than Pietra Serena, while the latter is less resistant to weathering. Therefore, very approximately, the first category often involves Pietra Serena, while the second is more typical of Pietraforte. This distinction is relevant for understanding the focus of this work: the second category will be treated here because it allows for kinematic analysis, since the discontinuities (joints) to be studied are already present, whereas the first category would require FEM or FDM models to analyze stress distribution. Moreover, this thesis addresses the second case because, at least in our case studies, it is the most frequent scenario, given that Pietraforte is used more extensively in the architectural context under investigation.

During the investigation campaigns carried out in this research project, numerous observations of this type of phenomenon have been made. Figure 2 shows several examples of this type of detachment that occurred on architectural elements of historic Florentine palaces. The cases have different characteristics and sliding mechanisms but are united by the basic principle of detachment: a rock block has detached along one or more discontinuities oriented in such a way as to make sliding by gravity possible.

The *Lapideous Materials, Engineering Geology, Environmental and Landscape Laboratory* at the Department of Earth Sciences, University of Florence, has been actively studying these phenomena in recent years, developing and utilizing various techniques derived from geomechanical practices [117][121][120][124][123][118][24][91]. The lab's work focuses on both natural and artificial stone materials, with particular attention to the physical and mechanical degradation processes that affect architectural heritage and monuments through in-situ evaluations. These years of experience in dozens of historical buildings in contact with operators from the restoration world have provided an important knowledge base and have madethe conservation needs of professionals in the field clearer. One of the problems that emerged is the need for a large-scale approach that can be used on buildings characterized by very extensive stone surfaces. Detailed methods that can be applied to limited cases become impossible to apply on buildings with hundreds or thousands of elements to investigate. Take as examples two case studies that will be revisited during the research: Palazzo Pitti and Palazzo Medici Riccardi (Figure 3). It immediately becomes evident how necessary it is to have a

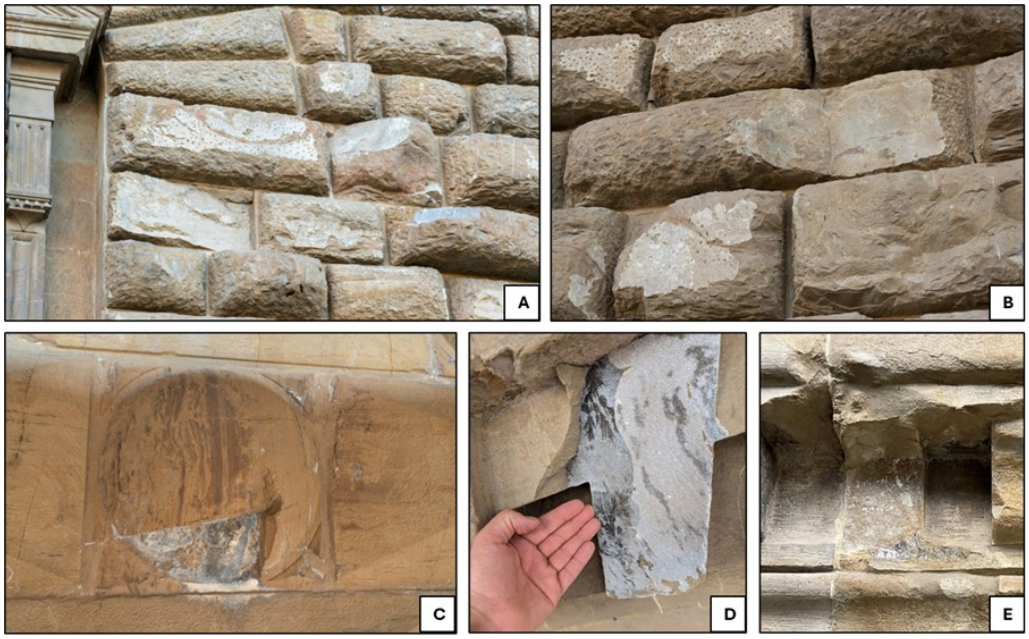


Figure 2: Examples of rock failure phenomena observed on the facades of historic buildings in Florence. A–B: Palazzo Pitti; C: Fortezza da Basso; D: Chiesa di San Firenze; E: Palazzo Medici Riccardi.

methodology that performs an initial selection of the blocks or portions to be studied.

The other main problem that emerged is the characterization that is made of detachment phenomena in the standard practices used today. The reference for categorizing stone material deterioration phenomena in restoration and maintenance contexts, the "Illustrated Glossary on Stone Deterioration Patterns" by ICOMOS [136], provides generic and insufficiently detailed categorization of various detachment scenarios. These existing classifications are further limited to describing already-documented phenomena, failing to consider potential evolution of instability conditions and effectively overlooking the possibility of large block failures [73] [43]. In the absence of procedural guidance for conservation activities, current interventions remain restricted to emergency responses to materials that have already detached or to removals performed by workers on a purely empirical basis, without any form of study, measurement, or investigation. The primary aim of this project is to develop a novel diagnostic methodology for investigating the detachment of overhanging stone elements from historic buildings. The methodology involves adapting techniques and workflows derived from

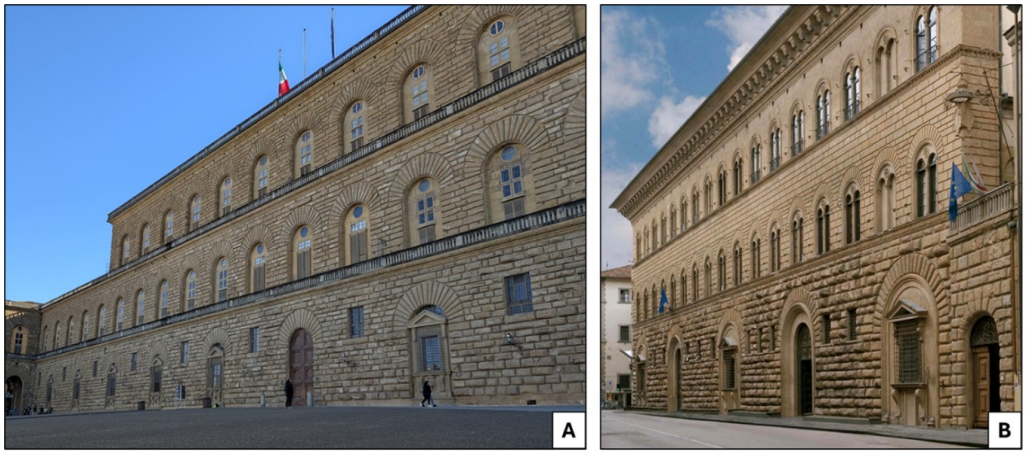


Figure 3: Examples of extensive natural rock facades in Florence. A: Palazzo Pitti; B: Palazzo Medici Riccardi

geomechanical studies of rock slopes to the architectural elements under investigation. To achieve this goal, the following specific objectives are required:

- Establish a geological framework for interpreting detachment phenomena in architectural stone elements
- Define failure mechanisms and classify susceptibility based on analogies with natural rock masses
- Develop a non-invasive, remote-sensing-based diagnostic protocol suitable for heritage structures
- Create a transferable and efficient software for conservation professionals to assess detachment risk
- Validate the methodology through application to representative case studies

1.2 METHODOLOGY OVERVIEW

This research work includes the development and application of an innovative workflow to an underdeveloped field of application. Consequently, beyond conceptualizing the methodological workflow, two dedicated

software tools were developed to enable this application. The work therefore involves describing both the workflow and the custom tools that were created. The proposed methodology integrates elements from rock mechanics and cultural heritage conservation. Although research in heritage conservation continues to evolve and increasingly incorporates techniques borrowed from various scientific and engineering disciplines, the application of methodologies derived from slope stability studies remains almost absent from literature. The initial component of this work therefore provides a comprehensive review of the current state of the art concerning established practices in the conservation of architectural stone elements. To begin framing the problem from a geological perspective, a description of the lithological characteristics of the material under investigation follows, specifically Pietraforte, a sandstone commonly employed in the construction of Florence's historic center. This is succeeded by an examination of the principal geomechanical techniques and concepts employed throughout the research, including rock slope stability analysis methods, kinematic analysis, and limit equilibrium methods. Once these concepts are established, their adaptation to the case study of architectural stone elements is clarified, along with the limitations inherent in this approach. The complete workflow developed through this research is then introduced, from data acquisition to results interpretation. The required characteristics for 3D point clouds serving as input data are discussed, along with the methodology for discontinuity mapping and extraction, the geological parameters necessary for analysis, and the application of the custom-developed Rock Discontinuity Analyzer (RoDiAn) software. RoDiAn, the central focus of this research, is then presented in details in all of its functions, both in their practical application and theoretical foundations. The chapter examining RoDiAn in detail also includes validation of the obtained outputs, conducted through both synthetic data with known characteristics and testing on real data, with results compared against commercially available software. Similar to RoDiAn, the functions of EZ_2JRC, a software developed in the project for Joint Roughness Coefficient (JRC) calculation, will be analyzed and validated. The research includes the application of the proposed workflow to three distinct case studies of historic buildings in Florence with overhanging stone elements differing in geometry and characteristics: Palazzo Pitti, Palazzo Medici Riccardi, Palazzo Zuccari. Finally, the obtained results are discussed in their implications for practical applications in conservation approaches and limitations identified throughout the research.

2

STATE OF THE ART

2.1 STONE CONSERVATION AND DEGRADATION

The conservation of stone materials that constitute our cultural heritage is a topic that has been addressed since the birth of the application of modern scientific techniques to restoration themes [75] [6] [64] [140]. Stone heritage conservation is a very broad research topic and includes the study of a multitude of chemical-physical phenomena that cause the worsening of the conservation state of stone artifacts. These phenomena can lead to an alteration of aesthetic characteristics or, in the worst cases, structural modifications capable of modifying the mechanical characteristics of the materials. The focus of this research is on phenomena capable of causing detachment of potentially dangerous materials. To address the topic of this kind of detachments it is appropriate to define a common language base, drawn from the world of conservation and restoration. This effort has been complicated by the multilingual nature of the discipline, where Italian and French have historically served as reference languages, and the presence of seemingly synonymous terms that often describe distinct phenomena. The most important work of recent years on the topic of standardization and terminological clarification is the Illustrated Glossary on Stone Deterioration Patterns by ICOMOS-ISCS (International Council on Monuments and Sites, International Scientific Committee - Stone) [136]. In this glossary, generic terms with different meanings are first defined, such as Alteration, Degradation, Decay, Weathering. The category to which we will mainly refer in this work is "Degradation: a decline in condition, quality, or functional capacity" [136]. In addition to these generic descriptions, individual phenomena are then described. Below are those considered relevant to the research, namely those capable of generating material detachments:

- Crack/Fracture: Individual fissure, clearly visible by the naked eye, resulting from separation of one part from another [136].
- Delamination/Exfoliation: Detachment process affecting laminated stones (most of sedimentary rocks, some metamorphic rocks...). It corresponds to a physical separation into one or several layers following the stone laminae. The thickness and the shape of the layers are variable. The layers may be oriented in any direction with regards to the stone surface [136].

These phenomena can obviously generate and manifest in various degrees of intensity, evolve over time and modify their characteristics. Situations that initially would not be capable of causing detachments can however evolve even rapidly and represent a possible danger. During the investigation campaigns on which this work is based, occurrences of this type of phenomena have been observed at various scales and on various lithotypes. Figure 4 reports two examples of this type of phenomena on sandstone material and their comparison with the example figures reported in the ICOMOS-ISCS glossary [136].

These degradation phenomena have complex causes and numerous reviews in the literature treat the main causes exhaustively [80] [128] [5]. Although the description of causes is beyond the objective of this work, it is necessary to specify a key concept that will be taken up in detail in paragraph 2.4: the conservation of stone material placed in historic buildings is influenced by three main factors:

- The intrinsic characteristics of the material: different lithotypes placed in the same environment are conserved in different ways. Porosity and the dimensional distribution of pores determine the capacity for water absorption and retention [88] [34] [93] [122] [53], mineralogical composition influences susceptibility to chemical attacks [127] [27] [137] [132]. The crystalline structure and texture of the rock condition mechanical resistance and the mode of fracture propagation [96] [8] [68]. The presence of clay inclusions [59] or easily alterable minerals can create points of weakness, structural anisotropies create preferential planes of failure [69] [54] [101].
- External environmental stress factors: different environmental conditions can lead the same material to develop different degradation phenomena. Meteoric water represents the main vector of alteration through mineral hydration, transport of soluble salts [110]



Figure 4: Examples of detachment phenomena on stone elements. A-B-C: Examples from the ICOMOS-ISCS GLOSSARY [136] of Fracture, Exfoliation and Delaminatoin; D-E Detachement phenomana observed is situ during the research campaign

and freeze-thaw cycles [61]. Atmospheric pollution in urban environments generates acid rain that accelerates carbonate dissolution. Thermal variations cause differential dilations and contractions.

- The conservation/intervention history of the material: different conservation histories can influence the current conservation state of the material. Counterintuitively, past conservation interventions may have compromised the the material they were meant to safeguard. In past years, treatments with wrong chemistry may have been applied [38] or reinforcement structures made of material possibly subject to corrosion may have been inserted [4].

2.2 CURRENT CONSERVATION PRACTICES AND REGULATORY FRAMEWORKS

The conservation of cultural heritage follows specific rules and practices based on the legislation of the country concerned. Despite this, efforts have been made to establish standardized principles for conservation. Among the most influential are the 1964 International Charter for the Conservation and Restoration of Monuments and Sites (commonly known as the Venice Charter) [66] and the 1999 Burra Charter [10]. Individual countries have then assimilated these directives based on their own sensitivities and traditions in the field of conservation, nevertheless differentiating the various aspects contained in these shared documents. For example, in Italy, monument conservation operates within the framework of the 2004 Cultural Heritage and Landscape Code (Codice dei Beni Culturali e del Paesaggio) [104], a series of legislations that regulates conservation and intervention protocols. This regulatory framework governs the identification, protection, conservation, and enhancement of Italy's cultural assets. It defines obligations for the preservation of monuments, archaeological sites, historic buildings, and landscape areas of cultural significance. It regulates conservation practices by mandating authorization procedures for any intervention on protected cultural properties, technical standards for restoration work, and protocols for materials usage and methodology. It also governs the administrative aspects of heritage protection through detailed provisions on property designation processes, institutional responsibilities across different governmental levels, and coordination mechanisms between the Ministry of Cultural Heritage and regional authorities. However, the Code's regulatory primary focus remains on the physical preservation and cultural integrity of

the heritage assets themselves rather than on public safety considerations or visitor management systems. The lack of risk assessment practices for heritage assets is a common problem and will be discussed in the next paragraph.

2.3 RISK ASSESSMENT IN CULTURAL HERITAGE

The topic of risk assessment in cultural heritage is addressed in the literature only through two perspectives:

1. The cultural heritage assets are the elements at risk from external natural phenomena. This field of research usually deals with seismic vulnerability of historic structures [102] [9] [72], climate change impacts on archaeological sites [50] [98] [125], and environmental degradation effects on architectural monuments [28] [114]. This approach usually employs traditional risk assessment frameworks where the heritage object represents the vulnerable element requiring protection from external hazards such as earthquakes, flooding [138], extreme weather events, or anthropogenic environmental changes [48] [134] [7].

2. Natural environmental hazards threaten both cultural heritage sites and their human occupants, focusing on geological instabilities such as landslides, rockfalls, and seismic events that endanger heritage locations and visitor safety simultaneously [45] [46] [89] [41] [35] [40]. This research framework typically applies conventional geological hazard assessment methodologies to heritage contexts, again using established techniques from natural hazard risk analysis while considering the additional complexity introduced by heritage value preservation requirements.

The risk assessment concept developed in this work consist of a different approach where the cultural heritage asset itself serves as the source of risk to human safety. This "heritage-as-hazard-source" approach addresses scenarios where architectural elements, decorative features, or structural components of historic buildings pose direct threats to visitors, residents, or passersby through potential detachment or collapse. This field is currently underdeveloped, despite the realization of initial studies in recent years [33] [74] [119] [130] [18]. Currently, the study of risk of material detachment from buildings constructed in stone focuses on the analysis of the physical-mechanical characteristics of the material [119]

through the use of non-destructive techniques [84] [20] [52]. Multidisciplinary approaches are often adopted that utilize chemical-physical and petrographic techniques to characterize the conservation state of the material [135] [31] [44]. One of the main problems of this type of studies is that they focus on individual elements and are often not applicable on a large scale to facades of large buildings. A comprehensive vision that analyzes broad portions of buildings in order to identify the areas most at risk, on which to then deepen investigations, is absent in the literature. This perspective of framing the problem on a broader scale is addressed in this research by assimilating it to what occurs on rock slopes. In a classic slope study, areas subject to possible stability problems are first identified, and these are then studied in detail [113][142]. This work therefore proposes the use of this scheme to define an investigation methodology that is capable of working on multiple scales, identifying the most susceptible elements and then analyzing the critical cases. To do this it is necessary to frame the problem from a geological and geomechanical point of view, characterizing the architectural elements from a material perspective.

2.4 FLORENTINE SANDSTONES: DISCONTINUITIES, FAILURE MODES AND SIMILARITIES TO NATURAL ROCKFALL PHENOMENA

Pietraforte represents the primary focus of this investigation due to its widespread utilization in Florence's historic architectural heritage and its distinctive geological characteristics that render it particularly susceptible to specific failure mechanisms. This sedimentary rock, whose name derives from the Italian words "pietra" (stone) and "forte" (strong), historically earned recognition for its exceptional mechanical properties, particularly its high compressive strength, which established it as a common construction material throughout the Roman period and subsequent architectural developments. Together with Pietra Serena, another locally sourced sandstone variety, Pietraforte constituted one of the most extensively employed building materials (Figure 5) in Florence's urban development, with its widespread adoption facilitated by proximate quarry locations, ease of extraction, and superior mechanical characteristics [79].

The geological formation and compositional characteristics of Pietraforte create specific structural features that directly influence its long-term stability performance in architectural applications. As a quartz rich arkosic sandstone, Pietraforte exhibits heterogeneous mineralogical composition including variable clay content that generates pronounced anisotropic

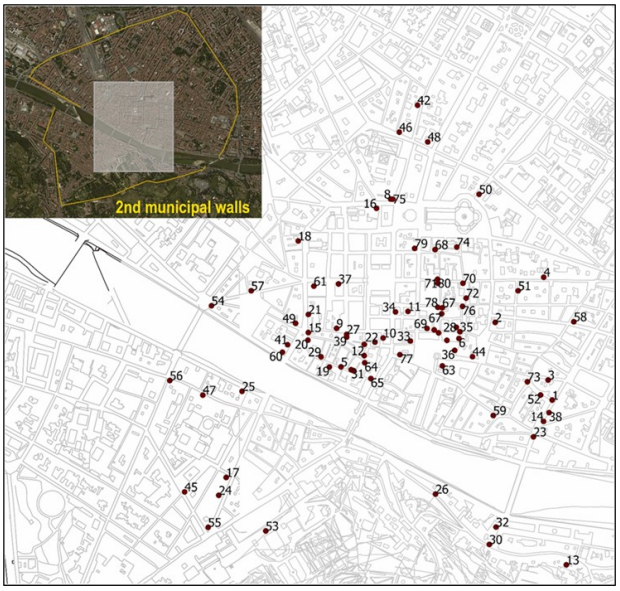


Figure 5: Florence main buildings made in Pietraforte. 1 Arco dei Peruzzi, 2 Bargello, 3 Bourbon del Monte, 4 Casa Altoviti, 5 Casa Buondelmonti, 6 Casa del Garbo, 7 Casa Guidacci, 8 Casa Marignolli, 9 Casa-torre dei Foresi, 10 Loggia del Mercato Nuovo, 11 Orsanmichele, 12 Palagio di Parte Guelfa, 13 Palazzo Alamanni, 14 Palazzo Alberti, 15 Palazzo Bartolini-Salimbeni, 16 Palazzo Bezzoli, 17 Palazzo Biliotti, 18 Palazzo Boni-Antinori, 19 Palazzo Borgherini, 20 Palazzo Buondelmenti, 21 Palazzo Cambi del Nero, 22 Palazzo Cavalcanti, 23 Palazzo Corsi-Horne, 24 Palazzo Corsini Suarez, 25 Palazzo Coverelli, 26 Palazzo da Uzzano, 27 Palazzo Davanzati, 28 Palazzo de' Cerchi, 29 Palazzo degli Altoviti, 30 Palazzo dei Mozzi, 31 Palazzo del Gran Siniscalco, 32 Palazzo Del Nero, 33 Palazzo dell'arte dei mercatanti, 34 Palazzo dell'Arte della Lana, 35 Palazzo della Condotta, 36 Palazzo della Mercatanzia, 37 Palazzo dello Strozzino, 38 Palazzo di Benedetto degli Alberti, 39 Palazzo Davanzati, 40 Palazzo Giandonati, 41 Palazzo Gianfigliazzi, 42 Palazzo Ginori, 43 Palazzo Giugni, 44 Palazzo Gondi, 45 Palazzo Guadagni, 46 Palazzo Lotteringhi della Stufa, 47 Palazzo Manetti, 48 Palazzo Medici, 49 Palazzo Minerbetti, 50 Palazzo Niccolini, 51 Palazzo Pazzi Quaratesi, 52 Palazzo Peruzzi-Lotti, 53 Palazzo Pitti, 54 Palazzo Ricasoli, 55 Palazzo Ridolfi, 56 Palazzo Rinuccini, 57 Palazzo Rucellai, 58 Palazzo Salviati, 59 Palazzo Soldani, 60 Palazzo Spini, 61 Palazzo Strozzi, 62 Palazzo Uguccioni, 63 Palazzo Vecchio, 64 Residenza dell'arte dei Galigai, 65 Torre de' Baldovinetti, 66 Torre de' Buondelmonti, 67 Torre de' Cerchi, 68 Torre de' Visdomini, 69 Torre degli Alepri, 70 Torre dei Donati, 71 Torre dei Ghiberti, 72 Torre dei Giuochi, 73 Torre dei Peruzzi, 74 Torre dei Pierozzi, 75 Torre del Vescovo, 76 Torre della Castagna, 77 Torre di Casa Ciacchi, 78 Torre Galigai, 79, 80 Torre degli Adimari.Some of the most famous buildings made in Pietraforte until the XVI century. (From [30])

behavior, calcite cement with irregular distribution patterns that create zones of differential strength, and micaceous laminations that establish preferential separation planes [95]. These intrinsic material properties interact with natural geological processes to produce systematic discontinuity networks including primary bedding planes inherited from original sedimentary deposition, tectonic joint systems developed during regional deformation events, secondary fracture networks created through stress relief and weathering processes, and calcite vein systems that often represent zones of mechanical weakness despite their apparent structural reinforcement. The urban environmental context of Florence significantly accelerates Pietraforte degradation through multiple synergistic mechanisms [116]. Atmospheric pollution creates acidic conditions that preferentially attack carbonate cement, while thermal cycling between daily and seasonal temperature variations induces differential expansion and contraction that progressively opens existing discontinuities. Moisture infiltration through these discontinuities facilitates freeze-thaw processes during winter months, salt crystallization from urban pollution sources, and chemical weathering reactions that further weaken material bonds along existing weakness planes. The cumulative effect of these processes creates progressive deterioration patterns that systematically exploit the natural discontinuity networks present within Pietraforte blocks. Historical quarrying practices and construction techniques have additional implications for understanding contemporary stability issues in Pietraforte elements. The principal historic quarries were located in the southern zone of Florence along the Arno River [30] [29], with different quarry sites producing stone with subtly different characteristics due to local geological variations. Construction practices historically recognized the anisotropic properties of sedimentary stones, with empirical knowledge guiding block orientation to optimize structural performance and minimize weathering susceptibility. However, modern analysis reveals that optimal placement practices were not universally applied, and many existing installations exhibit orientations that maximize rather than minimize instability potential. The morphological characteristics of gravitational failures in Pietraforte consistently demonstrate activation along pre-existing geological discontinuities, with detachment surfaces exhibiting fresh rock exposure that clearly indicates separation along natural weakness planes. Field observations conducted during this research have documented numerous examples of these failure mechanisms across various architectural elements, ranging from small-scale spalling of individual laminations to large-scale detachment of substantial block

portions. The consistency of these patterns across different building contexts suggests that gravitational failure mechanisms represent systematic rather than random processes, governed by predictable geometric relationships between discontinuity orientation, element geometry, and gravitational forces. Examples of such detachments are visible in Figure 6 and in Figure 7.



Figure 6: Example of detachment via gravitational failure in a Pietraforte facade element on the facade of the Fortezza da Basso, Florence



Figure 7: Example of detachment via gravitational failure in a Pietraforte facade element on the facade of the Fortezza da Basso, Florence

The most prevalent failure modes observed in Pietraforte elements can be categorized into two primary geometric configurations based on the number and orientation of activated discontinuity planes:

- Single-plane failures, which represent the most common occurrence, involve separation along a single bedding plane or lamination surface, creating detachment surfaces that closely resemble classical planar failure mechanisms in rock slopes. These failures typically manifest as sheet-like spalling or delamination events where material separates cleanly along one dominant weakness plane. An example is visible is Figure 8.

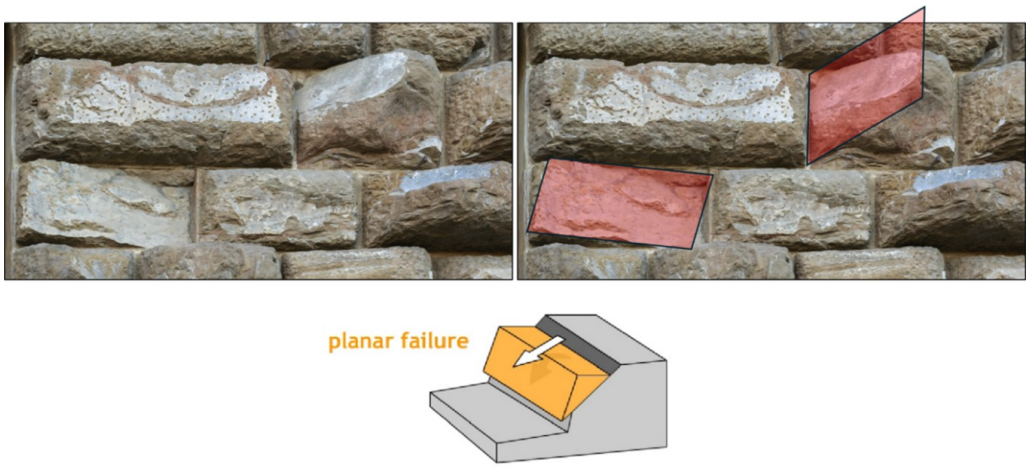


Figure 8: Example of a planar-like failure on a block on the facade of Palazzo Pitti, Florence

- Two-plane failures that create detachment geometries that resemble wedge failure mechanisms. These failures manifest as the spalling of blocks along two weakness plane. An example is visible is Figure 9.

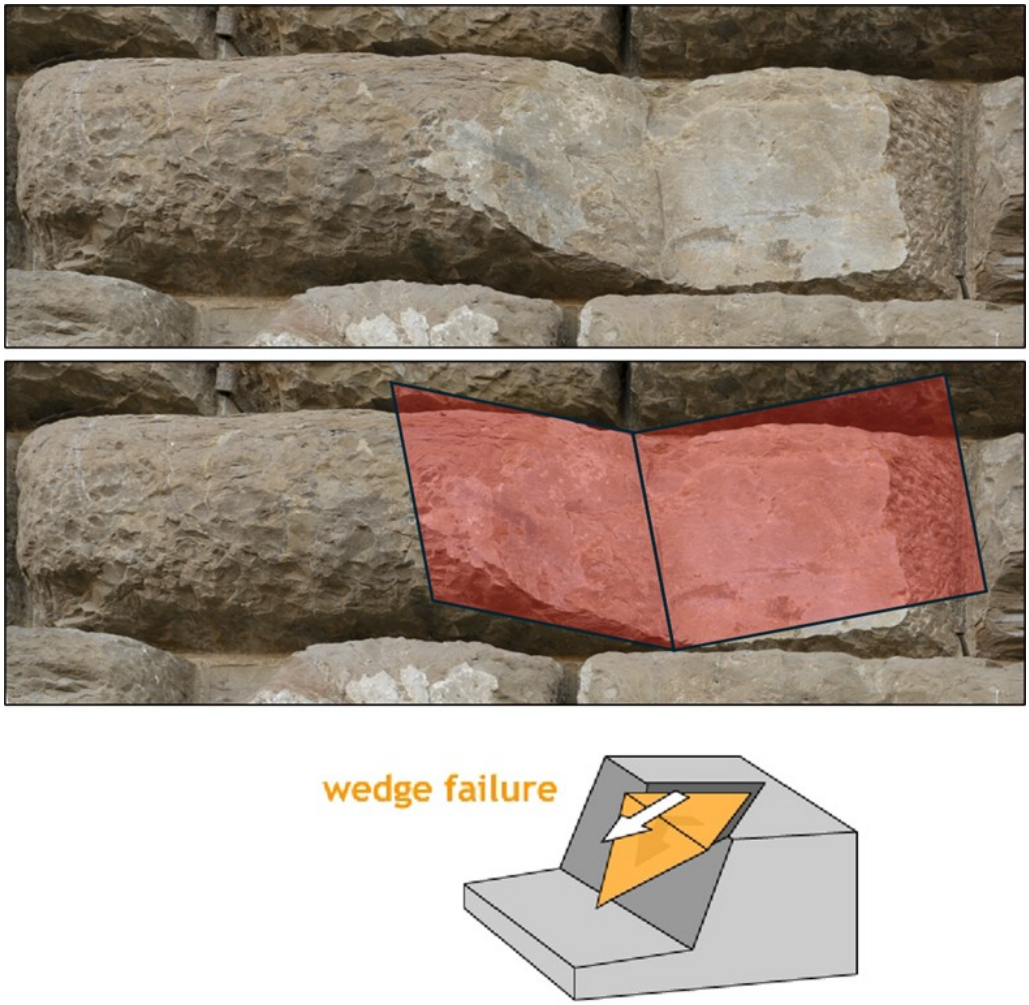


Figure 9: Example of a wedge-like failure on a block on the facade of Palazzo Pitti, Florence

- One or two-plane failures that create detachment geometries that resemble planar or wedge free fall failure mechanisms. These failures manifest as the falling of blocks along one or multiples weakness plane. An example is visible is Figure 10.

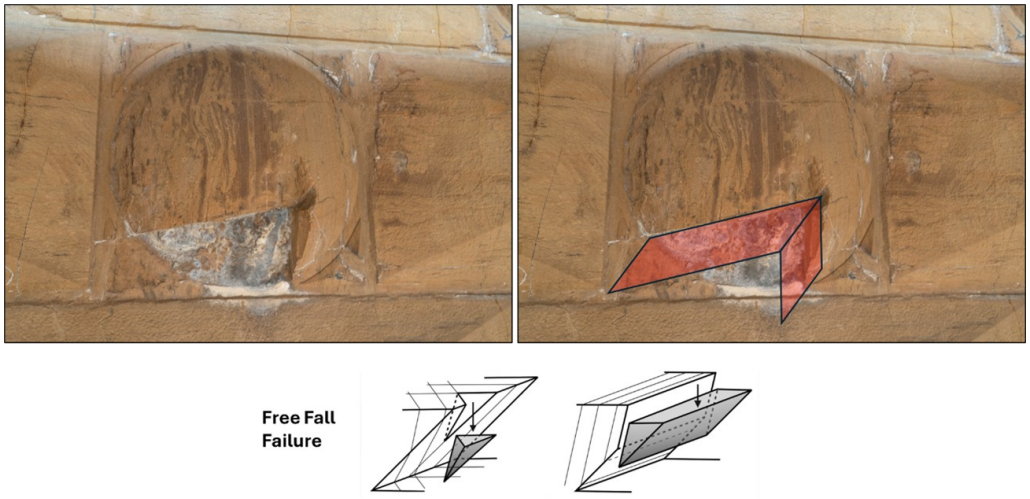


Figure 10: Example of a freefall-like failure on a block on the facade of Palazzo Pitti, Florence

The significance of these observations is in the recognition that stone material used in historical buildings can fail trough detachment mechanisms that follow predictable patterns governed by geological discontinuity networks. This suggests that systematic assessment methodologies can identify potentially unstable configurations before failure occurs. This proactive rather than reactive approach is currently lacking in conservation strategies and this research aims to contribute to an advancement in this direction.

2.5 GEOMECHANICAL APPROACHES IN ROCK ENGINEERING

Rock slope stability analysis represents a mature engineering discipline that has developed sophisticated methodologies for evaluating the potential for rock mass failure under various geological and environmental conditions. The fundamental approach to stability analysis involves systematic evaluation of the geometric, mechanical, and hydraulic factors that influence rock mass behavior, with particular emphasis on discontinuity-controlled failure mechanisms that dominate stability conditions in jointed rock masses [65]. The evolution of rock slope stability

analysis has been driven by the need to address increasingly complex engineering challenges in mining, civil engineering, and infrastructure development projects. Contemporary stability analysis methodologies integrate multiple analytical approaches, ranging from simple geometric assessments that identify kinematically feasible failure modes [36]. to complex numerical simulations that account for stress-strain behavior, time-dependent deformation, and dynamic loading conditions [143] [99]. The selection of appropriate stability analysis methods depends critically on the specific geological conditions, failure mechanisms of concern, and required level of analytical sophistication. For discontinuity-controlled failures, which represent the primary focus of this research, kinematic analysis provides the foundational framework for identifying feasible failure modes based purely on geometric relationships between discontinuity orientations and slope geometry [82] [51]. Kinematic analysis employs stereographic projection techniques to visualize three-dimensional geometric relationships in two-dimensional space, enabling rapid assessment of potential sliding directions, critical angles, and failure mode combinations across multiple discontinuity sets.

2.5.1 *Kinematic analysis*

Kinematic analysis constitutes the fundamental framework for evaluating potential failure mechanisms in jointed rock masses by examining the geometric relationships between discontinuity orientations and the overall geometry of rock slopes. This analytical approach, pioneered by Markland [82] and refined by numerous researchers, is an effective method for identifying kinematically feasible failure modes without requiring detailed knowledge of rock mass strength properties or stress conditions [51], [100]. The strength of kinematic analysis lies in its ability to eliminate impossible failure modes from and highlight geometrically feasible mechanisms that warrant further investigation through limit equilibrium or numerical analysis methods. The theoretical foundation of kinematic analysis rests on the principle that rock mass failure along discontinuities requires specific geometric conditions to be satisfied before failure can occur, regardless of the magnitude of applied forces or material strength characteristics. For planar sliding failure, the discontinuity plane must dip in a direction that allows gravitational forces to drive sliding motion, typically requiring the discontinuity dip direction to fall within approximately ±30° of the slope face direction, while the discontinuity dip angle must exceed the friction angle to overcome frictional resistance

[65]. These geometric constraints define "daylight envelopes" on stereographic projections that delineate orientations capable of producing specific failure modes under purely geometric considerations. Wedge failure mechanisms involve similar requirements as they depend on the intersection of two or more discontinuity planes to create potentially unstable rock wedges. The kinematic feasibility of wedge failure requires the intersection line (plunge direction) to daylight on the slope face while plunging at an angle steeper than the friction angle along the intersection [65].

2.5.2 *Limit equilibrium methods*

Limit equilibrium methods evaluate the balance between forces that drive potential failures and those that resist movement along defined failure surfaces. These methods assume that failure occurs when driving forces exceed available resistance, with the safety factor defined as the ratio of resisting to driving forces at the moment of incipient failure [37] [1]. For planar sliding failures, the analysis reduces to a two-dimensional problem where gravitational forces acting on the sliding mass are resolved into components parallel and perpendicular to the failure surface, with resistance provided by shear strength along the discontinuity plane and any external supporting forces [65]. The driving force component parallel to the failure surface must be balanced by available shear resistance, which typically follows non-linear strength criteria such as the Mohr-Coulomb model for intact rock or the Barton-Bandis criterion for rock joints. Wedge failure analysis requires decomposition of gravitational and external forces into components acting along each bounding surface, followed by evaluation of available shear resistance along each discontinuity plane [65]. The determination of discontinuity shear strength characteristics represents a critical aspect of limit equilibrium analysis, as the accuracy of stability assessments depends fundamentally on appropriate characterization of resistance parameters. The Barton-Bandis shear strength criterion has gained widespread acceptance for rock joint applications due to its ability to account for the effects of surface roughness, normal stress level, and joint wall strength on shear resistance [15]. This criterion expresses peak shear strength as:

$$\tau = \sigma_n \tan\left[\mathrm{JRC} \cdot \log_{10}\left(\frac{\mathrm{JCS}}{\sigma_n}\right) + \varphi_r\right] \tag{1}$$

where JRC represents the joint roughness coefficient, JCS denotes joint wall compressive strength, φ_r is the residual friction angle, and σ_n represents normal stress acting on the joint surface.

2.6 KNOWLEDGE GAP IN THE APPLICATION OF GEOMECHANICAL METHODOLOGIES TO HERITAGE MATERIALS AND THE PROBLEM OF USING SOFTWARE BUILT FOR NATURAL SLOPES

The direct application of conventional geomechanical software and methodologies developed for natural rock slope analysis to heritage architectural elements reveals fundamental incompatibilities. Commercial rock slope stability software packages such as RocScience Swedge, SLIDE, and Dips, while sophisticated and well-validated for natural slope applications, incorporate geometric assumptions and analytical frameworks that can't be adaptped to the characteristics of architectural heritage elements [106]. These limitations come from fundamental differences in scale, geometry and boundary conditions between natural rock slopes and built heritage structures. The geometric assumptions embedded in conventional slope stability software represent perhaps the most significant barrier to heritage applications. Natural slope analysis typically assumes semi-infinite slope geometries where failure surfaces extend from the slope face to theoretically infinite depths, with slope faces represented as planar or regularly curved surfaces extending over substantial lateral distances. In contrast, architectural elements exhibit finite, often complex three-dimensional geometries with multiple face orientations, irregular boundaries, and overhanging features that cannot be adequately represented within conventional slope analysis. Scale effects represent another critical limitation in applying conventional geomechanical approaches to heritage elements. Natural slope stability analysis typically addresses rock masses measuring tens to hundreds of meters in lateral extent, where discontinuity systems are assumed to be sufficiently persistent and well-connected to define continuous failure surfaces across the entire analysis domain [100]. Architectural elements, by contrast, typically measure from decimeters to a few meters in extent, creating situations where discontinuity persistence and connectivity become critical factors that cannot be assumed a priori. Individual stone blocks may contain discontinuities with limited trace lengths that terminate within the block boundaries, creating failure mechanisms that involve stepping between different discontinuity sets or failure through intact rock bridges rather than sliding along continuous surfaces. From the technical-application

point of view, this incompatibility is fundamentally reflected in the way planes are defined: in slope stability software, discontinuities are defined by a pair of angular values (Dip-Dip Direction or other angular orientation conventions), which defines not a single plane but a family of discontinuities. This is due to the assumption that plane families have semi-infinite extension within the slope and it is taken for granted that somewhere, if their orientations allow it, they will intersect to form wedges. This assumption is fundamentally wrong in the application case under examination, where one wants to evaluate the stability of individual planes with defined orientation and position. The definition of the position of planes relative to other planes and to the point cloud represents a crucial problem. Geometrically, it means setting up the problem no longer from a purely angular point of view but requires the integration of a different method for defining discontinuities, which also takes into account the position in three-dimensional space. The consequences and implications of all this are treated in detail, from a mathematical point of view, in chapter 4. This section only aims to introduce from a conceptual point of view the main limitations that led to the choice of developing an ad-hoc workflow and software.

It is important to note that software tools capable of modeling individual discontinuities do exist. Most of these adopt the conventional Baecher disc model [70] to represent discontinuity persistence and spatial position. Examples include commercially available packages such as RocScience RocSlope2 [107] and RocSlope3 [108], as well as research-oriented platforms like DICE [86] and ROKA [87]. These tools offer functionality for discrete discontinuity analysis, but remain fundamentally oriented toward slope stability contexts. Their kinematic analyses are typically statistical in nature, relying on stereonet-based plotting and probabilistic interpretation of discontinuity families, an approach well suited to geological surveys but misaligned with the needs of conservation scientists working on discrete architectural elements. Moreover, these platforms do not provide an integrated workflow that spans from kinematic to dynamic analysis. This gap is particularly critical in heritage applications, where the stability of individual blocks or features must be assessed with respect to their precise geometric configuration and material behavior.

A final fundamental difference in applying geological concepts to architectural elements concerns discontinuity detection methodology. Scanline methods, which form the foundation of conventional discontinuity characterization in rock masses, assume the ability to traverse continuous exposure surfaces and systematically record intersection points with dis-

continuities of various orientations [100]. In architectural contexts, the fundamental premise of scanline surveying, that discontinuities represent natural geological features with statistically predictable orientations and spacings, does not hold, as every single construction block is not geologically correlated with the next, as they may come from different part fo the quarry, or may have been shaped and oriented differently.

Similarly, automated discontinuity extraction algorithms developed for natural rock masses prove inadequate for heritage applications. These approaches typically employ surface morphology analysis to identify planar features, operating on the assumption that discontinuity surfaces create distinctive morphological signatures (e.g., planar breaks, linear traces, or surface roughness changes) that differ systematically from intact rock surfaces [47] [105] [25] [141] [55]. In architectural elements, however, the surface morphology has been intentionally modified through anthropogenic processes: stone blocks have been carved, and sculpted according to architectural and decorative requirements. Consequently, the morphological contrasts that automated algorithms rely upon to distinguish discontinuity surfaces from intact material are absent or not relevant.

While line-tracing and texture-based detection methods offer potentially more suitable approaches for heritage applications, they fail to address the fundamental heterogeneity of features requiring identification. In natural rock masses, discontinuity detection algorithms can be calibrated to recognize a relatively consistent set of morphological or chromatic signatures like the characteristic texture of joint surfaces or the color contrast of weathered discontinuity traces [103] [77] [56] [57]. In architectural heritage, however, the features to be traced vary dramatically not only between different structures but even between adjacent blocks within the same structure. In one block, the critical feature may be a geological discontinuity such as an infilled vein, where detection relies on identifying light linear traces against darker stone. In another element, the target may be a hairline fracture barely visible to the naked eye, requiring detection of subtle shadow patterns or minute surface offsets. In one case examined during this research, a finely sculpted decorative element contained a structurally significant crack that would be indistinguishable to trace detection algorithms from the numerous intentional carved lines.

The result is that automated discontinuity detection methods either fail to identify genuine structural discontinuities or generate false positives from architectural surface features. While these methods can potentially

be applied to heritage structures, their implementation requires the development of targeted approaches designed for specific subsets of cases with comparable characteristics. For instance, automated detection algorithms may prove effective for extensive facades composed of similarly dressed stone blocks with consistent surface treatments, where the morphological signatures of discontinuities exhibit sufficient homogeneity to enable reliable calibration. However, such approaches cannot be generalized across the full spectrum of heritage applications, necessitating case-by-case evaluation of their applicability.

3

METHODOLOGY

3.1 APPLYING GEOMECHANICAL METHODOLOGIES TO ARCHITECTURAL ELEMENTS

The proposed method is essentially an adaptation of principles, concepts, and methodologies that come from the field of rock mechanics and are applied to the study of architectural elements. Cross-disciplinary 'contamination' frequently occurs in multidisciplinary disciplines such as cultural heritage conservation, yet it usually tends to be confined to methodological approaches rather than deeper theoretical integration. It is common to see techniques from many disciplinary fields being applied directly, drawing results that we can define as standard for the technique: to give an example in the field of geosciences, the mineralogical study of a rock sample from a historic building is analyzed in the same way as a sample from any other source would be analyzed. This study, however, borrows the techniques and concepts of rock mechanics in a somewhat different way: it does not limit itself to applying the techniques but sets up the entire research by modifying the initial paradigm. The investigated architectural element therefore loses its intrinsic characteristics that we categorize according to the stylistic-conservative point of view and becomes a rock mass described by purely geological characteristics. This involves an inevitable reciprocal adaptation of terminology and definitions, that will be used in the most rigorous manner allowed by this compromise. This premise is made because many concepts have been adapted for this study and are not to be considered classic studies in the field. When, for example, concepts such as kinematic susceptibility or the calculation of the safety factor are dealt with, only some parts have been considered as they appear in literature, and many factors have been adapted. All this series of adaptations and concessions that are necessary must however be considered as a compromise made as an improvement in a more analytical direction compared to approaches that still today

are based almost solely on subjective considerations of restoration professionals. All the limits present in the approach, and the assumptions that are necessary for it to function, are made explicit and discussed in the appropriate sections.

3.2 PROPOSED WORKFLOW

The research presented in this work has as its objective the definition of a complete workflow and the creation of the necessary tools for its implementation. The study has therefore seen, in addition to the definition of the operational methodology, also the development of custom software, which was developed within the research to specifically respond to the analytical requirements of the study. The software, called RoDiAn (Rock Discontinuity Analyzer), which was created with the objective of being open source and publicly distributed on a public directory, will be presented in the next chapter in detail. In this chapter the proposed methodology will be described in each of its steps. The methodology workflow is structured as a sequential process that transforms raw building documentation into quantitative stability assessment results through five primary stages: building documentation, 3D data acquisition, element extraction, pre-processing, and analytical assessment using the custom-developed RoDiAn software (Figure 11) The workflow starts with the documentation of the target building through a 3D point cloud (3DPC) acquisition. From the building 3DPC individual architectural elements of interest are identified and extracted for detailed analysis. On the individual 3DPCs of the elements, features of interest (discontinuities) are traced. The results of this pre-processing finally serve as input for RoDiAn.

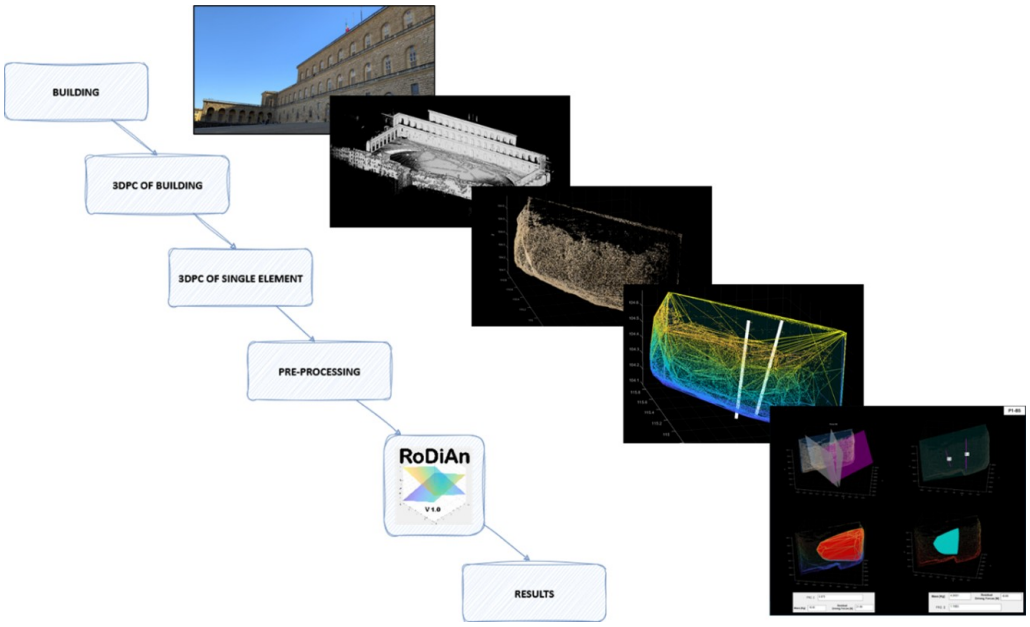


Figure 11: Methodology flowchart.

The operational workflow essentially consists of two parts, one of acquisition and pre-processing, and one of data analysis with the custom made software. Figure 12 shows a detailed logic flowchart of the methodology.

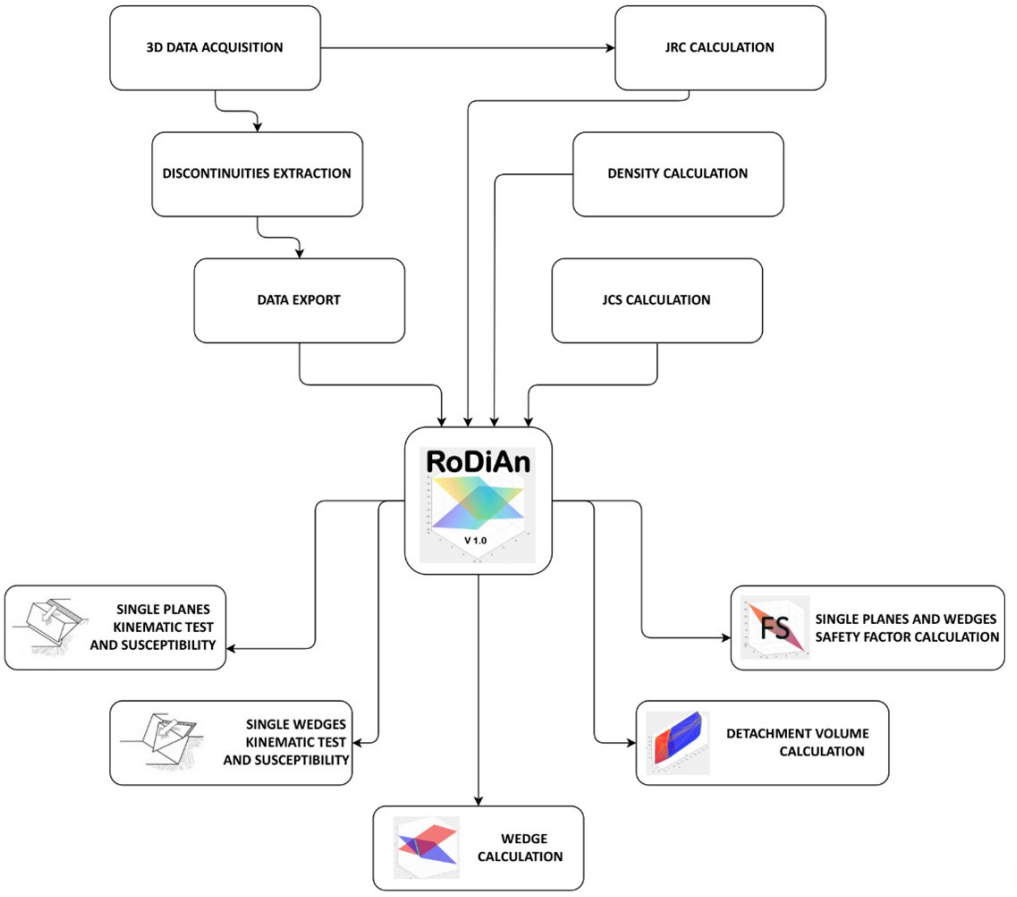


Figure 12: Logic flowchart of the methodology.

The data acquisition part includes all the entities that serve as input for processing through RoDiAn. The main data is the 3D point cloud of the element to be analyzed, on the basis of which the geometric and volumetric information of the element is extracted. Based on the point cloud, two other pieces of information are extracted: the orientation of the discontinuities and the Joint Roughness Coefficient (JRC) parameter. From the material (or from literature data), the other two parameters necessary for the analysis are extracted: the Joint Wall Compressive Strength (JCS) coefficient and the density of the rock under analysis. The data thus obtained flow as input to RoDiAn, which provides as output:

- The results of the kinematic analysis for planar kinematics on single discontinuity and relative kinematic susceptibility index (KSIp)
- The results of the kinematic analysis for wedge kinematics on single discontinuity and relative kinematic susceptibility index (KSIw)
- The calculation of the position of individual wedges that form in the element
- The calculation of the volume and mass of possible detachments, both planar and wedge
- The safety factor for the sliding of individual blocks and wedges

3.3 3D DATA ACQUISITION

The proposed method relies primarily on the processing of 3D point clouds. For this reason, a 3D point cloud acquisition strategy is required to obtain high-resolution geometric data of the building facades The methodology has been tested to work on 3DPC datasets coming from multiple sources:

- Structure from Motion (SfM) – Handheld Photogrammetry
- Structure from Motion (SfM) – Drone Photogrammetry
- Hybrid - Mobile Laser Scanner (MLS) + Structure from Motion (SfM)

In the hybrid approach the MLS acquisition is conducted first to create a reference model with accurate global coordinates. This model is also used for positioning the individual architectural elements within the broader facade context, a task that may look trivial but gets challenging in large buildings. The first model serves as spatial reference data and geometric registration of the architectural elements relative to their actual positions on the building. Photogrammetry is then performed on the individual architectural elements to capture fine-scale surface features, discontinuities and textural characteristics critical for the analysis. The individual SfM 3D models are then scaled and georeferenced using the MLS cloud as reference. A challenge that occurred during the data analysis of the work is the computational constraints related to file size and processing time limitations when using high resolution 3DPC. An alternative workflow was implemented using textured 3D meshes as the primary data source, from which point clouds were subsequently sampled as needed. This approach significantly reduced computational workloads while maintaining the visual information required for discontinuity identification and characterization. It is important to note that a tradeoff is made for the geometric accuracy of the model, so this approach is useful in the cases where the discontinuities identification is made on visual feature and not on geometric ones. The effectiveness and implications of this methodological adaptation, including comparative analysis, are discussed in detail in chapter 7.

3.4 DISCONTINUITIES EXTRACTION (CLOUDCOMPARE)

One of the key steps in the data pre-processing phase is the identification and extraction of discontinuities within the elements. In this work, the extraction of discontinuities is carried out manually. The 3DPC or mesh of the individual element is imported into CloudCompare, which is used for plane fitting. To illustrate the procedure for manual discontinuity fitting, we examine Block P3-B3 (Figure 13) from the facade of Palazzo Pitti as a representative case:



Figure 13: Example Block P3-B3, Palazzo Pitti

The 3D entity is imported into CloudCompare, where each discontinuity intended for analysis requires the fitting of a plane that best approximates its spatial orientation. This is achieved using the 'Point List Picking' tool (Figure 14), which enables the user to trace points along the discontinuity line generating a new point cloud made of the selected points.

By selecting the newly obtained point cloud, composed of points belonging to the discontinuity trace, it is possible to obtain the best-fit plane through the 'Fit -> Plane' tool (Figure 15).

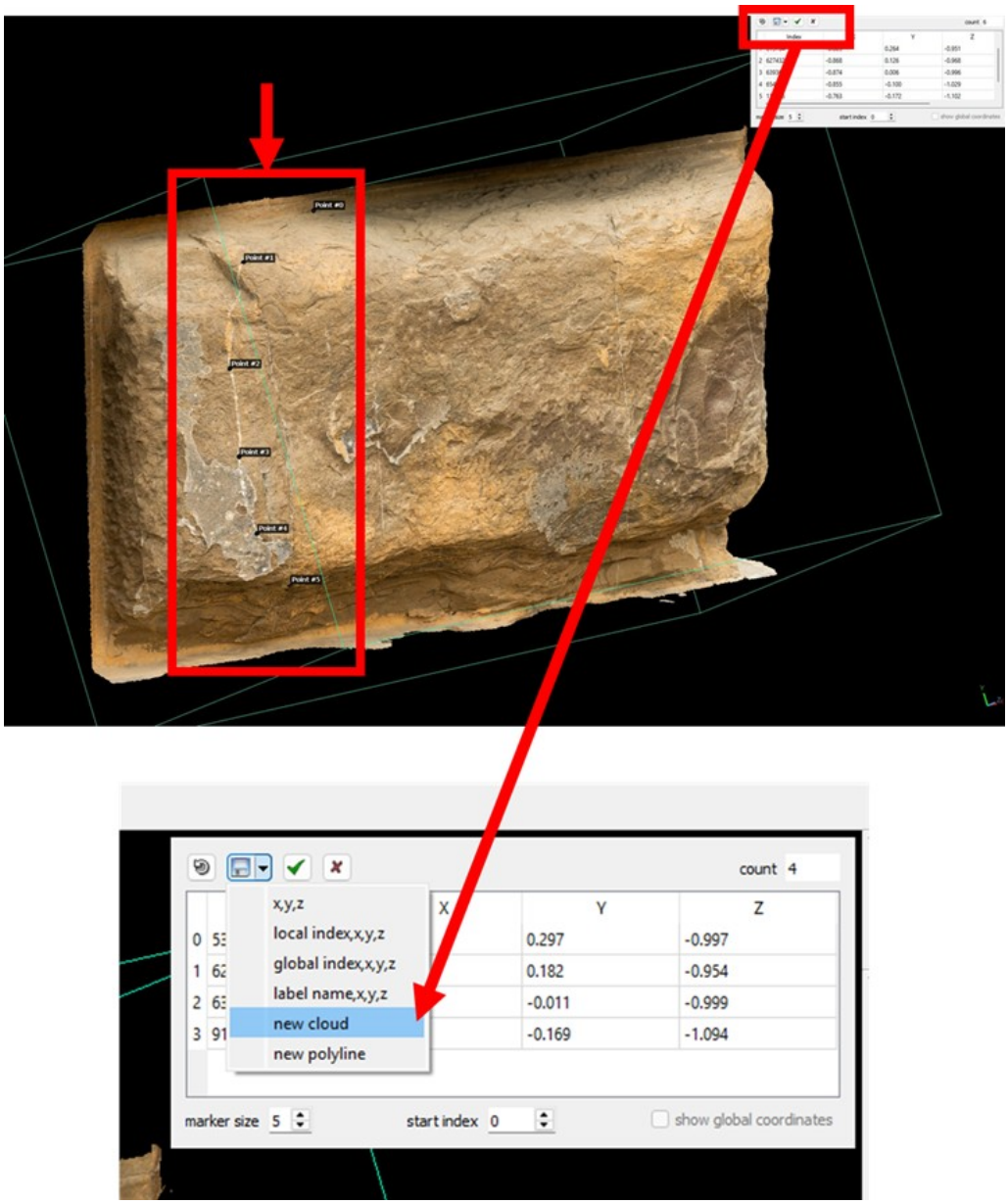


Figure 14: Manual discontinuity tracing in CloudCompare. Points are laid of the trace of the discontinuity (left red square) and a new cloud is created containing the selected points of the trace

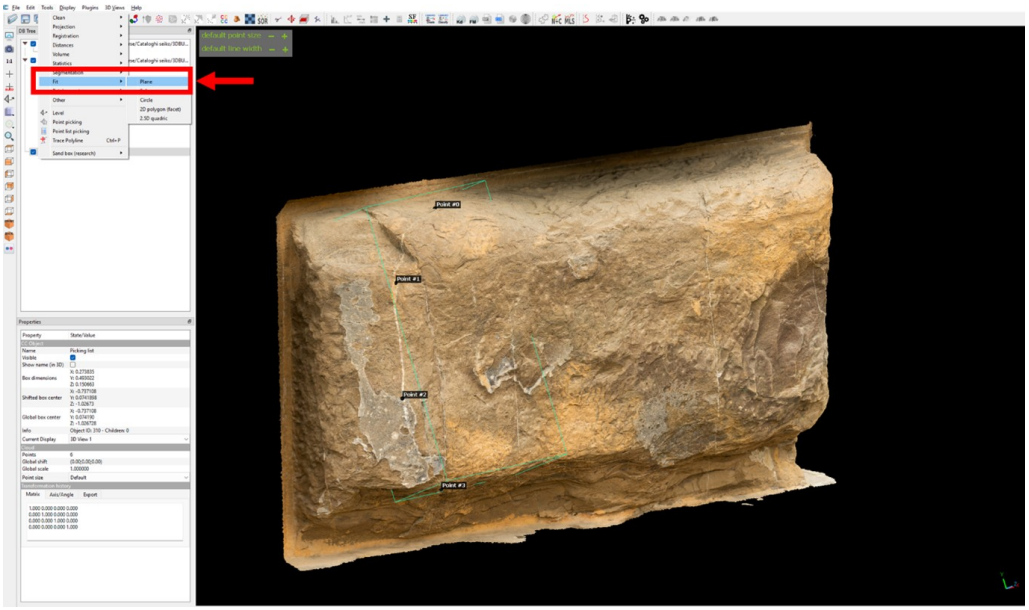


Figure 15: Plane fitting in CloudCompare via the 'Fit -> Plane' tool

This process is repeated for each discontinuity. The result is a set of planes whose information is exported through the 'Batch Export -> Export Plane Info' tool (Figure 16).

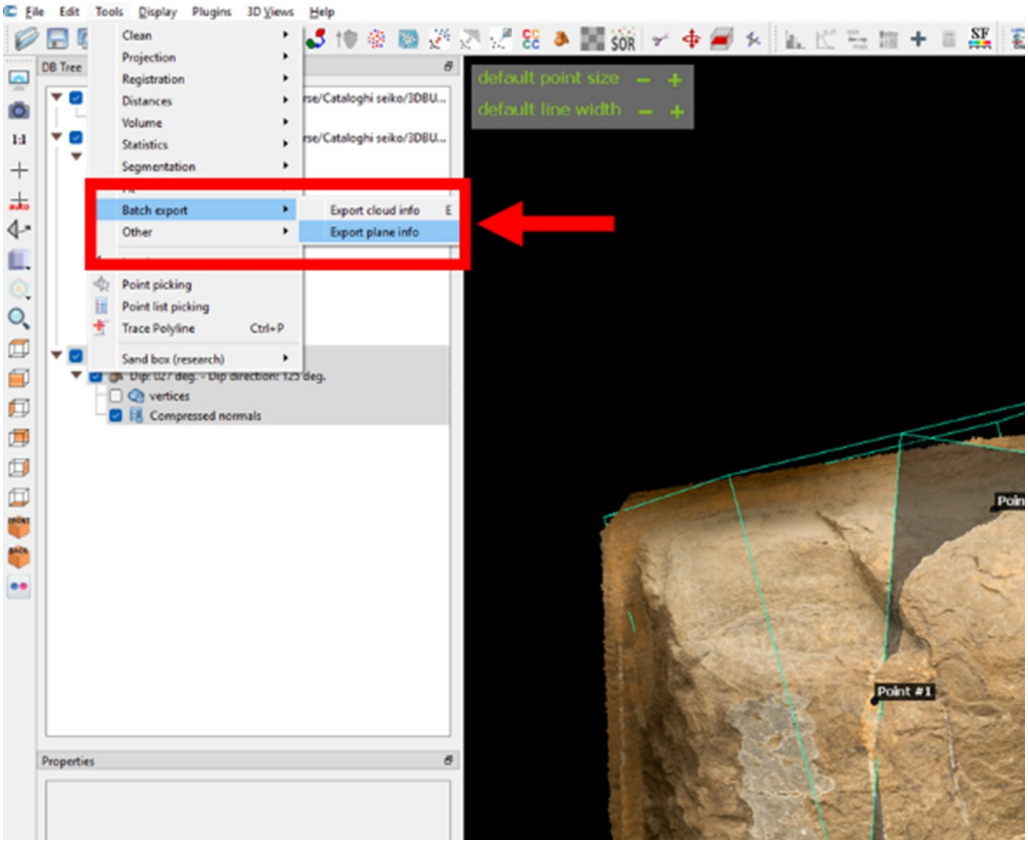


Figure 16: Planes info export in CloudCompare via the 'Batch Export -> Export Plane Info' tool

The .csv file generated by CloudCompare through the 'Batch Export -> Export Plane Info' command contains the following columns: 'Name, Width, Height, Cx, Cy, Cz, Nx, Ny, Nz, Dip, Dip Direction'. This information is automatically processed by RoDiAn, which analyzes the .csv file and extracts the information related to each plane. Two important clarifications regarding discontinuity fitting:

- The user can consider as a discontinuity any planar anisotropy, whether this is bedding, schistosity, foliation, joint, cleavage, fracture, fissure, crack, or fault plane. The methodology can also be used by fitting fictitious or hypothetical planes to verify different potential scenarios. The only limitation is that the discontinuities must be sufficiently approximable by a plane; at the moment it is not possible to create sliding surfaces with non-planar geometries (e.g. concave, convex, irregular)
- The discontinuities are always considered as lacking cohesive forces given by infill: the model used in the current iteration RoDiAn does not provide for the calculation of cohesive forces but only frictional ones. Consequently, in cases where fractures contain infill, the resulting resistance forces are systematically underestimated. This modeling choice is justified by two primary considerations: first, the deliberate underestimation of resistance serves as a conservative simplification that enhances safety; second, empirical experience indicates that the condition of infill within the innermost regions of discontinuities is typically unknown, and incorporating cohesive forces in such zones could result in an overestimation of the actual resistance to sliding.

3.5 GEOMECHANICAL PARAMETERS NEEDED FOR DYNAMIC ANALYSIS IN RODIAN

The workflow proposed integrates the possibility and the tools to perform dynamic analysis of the blocks or wedges identified as susceptible to any kinematics. The calculation of resistance and driving forces is performed within the RoDiAn software which automatically calculates the geometric factors necessary for the analysis, such as volume and sliding area. However, it is necessary to know other intrinsic parameters of the material under analysis that are not automatically calculable. The software uses the Barton criterion [15] for calculating resistance forces,

and it is therefore necessary to know the parameters that are embedded within the criterion itself:

- Joint Roughness Coefficient (JRC): Quantifies the surface irregularity of the joint
- Residual Friction Angle (ϕ): the basic friction angle of the rock surface with no roughness induced strength
- Joint Wall Compressive Strength (JCS): compressive strength of the rock material forming the joint walls

These parameters used in the Barton shear strength criterion are extensively documented in the rock mechanics literature. Barton and Choubey [14] first introduced JRC as a quantitative descriptor of joint surface roughness and provided standard roughness profiles that remain widely used for visual estimation. Subsequent studies by Barton and Choubey and Barton and Bandis [12] refined the methodology, presenting empirical correlations and charts that link JRC, JCS, and ϕr to shear strength under varying normal stresses. JCS has been shown to correlate with the uniaxial compressive strength of the intact rock, adjusted to account for weathering and joint wall alteration, and can be estimated using point load strength indices or Schmidt hammer rebound values. The residual friction angle, often interpreted as the basic friction angle of the rock material, can be determined through direct shear testing on planar joint surfaces or simpler tilt tests. These parameters, along with recommended ranges for different lithologies and joint conditions, are summarized in standard references such as Hoek and Brown [22], Hoek and Bray 1981 [65], and ISRM suggested methods [67]. For this reason, their determination in various application cases is feasible using literature data or direct tests. In the case of this work, the values of JCS and ϕr were taken from literature, while the JRC value was calculated directly and was the subject of an in-depth study that led to the definition of a methodology for calculating its value on 3D point clouds.

3.6 JRC CALCULATION USING EZ$_2$JRC

The JRC is one of the key parameters in Barton's shear strength criterion. Since its introduction, JRC has traditionally been estimated through visual comparison with ten standard profiles published by Barton and Choubey [14]. However, this method is inherently subjective and prone to human

bias [16]. To address these limitations, various statistical approaches have been proposed, beginning with Tse and Cruden [131] that were the first to correlate statistical parameters (e.g. Z_2) to the JRC value of the standard profiles. Subsequent studies refined these statistical approaches, and a very large number of statistical correlations is nowadays available. A recent review on the subject by Li and Zhang [78] counts 47 different empirical equations for estimating the JRC from statistical parameters. In parallel, fractal approaches were proposed, beginning with the methods of Turk et al. [133] and Lee et al. [76]. As with the statistical approach, fractal approaches have also become very numerous; in the recent review by Li and Huang [78], about 20 are counted. However, as Marsch and Fernandez-Steeger [83] emphasize, this trend has largely deviated from the intended purpose of the type-profiles, which were designed merely as a practical tool for visual estimation rather than as an axiomatic definition of JRC. The repeated re-digitization and parameter fitting of the same low-resolution profiles has led to a confusing number of correlations, often poorly documented and not universally consistent when applied to natural surfaces. The excessive mathematical elaboration is unnecessary and sometimes counterproductive, as simple metrics such as Z_2 perform equally well for classifying JRC ranges [83]. Marsch and Fernandez-Steeger then propose a simple, "good enough" workflow for calculating the JRC on rock surfaces, visible in Figure 17

This workflow, ideal for the application of this research, currently lacks a tool for its execution. This prompted the development of "EZ$_2$JRC", a software built for calculating the JRC on the 3D point cloud of a rock surface. The details on the functionalities and logic of the software are described in chapter 5, in the next paragraph is instead reported its operational workflow.

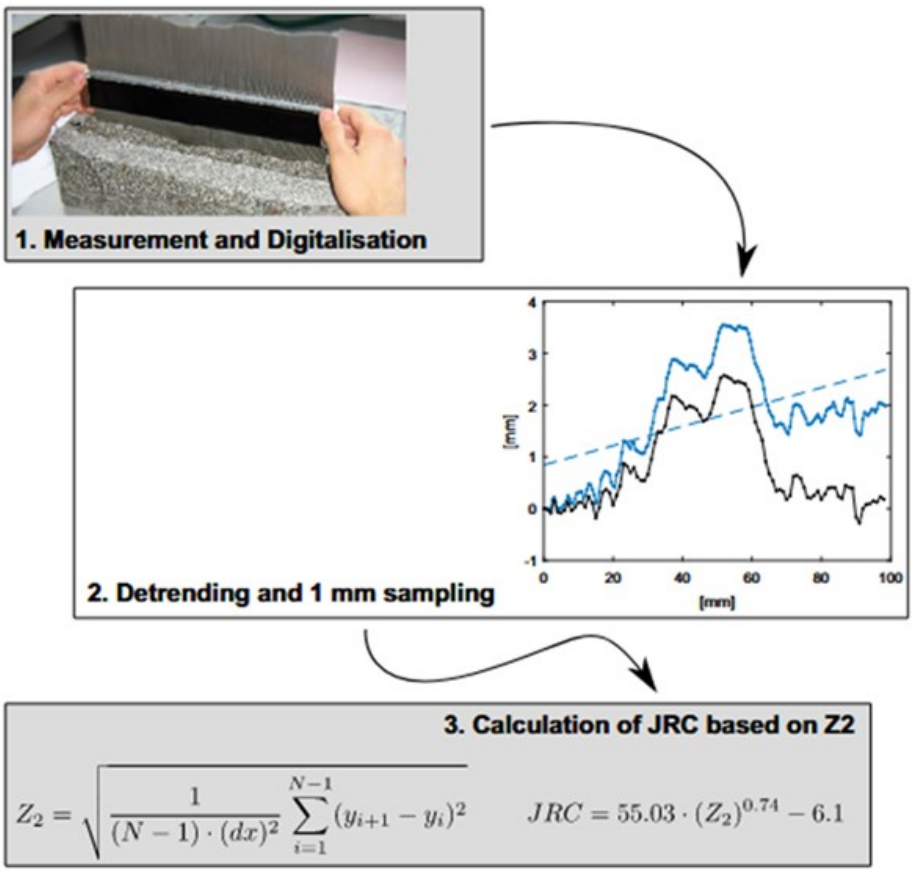


Figure 17: A simple, "good enough" workflow for the calculation of JRC, from [83]

3.6.1 *EZ$_2$JRC processing*

The software accepts 3D point clouds in either XYZ or XYZRGB format as input data. For the JRC calculation to be performed, the point cloud must have a minimum extent of 100 mm along the target direction of analysis. File importation is prompted by selecting the 'Load Point Cloud' button, which opens a dialog window where the user can select the desired file (Figure 18).

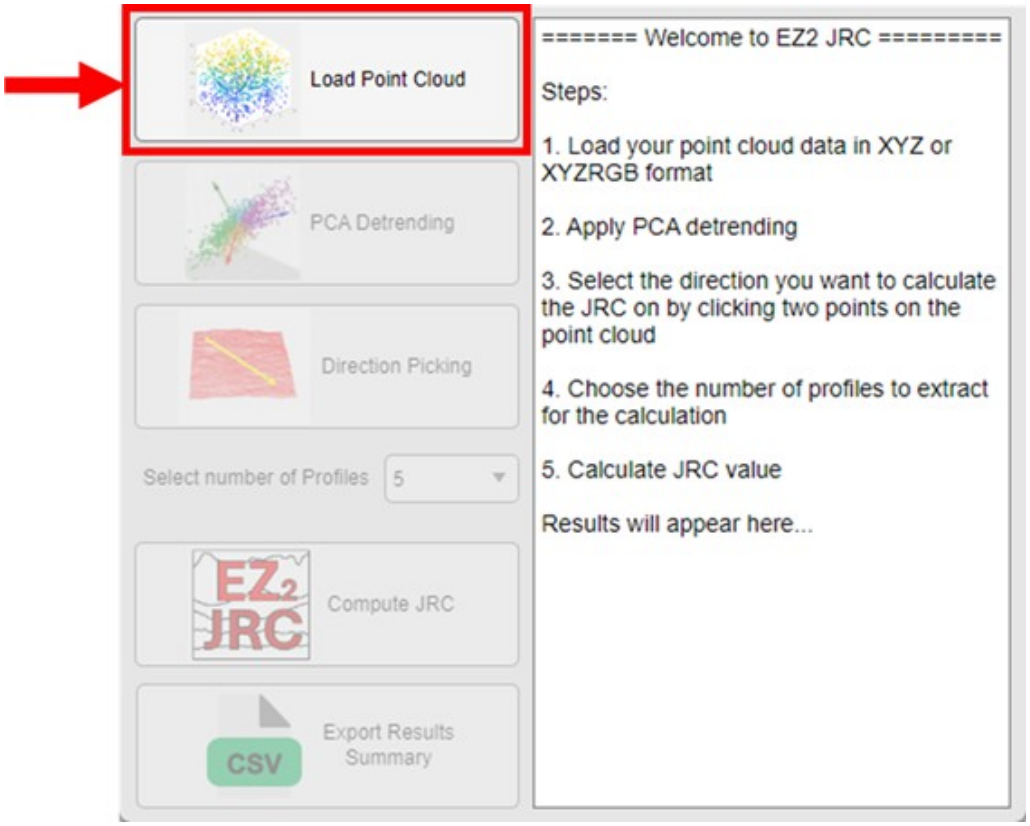


Figure 18: Point cloud loading in EZ$_2$JRC via the 'Load Point Cloud' button

The app then opens a 3D visualization window in which it is possible to observe and interact with the loaded 3DPC (Figure 19).

The next step is to perform the detrending of the point cloud through the 'PCA Detrending' button as shown in Figure 20.

The user must then specify the direction along which the Joint Roughness Coefficient (JRC) is to be calculated. Pressing the 'Direction Picking' button (Figure 21), the application prompts the user to click on two points within the point cloud, defining a direction vector for the JRC

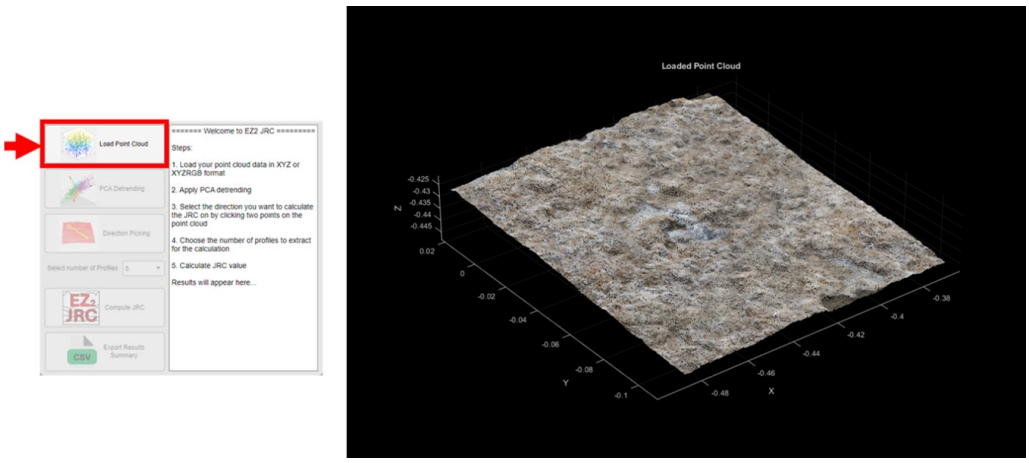


Figure 19: 3D visualization windows that opens in EZ_2JRC upon the point cloud loading

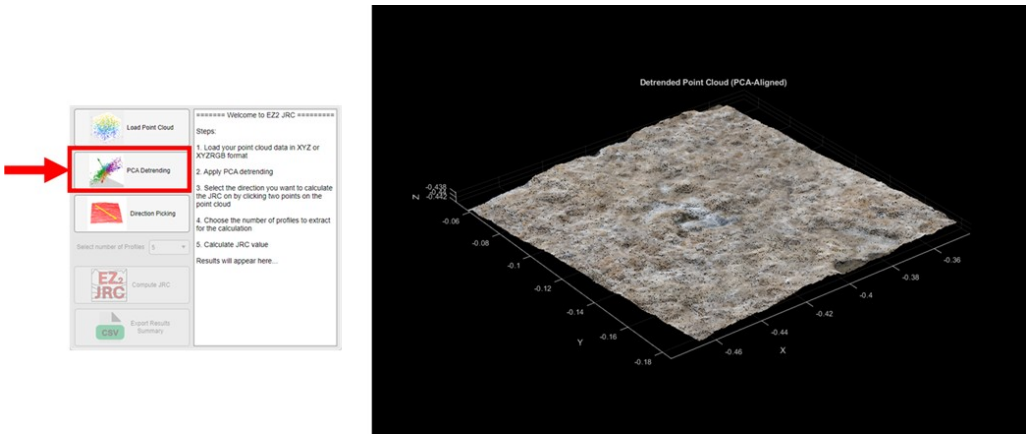


Figure 20: Point cloud detrendinf in EZ_2JRC via the 'PCA Detrending' button

computation. The chosen direction is visualized on the point cloud in the form of a red segment (Figure 21)."

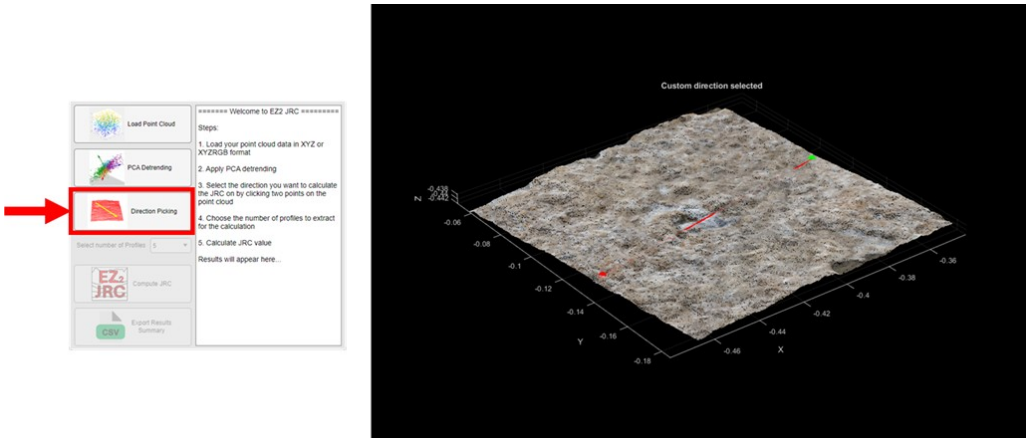


Figure 21: Direction selection in EZ$_2$JRC via the 'Direction Picking' button

The user now selects the number of profiles to use for the JRC calculation. Activation of the 'Compute JRC' button (Figure 22) initiates the calculation of the JRC value for each individual profile. The results are shown in the dialog window and are exportable in the form of a .csv file. The profiles used for the calculation are traced overlaid on the point cloud and are visible in the 3D visualization window which is automatically updated (Figure 22).

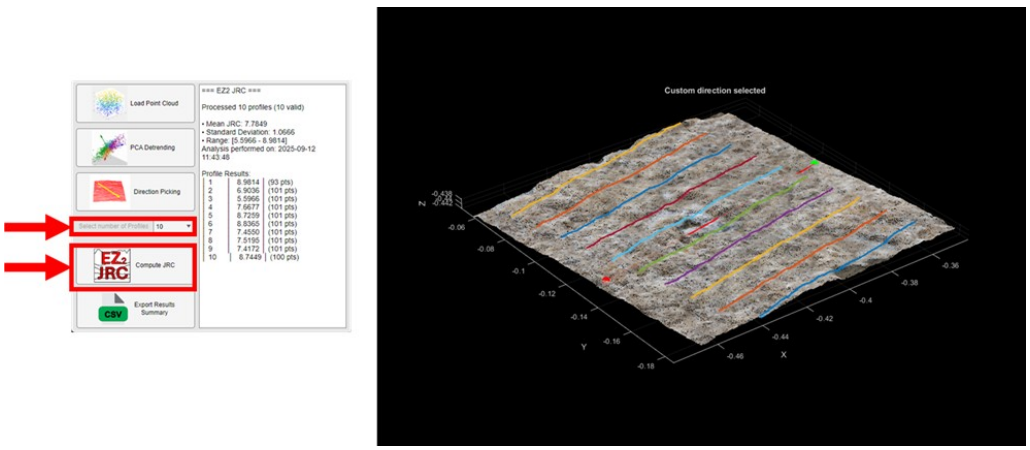


Figure 22: Number of profiles and JRC computation prompt in EZ$_2$JRC via the 'Number of profiles' and 'Compute JRC' buttons

3.7 RODIAN PROCESSING

[1] The functionalities and operational logic of the software are described in detail in chapter 4. In this chapter the analysis workflow of the program is described, from input data to output results. A logical diagram of the RoDiAn workflow is visible in Figure 23.

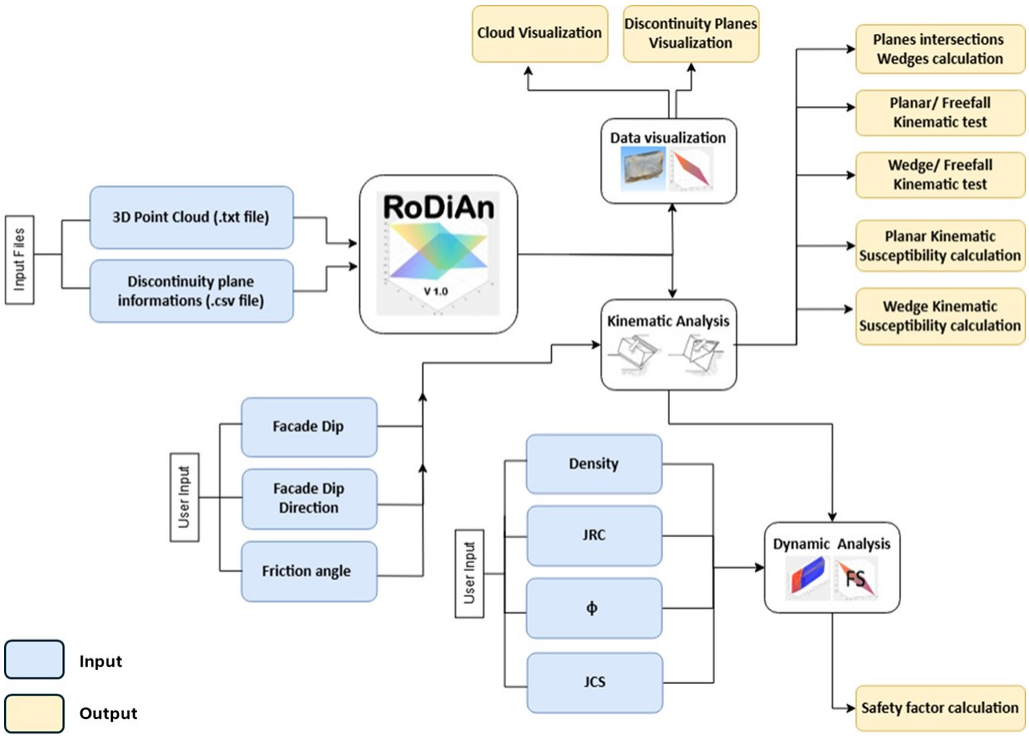


Figure 23: Logical diagram of RoDiAn functionalities

1 RoDiAn can be donwloaded at: https://drive.google.com/drive/folders/1tUqxyq3V4hoMNNXsJXHbOJN0-Hh17Yky?usp=sharing
The folder is complete of the installation instruction and test files.

3.7.1 *Input Files*

RoDiAn uses two files as input data:

- A 3DPC of the architectural element to be analyzed in the form of an .txt XYZ or XYZRGB file
- A .csv file containing information on discontinuity planes obtained from pre-processing on CloudCompare. RoDiAn is developed to automatically read the .csv file obtained from the '/batchexport' tool of CloudCompare without any modification.

To load the files, the user uses the two buttons 'Load TXT', for the 3DPC, and 'Load CSV' for the .csv file. The software opens two file selection windows and the user selects the files. The position of the buttons within the RoDiAn interface is visible in Figure 24

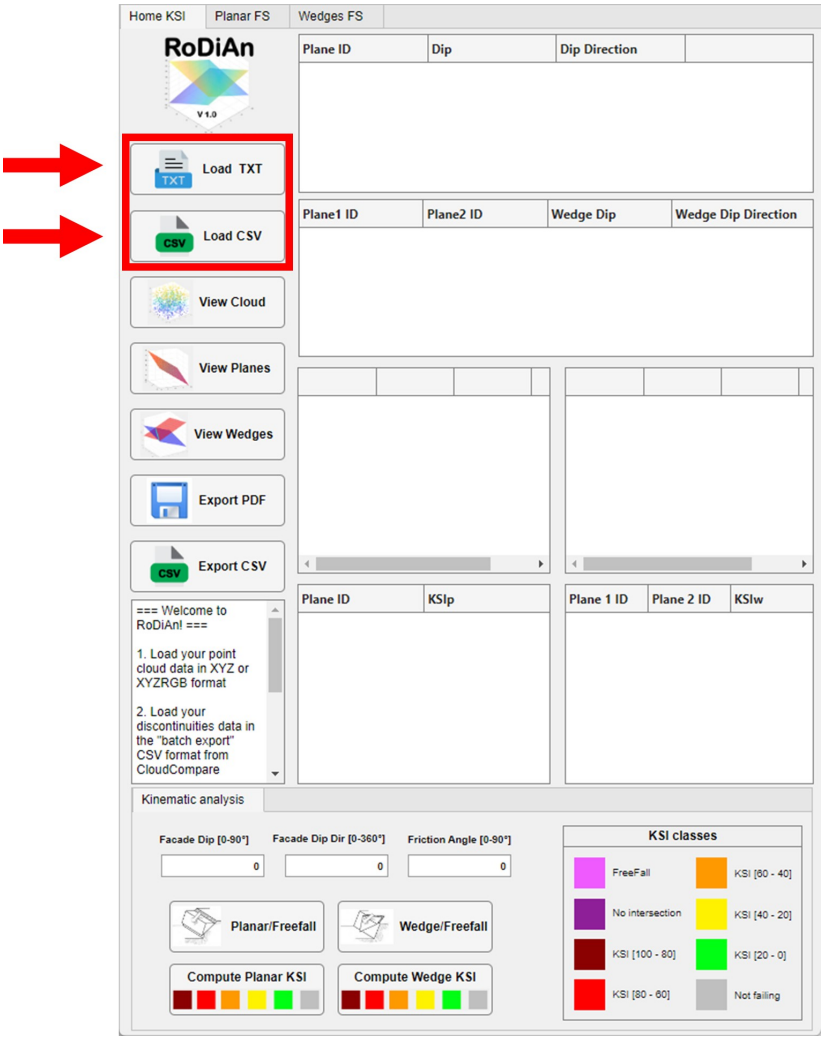


Figure 24: Point cloud and plane info files loading in RoDiAn via the 'Load TXT' and 'Load CSV' buttons

3.7.2 *Data Visualization*

The first available functions are data visualization. With the 'View Cloud' button (Figure 25) it is possible to visualize the 3DPC in a resizable interactive window. From the window it is possible to interact with the point cloud and perform basic visualization operations such as rotation/-pan/zoom. Through the 'View Planes' button, the discontinuity planes contained in the .csv file are plotted. The planes are plotted above the already loaded point cloud and it is possible to interact with them in 3D. Labels with the identification number of each plane are attached to the planes, which will be used later in other functionalities.

Figure 26) shows an example of how a block and its planes appear in the 3D visualization window.

Upon pressing the 'View Planes' button, the table with the attributes of individual planes visible in Figure 27 is also populated. Each row of the table corresponds to a plane, for which the identifier used on CloudCompare at the time of export (Plane ID), its Dip value (Dip) and Dip Direction (Dip Direction) are reported. This information can be used by the user but is also necessary for the automatic kinematic analysis functions present in the software.

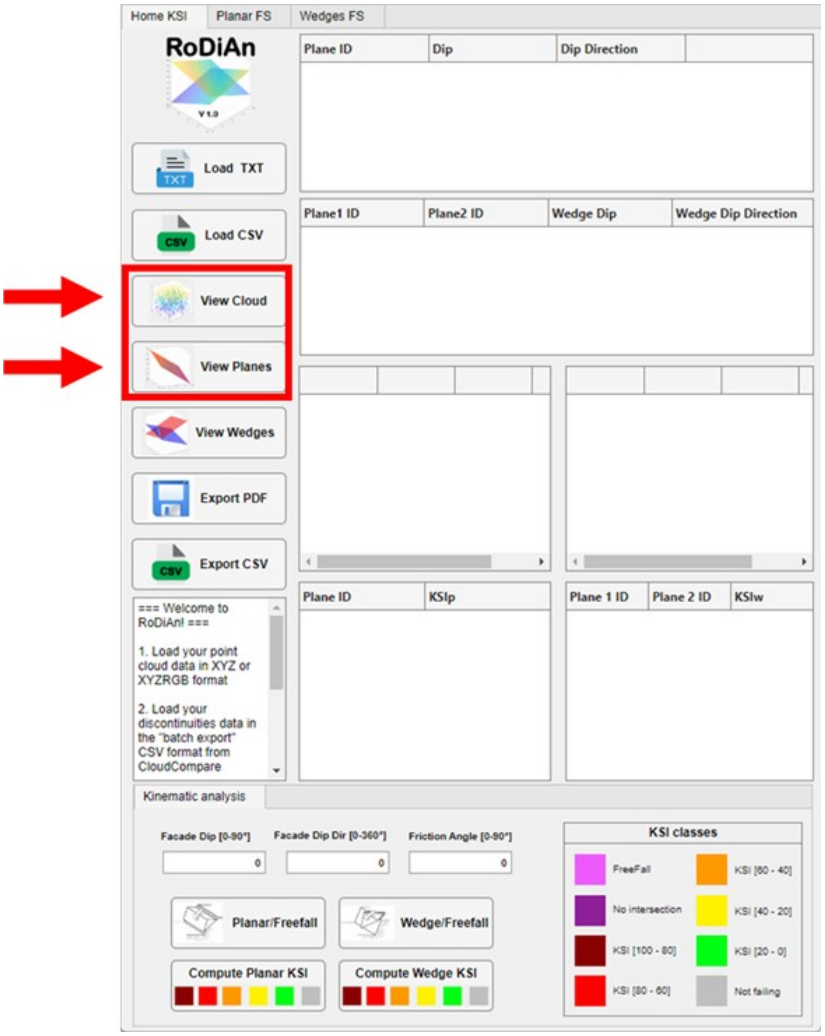


Figure 25: Point cloud and planes visualization in RoDiAn via the 'View Cloud' and 'View Planes' buttons

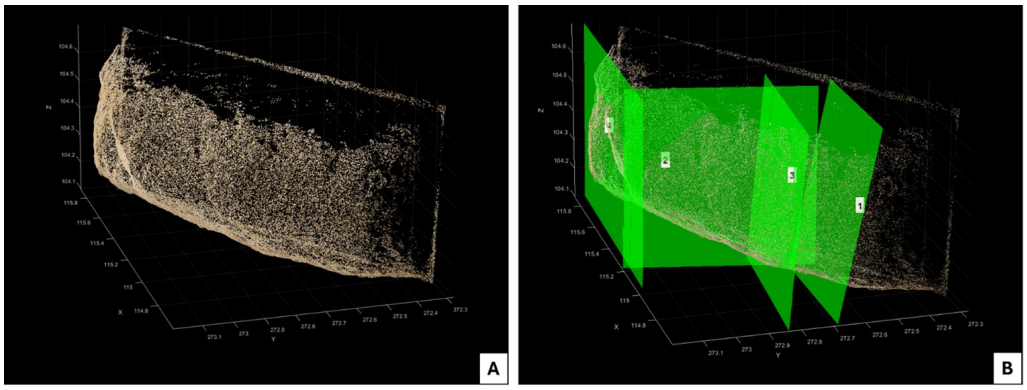


Figure 26: Point cloud (A) and planes (B) visualization in RoDiAn's 3D visualization window

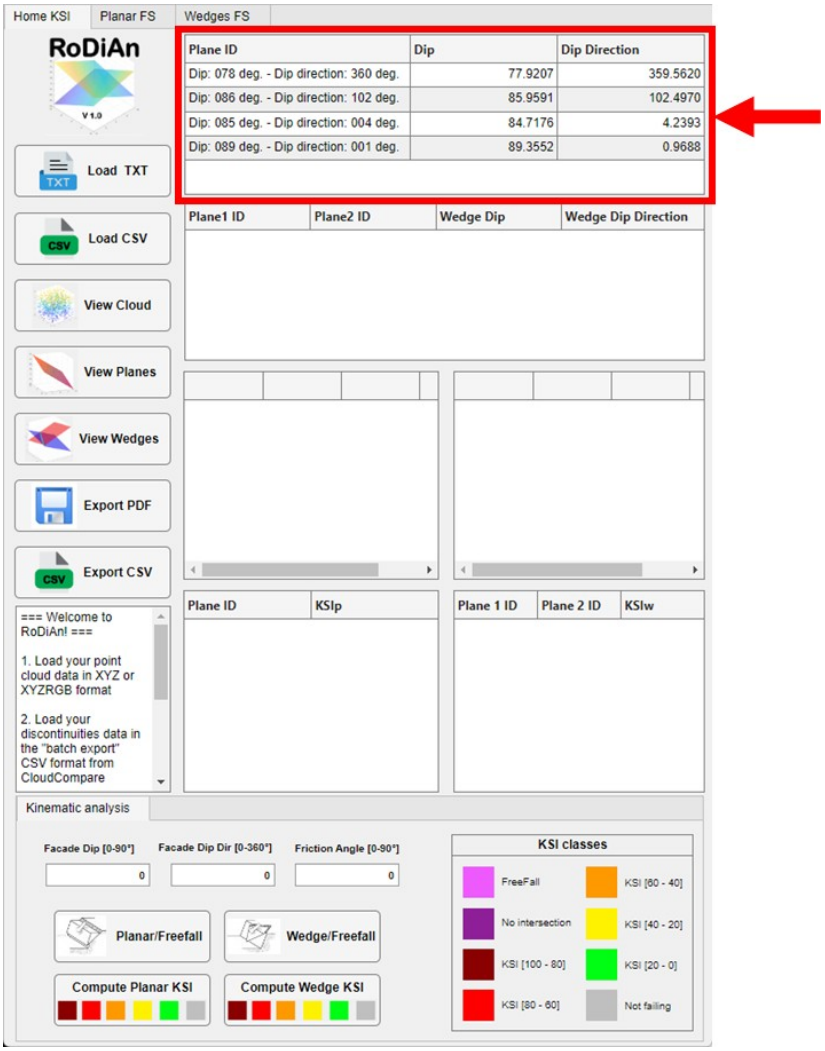


Figure 27: Table of planes attribute in RoDiAN. Each row of the table corresponds to a plane, and the columns show each plane name (Plane ID), its Dip value (Dip) and Dip Direction (Dip Direction)

3.7.3 *Kinematic Analysis*

The kinematic analysis functions of RoDiAn are all contained in the first tab of the program ('Home KSI'). The first function is the 'View Wedges' button which calculates the intersections of planes that form wedges within the analyzed element. An in-depth analysis of the operational logic of this function is present in chapter 4. From a functional point of view, upon pressing this button a new 3D visualization window is created in which an animation plots the intersection lines of the planes that develop within the block. For each intersection or wedge, in addition to the intersection line, the pair of planes responsible for wedge formation are also plotted. An example of wedge visualization in RoDiAn is visible in Figure 28. The wedges are plotted with a label that shows the ID of the planes that formed the wedge

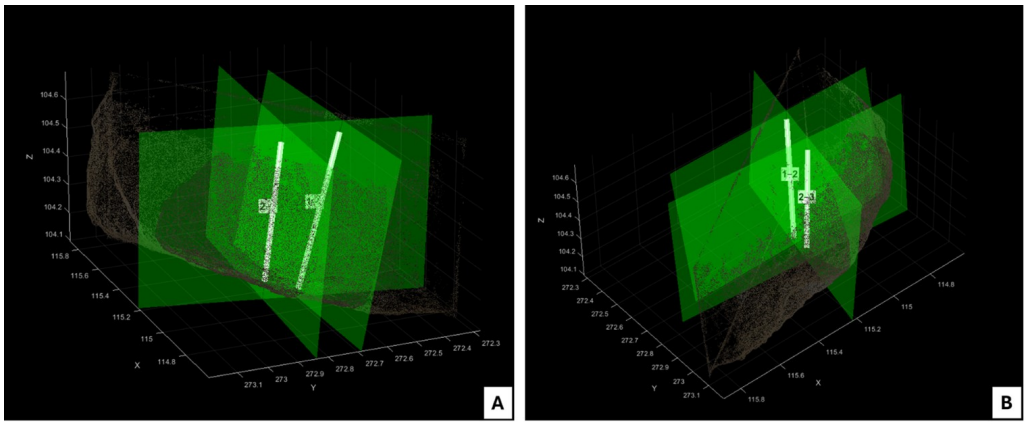


Figure 28: 3D views (A-B different camera position) of the graphical results of the 'Wiew Wedges' button. For each pair of planes that form an interesection inside of the block (a wedge), the function plots the intersection line (plunge line of the wedge)

For each wedge, the Dip and Dip Direction of the plunge line are also calculated, which are shown in the table related to wedges visible in Figure 29, in addition to the ID of the planes that form the intersection.

Once the wedges have been calculated, it is possible to carry out the actual kinematic analysis, both for the individual discontinuities and for the wedges. To proceed with the kinematic analysis, orientation data for the discontinuities and wedges are required, these are automatically obtained by the software, as well as data related to the slope (in our case, the facade), which must be entered by the user. To do this, three

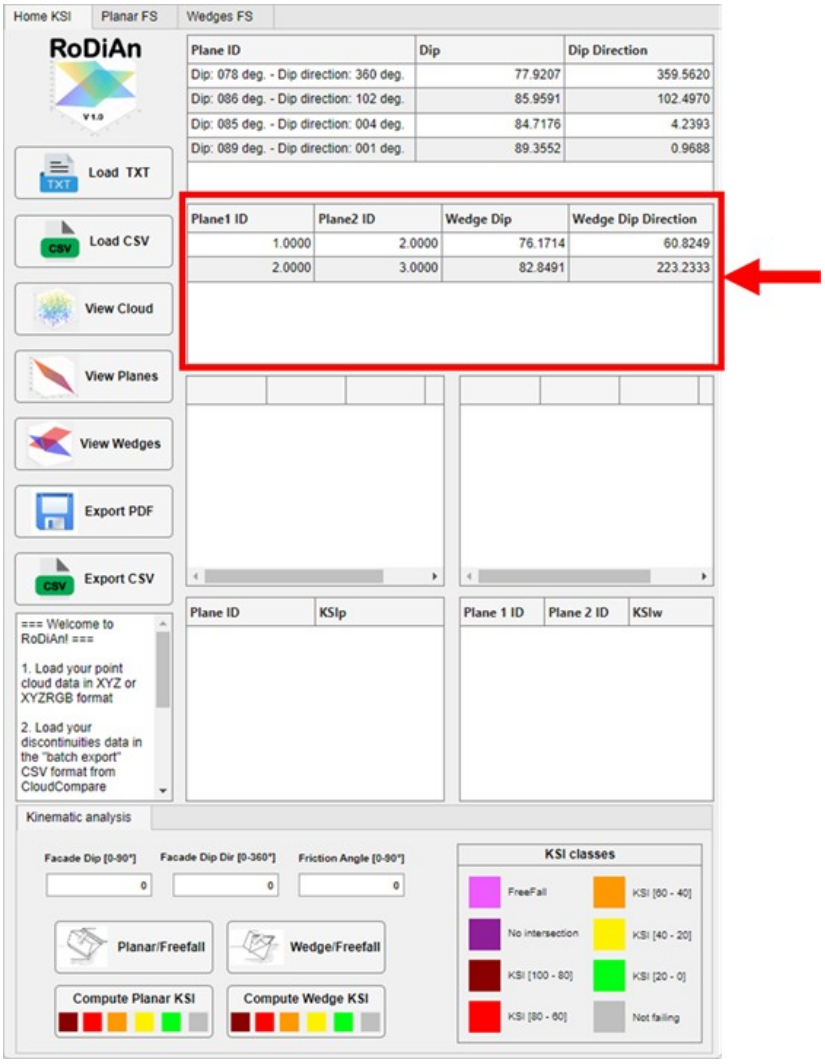


Figure 29: Table of wedges attribute in RoDiAN. Each row of the table corresponds to a wedge, and the columns show each of the planes that form the inserction name (Plane 1-2 ID), the wedge Dip value (Wedge Dip) and Dip Direction (Wedge Dip Direction)

interactive fields are located at the bottom left (Figure 30), where it is possible to enter the dip of the facade ("Facade Dip"), the dip direction ("Facade Dip Dir"), and the friction angle ("Friction Angle"). These fields are interactive, and the parameters can be modified in real time.

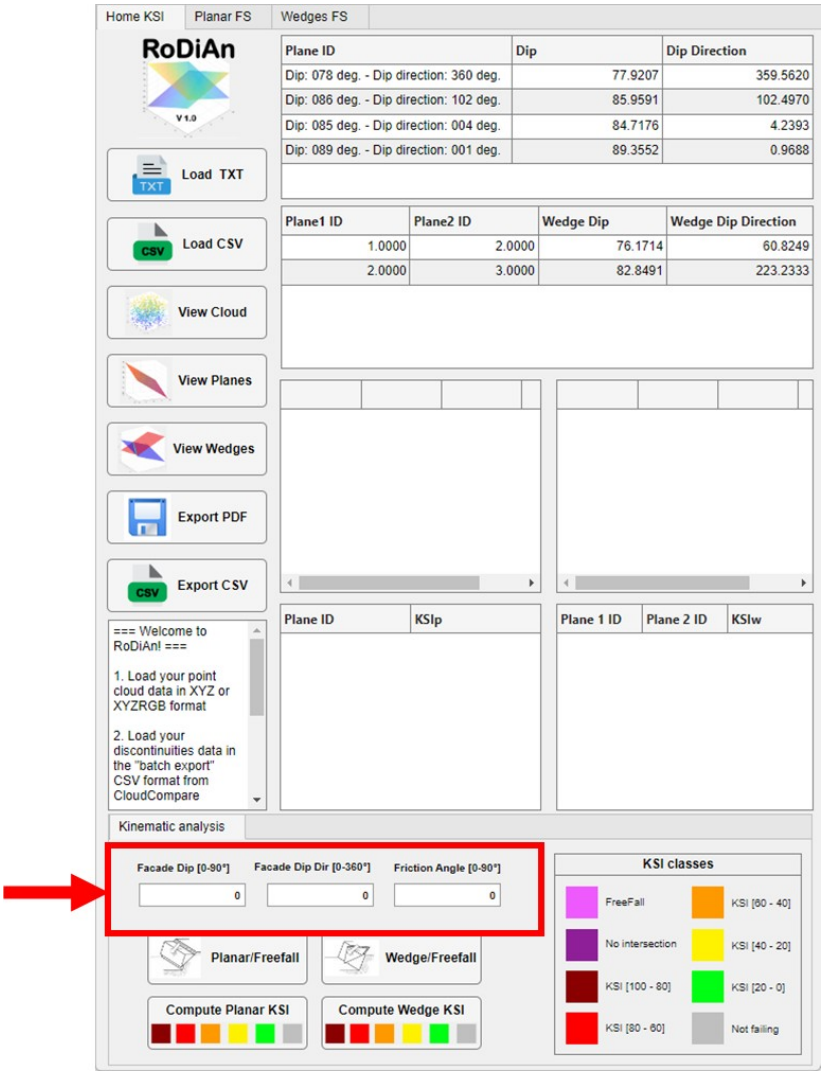


Figure 30: Interactive fields in the GUI of RoDiAn to enter the dip of the facade ("Facade Dip"), the dip direction ("Facade Dip Dir"), and the friction angle ("Friction Angle")

Once the orientation values of the facade and the friction angle have been entered, it is possible to proceed with the kinematic analysis of planar sliding or freefall for individual planes. To access this function, the "Planar/Freefall" button is used as shown in Figure 31.

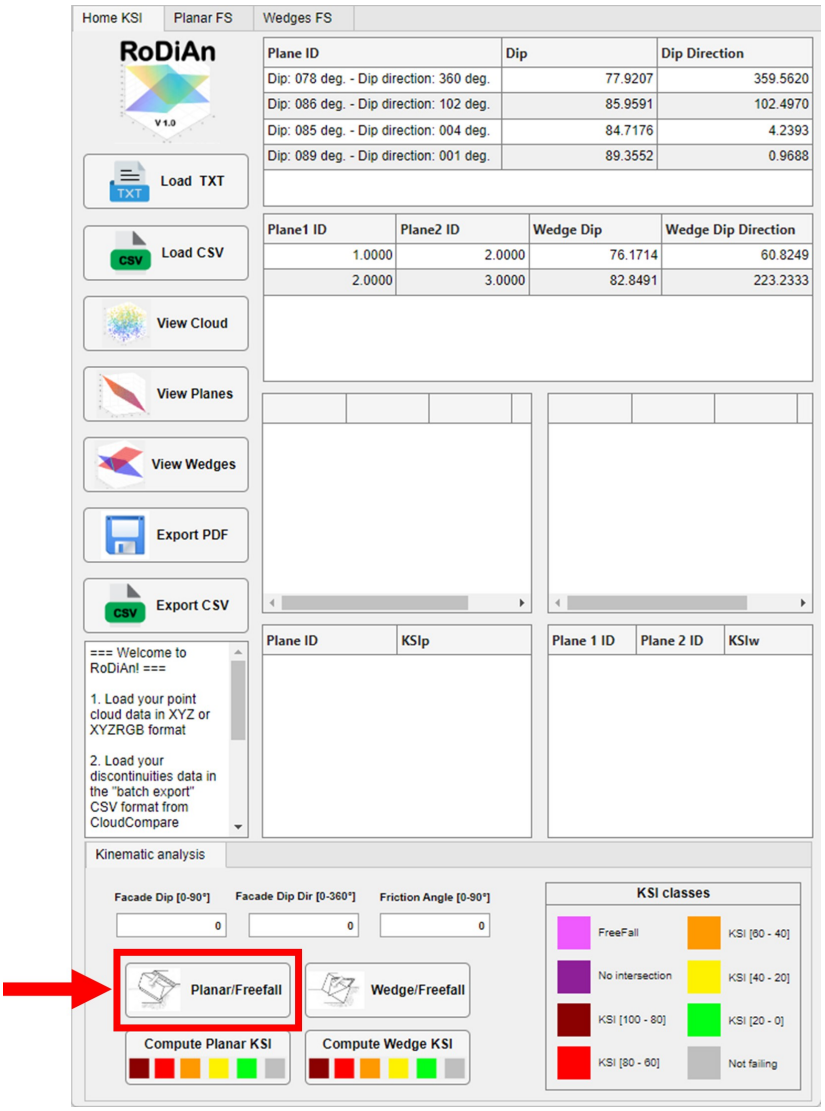


Figure 31: Planar and Freefall kinematic test in RoDiAn via te 'Planar/Freefall' button

Pressing the "Planar/Freefall" button initiates the automatic calculation planar sliding and free fall kinematic for each plane. The result of this function is displayed in the table related to planar kinematics (Figure 32). The table is populated with a text string for each individual plane. The four possible text strings are:

- Plane Id → Planar failure not possible: In cases where the orientation of the plane relative to the facade does not allow for planar sliding or Free Fall failure
- Plane Id → Planar failure possible: In cases where the orientation of the plane relative to the facade allows for planar sliding and an intersection between the plane and the facade is detected. The possible effects of the intersection between the planes and the facade are discussed in detail in Paragraph 4.2.3
- Plane Id → Freefall failure possible: In cases where the orientation of the plane relative to the facade allows for detachment by free fall
- Plane Id → Planar failure possible - no facade intersection: In cases where the orientation of the plane relative to the facade allows for detachment by planar sliding and no intersection between the plane and the facade is detected.

Figure 32 shows a sample block in which planes 1, 2, and 3 are oriented in such a way that planar sliding is not possible, and are therefore classified as "Planar failure not possible." Plane 4, on the other hand, may be subject to free fall and is classified as "Freefall failure possible."

Figure 33, on the other hand, shows a block containing a plane that may undergo planar sliding and does not intersect with the wall. It is therefore classified as "Planar failure possible - no facade intersection." Plane 2 is oriented in such a way that sliding is not possible and is classified as "Planar failure not possible."

As a final example of the output from the "Planar/Freefall" function, Figure 34 shows a block in which one plane (Plane 2) may undergo planar sliding and does not intersect with the wall. It is therefore classified as "Planar failure possible - no facade intersection." Planes 1 and 3 are oriented in such a way that sliding is possible, but they intersect the wall and are classified as "Planar failure possible."

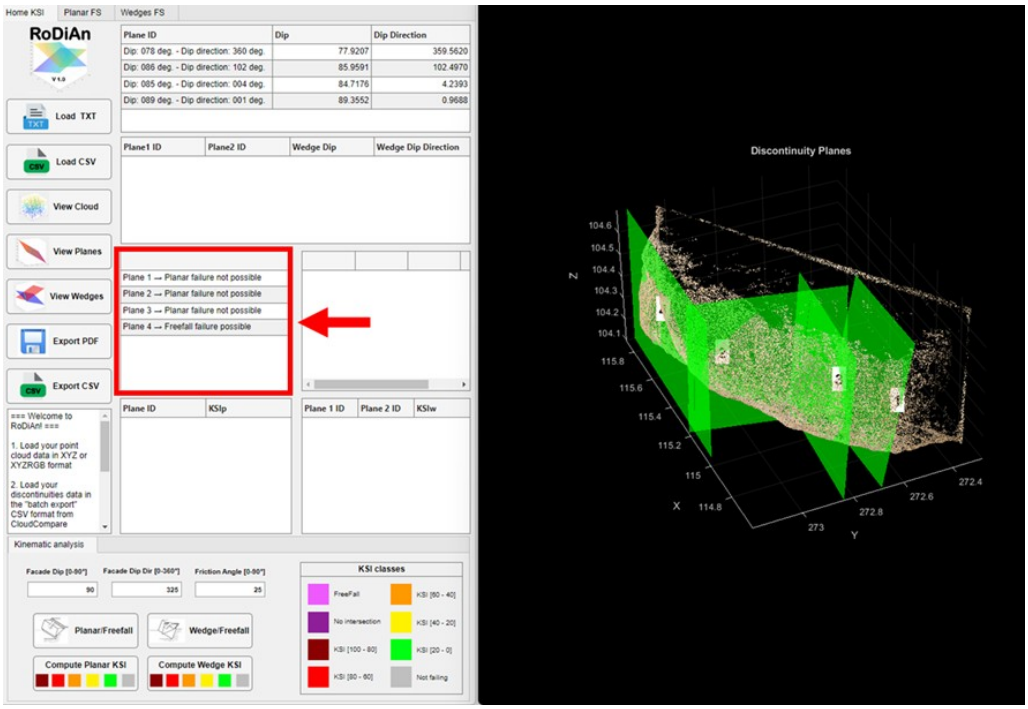


Figure 32: Planar and Freefall kinematic results table (in red). Sample block that illustrates possible results of the planar/freefal kinematic test

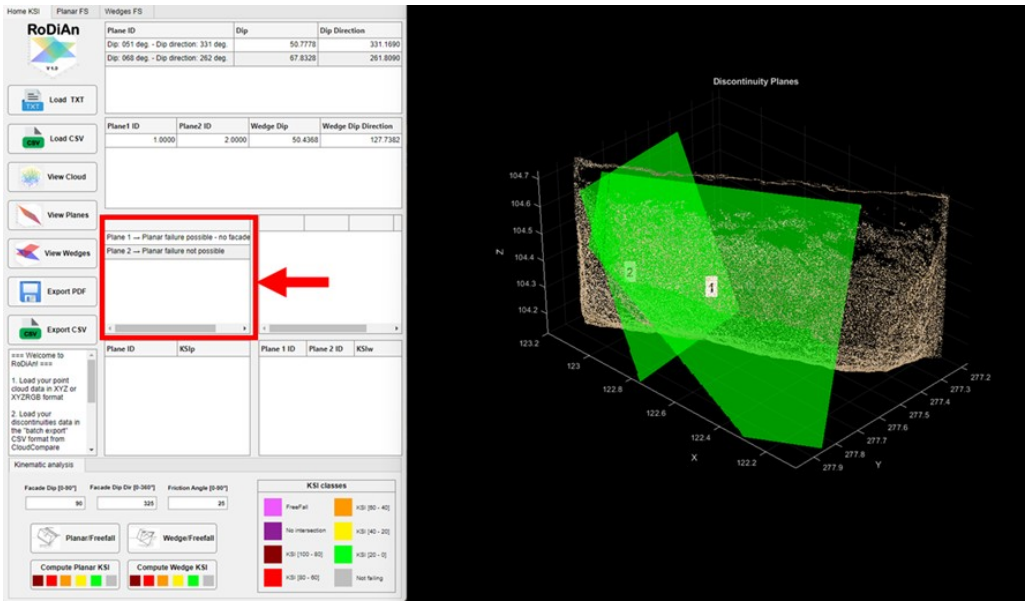


Figure 33: Planar and Freefall kinematic results table (in red). Sample block that illustrates possible results of the planar/freefal kinematic test

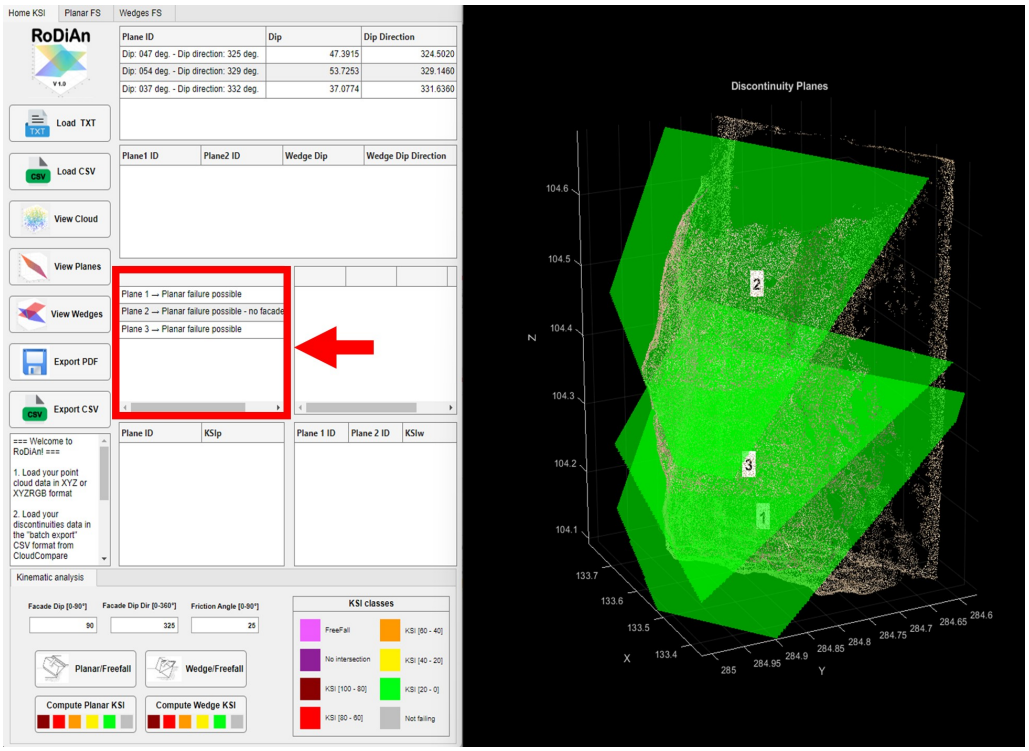


Figure 34: Planar and Freefall kinematic results table (in red). Sample block that illustrates possible results of the planar/freefal kinematic test

RoDiAn can perform the same type of analysis just described also for wedge sliding. Pressing the "Wedge/Freefall" button initiates the automatic calculation of kinematic movement by sliding or free fall for each wedge. The result of this function is displayed in the table related to wedge kinematics (Figure 35). The table is populated with a text string for each individual wedge. The four possible text strings are:

- Wedge Id → Sliding failure not possible: In cases where the orientation of the wedge relative to the facade does not allow sliding.
- Wedge Id → Sliding failure possible: In cases where the orientation of the wedge relative to the facade allows sliding and an intersection between the wedge and the facade is detected. The possible effects of wedge–facade intersections are discussed in detail in paragraph 4.2.3
- Wedge Id → Freefall failure possible: In cases where the orientation of the wedge relative to the facade allows detachment by free fall.
- Wedge Id → Sliding failure possible - no facade intersection: In cases where the orientation of the wedge relative to the facade allows detachment by sliding and no intersection between the wedge and the facade is detected.

An example of the first two cases is shown in Figure 35. The sample block contains three wedges (wedges 1, 2, and 4) with stable orientations, which are therefore flagged as "Wedge Id → Sliding failure not possible," while wedge 3 has an orientation that allows sliding and is therefore marked as "Sliding failure possible."

Figure 36 shows a block containing two wedges that do not intersect with the facade and may undergo kinematic movement by sliding (wedge 2 – "Sliding failure possible - no facade intersection") and by free fall (wedge 1 – "Freefall failure possible").

The last two functions of the kinematic analysis module are the "Compute Planar KSI" and "Compute Wedge KSI" buttons, designed to calculate the Kinematic Susceptibility Index (KSI) for planar sliding (KSIp) and wedge sliding (KSIw). The definition and the discussion of the Kinematic Susceptibility Index are presented on paragraph 4.2.5. When the "Compute Planar KSI" button is pressed, RoDiAn generates a new interactive 3D figure in which the 3D point cloud and discontinuity planes are plotted and color-coded according to the susceptibility index of each plane. The color coding, also shown in RoDiAn's graphical interface, is

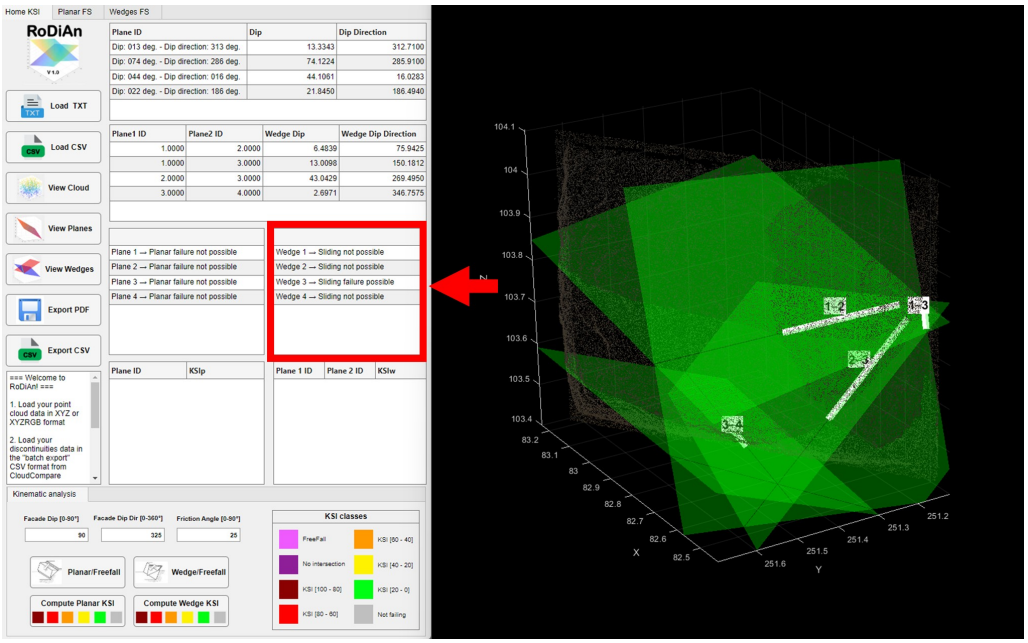


Figure 35: Wedge and Freefall kinematic results table (in red). Sample block that illustrates possible results of the wedge/freefal kinematic test

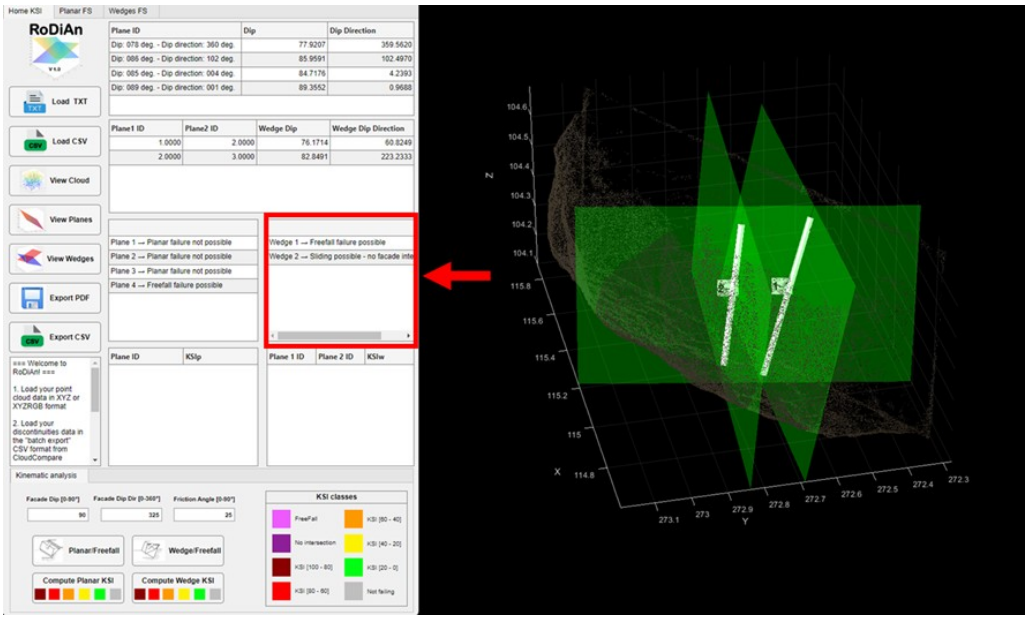


Figure 36: Wedge and Freefall kinematic results table (in red). Sample block that illustrates possible results of the wedge/freefal kinematic test

visible in Figure 37. Planes that are not susceptible to planar sliding are colored gray. Planes that are susceptible to planar sliding and intersect the facade are color-coded on a scale from green (less critical) to red (more critical). The five color codes correspond to the quintiles of the KSI value distribution (0–100). Two distinct shades of purple identify the two most critical cases: dark purple for planes susceptible to planar sliding without intersecting the facade, and light purple/pink for those susceptible to free fall. The 3D figure that gets plotted also includes a dark blue plane representing the facade, used to calculate intersections between planes/wedges and the facade. This facade plane is computed based on the coordinates of the point cloud and the Dip and Dip Direction parameters entered by the user in the editable fields. It is plotted as a safety measure to allow the user to verify that it is correctly positioned.

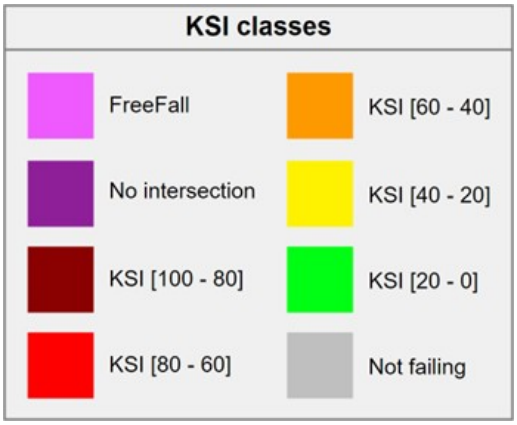


Figure 37: RoDiAn susceptibilty legend of KSI classes

Figure 38 shows several examples of the output of the Compute Planar KSI" and "Compute Wedge KSI" function.

The numerical results from the susceptibility index calculation populate the corresponding tables for planar and wedge kinematics, as shown in Figure 39.

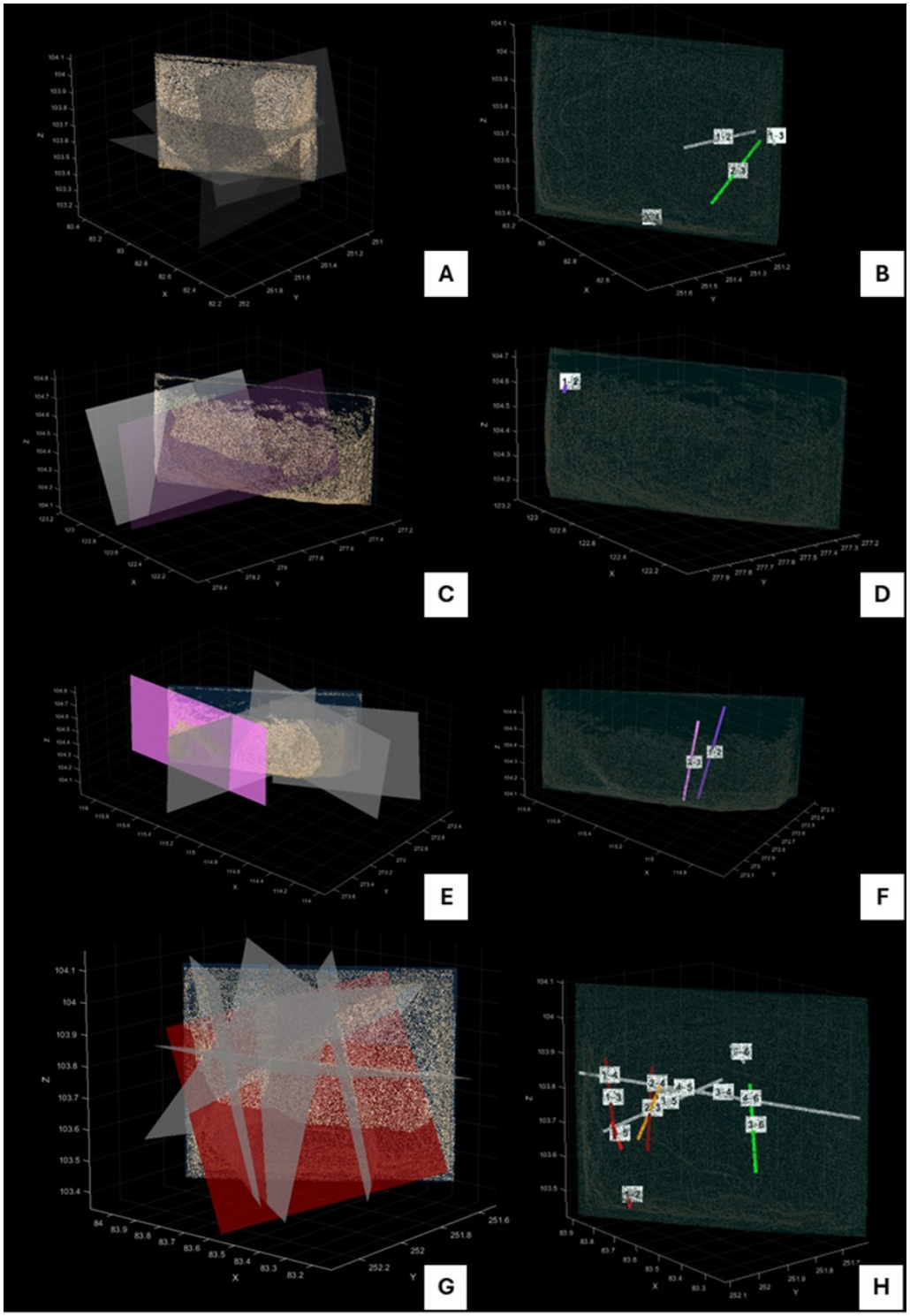


Figure 38: Examples of susceptibility output of RoDiAn. A-B: Block with no susceptible planes and one susceptible wedge; C-D: Block with a non-intersecting sliding plane and one non-intersecting sliding wedge; E-F: Block with one plane susceptible to freefall failure and two suscpetibile wedges, one to freefaal failure, one to sliding with no facade interesection; G-F: Block with a plane susceptibile to planar failure and multiple susceptibile wedges.

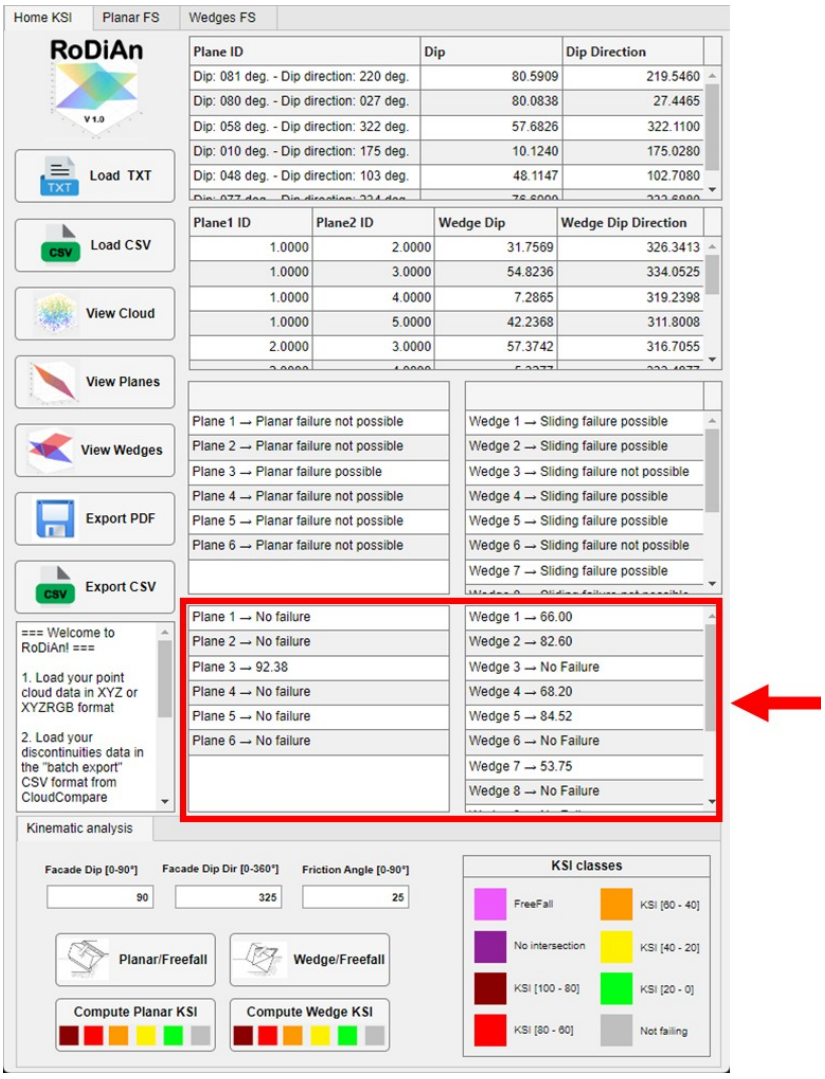


Figure 39: Example of numerical results of the 'Compute Planar KSI' and 'Compute Wedge KSI' in RoDiAn, populating the corrisponding table (in red)

3.7.4 *Dynamic Analysis*

The dynamic analysis features of RoDiAn are accessible through the tabs labeled "Planar FS" and "Wedges FS," as shown in Figure 40. These two tabs contain the dynamic analysis tools for planar sliding and wedge sliding, respectively.

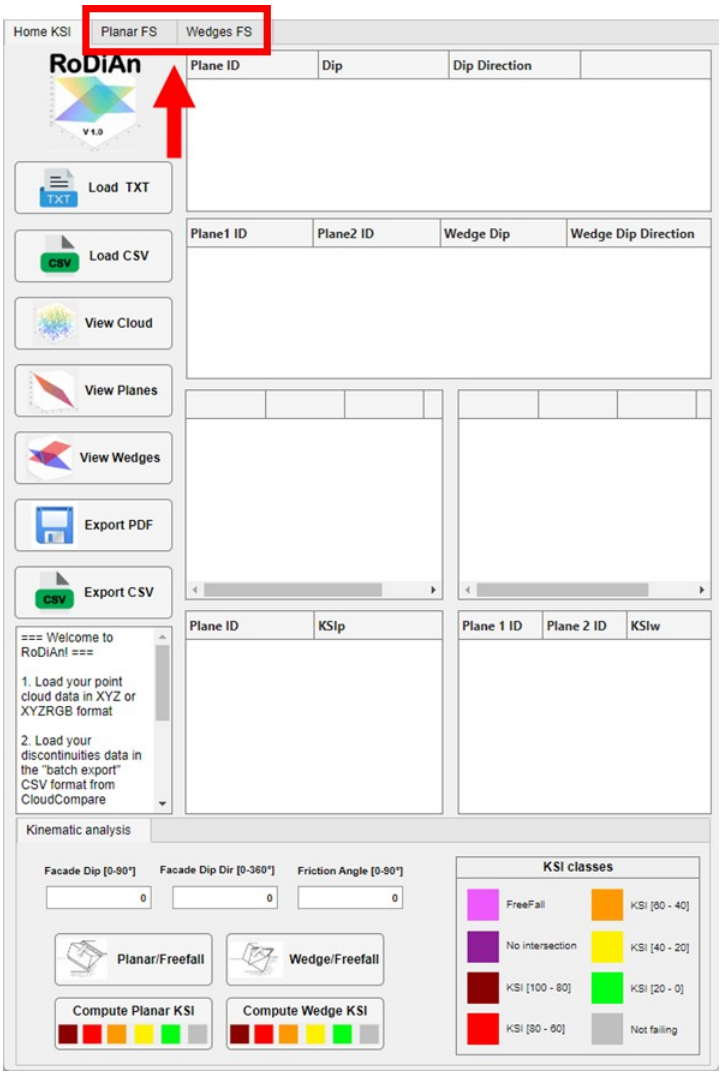


Figure 40: Position of the 'Planar FS' 'Wedges FS' tabs in the RoDiAn GUI, to access the dynamic analysis pages

By accessing the "Planar FS" page the user can view the tools for dynamic analysis related to planar sliding. There are no file upload functions on this page, as the software uses files previously uploaded in the "Home KSI" page (the functions are not interdependent, analysis can be performed on this page even if no tools were used on the previous one. The only dependency is the file selection function).

The first button required for the analysis is "View Cloud and Planes" shown in Figure 41. This button populates the tables containing information about the discontinuity planes (Figure 41). The upper table, similar to what is shown on the "Home KSI" page, contains the ID, Dip, and Dip Direction of each plane. The lower table (Figure 41) contains the geometric data needed to calculate detachment volumes. Specifically, it includes the spatial coordinates of the center of each plane (Cx, Cy, Cz) and the components of the plane's normal vector (Nx, Ny, Nz). The button also opens a 3D visualization window where the 3D point cloud (3DPC) and discontinuity planes can be viewed.

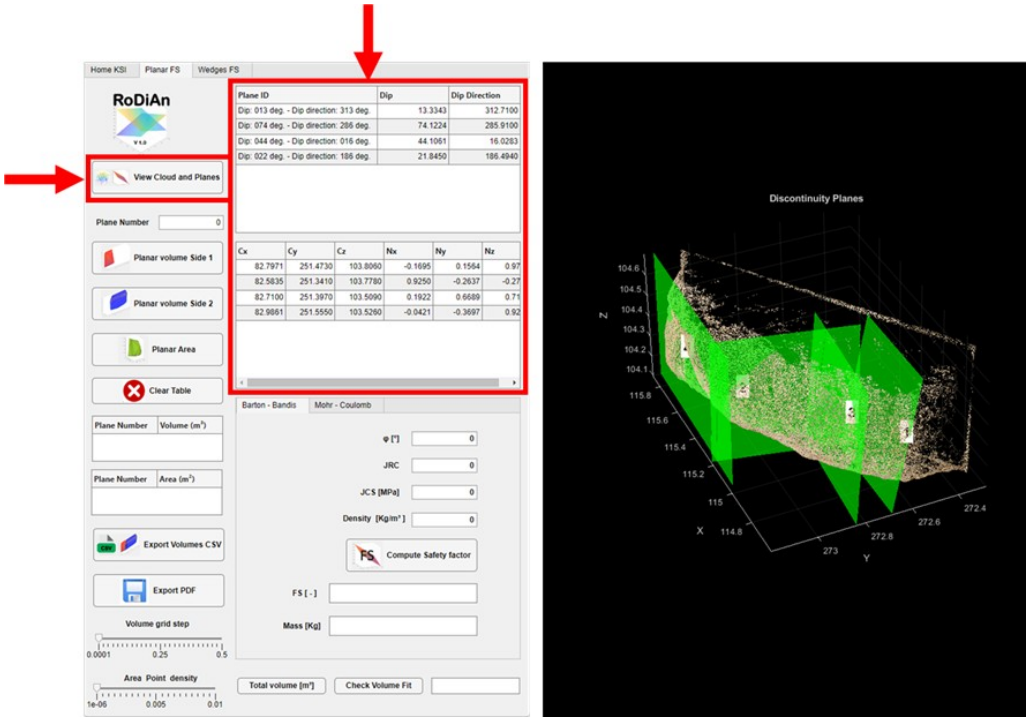


Figure 41: Visualization tools in the dynamic analysis tab of RoDiAn. 'The button View Cloud and Planes' (left) prompts the 3D visualization of the 3DPC and planes (right). The information of the planes populate the two tables, upper and lower

After visualizing the 3DPC and the planes, the workflow continues with the editable field "Plane Number," highlighted in Figure 42. In this field, the user must enter the number of the plane to be analyzed.

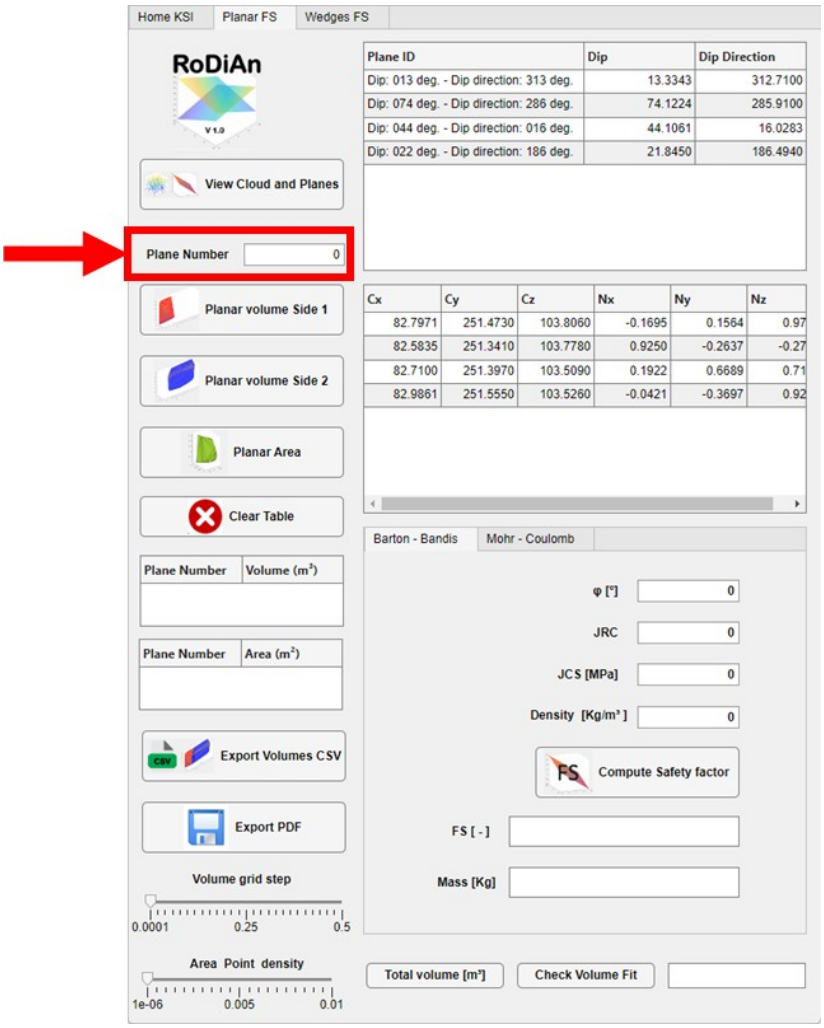


Figure 42: Input field to select to plane to be analyzed

Once the plane has been selected using the editable field, the user can proceed with calculating the volume of the potential detachment portion. To do this, the buttons "Planar Volume Side 1" and "Planar Volume Side 2" are used, as highlighted in Figure 43.

The two buttons perform the same function: calculating the volume of the portion of the 3DPC obtained from its intersection with the selected plane. The detailed operation is described in paragraph 4.2.7, but a key concept to clarify is that the two buttons compute the two complementary

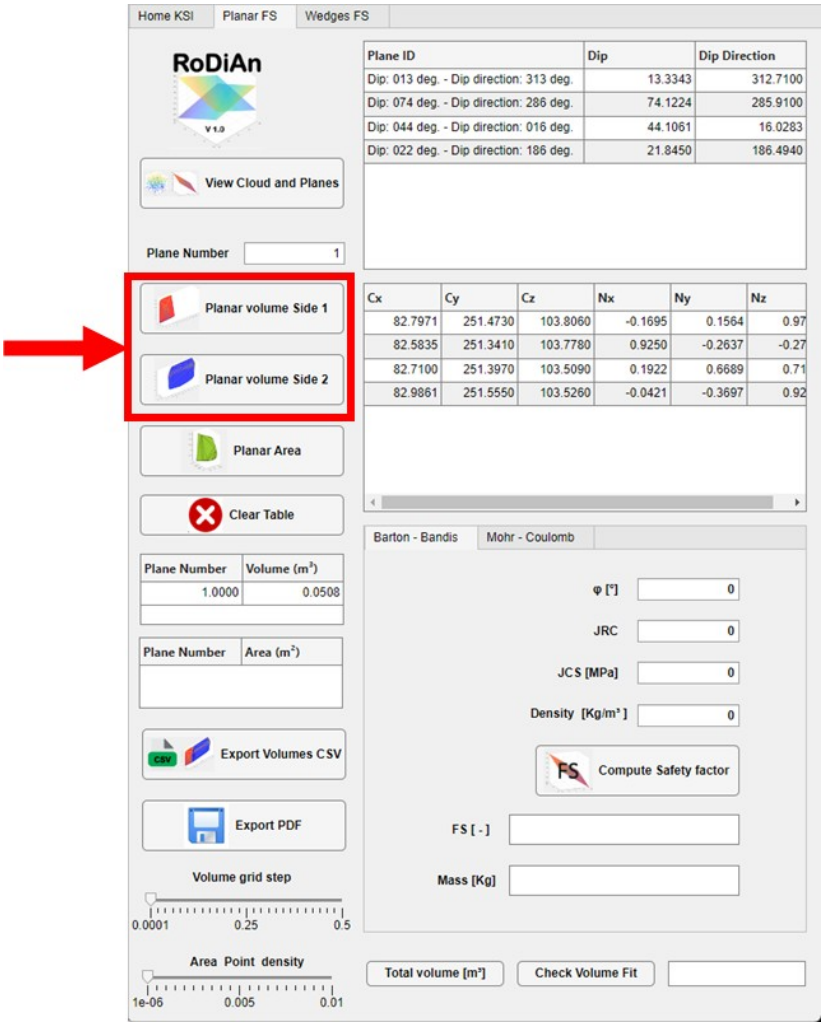


Figure 43: Volume calculation of the potentially unstable block in RoDiAn via the 'Planar Volume Side 1' and 'Planar Volume Side 2' buttons

volumes that make up the point cloud. Due to geometric factors and the spatial orientation of the cloud, it is not possible to determine in advance which of the two portions is subject to sliding, and therefore the selection of the unstable side cannot be automated. To address this, the user can activate both buttons and check which of the two volumes is correctly oriented to allow sliding. To assist in selecting the correct volume, the two buttons generate a 3D plot in which the volumes are color-coded (red and blue). An example of volume visualization within a block is shown in Figure 44.

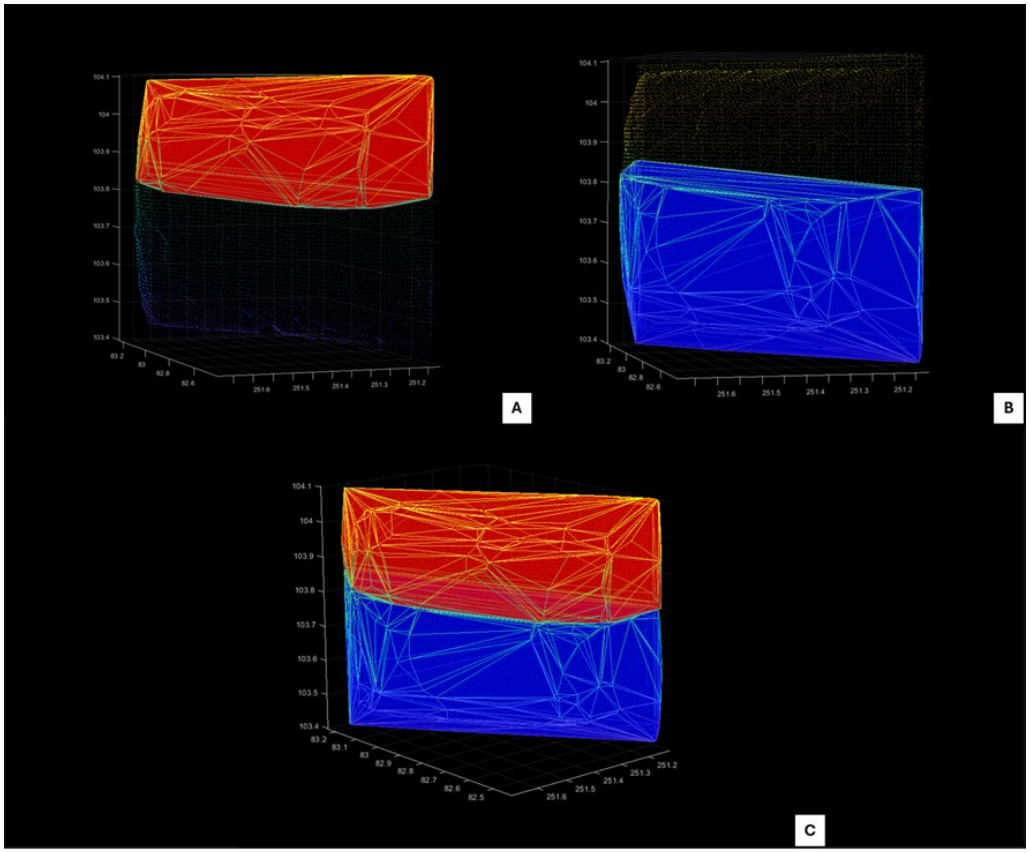


Figure 44: Example of the graphical output of the volume calculation in RoDiAn. A-B: the two complementary volumes calculated via the Side 1 or Side 2 buttons; C: The two volumes overlaid to show how they form the whole block

The calculated volume populates the corresponding table shown in Figure 45. The reported volume value refers to the side that was selected

last (via the “Planar Volume Side 1” or “Planar Volume Side 2” buttons). This value is automatically used in the safety factor calculation.

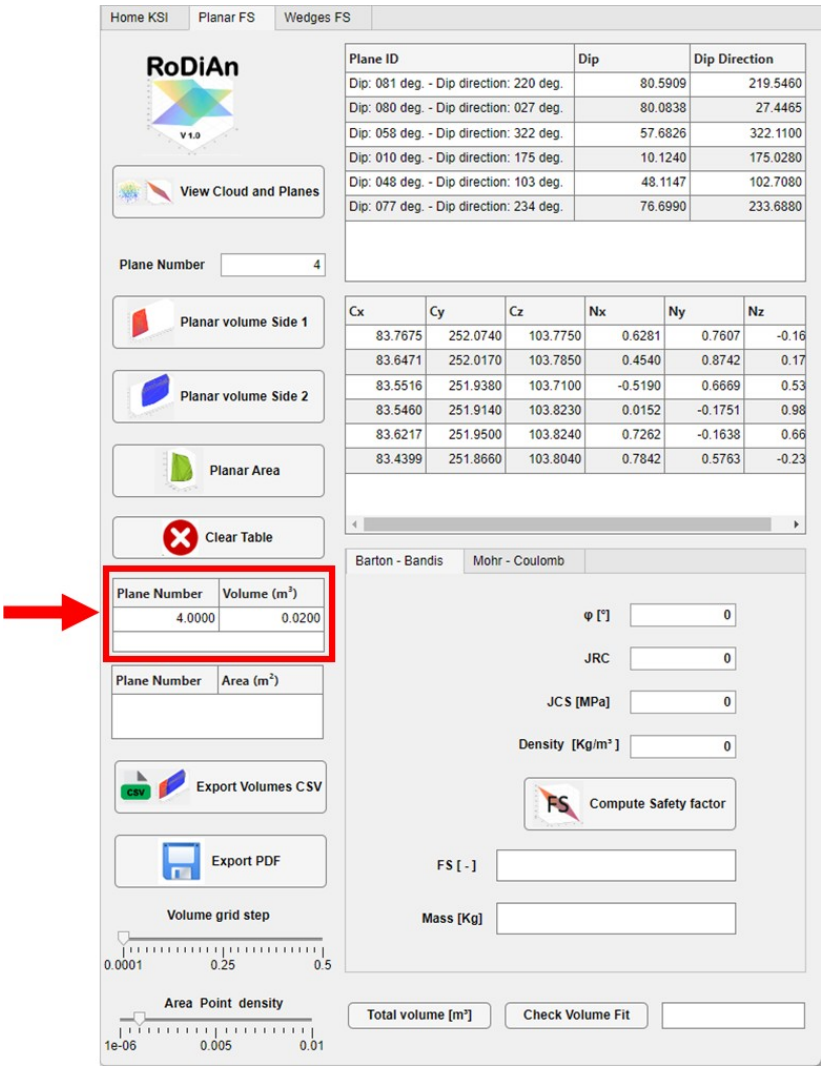


Figure 45: Numerical output of the ’Planar Volume’ functions in RoDiAn. The results appear in the dedicated table (in red)

To calculate the volume of block portions, the software generates a mesh from the 3DPC. For computational efficiency, it automatically performs downsampling of the point cloud to ensure the volume calculation can be completed within a reasonable time frame. However, it is possible to adjust the intensity of the downsampling using the “Volume grid step” slider, highlighted in Figure 46. This slider controls the minimum volume size considered during downsampling: moving the slider toward lower

values results in a denser point cloud and a more accurate volume. Due to geometric constraints, the volume is calculated using convex triangulation, which tends to overestimate the computed volume compared to the actual one. This is especially true in cases where the shape of the element includes concave geometries.

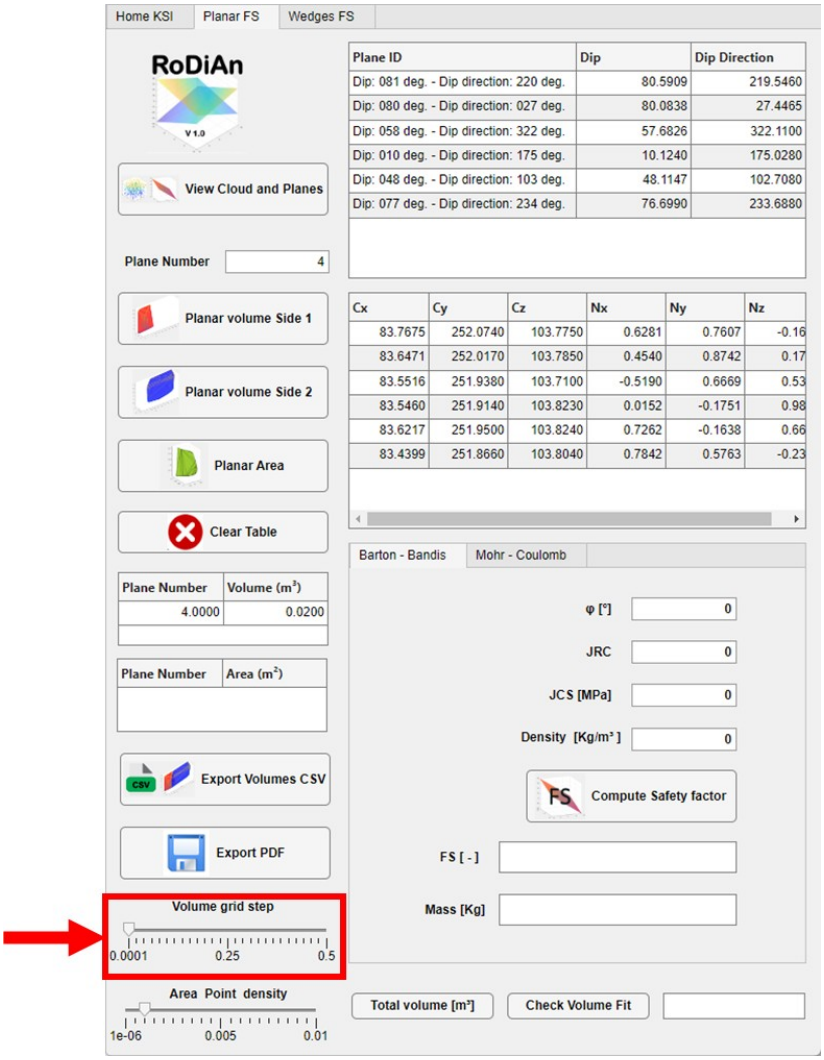


Figure 46: Volume grid step slider in RoDiAn, to modify the intensity of the downsampling of the mesh used in the volume calculation

The next step required to calculate the safety factor is defining the sliding surface of the discontinuity. To do this, the "Planar Area" button is used, as highlighted in Figure 47.

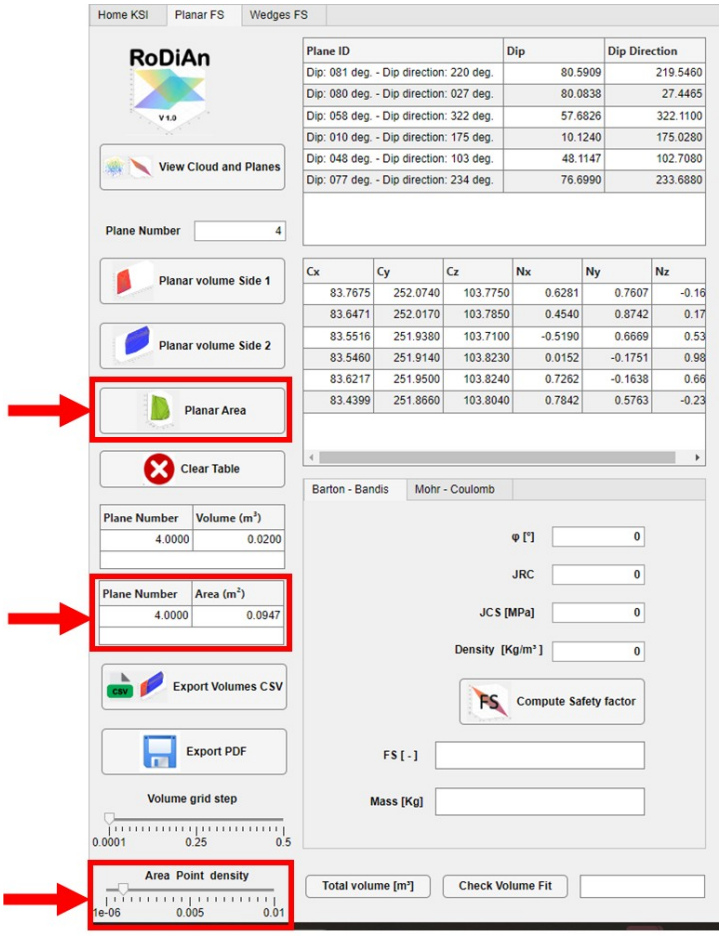


Figure 47: Calculation of the sliding area of the potentially unstable block in RoDiAn via the 'Planar Area' button. The numerical results populate the corresponding table. It is possible to adjust the volume of the space within which the 3DPC points are projected onto the plane using the 'Area Point Density'

When the button is pressed, the area is calculated and displayed in the corresponding table (Figure 47). Similar to the volume calculation, the area is approximated using a convex polyline. In cases of complex morphologies with numerous concave sections, this may result in a significant error. As a control measure, the user can view the automatic fitting performed by the software on the point cloud. This is displayed in an image that opens automatically upon pressing the button, showing the local slice of the point cloud at the position of the selected plane and the polyline used for area calculation (in red, Figure 48). It is possible to adjust the volume of the space within which the 3DPC points are projected onto the plane using the "Area Point Density" slider, visible in Figure 47.

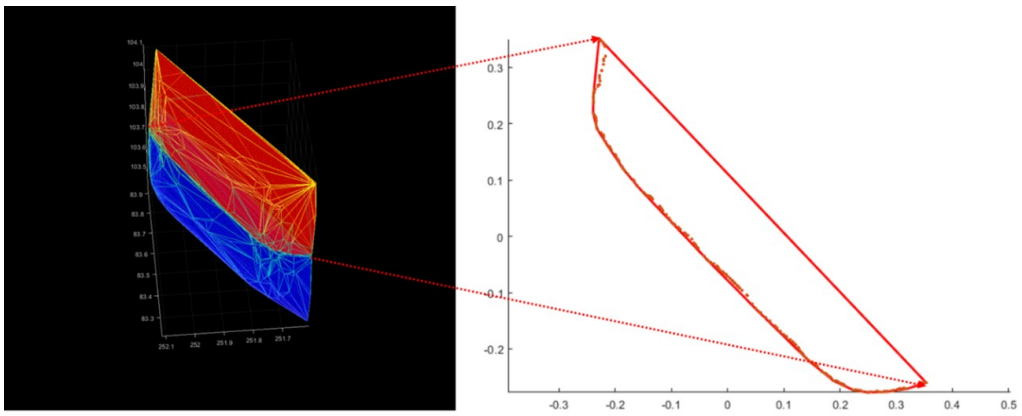


Figure 48: Example of the graphical output of the area calculation in RoDiAn

Once the geometric parameters have been calculated, the user can enter the physical and geomechanical parameters into the box highlighted in Figure 49. Based on the desired failure criterion, the relevant parameters are entered, and the calculation is performed by pressing the "Compute Safety Factor" button shown in Figure 49.

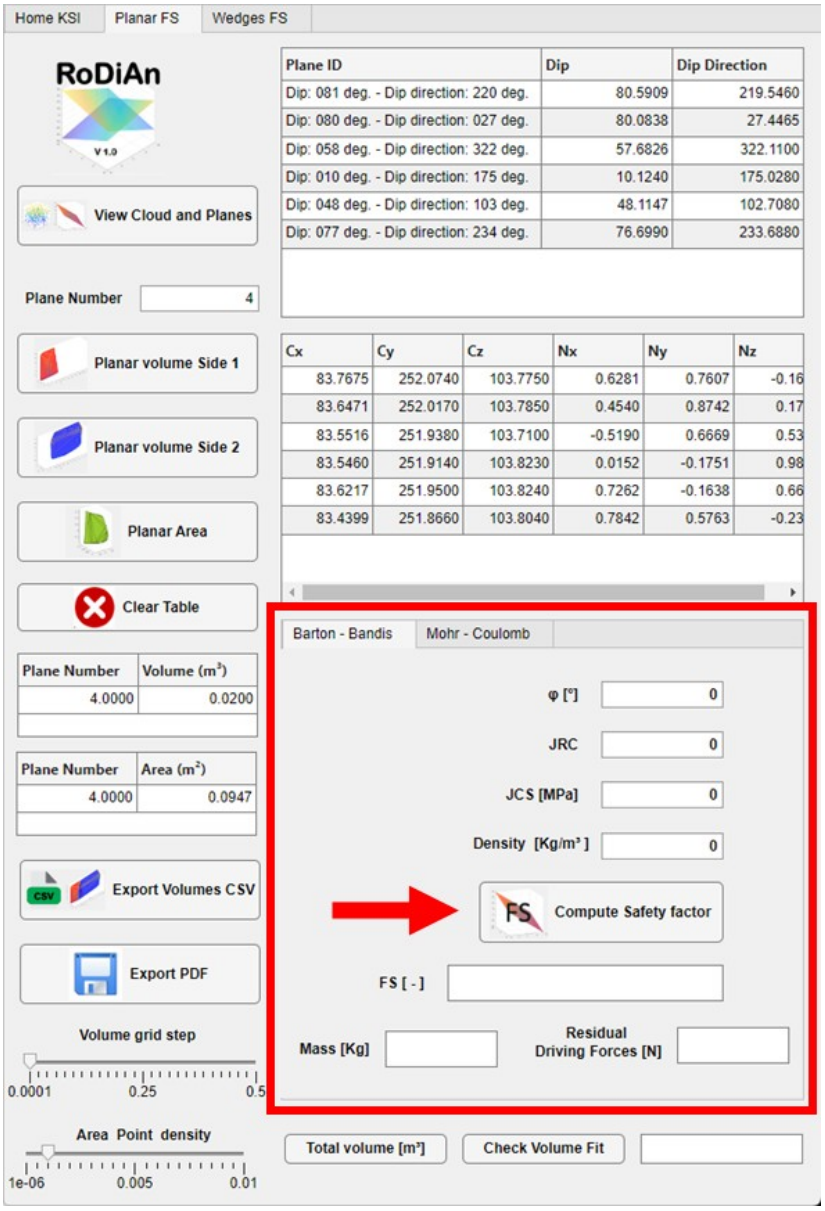


Figure 49: Input box for the physical and geomechanical parameters needed in the dynamic analysis in RoDiAn

The calculation results are displayed in the corresponding fields shown in Figure 50. In addition to the safety factor, the mass of the potentially detached portion is also calculated and reported in the "Mass" field, which is useful for designing anchoring or protection systems. For the same purpose, the "Residual Driving Forces" field is populated. This number equals the difference between the resisting forces and the driving forces. It numerically identifies the force gap required to reach a safety factor of 1 for blocks with FS<1. It is also possible to calculate the total volume of the block using the "Total Volume" button (Figure 50). The adjacent "Check Volume Fit" button allows the user to visually assess the quality of the mesh fit used for volume calculation in a 3D figure that opens when the function is activated (Figure 50).

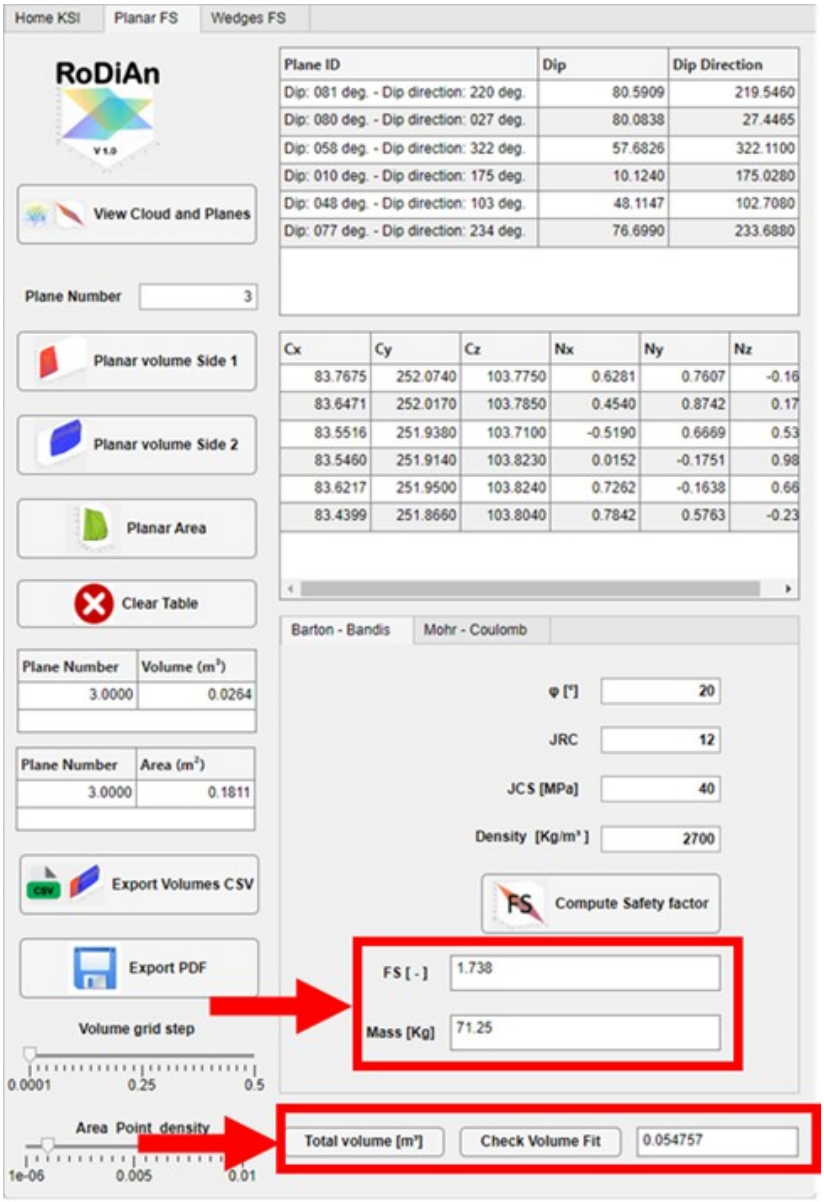


Figure 50: Example of numerical results of the dynamic analysis of a sliding block. The results populate the corresponding field (in red)

By accessing the "Wedges FS" page the user can view the tools for dynamic analysis related to wedge sliding. As with the "Planar FS" page, there are no file upload functions, since the software uses files previously uploaded in the "Home KSI" page. The first button required for analysis is "View Cloud and Planes," shown in Figure 51. This button populates the tables containing information about discontinuity planes and wedges (Figure 51). The top-right table, similar to the one in the "Planar FS" page, contains the ID, Dip, and Dip Direction of each plane. The top-left table contains information related to the wedges. The bottom table (Figure 51) includes the geometric data needed to calculate detachment volumes. Specifically, it contains the spatial coordinates of the center of each plane (Cx, Cy, Cz) and the components of the plane's normal vector (Nx, Ny, Nz). The button also opens a 3D visualization window where users can view the 3DPC and the intersection lines of the planes that form the wedges (Figure 51).

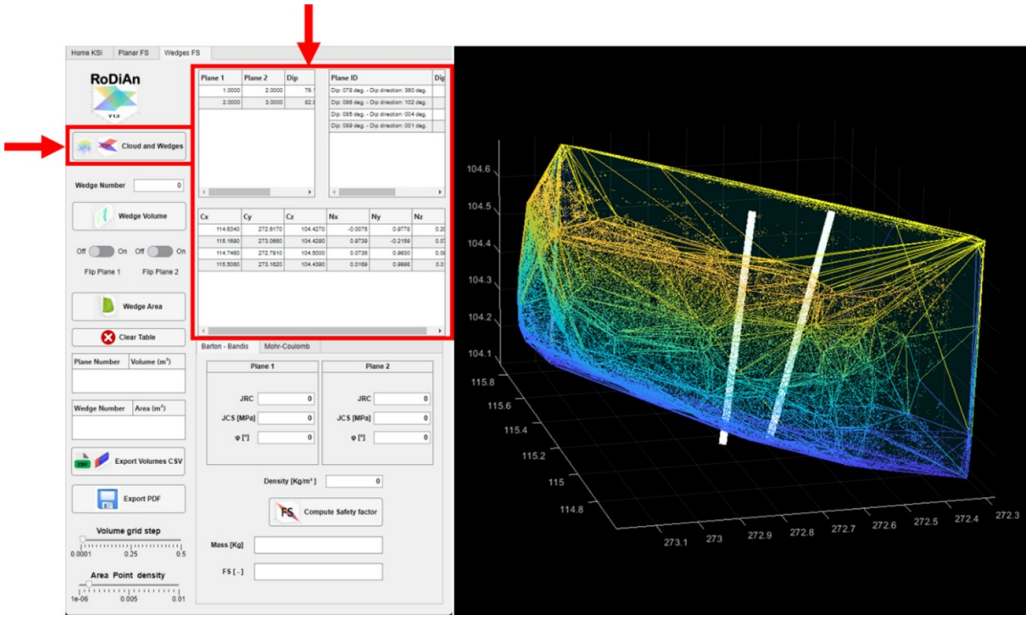


Figure 51: Visualization tools in the dynamic analysis tab for wedegs in RoDiAn. The button 'Cloud and Wedges' (left) prompts the 3D visualization of the 3DPC with the convex hull overlaid used for wedge filtering on top. The plunge lines of the wedges are also plotted (in white). The information of the wedges populate the two tables, upper and lower

The user selects the wedge to be analyzed by modifying the editable field "Wedge Number" (Figure 52) and proceeds to calculate the wedge

volume by pressing the “Wedge Volume” button. The exact logic of this function is described in detail in paragraph 4.2.7, but it is still necessary to introduce the basic logic behind its operation to clarify the choice the user must make when using the “Flip Plane 1” and “Flip Plane 2” switches.

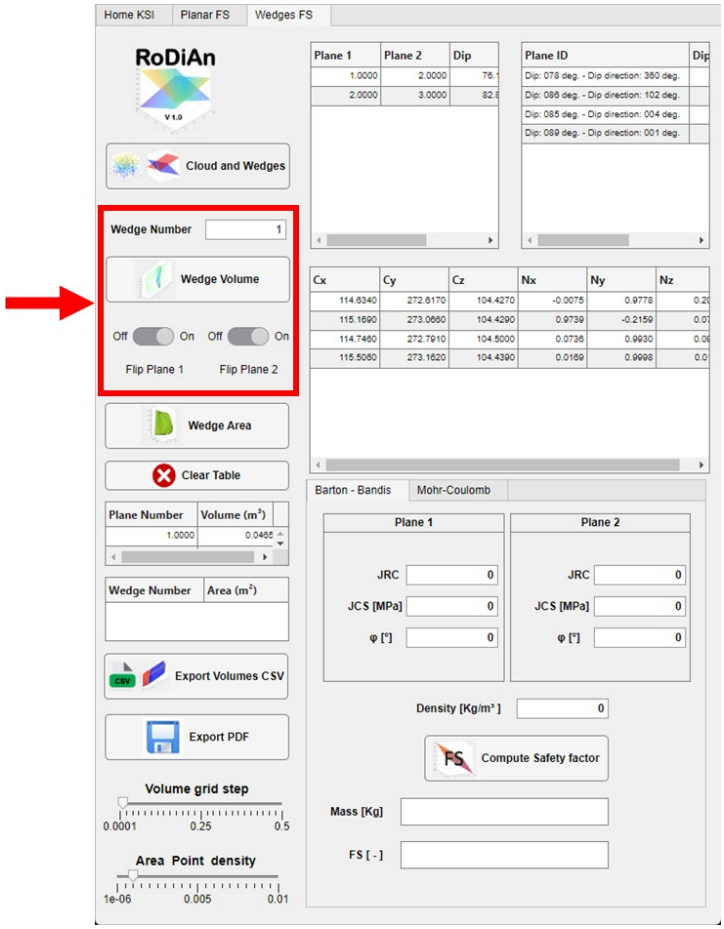


Figure 52: Wedge selection and volume calculation via the ’Wedge Number’ edit field and ’Wedge Volume’ button

For geometric reasons, it is not possible to automate the selection of the spatial area in which to calculate the wedge volume. Therefore, the user must manually select the correct area using the "Flip Plane 1" and "Flip Plane 2" switches. To explain how these buttons work, let's take the block shown in Figure 53 as an example. We'll consider the wedge formed by planes 2 and 3.

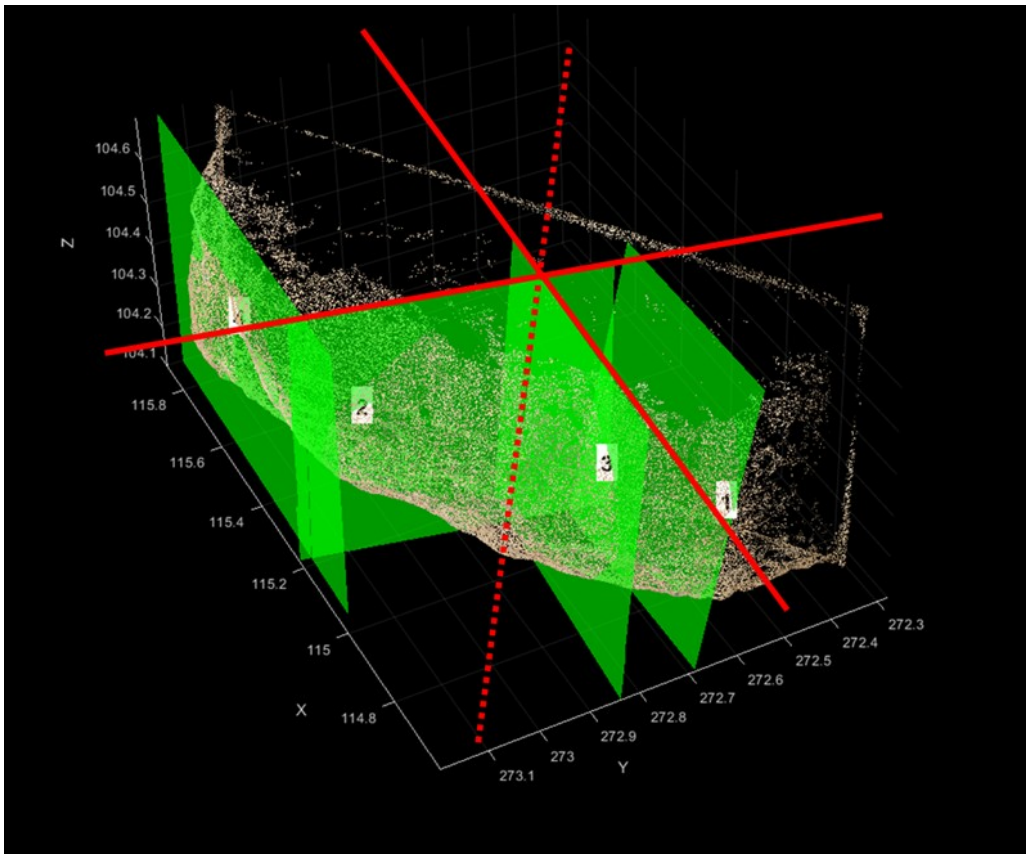


Figure 53: Sample block for explaining how to select the correct wedge volume. The wedge considered in the exmaple is the one formed by Plane 2 and 3 (in red)

Planes 2 and 3 divide the block into four distinct spatial regions, labeled A, B, C, and D in Figure 54. Only one of these regions correctly represents the wedge volume, in this example, Region C.

The two switches, "Flip Plane 1" and "Flip Plane 2," allow the user to choose, for each of the two planes forming the wedge, which side to consider when calculating the intersection points with the other plane. As a result, each pair of planes forming a wedge corresponds to four

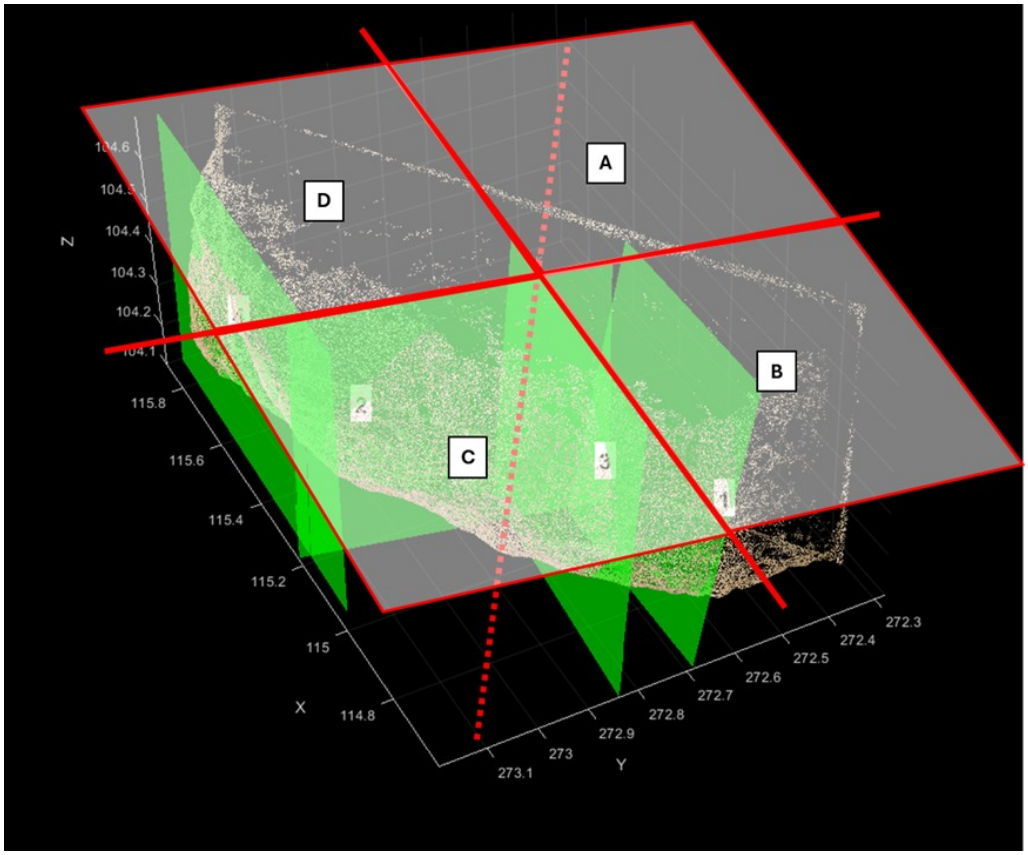


Figure 54: The planes forming the wedge divide the block in four different spatial regions (A-B-C-D)

internal volumes within the block, only one of which represents the wedge potentially subject to sliding. When the "Wedge Volume" button is pressed, one of the four possible volumes is displayed based on the current configuration of the "Flip Plane 1" and "Flip Plane 2" buttons. An example of the four possible volumes is shown in Figure 55, where each sector A, B, C, and D is associated with its corresponding 3D volume. Once the user has identified the combination that correctly represents the wedge volume, they can proceed with calculating the sliding area of the discontinuity planes.

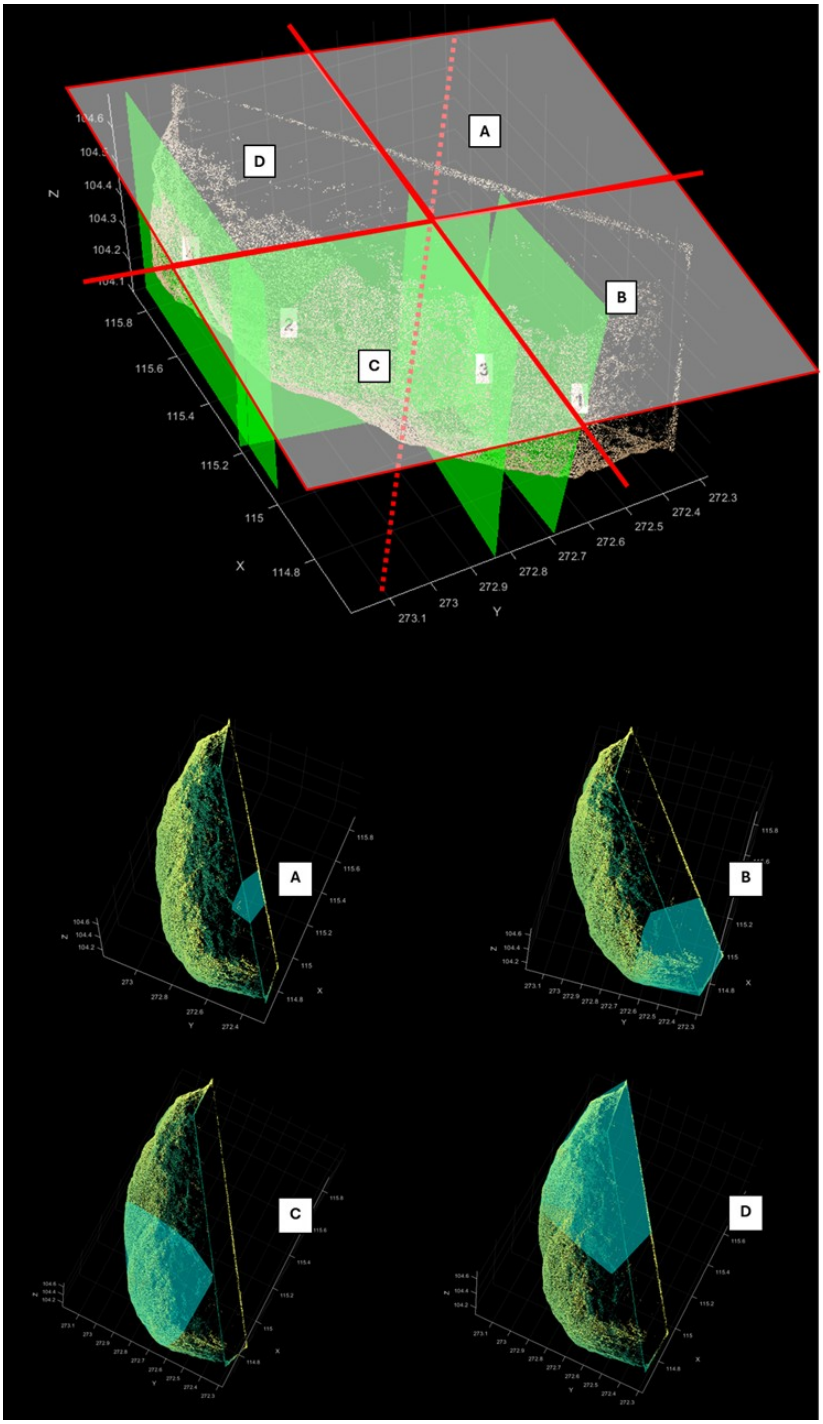


Figure 55: The four different spatial regions (Top A-B-C-D) correspond to four parts of the block. Only one portion correspond to the wedge volume (C in this example)

The area is calculated using the "Wedge Area" button, highlighted in Figure 56. When the button is pressed, the area is computed for both planes forming the wedge and displayed in the corresponding table (Figure 56).

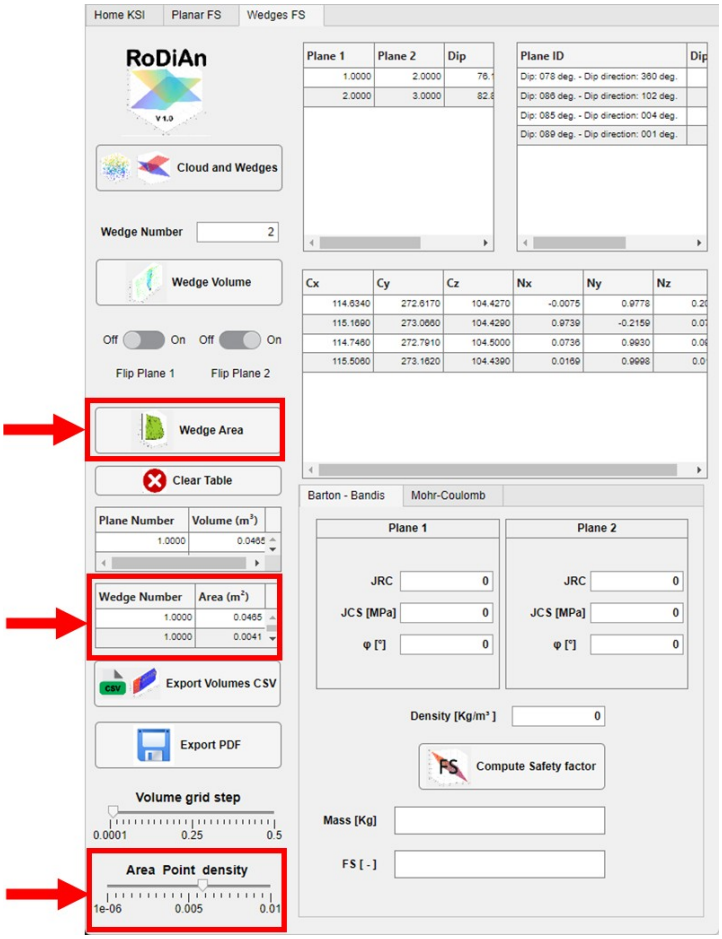


Figure 56: Wedge sliding area calculation in RoDiAn via the 'Wedge Area' button. The numerical output populates the corresponding table (in red). The 'Area Point Density' slider defines the spatial volume within which the 3DPC is projected onto the reference plane

As with the volume calculation, the area is approximated using a convex polyline. In cases of complex morphologies with numerous concave sections, this approximation may lead to significant errors.

As a control measure, the user can view the automatic fitting performed by the software on the point cloud. This is visualized through two images that open automatically upon pressing the button, showing the local slice of the point cloud at the position of the selected plane and the polyline used for area calculation (in red, Figure 57). The volume of space within which the 3DPC points are projected onto the plane can be adjusted using the "Area Point Density" slider, visible in Figure 56.

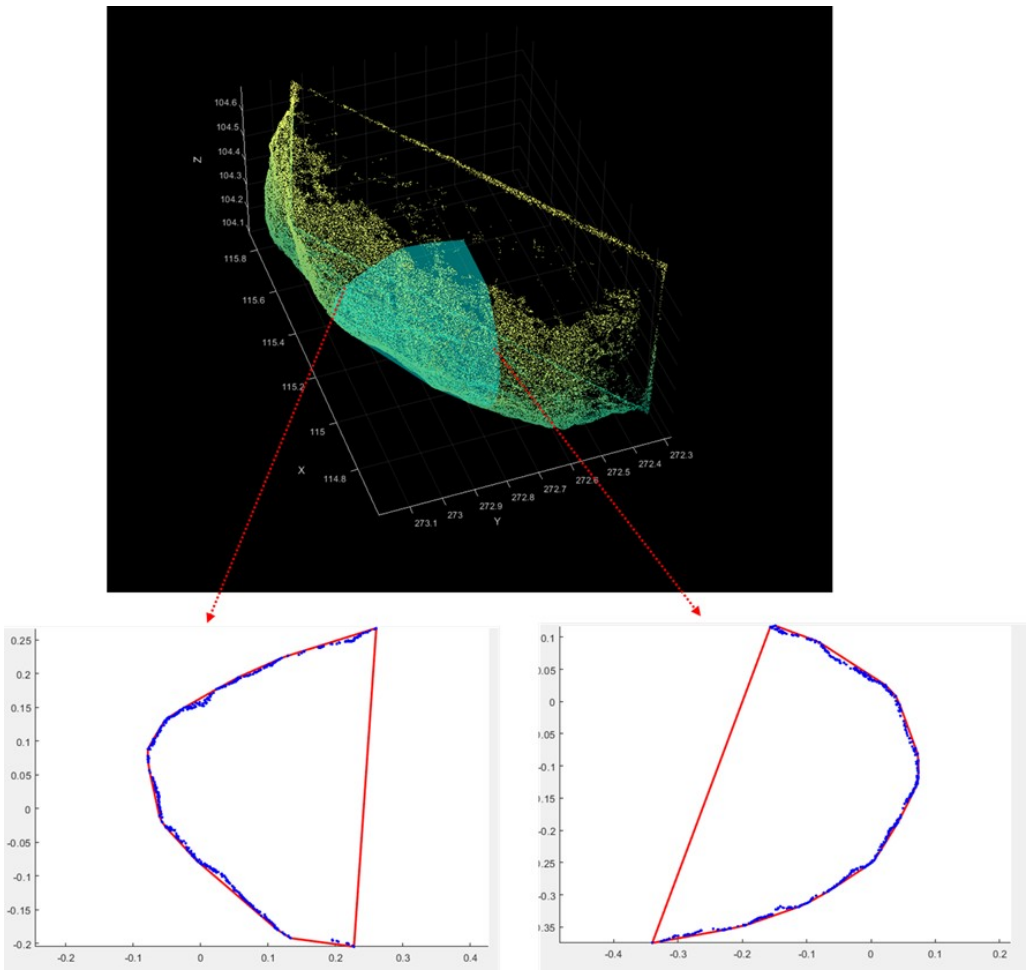


Figure 57: Example of the graphical output of the wedge sliding area calculation in RoDiAn

To proceed with the safety factor calculation, the geomechanical parameters must be entered into the box corresponding to the selected failure criterion (Figure 58). These parameters must be specified for each of the two planes. If the characteristics of both surfaces are identical, the same values should be entered in both fields.

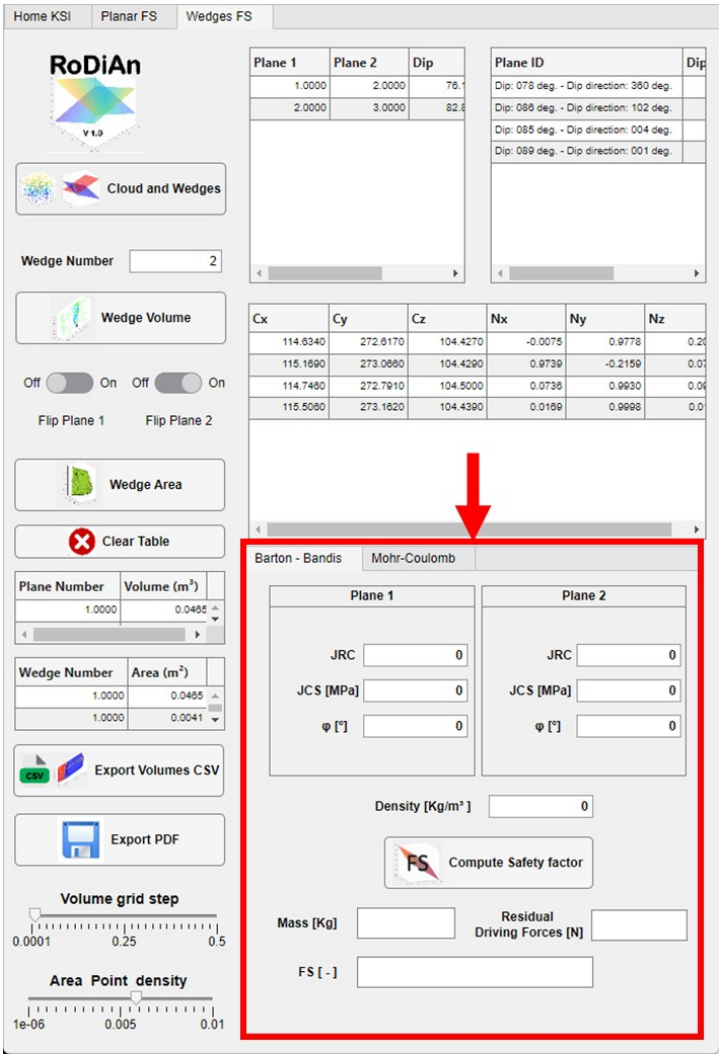


Figure 58: Input box for the physical and geomechanical parameters needed for wedge dynamic analysis in RoDiAn

4

SOFTWARE DEVELOPMENT: RODIAN

4.1 INTRODUCTION

The software is implemented as a MATLAB App Designer application to have a graphical interface (GUI) that is as user friendly as possible. The purpose of the software is to be accessible by operators both geomechanics and in the heritage conservation field that may not be familiar with geology and slope stability software. For this reason, the App is built to follow a simple workflow that requires no code input from the user, that interacts with the functionalities of the software via intuitive buttons, sliders or editable fields. All graphical visualization panels are 3D fields, where the user can interact with the data and extract views. The App is divided into three main tabs (FIgure 59) :

- Home KSI: The main tab, where the user can load the files needed for the analysis (a point cloud identity in .txt file and plane information as a .csv file). In this tab the user can then perform the wedges calculations and perform the kinematics analysis on each discontinuity. After the kinematic test it is possible to calculate the Kinematic Susceptibility Index both for planes and wedges identities. The identities that are marked as possible failure points can then be analyzed in detail in the following tabs.
- Planar FS: The planar safety factor tab is meant to be used after the user has identified the planes/discontinuity that can fail. In this tab it is possible to calculate the volume of the unstable mass, the area of sliding and the safety factor using different failure criterion (Barton/Coulomb)
- Wedge FS: Similarly to the Planes FS tab, this area is used to analyze the wedges that have been identified as critical/potentially unstable.

It is possible to calculate the volume of the wedges, their sliding area and their safety factor.

The tabs act as a control panel for the 3D figures, which are plotted alongside the interface.

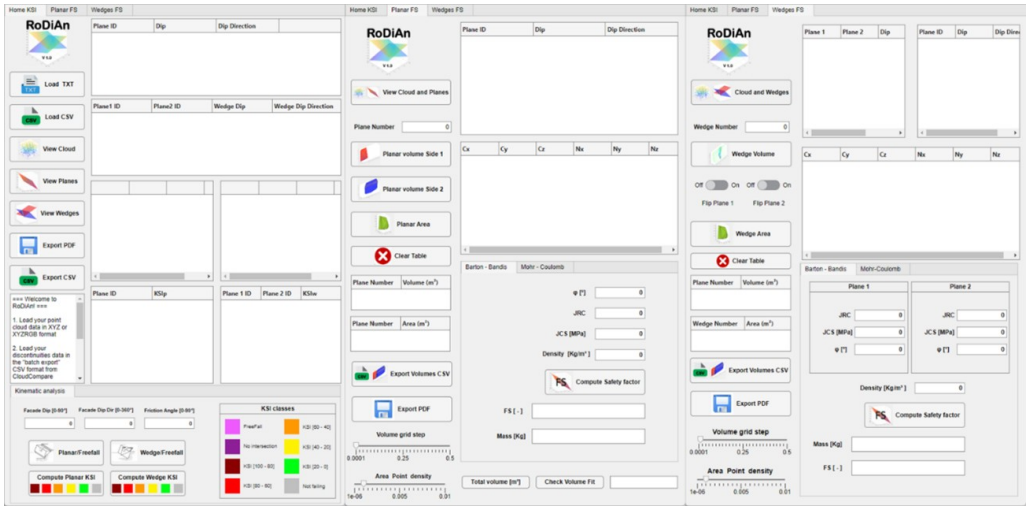


Figure 59: RoDiAn's user graphical interface

4.2 MAIN FUNCTIONS

This section presents the main functions implemented in RoDiAn. Functions without noteworthy or innovative features, such as data loading, visualization, and saving, will not be included. For each function, snippets the code will be commented in natural language to clearly explain the underlying logic.

4.2.1 *View Planes*

This function is designed to load the discontinuity plane data. As discussed in chapter 3, the first step of the workflow involves preprocessing the point clouds in CloudCompare. The outcome of this process is the export of a properly formatted .csv file. This file is then loaded into the software by the user via the "Load CSV" button. The function attempts to read the point cloud from the TXT file and the planes information from the CSV file. If the files are not available or fail to load, a popup alert is

shown prompting the user to load a point cloud or a .csv, and execution stops.

```
% Button pushed function: ViewPlanesButton
      function ViewPlanesButtonPushed(app, event)
%---------------------------------------------------
% ViewPlanesButtonPushed
%
% Plot the planes in the CSV file on the point cloud in the
   TXT file
%---------------------------------------------------

%--- Load Point Cloud from TXT ---
try
   txtdata = readmatrix(app.txtFilePath);
catch
   uialert(app.UIFigure, 'Please select a TXT file using the
      Load TXT Button', 'File Error');
   return;
end
%--- Load Plane Definitions from CSV ---
try
   csvData = readtable(app.csvFilePath, 'Delimiter', ';');
catch
   uialert(app.UIFigure, 'Please select a file using the Load
      CSV Button', 'File Error');
   return;
end
```

Retrieves the 3D spatial coordinates (X, Y, Z) of the point cloud from the TXT file, and normalizes the RGB values (range 0–255) so they're compatible with graphical rendering in MATLAB and saves both the geometric coordinates and the color values into variables. This makes them accessible for visualization, analysis or any re-use in other parts of the App.

```
%--- Extract XYZ Coordinates and RGB Colors from Point Cloud
   ---
X = txtdata(:, 1); Y = txtdata(:, 2); Z = txtdata(:, 3);
```

```
colors = [txtdata(:, 4:6)] / 255;

%--- Store Data for Future Use ---
app.PointCloudXYZ = [X, Y, Z];
app.PointCloudColors = colors;
```

Updates the table in the UI with the data in the columns from the CSV file showing each plane's name and orientation details (dip and dip direction). Determines the minimum and maximum XYZ bounds of the point cloud to define a bounding box in which it plots the plane. Without a bounding box the planes would have infinite extension (the .csv contains informations on the position of the center of the plane and its orientation, there are no information about the dimensions).

```
%--- Update Table View with Plane Metadata ---
app.UITable.Data = csvData(:, {'Name', 'Dip', 'DipDir'});

%--- Check if Cloud Visualization is Available ---
if isempty(app.cloudFig) || ~isvalid(app.cloudFig)
   uialert(app.UIFigure, 'Please load the point cloud
      first.', 'No Point Cloud');
   return;
end

%--- Compute Bounding Box Dimensions ---
boundsMin = min(app.PointCloudXYZ, [], 1);
boundsMax = max(app.PointCloudXYZ, [], 1);
cloudSpan = boundsMax - boundsMin;
patchSize = 0.5 * mean(cloudSpan);

hold(app.cloudAxes, 'on');
```

This part of the function handles the plotting iteratively. The .csv output from CloudCompare is formatted that every row define a different plane, so the function cycles through every row in the file. For the current plane, this extracts its normal vector (which defines orientation) and the center

point (its location in 3D space). If the plane's normal vector is too small (i.e., close to zero), it's likely invalid or undefined so the function skips it.

```
%--- Iterate Over Planes in CSV ---
for i = 1:height(csvData)
   N = csvData{i, {'Nx', 'Ny', 'Nz'}}; % Normal vector
   C = csvData{i, {'Cx', 'Cy', 'Cz'}}; % Center point

   %--- Skip Invalid Normals ---
   if norm(N) < 1e-6, continue; end
```

To render a planar surface in 3D space, its position and orientation via a center point and normal vector (the data in the .csv file) is not enough, we also need to construct a local coordinate system lying within the plane itself. This internal basis (orthonormal basis) can be used to create a grid inside the plane, necessary for plotting purposes. The first vector of the orthonormal basis (u) is created by the cross product of the normalized normal vector (N, extracted from the .csv) and a reference vector (a random vector that is not colinear to the normal vector, any vector will do since the vector obtained by the cross product with the normal vector always lies on the plane). The second vector of the orthonormal basis is obtained with the cross product of N x u (figure 60). Once u and v are defined, the function creates a 2D grid over the plane's surface, using the center point C and the vectors.

```
   %--- Construct Orthonormal Basis (u, v) in the Plane ---
   n = N / norm(N); % Normalized normal
   ref = [0 0 1]; % Reference vector
   if abs(dot(ref, n)) > 0.99 % Avoid colinearity
      ref = [0 1 0];
   end
   u = cross(n, ref); u = u / norm(u);
   v = cross(n, u); v = v / norm(v);

   %--- Generate Grid of Points in Plane ---
   [a, b] = meshgrid(linspace(-patchSize, patchSize, 200));
   Xp = C(1) + a * u(1) + b * v(1);
   Yp = C(2) + a * u(2) + b * v(2);
   Zp = C(3) + a * u(3) + b * v(3);
```

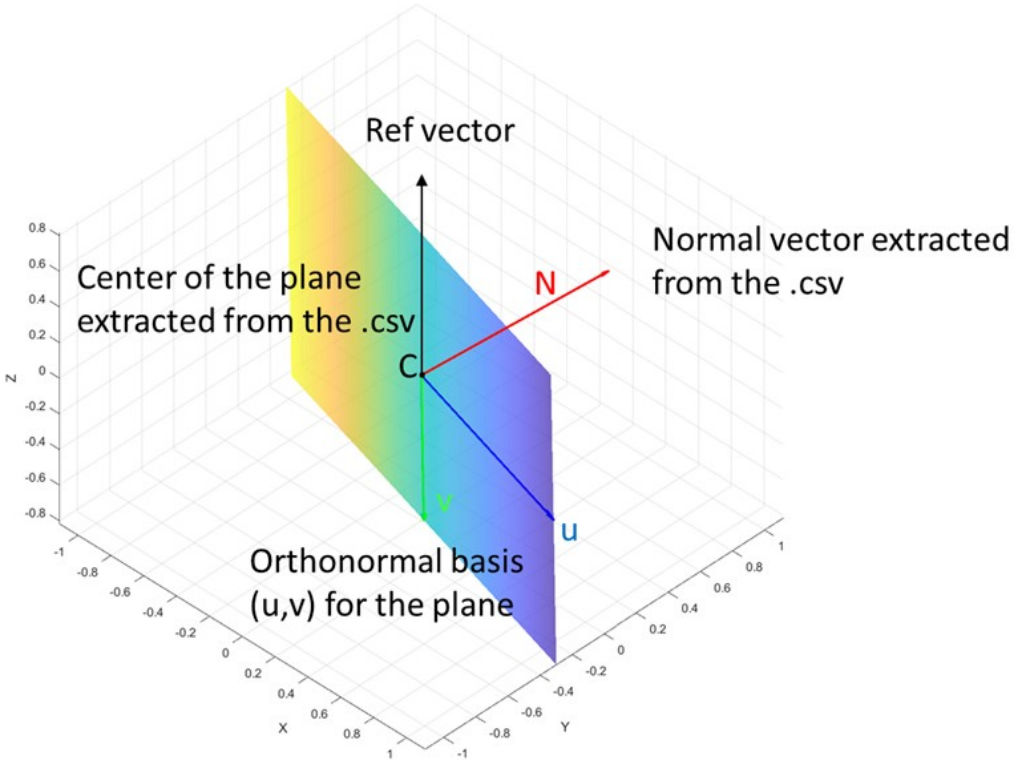


Figure 60: Construction of a planar surface in 3D space using center point (C) and normal vector (red) extracted from the .csv data. The orthonormal basis (u, blue; v, green) is derived via cross products with a reference vector (black)

The plotting section starts by creating a logical mask that checks whether each point of the generated plane grid falls inside the bounding box defined by the point cloud at the start of the function. Only points within the 3D domain are allowed to remain visible, so the planes have a reasonable extent (if none of the grid points land in the bounding box, the plane is skipped.) The planes are then plotted and labeled by their row number in the .csv file (they are not labeled by the ID assigned by the automatic export of CloudCompare since it is a long string that would overlay on the 3D image)

```
%--- Clip to Bounding Box ---
   mask = ...
      Xp >= boundsMin(1) & Xp <= boundsMax(1) & ...
      Yp >= boundsMin(2) & Yp <= boundsMax(2) & ...
      Zp >= boundsMin(3) & Zp <= boundsMax(3);

   if ~any(mask, 'all'), continue; end % Skip empty planes

   Xp(~mask) = NaN; Yp(~mask) = NaN; Zp(~mask) = NaN;

   %--- Render Clipped Plane Patch ---
   surf(app.cloudAxes, Xp, Yp, Zp, ...
      'FaceColor', 'g', 'FaceAlpha', 0.6, 'EdgeColor',
         'none');

   %--- Label the Plane ---
   labelName = sprintf('%d', i); % Use row index
   offset = 0.02 * norm(cloudSpan); % Visibility offset
   text(app.cloudAxes, C(1), C(2), C(3) + offset, labelName,
      ...
      'Color', 'k', 'FontSize', 16, 'FontWeight', 'bold', ...
      'HorizontalAlignment', 'center', 'BackgroundColor',
         'w');
end

%--- Finalize Plot ---
axis(app.cloudAxes, 'equal');
```

```
xlabel(app.cloudAxes, 'X'); ylabel(app.cloudAxes, 'Y');
   zlabel(app.cloudAxes, 'Z');
title(app.cloudAxes, 'Discontinuity Planes');

      end
```

4.2.2 *View Wedges*

This function is one of the cornerstones of the application and one of the main reasons behind its development. The automatic identification of wedges within a block is one of the key challenges that emerged when using existing software. Shifting the problem from a geomechanical to a geometric perspective, wedge identification can be described as the search for the line of intersection between two planes. As discussed in paragraph 2.6, slope stability analysis software that uses angular parameters of discontinuity families (Dip and Dip Direction) as input all operate in a similar way: they compute the cross product of the normal vectors of the discontinuity families. The result of this vector product is another vector that describes the multiple lines of intersection between the families. This approach is optimized and acceptable for slope-scale studies, where the scale ensures that families intersect in space. However, this is not the case at the scale relevant to this study, which is why a different approach is needed to study discontinuity plane intersections. Working solely with angular parameters (Dip and Dip Direction) is insufficient, as they provide no information about the spatial relationship between planes, and therefore about their actual intersection. Two non-parallel planes will always intersect, but the intersection may occur in a region of no interest, in our case outside the boundaries of the block. A practical example of this concept is shown in Figure 61. All possible plane pairs within the block form an intersection, but only the intersections between planes 1–2 and 1–3 are relevant and actually occur in the block. A Slope kinematics software applied to this block will indiscriminately display all intersections as potentially critical, as shown in the RocScience Dips output in Figure 62.

To better illustrate this concept, Figure 63 shows the block with all intersection lines formed by the planes highlighted in red. As can be observed, the intersections between planes are not necessarily confined

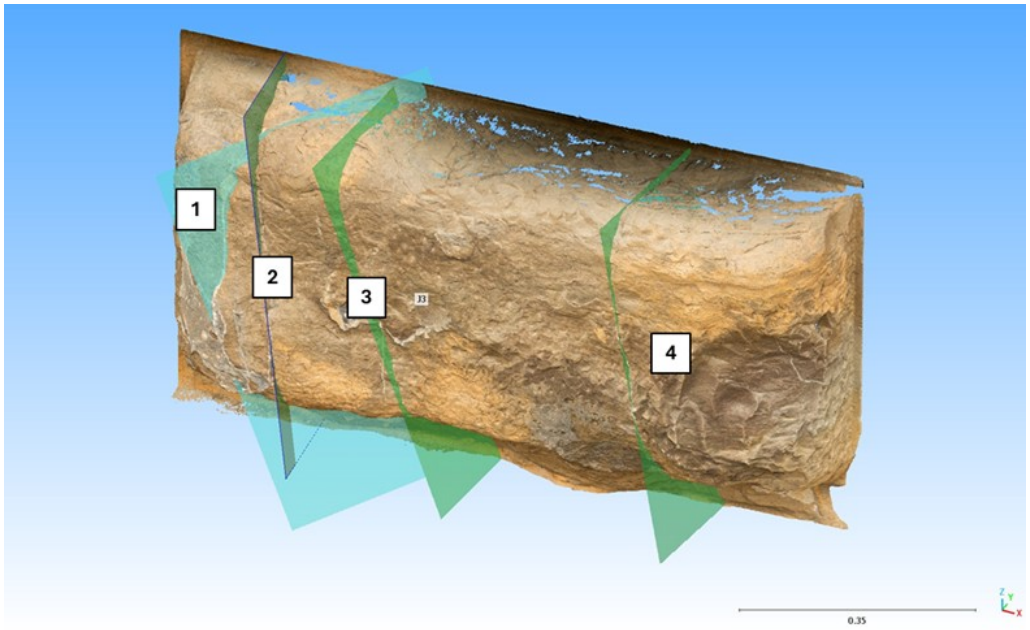


Figure 61: Block that contains four discontinuity planes (1-2-3-4). Only the intesections between the planes 1–2 and 1–3 acrutally create wedges in the block

within the block's geometry and may occur in spatial regions that are not relevant to the analysis.

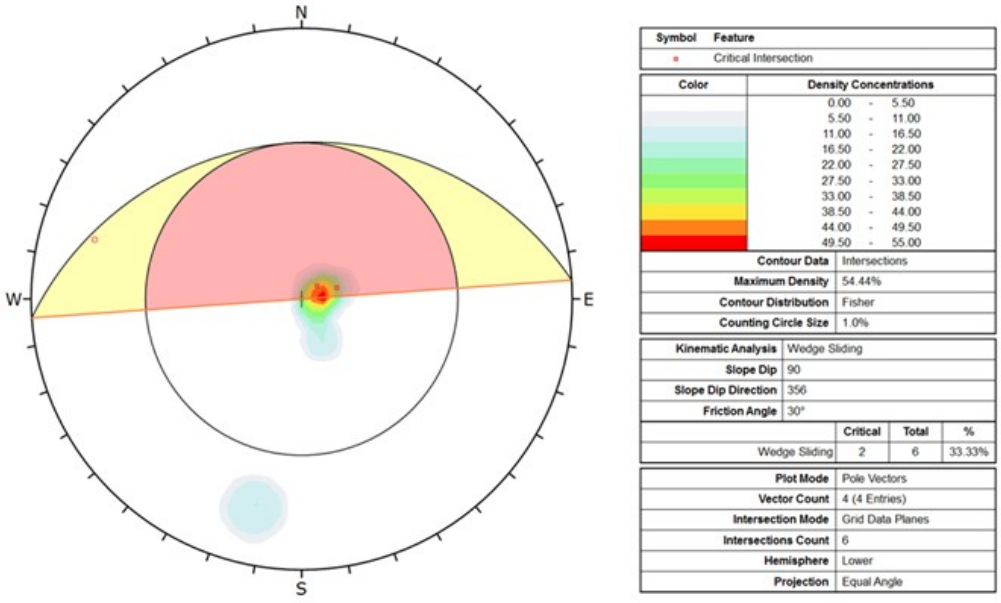


Figure 62: Wedge sliding output from RocScience Dips for the example block. All the intersections between the planes are considered as revelant, regardless of theu actual position in the space

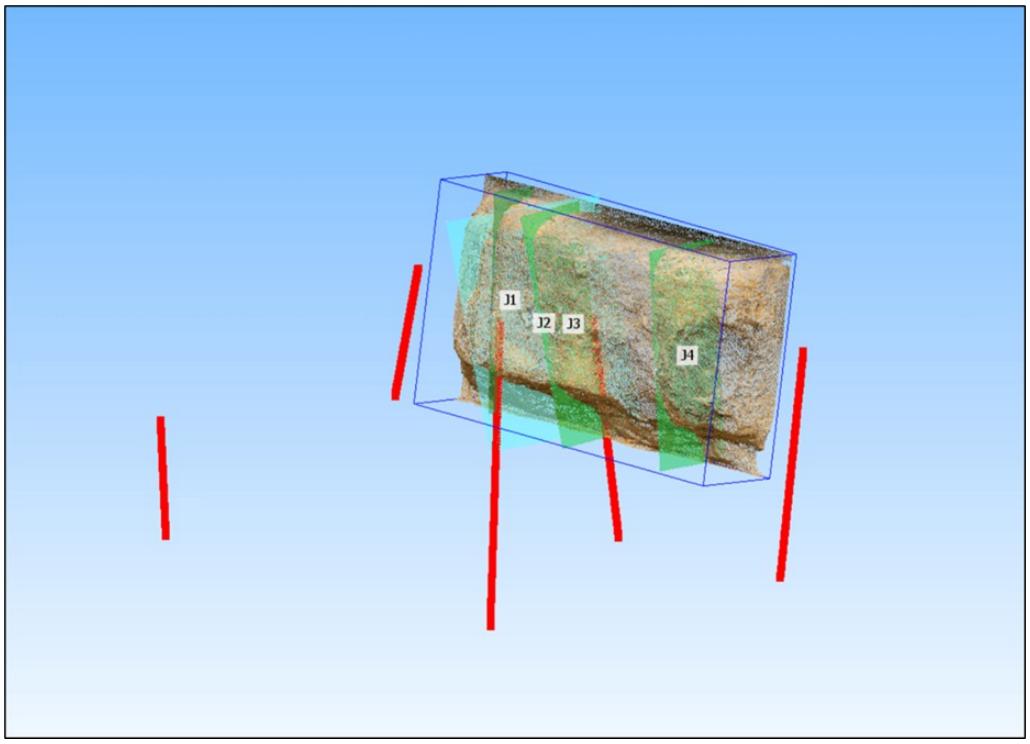


Figure 63: Visualization of the example block model showing all computed intersection lines between discontinuity planes, highlighted in red. As illustrated, several plane intersections extend beyond the block's geometry, occurring in spatial regions not relevant to the analysis

The issue of individual intersections primarily lies in the type of input data: two angular entities alone are not sufficient. For this reason, RoDiAn uses a `.csv` file as input, which, for each plane, includes the spatial coordinates of the plane's center and the components of its normal vector. If we consider a pair of vectors:

$$\mathbf{A} = \begin{bmatrix} a_1 \\ a_2 \\ a_3 \end{bmatrix} \quad \mathbf{B} = \begin{bmatrix} b_1 \\ b_2 \\ b_3 \end{bmatrix}$$

The result of their cross product:

$$\mathbf{A} \times \mathbf{B} = \begin{bmatrix} a_2 b_3 - a_3 b_2 \\ a_3 b_1 - a_1 b_3 \\ a_1 b_2 - a_2 b_1 \end{bmatrix}$$

describes the infinite intersections of two sets of parallel planes. The problem is represented geometrically in Figure 63. Vectors A and B each describe an infinite set of parallel planes (comparable in geology to a discontinuity family), but cannot describe a single plane. Their cross product is a vector that describes the direction of their intersection.

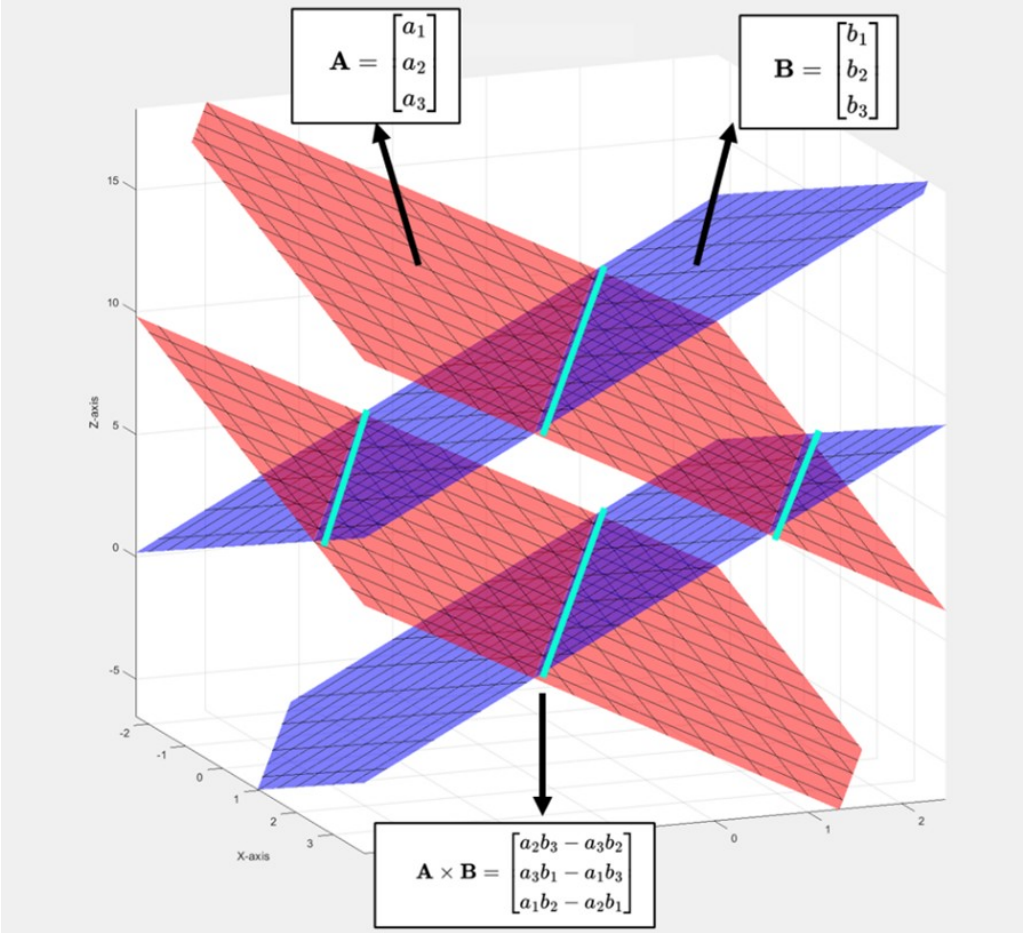


Figure 64: Geometric interpretation of the cross product between vectors **A** and **B**. Vectors **A** and **B** define two distinct families of parallel planes, each representing a directional discontinuity set. Their cross product, $\mathbf{A} \times \mathbf{B}$, yields a vector orthogonal to both inputs, corresponding to the lines of intersection between the two plane families.

If however, in addition to the normal vectors, we also have the coordinates of a point belonging to each plane (in our case we have the coordinates of the plane center in the .csv file we get from the preprocessing in CloudCompare) then we can describe the planes not only as angular entities but through their equation. If we know the coordinates of a point on a plane:

$$P_0 = (x_0, y_0, z_0)$$

And the normal vector to the plane:

$$\mathbf{n} = (a, b, c)$$

we can describe the plane through an equation of the type

$$a(x - x_0) + b(y - y_0) + c(z - z_0) = 0$$

If we have two planes, defined by two equations, we can therefore obtain not only the direction of the intersection line (defined by the cross product of the two direction vectors, as we did in the previous case) but also its position in space. If we know the coordinates of two points belonging to two planes (Figure 65):

$$C_1 = (x_1, y_1, z_1) \qquad C_2 = (x_2, y_2, z_2)$$

And their normal vectors (Figure 65):

$$\mathbf{N}_1 = (a_1, b_1, c_1) \qquad \mathbf{N}_2 = (a_2, b_2, c_2)$$

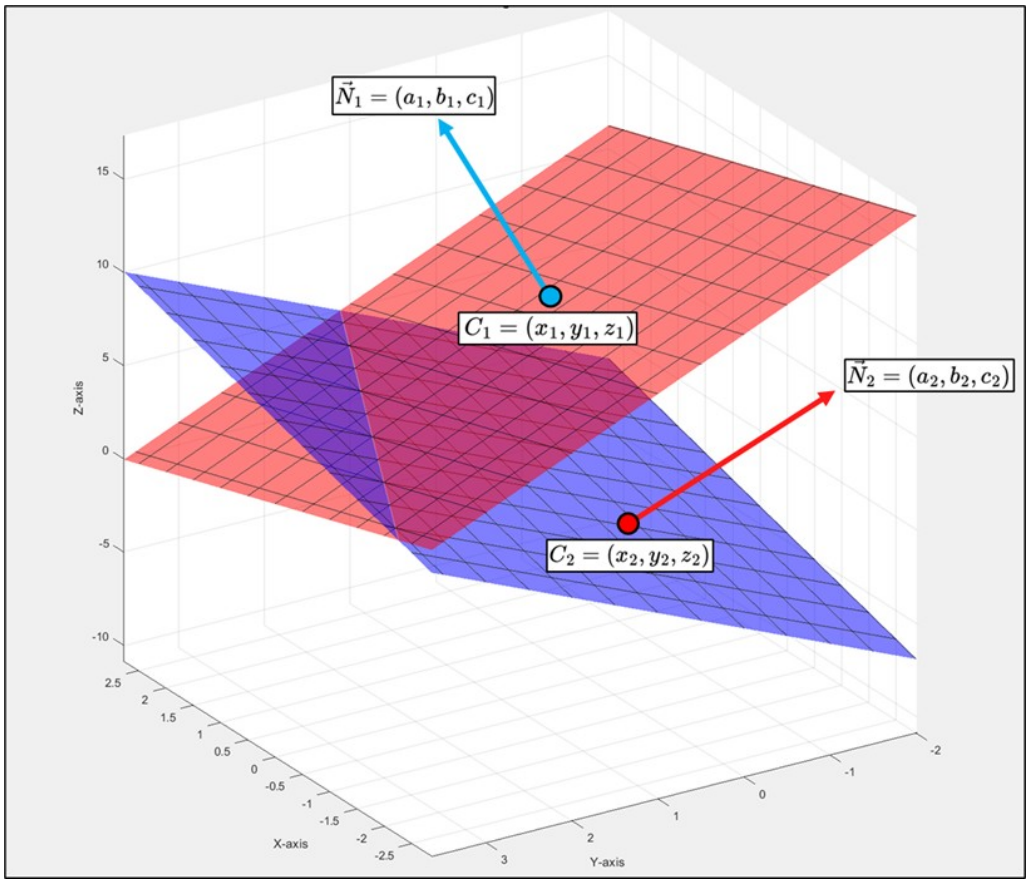


Figure 65: Two planes defined by point coordinates ($C_1 = (x_1, y_1, z_1)$ and $C_2 = (x_2, y_2, z_2)$) and normal vectors ($\vec{N}_1 = (a_1, b_1, c_1)$ and $\vec{N}_2 = (a_2, b_2, c_2)$)

then the two planes can be described by the equations:

$$a_1(x - x_1) + b_1(y - y_1) + c_1(z - z_1) = 0$$

$$a_2(x - x_2) + b_2(y - y_2) + c_2(z - z_2) = 0$$

The direction of the intersection is defined by the cross product of the two direction vectors:

$$\vec{d} = \vec{N}_1 \times \vec{N}_2 = (d_1, d_2, d_3)$$

To define the position of the intersection line we must find the coordinates of any point belonging to it. This point corresponds to any point that lies on both planes, therefore a point that satisfies both plane equations. We can set up a linear system that contains both plane equations and solve it:

$$\begin{cases} a_1(x - x_1) + b_1(y - y_1) + c_1(z - z_1) = 0 \\ a_2(x - x_2) + b_2(y - y_2) + c_2(z - z_2) = 0 \end{cases}$$

The infinite solutions of this linear system are the coordinates of the points belonging to the intersection line. We just obtained, in addition to the direction of the intersection, also its position in space. From a computational point of view, it is simpler to solve the system by fixing one solution and using the single point found and projecting it using the direction vector, and in the function the wedges are obtained this way (FIgure 66).

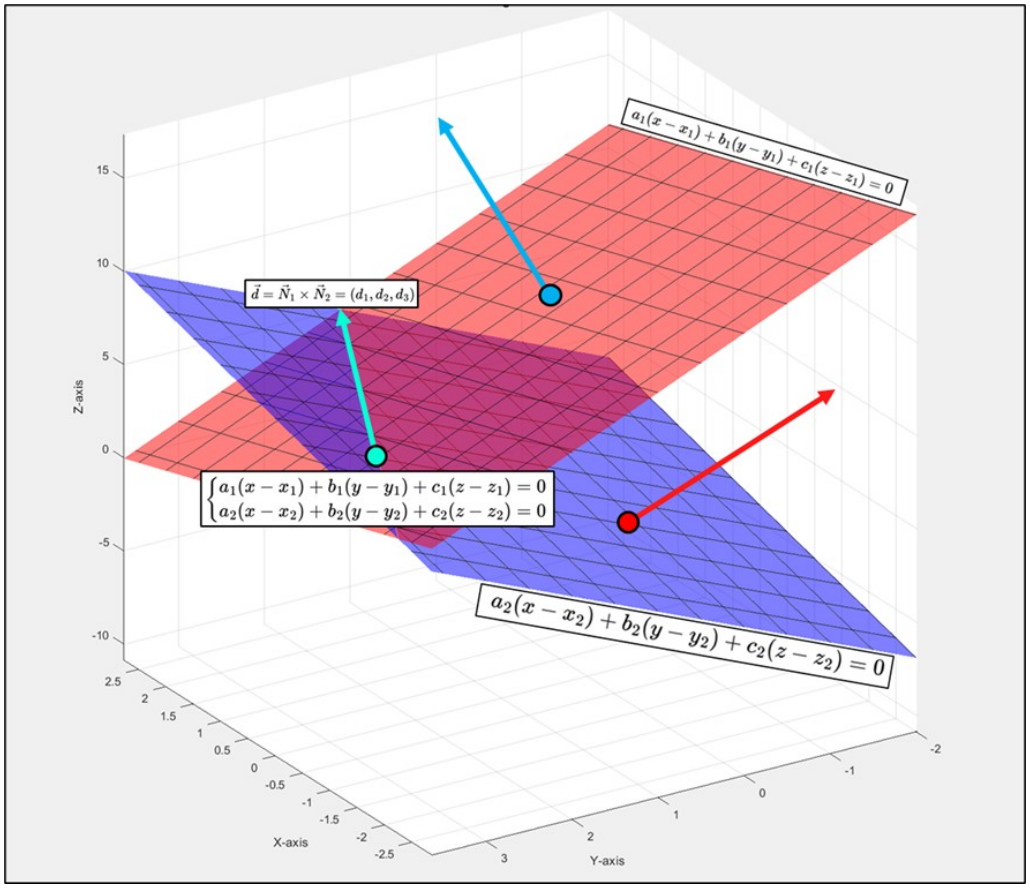


Figure 66: Determination of the intersection line between two planes in three-dimensional space. The direction vector $\vec{d} = \vec{N}_1 \times \vec{N}_2$ defines the orientation of the intersection line, obtained as the cross product of the normal vectors of the two planes. The coordinates of a point on the intersection are computed by solving the linear system defined by the two plane equations

Having thus obtained the position of individual points belonging to the wedges, we have a reference system in which all entities are reciprocally spatially referenced, and it is therefore possible to perform operations between the parts. In addition to the wedge filtering function presented below, this characteristic will also be exploited in other functions and is one of the core functionalities that distinguishes the RoDiAn workflow.

The function starts with an attempt to read the point cloud from the TXT file and the planes information from the CSV file. If the files are not available or fail to load, a popup alert is shown prompting the user to load a point cloud or a .csv, and execution stops. Determines the minimum and maximum extents of the point cloud in each spatial dimension. These bounds will later be used to clip and validate wedge geometries so that only the visible or relevant intersections are displayed.

```
%-------------------------------------------------
% ViewWedgesButtonPushed - Visualizes intersections between
    plane pairs
% using the planes data from CSV and the point cloud in the
    TXT file.
%-------------------------------------------------


  % Load CSV and TXT input files
   try
      csvData = readtable(app.csvFilePath, 'Delimiter', ';');
   catch
      uialert(app.UIFigure, 'Please select a file using the
          Load CSV Button', 'File Error');
      return;
   end

   try
      ptCloudRaw = readmatrix(app.txtFilePath);
   catch
      uialert(app.UIFigure, 'Please select a file using the
          Load TXT Button', 'File Error');
      return;
   end

   % Extract bounds from raw point cloud
```

```
Xraw = ptCloudRaw(:, 1);
Yraw = ptCloudRaw(:, 2);
Zraw = ptCloudRaw(:, 3);
xlimBounds = [min(Xraw), max(Xraw)];
ylimBounds = [min(Yraw), max(Yraw)];
zlimBounds = [min(Zraw), max(Zraw)];
```

The point cloud is first downsampled using a grid average filter of 1mm to reduce density. Denser cloud provide no advantage in precision, being here used to calculate an hull, and render the function computationally heavy causing crashes. The idea of building an hull is dictated by the need of having an enclosed portion of space to test the wedges: if a line of intersection falls within or touch the edges of the hull it can be considered inside the block and relevant, otherwise it can be filtered out. The meshing algorithm of choice is the Delaunay Triangulation (DT) to get a convex hull (the smallest convex polyhedron that encloses all the points). DT was chosen against Alpha Shape or Poisson Reconstruction mainly for topology needs: a point cloud obtained on a facade/wall/slope is dense on the scanning surface and 'empty' on the backside, a convex shape usually better describe the volume (Figure 67). A trade-off is clearly made, and in case of irregular morphology rich in concave areas, this must be taken into account.

```
% Downsample point cloud and compute convex hull
ptCloudObj = pointCloud(ptCloudRaw(:, 1:3));
ptCloudDS = pcdownsample(ptCloudObj, 'gridAverage', 0.001);
ptCloud = ptCloudDS.Location;
DT = delaunayTriangulation(ptCloud);
hull = convexHull(DT);

% Fade colors for background cloud visualization
dimFactor = 0.3;
fadedColors = min(max(app.PointCloudColors * dimFactor,
   0), 1);

% Initialize visualization window
screenSize = get(0, 'ScreenSize');
fig = figure('Name', app.inputName, ...
```

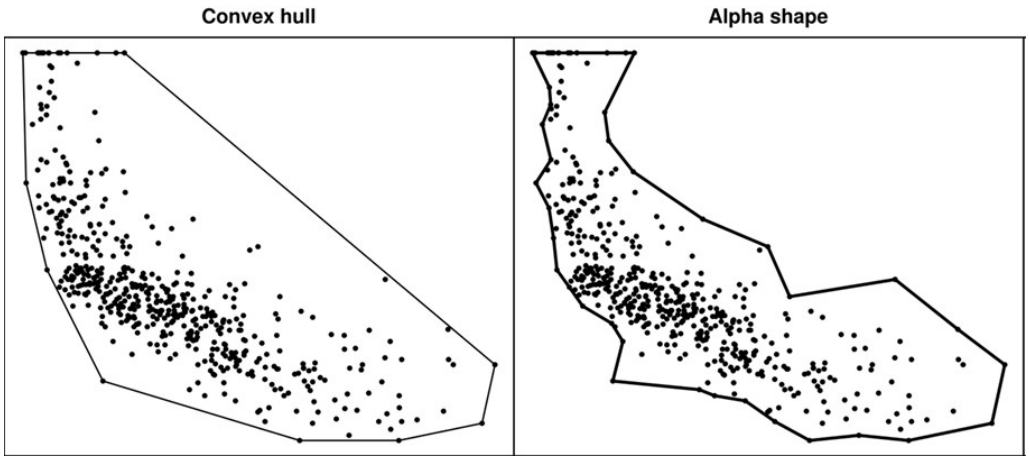


Figure 67: Comparison between convex hull and alpha shape representations of point cloud. The alpha shape captures concave features with greater fidelity but assumes that point clouds with an 'hollow' side have concave features

```
            'Position', [screenSize(3)*0.366,
               screenSize(3)*0.1, screenSize(3)*0.6,
               screenSize(4)*0.6], ...
            'Color', 'w');
ax = pcshow(app.PointCloudXYZ, fadedColors, 'MarkerSize',
   5);
hold on;
xlabel('X'); ylabel('Y'); zlabel('Z');
view(3); axis equal; grid on;
xlim(xlimBounds); ylim(ylimBounds); zlim(zlimBounds);
set(gca,
   'XLimMode','manual','YLimMode','manual','ZLimMode','manual');
axis vis3d;
camva('manual'); camproj('perspective');
camtarget(mean([xlimBounds; ylimBounds; zlimBounds], 2)');

% Prepare meshgrid for plane visualization
[Xgrid, Ygrid] = meshgrid(linspace(-1, 1, 5));
```

Once the convex hull is built the function iterates through every unique pair of planes from the CSV in a nested loop that ensures no duplicate

or reversed pairings (e.g., plane 2 vs. 3 and 3 vs. 2). It then calculates the cross-product of the two normal to get the direction of the wedge. The linear system is solved to find a point that lies on both planes. This point is used to create a line segment centered on it extending in both directions along the computed direction vector. After the intersection line is calculated, it checks which points on the line lie inside the convex hull. If the wedge is found to be outside of the convex hull, it is ignored. This automatically filters out every intersection that does not form a wedge inside the block.

```
for i = 1:numPlanes
   for j = i+1:numPlanes
      Ni = csvData{i, {'Nx', 'Ny', 'Nz'}};
      Nj = csvData{j, {'Nx', 'Ny', 'Nz'}};
      Ci = csvData{i, {'Cx', 'Cy', 'Cz'}};
      Cj = csvData{j, {'Cx', 'Cy', 'Cz'}};

      direction = cross(Ni, Nj);
      if norm(direction) < 1e-6, continue; end

      A_sys = [Ni; Nj; direction];
      B_sys = [dot(Ni, Ci); dot(Nj, Cj); dot(direction,
         Ci)];
      intersectionPoint = A_sys \ B_sys;

      % Generate line segment
      maxSpread = max(range([Xraw Yraw Zraw]));
      t = linspace(-1, 1, 100)' * maxSpread;
      linePts = intersectionPoint' + t .* direction;

      % Trim intersection line to convex hull
      insideMask = false(size(linePts,1),1);
      for k = 1:size(linePts,1)
         insideMask(k) =
            app.pointInConvexHull3D(linePts(k,:), ptCloud,
            hull);
      end
      if ~any(insideMask), continue; end

      iStart = find(insideMask, 1, 'first');
```

```
iEnd = find(insideMask, 1, 'last');
trimmedLine = linePts(iStart:iEnd, :);

% Render intersecting planes
Z1 = -(Ni(1)*Xgrid + Ni(2)*Ygrid) / Ni(3) + Ci(3);
X1 = Xgrid + Ci(1); Y1 = Ygrid + Ci(2);
plane1 = surf(X1, Y1, Z1, 'FaceColor', 'g',
   'FaceAlpha', 0.3, ...
          'EdgeColor', 'none', 'HandleVisibility',
             'off');

Z2 = -(Nj(1)*Xgrid + Nj(2)*Ygrid) / Nj(3) + Cj(3);
X2 = Xgrid + Cj(1); Y2 = Ygrid + Cj(2);
plane2 = surf(X2, Y2, Z2, 'FaceColor', 'g',
   'FaceAlpha', 0.3, ...
          'EdgeColor', 'none', 'HandleVisibility',
             'off');
```

For every wedge calculates the Dip and the Dip Direction, and it stores it at data inside the app to be later retrieved for the kinematics analysis.

```
lineVec = direction / norm(direction);

if lineVec(3) > 0
   lineVec = -lineVec; % Flip to point downward
end

% Calculate plunge (angle below horizontal)
% Plunge is always positive (0-90 degrees)
horizontal_magnitude = sqrt(lineVec(1)^2 +
   lineVec(2)^2);
if horizontal_magnitude > 0
   plunge = atand(-lineVec(3) /
      horizontal_magnitude);
else
   plunge = 90; % Vertical line
end

% Calculate trend (azimuth of horizontal projection)
```

```
            % Get azimuth in mathematical convention (0 = +X,
                counterclockwise)
            azimuth_math = atan2d(lineVec(2), lineVec(1));

            % Convert to geological convention (0 = +Y/North,
                clockwise)
            trend = 90 - azimuth_math;

            % Ensure trend is in range [0, 360)
            trend = mod(trend, 360);

            % Assign final values
            dip = plunge;   % Plunge angle (0-90)
            dipDir = trend; % Trend/azimuth (0-360)

            intersections = [intersections; {i, j, dip, dipDir}];
            pause(0.05);
        end
    end

    % Store results
    app.UITable2.Data = intersections;
    app.WedgeData = struct();

    for k = 1:length(app.lineHandles)
        app.WedgeData(k).pair = app.UITable2.Data(k, 1:2);
        app.WedgeData(k).line = [app.lineHandles{k}.XData', ...
                                 app.lineHandles{k}.YData', ...
                                 app.lineHandles{k}.ZData'];
        app.WedgeData(k).dip = app.UITable2.Data{k, 3};
        app.WedgeData(k).dipDir = app.UITable2.Data{k, 4};
    end
```

4.2.3 *Planar/Freefall*

The first function of kinematic analysis has two main purposes: to perform the kinematic test for planar sliding and free fall and to verify whether the discontinuity planes intersect the wall.

The function uses the parameters entered by the user in the GUI: facade dip direction (0–360°), facade dip angle (0–90°), and friction angle (0–90°). A series of geometrical parameters are extracted from the point cloud to facilitate later plotting and calculations, particularly for defining the facade position.

```
%-----------------------------------------------------
% PlanarFreefallButtonPushed
%
% Evaluates planar failure kimeatism based
% on facade orientation, friction angle, and dip/dip
   direction.
%
% - Samples points on each plane
% - Checks intersection with facade projection
% - Classifies kinematic behavior per plane
% - Displays results in UI
%-----------------------------------------------------

   %--- Load CSV Data ---
   try
      csvData = readtable(app.csvFilePath, 'Delimiter', ';');
   catch
      uialert(app.UIFigure, 'Please select the files using
         the Load CSV and TXT Button', 'File Error');
      return;
   end

   %--- Retrieve Input Parameters from UI ---
   FDipDir = app.FacadeDipDir0360EditField.Value;
   FDip  = app.FacadeDip090EditField.Value;
   phi   = app.FrictionAngle090EditField.Value;
   num_planes = height(csvData);

   %--- Geometry Setup ---
```

```
XYZ = app.PointCloudXYZ;
minVals = min(XYZ, [], 1);
maxVals = max(XYZ, [], 1);
bbox_center = mean([minVals; maxVals]);

block_width = maxVals(1) - minVals(1);
block_height = maxVals(3) - minVals(3);
scaleFactor = 2.0;
num_samples = 30;
threshold = 0.05;
```

The function creates a plane that serves as a marker for the position of the facade relative to the point cloud. In addition to calculating planar kinematics, this function also determines whether a plane intersects the facade. The decision to make this distinction arises from the need to differentiate cases where a portion of an element in contact with the rear wall may provide a stabilizing effect. Figure 68 shows an example of what is meant by a plane that intersects the wall (Figure 68, Plane 2) and one that does not (Figure 68, Plane 1). These two cases are treated differently because they may have different resistance characteristics against sliding. In cases where there is no intersection, the only resisting forces against sliding are those due to friction and cohesion along the discontinuity. In cases where an intersection is present, in addition to the resistance offered by discontinuity, there are also cohesion forces within the facade material, although these are difficult to quantify. At this stage of the research these forces are not considered, as it is not possible to know the actual adhesion state of the analyzed portions to the wall. To err on the side of safety, it was decided not to account for these resisting forces, and planar slides that intersect the wall are treated as if these forces were null. However, the case where there is no contact with the wall is still differentiated, as this scenario is clearly more at risk due to the absence of any possible cohesive forces.

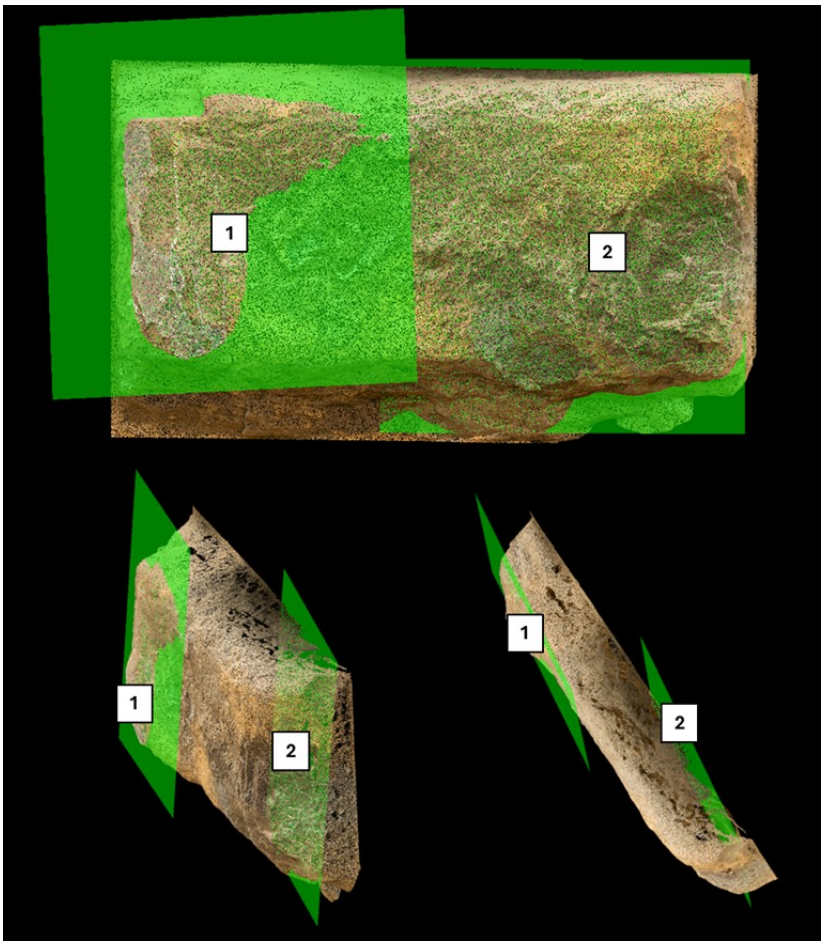


Figure 68: Possible interaction scenarios between discontinuities and the facade. Plane 1 does not intersects the wall, Plane 2 does

To check whether each plane intersects the wall, the function generates a fictitious plane for each point cloud that represents the position of the back wall. The plane is oriented based on the input data Facade Dip and Facade Dip Direction provided by the user.

```
    %--- Define Facade Basis Vectors ---
DD_rad  = deg2rad(FDipDir);
n_facade = [sin(DD_rad), cos(DD_rad), 0];
n_facade = n_facade / norm(n_facade); % Normal vector
u       = [-cos(DD_rad), sin(DD_rad), 0]; %


Dip_rad = deg2rad(FDip); % Dip angle from horizontal

% Dip vector (inclined, but aligned with dip direction)
v_x = sin(DD_rad) * cos(Dip_rad);
v_y = cos(DD_rad) * cos(Dip_rad);
v_z = -sin(Dip_rad); % Negative for downward dip

% Normalize
v = [v_x, v_y, v_z] / norm([v_x, v_y, v_z]);
```

Once the orientation of the facade plane is calculated, the function projects the entire point cloud into the facade's normal direction to determine how deeply each point sits in relation to the facade surface. It then translates every point in the cloud so that the origin point becomes the reference point. Each translated point is subsequently projected onto the facade's internal basis vectors, horizontal and vertical, which gives us each point's position within the facade's 2D plane.

```
%--- Compute Facade Plane Projection Origin ---
projections = XYZ * n_facade';
minProj  = min(projections);
P0       = bbox_center - (dot(bbox_center, n_facade) -
    minProj) * n_facade;

%--- Project All Points Relative to Facade ---
pts_rel = XYZ - P0;
u_coords = pts_rel * u';
v_coords = pts_rel * v';
```

```
minU = min(u_coords); maxU = max(u_coords);
minV = min(v_coords); maxV = max(v_coords);

%--- Output Initialization ---
outputData    = cell(num_planes, 1);
facadeIntersects = false(num_planes, 1);
```

The function iterates trough every plane in the .csv file, for the current plane retrieves dip direction, dip angle, center coordinates, and normal vector components. These values define the plane's spatial orientation (necessary for kinematic test) and location (necessary for checking any facade intersection). For valid planes, it normalizes the normal vector and creates two perpendicular vectors that lie flat on the plane surface, creating a 2D coordinate system within the 3D tilted plane. In this coordinate system it generates a grid of sample points spread across the plane's surface. For each sample point, the function tests whether that point intersects with the building facade. It accomplishes this by transforming the 3D coordinates into the facade's local coordinate system using three directional vectors (u, v, and w). The code then checks three conditions: whether the point falls within the facade's horizontal boundaries, whether it falls within the vertical boundaries, and whether it's close enough to the facade plane surface within a specified threshold distance (the 5cm threshold value present in the geoemetric setup in the first part of the function). If any sample points meet all three intersection criteria, the entire plane in marked as intersecting with the facade. In Figure 69 an example of the logic used is provided. Two planes are plotted, the green one does not intersect the facade (represented by the the grey plane), while the red does. On each plane a number of point are plotted, and the function checks if the any point of the planes touch the facade. In the case of the red plane, the points that determine the intersection are plotted in blue.

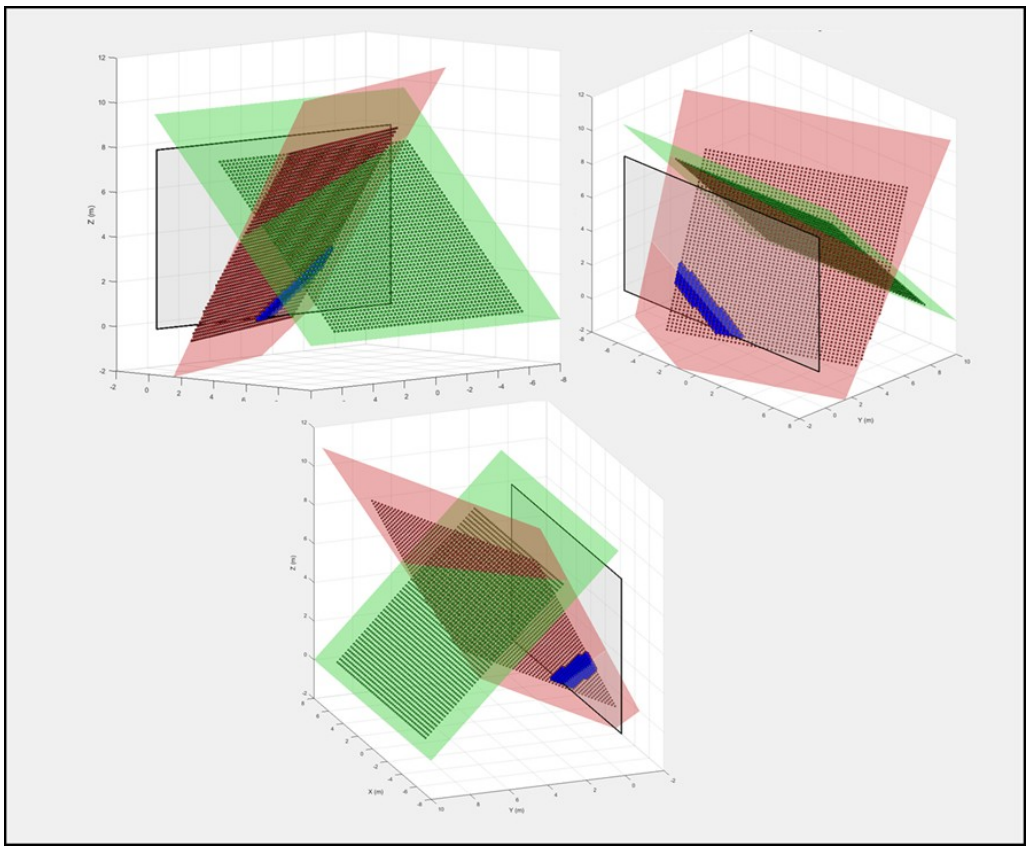


Figure 69: Projection of sample points onto a plane for intersection testing. A grid of sample points is generated and tested for intersection by verifying horizontal/vertical bounds and crossing relative to the facade

```
%--- Analyze Each Plane ---
   for i = 1:num_planes
      PDipDir = csvData.DipDir(i);
      PDip  = csvData.Dip(i);
      C     = [csvData.Cx(i), csvData.Cy(i), csvData.Cz(i)]';
      N     = [csvData.Nx(i), csvData.Ny(i), csvData.Nz(i)]';

      %--- Validate Normal Vector ---
      if norm(N) < 1e-6
         outputData{i} = sprintf('Plane %d Invalid normal
            vector', i);
         continue;
      end

      N    = N / norm(N);
      basis = null(N'); % Get orthonormal basis in the plane

      if size(basis, 2) < 2
         outputData{i} = sprintf('Plane %d Degenerate basis
            for sampling', i);
         continue;
      end

      %--- Sample Points on Plane Surface ---
      range_x = (block_width * scaleFactor) / 2;
      range_y = (block_height * scaleFactor) / 2;
      step_x = range_x * 2 / num_samples;
      step_y = range_y * 2 / num_samples;

      samples = [];
      for a = -range_x:step_x:range_x
         for b = -range_y:step_y:range_y
            samples(:, end+1) = C + a * basis(:,1) + b *
               basis(:,2);
         end
      end

      %--- Check Facade Intersection ---
      vecs = samples - P0';
```

```
u_pts = (u * vecs)';
v_pts = (v * vecs)';
w_pts = (n_facade * vecs)';

in_u    = (u_pts >= minU) & (u_pts <= maxU);
in_v    = (v_pts >= minV) & (v_pts <= maxV);
on_plane = abs(w_pts) < threshold;
hits_facade = any(in_u & in_v & on_plane);
facadeIntersects(i) = hits_facade;
```

The function ends with the actual kinematic test for every plane: Firstly it calculates the shortest angular difference between the plane's dip direction and the facade's dip direction. This is to avoid the wraparound nature of the geological angular conventions, where for example the difference between 350° and 10° should be 20° and not 340°. The kinematic classification section then uses this angular difference along with the other kinematics conditions to classify four possible outcomes:

- Planes that don't intersect the facade and their geometry could allow planar sliding failure, flagged as 'Plane id → Planar failure possible - no facade intersection'
- Non-intersecting planes that do not meet the kinematic conditions for planar slide. This does not make them safer, as they can fail via freefall and get flagged as 'Plane id → Freefall failure possible'
- Intersecting planes with the geometric requirements for planar failure, flagged as 'Plane id → Planar failure possible'
- Planes that don't meet the geometric criteria for planar sliding and intersect the facade, making them the more stable configuration. Flagged 'Plane id → Planar failure not possible'

```
%--- Angular Difference Wraparound Logic ---
diffDipDir = abs(mod(PDipDir - FDipDir + 180, 360) -
    180);

%--- Kinematic Classification ---
if ~hits_facade && diffDipDir <= 20 && PDip < FDip &&
    PDip > phi
```

```
            outputData{i} = sprintf('Plane %d Planar failure
                possible - no facade intersection', i);
        elseif ~hits_facade
            outputData{i} = sprintf('Plane %d Freefall failure
                possible', i);
        elseif diffDipDir <= 20 && PDip < FDip && PDip > phi
            outputData{i} = sprintf('Plane %d Planar failure
                possible', i);
        else
            outputData{i} = sprintf('Plane %d Planar failure not
                possible', i);
        end
    end
```

4.2.4 *Wedge/Freefall*

This function, similarly to the one just presented, is designed to perform the kinematic test for wedge sliding and to verify whether the wedge intersects the wall.

This part of the function is analogous to what was seen in Planar/Freefall. The user's input parameters are incorporated into the logic, and a plane representing the facade is constructed, which is necessary for calculating the intersection.

```
%-------------------------------------------------
% WedgeFreefallButtonPushed
%
% Evaluates the kinematic interaction between wedges and a
   defined
% facade plane using dip, dip direction, and friction angle
   parameters.
%
% Results are classified per wedge:
% - Freefall failure
% - Sliding failure
% - Sliding possible without facade intersection
% - Not sliding
%
%-------------------------------------------------


   %--- Load CSV Data (Wedge Information) ---
   try
      csvData = readtable(app.csvFilePath, 'Delimiter', ';');
   catch
      uialert(app.UIFigure, 'Please select the files using
         the Load CSV and TXT Button', 'File Error');
      return;
   end

   %--- Retrieve User Input Values ---
   FDipDir = app.FacadeDipDir0360EditField.Value; % Facade
      dip direction
```

```
FDip  = app.FacadeDip090EditField.Value; % Facade dip angle
phi   = app.FrictionAngle090EditField.Value; % Friction
   angle
%
% %--- Setup Facade Plane Geometry ---
 threshold = 0.05; % Intersection proximity threshold

DD_rad = deg2rad(FDipDir); % Dip Direction (azimuth)
Dip_rad = deg2rad(FDip); % Dip Angle (inclination from
   horizontal)

% inclined normal vector for the facade plane
n_facade = [sin(DD_rad) * sin(Dip_rad), ...
         cos(DD_rad) * sin(Dip_rad), ...
         cos(Dip_rad)];
n_facade = n_facade / norm(n_facade); % Normalize to unit
   vector

%--- Determine Facade Location Based on Bounding Box ---
minVals = min(app.PointCloudXYZ, [], 1);
maxVals = max(app.PointCloudXYZ, [], 1);
bbox_center = (minVals + maxVals) / 2;

projections = app.PointCloudXYZ * n_facade';
minProj = min(projections);
distance_to_plane = dot(n_facade, bbox_center) - minProj;
P_facade_centered = bbox_center - distance_to_plane *
   n_facade;

%--- Initialize Output Structures ---
numRows = size(app.UITable2.Data, 1);
outputData = cell(numRows, 1);
app.FacadeKinematicResults = cell(numRows, 3); %
   [Intersect, Slide, Label]
```

The function iterates through each wedge calculated in the "View Wedges" function, retrieving information about orientation (Dip and Dip Direction) and spatial position. To calculate any potential intersection, the individual points forming the intersection line are projected onto

the facade plane. If at least one of the points lies within the threshold distance (set as 5 cm at the start of the function), the wedge is considered to be intersecting. The function ends with the actual kinematic test for every wedge: As seen in planar sliding kinematics, it first calculates the shortest angular difference between the wedge dip direction and the facade's dip direction. The kinematic classification section then uses this angular difference along with other kinematic conditions to classify four possible outcomes:

- Wedges that don't intersect the facade and their geometry could allow sliding failure, flagged as 'Wedge id → Sliding failure possible - no facade intersection'
- Non-intersecting wedges that do not meet the kinematic conditions for sliding. This does not make them safer, as they can fail via freefall and get flagged as 'Wedge id → Freefall failure possible'
- Intersecting wedges with the geometric requirements for sliding, flagged as 'Wedge id → Sliding failure possible'
- Wedges that don't meet the geometric criteria for sliding and intersect the facade, making them the more stable configuration. Flagged 'Wedge id → Sliding failure not possible'

```
    %--- Evaluate Each Wedge ---
for i = 1:numRows

    % Extract dip/dip direction
    WDip  = cell2mat(app.UITable2.Data(i, 3));
    WDipDir = cell2mat(app.UITable2.Data(i, 4));

    % Get geometry from drawn wedge line
    if i <= length(app.lineHandles) &&
        ~isempty(app.lineHandles{i})
        wedge_line_handle = app.lineHandles{i};
        wedge_line_points = [wedge_line_handle.XData', ...
                             wedge_line_handle.YData', ...
                             wedge_line_handle.ZData'];
    else
        % No geometry available
        outputDat a{i} = sprintf('Wedge %d has no geometry,
            skipping.', i);
```

```
            app.FacadeKinematicResults(i,:) = {false, false, 'No
                geometry'};
            continue;
        end

        % Check facade intersection (projected distance from
            plane)
        distances_to_facade = abs((wedge_line_points -
            P_facade_centered) * n_facade');
        isIntersecting = any(distances_to_facade < threshold);

        diffDipDir = abs(mod(WDipDir - FDipDir + 180, 360) -
            180);

        % Check sliding conditions using dip logic
        isSliding = diffDipDir <= 90 && WDip < FDip && phi <
            WDip;


        % Classify failure mode
        if ~isIntersecting && isSliding
            label = sprintf('Wedge %d
    Sliding failure possible - no facade intersection', i);
        elseif ~isIntersecting
            label = sprintf('Wedge %d Freefall failure
                possible', i);
        elseif isSliding
            label = sprintf('Wedge %d Sliding failure possible',
                i);
        else
            label = sprintf('Wedge %d Sliding failure not
                possible', i);
        end

        % Store results
        outputData{i} = label;
        app.FacadeKinematicResults(i,:) = {isIntersecting,
            isSliding, label};
    end
```

```
%--- Display Results in UI Table ---
app.UITable3.Data = outputData;
```

4.2.5 *Compute Planar KSI*

This function has two main purposes: to calculate a kinematic susceptibility index for each discontinuity and create a graphical output that is easy to interpret in which each discontinuity plane is color-coded and readable with a graphical legend. The first part of the function is dedicated to configuring the kinematic parameters and facade geometry, similar to what was already seen in the "Planar/Freefall" and "Wedge/Freefall" functions.

```
%--------------------------------------------------
% ComputePlanarKSIButtonPushed
% Calculates the Planar KSI (Kinematic Susceptibility Index)
   for every
% plane
%--------------------------------------------------

   %--- Load CSV Data ---
   try
      csvData = readtable(app.csvFilePath, 'Delimiter', ';');
   catch
      uialert(app.UIFigure, 'Please select the files using
         the Load CSV and TXT Button', 'File Error');
      return;
   end

   screenSize = get(0, 'ScreenSize'); % For display window
      sizing

   %--- Retrieve UI Parameters ---
   FDipDir = app.FacadeDipDir0360EditField.Value;
   FDip  = app.FacadeDip090EditField.Value;
   phi   = app.FrictionAngle090EditField.Value;

   %--- Constants ---
   threshold = 0.05;
   num_samples = 100;
   DD_rad    = deg2rad(FDipDir);

   %--- Compute Bounding Box ---
```

```
XYZ      = app.PointCloudXYZ;
minVals  = min(XYZ, [], 1);
maxVals  = max(XYZ, [], 1);
bbox_center = mean([minVals; maxVals]);
block_width = maxVals(1) - minVals(1);
block_height = maxVals(3) - minVals(3);

%--- Define Facade Plane ---
n_facade = [sin(DD_rad), cos(DD_rad), 0];
n_facade = n_facade / norm(n_facade);
u = [-cos(DD_rad), sin(DD_rad), 0];

% Convert angles to radians
Dip_rad = deg2rad(FDip); % Dip angle from horizontal

% Dip vector (inclined, but aligned with dip direction)
v_x = sin(DD_rad) * cos(Dip_rad);
v_y = cos(DD_rad) * cos(Dip_rad);
v_z = -sin(Dip_rad); % Negative for downward dip

% Normalize for direction only
v = [v_x, v_y, v_z] / norm([v_x, v_y, v_z]);

projections = XYZ * n_facade';
minProj  = min(projections);
P0       = bbox_center - (dot(bbox_center, n_facade) -
   minProj) * n_facade;

pts_rel = XYZ - P0;
u_coords = pts_rel * u';
v_coords = pts_rel * v';
minU = min(u_coords); maxU = max(u_coords);
minV = min(v_coords); maxV = max(v_coords);

%--- Build Mesh for Facade Visualization ---
[Uf, Vf] = meshgrid(linspace(minU, maxU, 2),
   linspace(minV, maxV, 2));
Xf = P0(1) + Uf * u(1) + Vf * v(1);
Yf = P0(2) + Uf * u(2) + Vf * v(2);
Zf = P0(3) + Uf * u(3) + Vf * v(3);
```

```
    %--- Initialize Classification Structures ---
    num_planes = height(csvData);
    outputData3 = cell(num_planes, 1);
    SMRclasses = cell(num_planes, 1); % Changed from 5 columns
        to 1
    app.surfHandles = cell(num_planes, 1);
```

The function continues by calculating the possible intersection of each individual plane using the same logic explained in Figure 66.

```
%--- Analyze Each Plane ---
    for i = 1:num_planes
        PDipDir = csvData{i, 'DipDir'};
        PDip  = csvData{i, 'Dip'};
        C     = csvData{i, {'Cx','Cy','Cz'}}';
        N     = csvData{i, {'Nx','Ny','Nz'}}'; N = N / norm(N);
        basis = null(N');

        % Sample grid points on plane
        patchScale = 2;
        range_x = (block_width * patchScale) / 2;
        range_y = (block_height * patchScale) / 2;
        step_x = (block_width * patchScale) / num_samples;
        step_y = (block_height * patchScale) / num_samples;

        samples = [];
        for a = -range_x:step_x:range_x
            for b = -range_y:step_y:range_y
                samples = [samples, C + a*basis(:,1) +
                    b*basis(:,2)];
            end
        end

        % Project sampled points into facade coordinates
        vecs = samples - P0';
        u_pts = u * vecs;
        v_pts = v * vecs;
        w_pts = n_facade * vecs;
```

```
in_u   = (u_pts >= minU) & (u_pts <= maxU);
in_v   = (v_pts >= minV) & (v_pts <= maxV);
in_plane = abs(w_pts) < threshold;
isIntersecting = any(in_u & in_v & in_plane);
```

The function classifies each plane into one of the four categories already introduced in the "Planar/Freefall" function:

- Planes that do not intersect the facade and have a geometry that may lead to planar sliding. These are considered more hazardous than planes that intersect the facade and are therefore categorized separately, disregarding their potential susceptibility index. For this reason, they are plotted in a distinct color, dark purple, so they can be immediately identified. An example of this case is shown in Figure 70

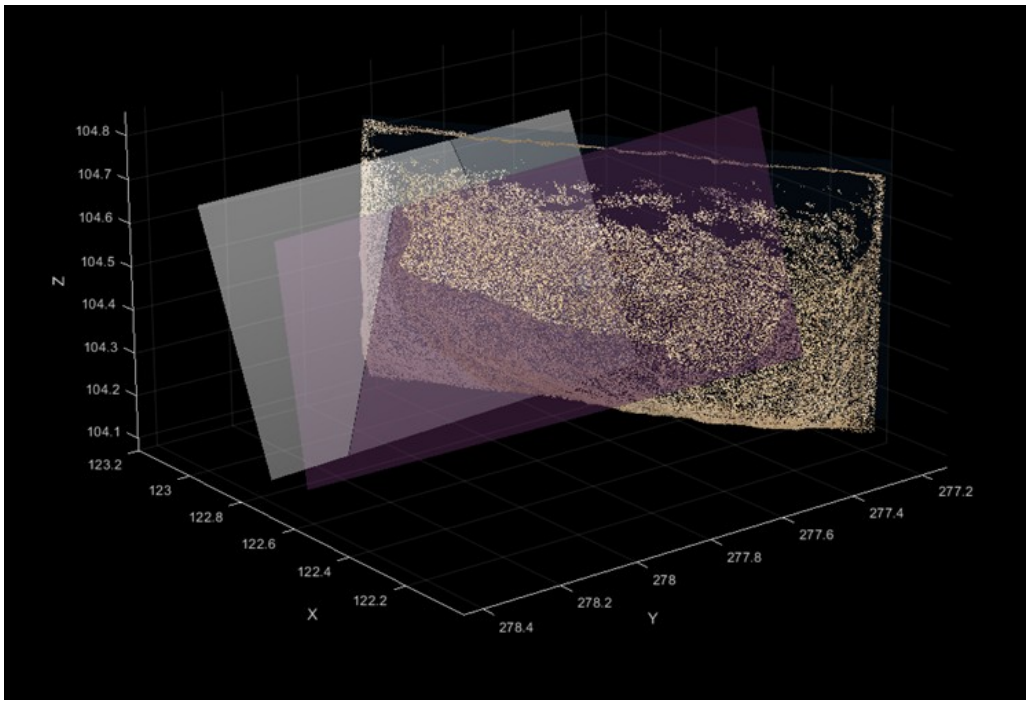


Figure 70: Planes with geometries susceptible to planar sliding and lacking contact with the facade are considered more critical and are categorized separately and plotted in dark purple

- Planes that do not intersect the facade and have a geometry that may lead to failure by free fall. This represents the highest-risk scenario, as the resisting forces from friction are absent. It is categorized with a distinct color, light purple. An example of blocks in this category is shown in Figure 71

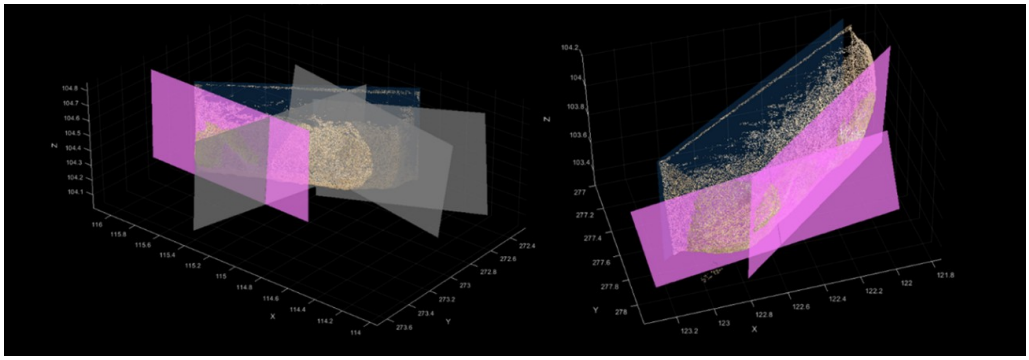


Figure 71: Planes with geometries susceptible to freefall failure are plotted in bright purple

- Planes that intersect the facade and have a geometry that may lead to planar sliding. In this case a planar kinematic susceptibility index (KSI_p) is calculated. This susceptibility index, adapted from Kundu et al. [71], aims to provide a more nuanced indication than the binary 0–1 result obtained through traditional kinematic testing. The index is derived from the unfavourability criteria of the Slope Mass Rating (SMR) system [111] for kinematic analysis.

  The SMR system is a widely accepted rock mass classification framework, used globally with consistently successful results. It has been endorsed by numerous researchers as an effective tool for assessing rock slope stability [112] [126]. The SMR adjustment factors (F_1, F_2, F_3, F_4) have proven effective in evaluating the likelihood of unfavorable discontinuity configurations since their introduction. In this application, the continuous functions developed by Tomas et al. [129] are used. They are defined as:

$$F_1 = \frac{16}{25} - \frac{3}{500}\tan^{-1}\left(\frac{1}{10}(|A| - 17)\right) \tag{2}$$

$$F_2 = \frac{9}{16} + \frac{1}{195}\tan^{-1}\left(\frac{17}{100}B - 5\right) \tag{3}$$

$$F_3 = -30 + \frac{1}{3}\tan^{-1}(C) \tag{4}$$

  Factor F_1 quantifies how closely aligned the discontinuity orientation is with the slope face, with greater parallelism indicating higher failure susceptibility. It depends on angle A (Figure 72), which represents the angular relationship between discontinuity and slope orientations: for planar failure it is the angle between discontinuity dip direction and slope dip direction, indicating the parallelism between the strikes of the discontinuity and the slope. For wedge failure it is the angle between the azimuth of the line of intersection and the dip direction of the slope.

  Factor F_2 quantifies how much the dip angle of the discontinuity influences the normal and shear stress distributions acting on the failure plane. It depends on angle B, the discontinuity dip angle. A higher dip angle corresponds to an higher susceptibility value.

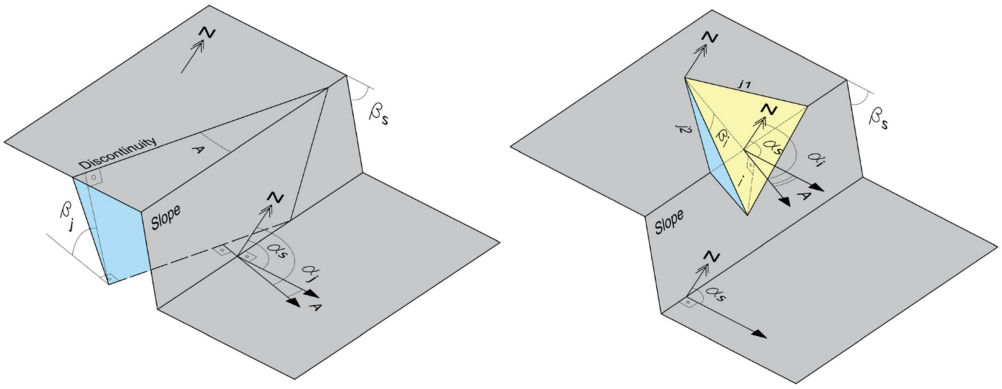


Figure 72: Parallelism (A) between discontinuity and slope strikes for planar failure (left). Parallelism (A) between the plunge direction of the line of intersection of two discontinuities (α_i) and the slope dip direction (α_s) for wedge failure (right). Adapted from Pastor et al. (2018)

Factor F_3 evaluates whether the geometric configuration allows the discontinuity to intersect the slope face, which is a prerequisite for kinematic instability. Without daylighting, the discontinuity cannot contribute to slope failure regardless of other unfavorable conditions. F_3 depends on angle C and has two formulations depending on failure type, representing the probability that joints daylight (intersect and become visible) in the slope face. For planar failure the angle C is the difference between the discontinuity dip angle and the slope dip angle. For wedge failure the angle C is the difference between the plunge of the line of intersection and the slope dip angle.

The factors F_1, F_2, F_3 when multiplied give a value that can range from 0 (minimum susceptibility) to -60 (maximum susceptibility). This range of value can be used as a susceptibility scale (Kundu et al). To obtain a more readable and understandable range the scale is normalized to 100:

$$\text{Susceptibility}(\%) = -\left(\frac{F_1 \cdot F_2 \cdot F_3}{60}\right) \cdot 100 \tag{5}$$

To make an even simpler representation of this susceptibility index, the function creates a color coded 3D image in which every plane is plotted in a color shown in Figure 37. An example of the graphical output is shown in Figure 73.

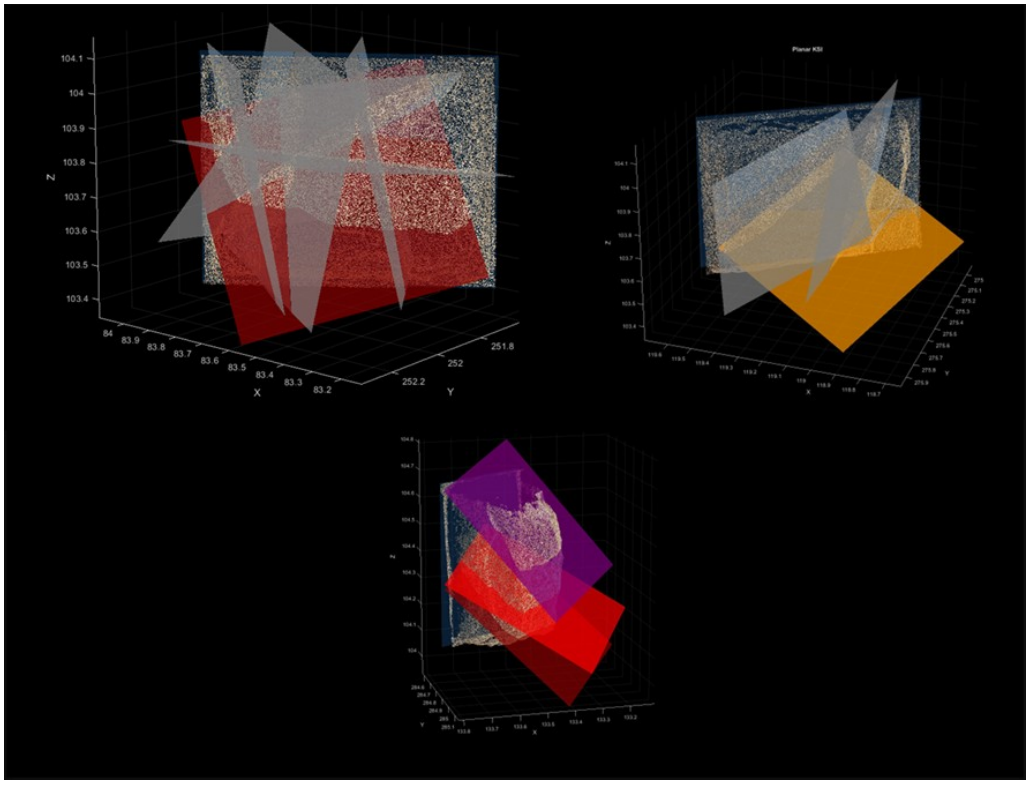


Figure 73: Planes with geometries susceptible to planar sliding and that contact the facade are categorized using the KSIp and color coded accordingly

- Planes that intersect the wall but do not meet the kinematic conditions for planar sliding: these are plotted in gray in the 3D graph

---

```
%--- KSI Legend ---
classes   = {'V','IV','III','II','I'};
SMR_ranges = [0 20; 20.01 40; 40.01 60; 60.01 80; 80.01
   100];
colors = {[0.0, 0.9961,
   0.0784],[1,1,0],[1,0.6,0],[1,0,0],[0.5451,0.0039,0.0039]};
   % Classify Failure Mode and SMR
   diffDipDir = abs(mod(PDipDir - FDipDir + 180, 360) -
      180);

   % Check if plane intersects facade first
   if ~isIntersecting
      % No facade intersection - check if it would meet
         failure conditions IF it intersected
      if diffDipDir <= 20 && PDip < FDip && PDip > phi
         % Would be dangerous if it intersected the facade
         outputData3{i} = sprintf('Plane %d No Facade
            Intersection', i);
         SMRclasses{i} = 'Potential';
         color = [0.5, 0, 0.5]; % Dark purple
      else
         % Doesn't meet failure conditions anyway - true
            freefall
         outputData3{i} = sprintf('Plane %d FreeFall', i);
         SMRclasses{i} = 'N/A';
         color = [1, 0.5, 1]; % Bright purple
      end
   else
      % Facade intersection exists - check failure
         conditions
      if diffDipDir <= 20 && PDip < FDip && PDip > phi
         % Has intersection AND meets failure conditions -
            calculate KSI
         F1 = 16/25 - 3/500 * atan((diffDipDir - 17)/10) *
            180/pi;
```

```
            F2 = 9/16 + 1/195 * atan(17/100 * PDip - 5) *
                180/pi;
            F3 = -30 + 1/3 * atan(PDip - FDip) * 180/pi;
            SMR = -((F1 * F2 * F3)/60) * 100;

            outputData3{i} = sprintf('Plane %d %.2f', i, SMR);
            classIndex = find(SMR >= SMR_ranges(:,1) & SMR <=
                SMR_ranges(:,2), 1);
            if isempty(classIndex), classIndex = 1; end
            SMRclasses{i} = classes{classIndex};
            color = colors{classIndex};
        else
            % Has intersection but doesn't meet failure
                conditions
            outputData3{i} = sprintf('Plane %d No failure',
                i);
            SMRclasses{i} = '-';
            color = [0.5, 0.5, 0.5]; % Gray
        end
    end
```

4.2.6 *Compute Wedge KSI*

This function is the counterpart of the "Planar KSI" function, with its features adapted from planar to wedge kinematics. As in the previous function, its objectives are:

- To calculate a kinematic susceptibility index for each wedge occurring within the block
- To create a graphical output that is easy to interpret, in which each wedge is color-coded and readable with a graphical legend

The first part of the function sets up the structures for 3D visualization and kinematic classification

In the kinematic analysis section of the function, individual wedges are classified into one of the four categories already introduced in

```
%-----------------------------------------------------
% ComputeWedgeKSIButtonPushed
% Computes the Wedge KSI (Kinematic Susceptibility Index) for
    every wedge
%-----------------------------------------------------

    screenSize = get(0, 'ScreenSize');

    %--- Load TXT file containing point cloud ---
    try
        ptCloud2 = readmatrix(app.txtFilePath);
    catch
        uialert(app.UIFigure, 'Please select a file using the
            Load TXT Button', 'File Error');
        return;
    end

    %--- Point cloud geometry and downsampling ---
    A = ptCloud2(:,1); D = ptCloud2(:,2); C = ptCloud2(:,3);
    minXa = min(A); maxXa = max(A);
    minYa = min(D); maxYa = max(D);
    minZa = min(C); maxZa = max(C);

    ptCloudObj = pointCloud(ptCloud2(:,1:3));
    ptCloudDS = pcdownsample(ptCloudObj, 'gridAverage', 0.001);
```

```
ptCloud = ptCloudDS.Location;

DT  = delaunayTriangulation(ptCloud);
hull = convexHull(DT);

%--- Dim background colors for clarity ---
fadedColors = min(max(app.PointCloudColors * 0.3, 0), 1);

%--- Create 3D viewer ---
fig = figure('Name', app.inputName, 'Color', 'w', ...
          'Position', [screenSize(3)*0.366,
             screenSize(3)*0.1, screenSize(3)*0.6,
             screenSize(4)*0.6]);
pcshow(app.PointCloudXYZ, fadedColors, 'MarkerSize', 5);
hold on; grid on; axis equal; view(3);
xlabel('X'); ylabel('Y'); zlabel('Z');
xlim([minXa, maxXa]); ylim([minYa, maxYa]); zlim([minZa,
   maxZa]);
axis vis3d; camva('manual'); camproj('perspective');
trimesh(hull, ptCloud(:,1), ptCloud(:,2), ptCloud(:,3), ...
      'FaceColor', 'cyan', 'FaceAlpha', 0.05, 'EdgeColor',
         'none');

app.lineHandles = {};
num_wedges = length(app.WedgeData);
outputData3 = cell(num_wedges, 1);
SMRclasses = cell(num_wedges, 1);

%--- Classification parameters ---
FDipDir = app.FacadeDipDir0360EditField.Value;
FDip  = app.FacadeDip090EditField.Value;
phi   = app.FrictionAngle090EditField.Value;

classes   = {'V','IV','III','II','I'};
SMR_ranges = [0 20; 20.01 40; 40.01 60; 60.01 80; 80.01
   100];
colors = {[0.0, 0.9961,
   0.0784],[1,1,0],[1,0.6,0],[1,0,0],[0.5451,0.0039,0.0039]};
```

the "Wedge/Freefall" function:

- Wedges that do not intersect the facade and whose geometry could allow sliding failure. Since they lack intersection with the facade, they are considered more hazardous and are therefore plotted in a color outside the susceptibility scale, dark purple. An example of this case is shown in Figure 74

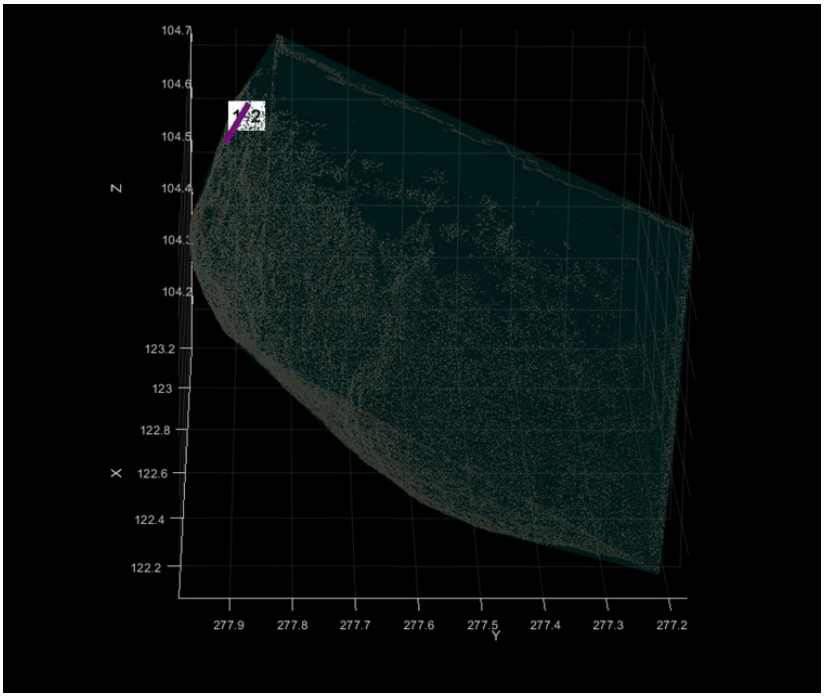


Figure 74: Wedges with geometries susceptible to planar sliding and lacking contact with the facade are considered more critical and are categorized separately and plotted in dark purple

- Wedges that do not intersect the facade and do not meet the kinematic conditions for sliding. This does not make them safer, as they may still fail by free fall. They are plotted in bright purple. An example of this case is shown in Figure 75.

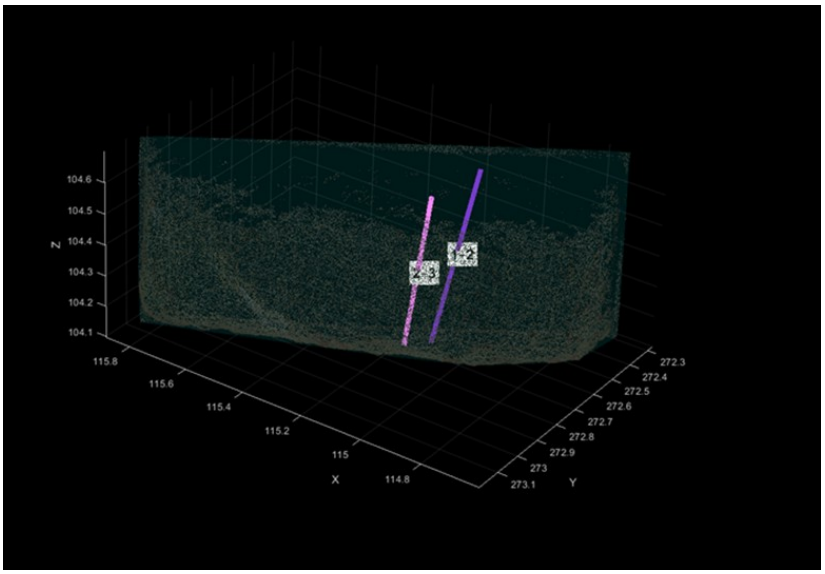


Figure 75: Wedges with geometries susceptible to free fall are plotted in bright purple

- Intersecting wedges that meet the geometric requirements for sliding. In these cases, the wedge kinematic susceptibility index (KSIw) is calculated. This index follows the same principle as the one presented in paragraph 4.2.5 for planar sliding. As with the planar slide case, a 3D representation is produced in which the wedges are plotted according to the color scale shown in Figure 37, to enhance readability. An example of this case is shown in Figure 76.

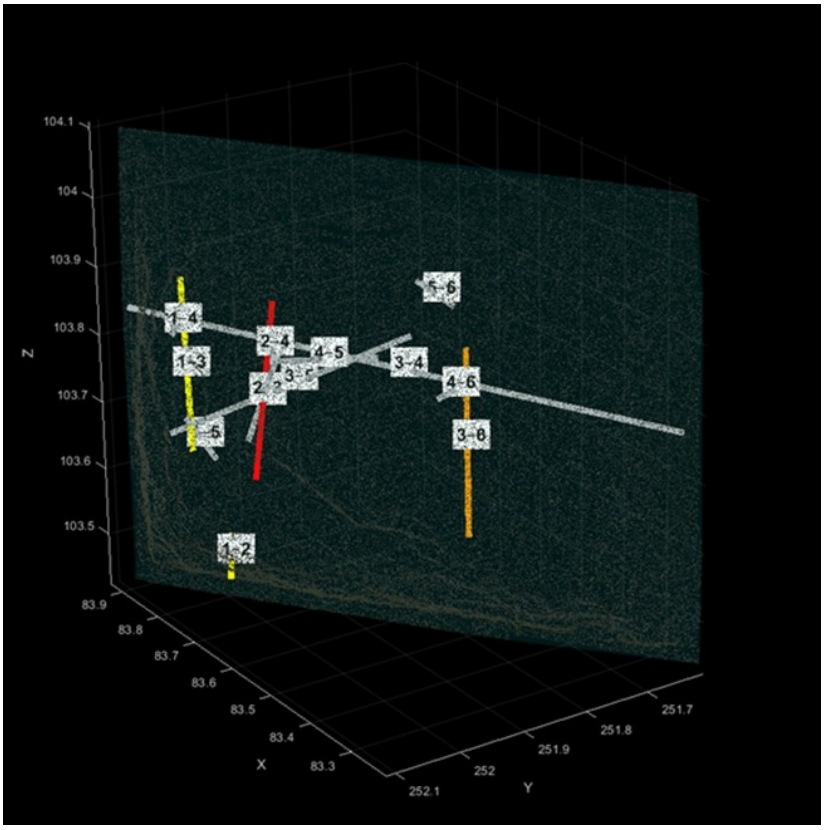


Figure 76: Wedges with geometries susceptible to planar sliding and that contact the facade are categorized using the KSIw and color coded accordingly

- Wedges that do not meet the geometric criteria for sliding but intersect the facade. These are plotted in gray in the 3D figure.

4.2.7 *Planar volume Side 1/Side 2 - Wedge Volume*

The "Planar Volume Side 1/Side 2" functions are the first components of RoDiAn's dynamic analysis module. Their purpose is to calculate the volume of the two portions of the point cloud obtained by intersecting the 3DPC of the element under analysis. The volume of the potential detachment is essential for computing the sliding and resisting forces that govern the possible movement. The function loads the 3DPC and reads the plane selected by the user via the input field. To optimize computational performance, a downsampling of the 3DPC is applied with a minimum grid step size of 5 mm. This decision was based on resolution testing, where the 5 mm value provided the best compromise between computational speed and geometric fidelity.

```
%---------------------------------------------------
% PlanarvolumeSide1ButtonPushed2
%
% Computes and visualizes the Volume of the portion of the
   point cloud
% lying on one side of a user-specified plane.
%---------------------------------------------------

   % Read matrix data from TXT point cloud file
   txtdata = readmatrix(app.txtFilePath);
   screenSize = get(0, 'ScreenSize'); % Used for figure sizing

   % Extract user-selected plane index
   planeNumber = app.PlaneNumberEditField.Value;

   % Initialize container for hull areas
   app.ConvexHullAreas = {};

   % Extract XYZ coordinates from point cloud
   A = txtdata(:, 1); D = txtdata(:, 2); C = txtdata(:, 3);

   % Compute bounding box limits
   minX = min(A); maxX = max(A);
   minY = min(D); maxY = max(D);
   minZ = min(C); maxZ = max(C);
```

```
% Load plane definitions from UI table
tableData = app.UITable_3.Data;

% Reload point cloud and extract XYZ subset
ptCloud2 = readmatrix(app.txtFilePath);
ptCloud3 = ptCloud2(:, 1:3);

% Downsample the cloud to reduce complexity
ptCloudObj = pointCloud(ptCloud3);
ptCloud8 = pcdownsample(ptCloudObj, 'gridAverage', 0.005);
points = ptCloud8.Location;

% Validate selected plane index
if planeNumber < 1 || planeNumber > size(tableData, 1)
   error('Plane number out of range.');
end
```

The ability to calculate the volume of block portions separated by a plane is one of the advantages of RoDiAn, that considers discontinuity planes through their equation rather than solely through their orientation parameters (Dip and Dip Direction). In this part of the function, the coordinates of the selected plane's center and the components of its normal vector are extracted, both of which are automatically generated during the CloudCompare pre-processing and stored in the input .csv file. To calculate the two volumes, the function loops through every point in the downsampled cloud and for each one:

- Subtracts the plane center from the point to obtain a vector
- Computes the dot product with the plane's normal vector
- If the result is non-negative, the point lies on the same side as the normal vector (Side 1); otherwise, it lies on the opposite side (Side 2)

The logic is illustrated in Figure 77.

The function is able to classify the entire 3DPC and create two different sub-clouds (Figure 78) that can be used for the volume calculation.

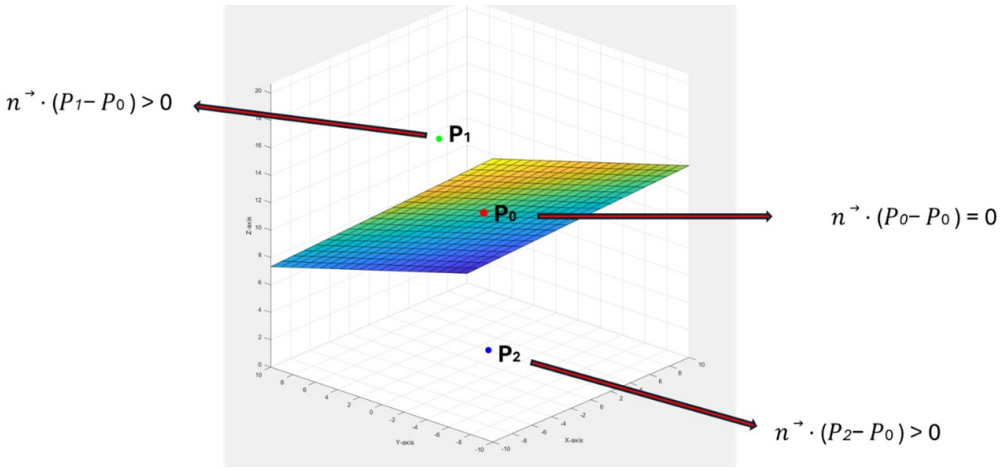


Figure 77: Illustration of the volume calculation logic in RoDiAn. The plane separates the downsampled point cloud into two sides based on the dot product between the plane's normal vector $\vec{n}$ and the vector from the plane center P_0 to each point P_i. Points with non-negative dot products ($\vec{n} \cdot (P_i - P_0) > 0$) are assigned to Side 1, while points with negative dot products ($\vec{n} \cdot (P_i - P_0) < 0$) are assigned to Side 2. Points lying on the plane satisfy $\vec{n} \cdot (P_i - P_0) = 0$.

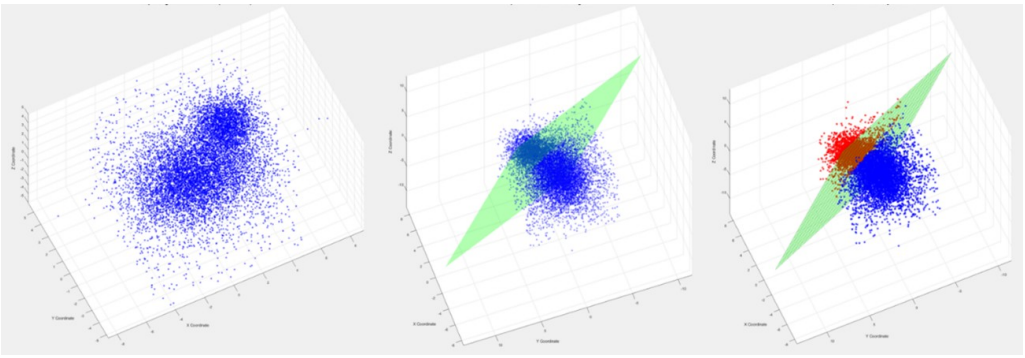


Figure 78: Point cloud classification and separation by a discontinuity plane. Left: Original 3DPC (3D Point Cloud). Center: Plane intersecting the point cloud. Right: Separated sub-clouds with points classified into Side 1 (red) and Side 2 (blue) based on their position relative to the plane.

```
% Extract center and normal of the selected plane
   Cx = tableData{planeNumber, 1};
   Cy = tableData{planeNumber, 2};
   Cz = tableData{planeNumber, 3};
   Nx = tableData{planeNumber, 4};
   Ny = tableData{planeNumber, 5};
   Nz = tableData{planeNumber, 6};
   pointP = [Cx, Cy, Cz];
   normalVectorN = [Nx, Ny, Nz];

   % Initialize containers for each half-space
   pointsSide1 = [];
   pointsSide2 = [];

   % Evaluate point orientation relative to plane
   for i = 1:size(points, 1)
      point = points(i, :);
      planeValue = dot(normalVectorN, (point - pointP));
      if planeValue >= 0
         pointsSide1 = [pointsSide1; point];
      else
         pointsSide2 = [pointsSide2; point];
      end
   end
```

The sub-cloud is used to calculate the volume of the selected side (Side 1 or Side 2, as chosen by the user). The calculation is performed using MATLAB's built-in convhull function, which computes the convex hull of a point cloud and its volume. As anticipated in paragraph 3.7.4, the function calculates volume by generating a convex mesh over the point cloud. This approach involves a necessary compromise, especially in cases where the shape contains significant concavities. When the function is used within the wedge sliding module, its behavior mirrors that of the planar sliding case. The only difference lies in the presence of two intersecting planes, which results in four possible partition pairs of the point cloud. As shown in paragraph 3.7.4, the user manually selects which partitions to intersect.

```
% Create visualization figure
   fig = figure('Name', 'Point Cloud with Convex Hull', ...
      'Position', [screenSize(3)*0.366, screenSize(3)*0.1,
         screenSize(3)*0.6, screenSize(4)*0.6], ...
      'Color', 'w');
   ax = axes('Parent', fig);
   pcshow(ptCloud8, 'Parent', ax); % Show downsampled cloud
   hold(ax, 'on');

   % Compute and render convex hull on Side 1
   [k, av] = convhull(pointsSide1);
   trimesh(k, pointsSide1(:,1), pointsSide1(:,2),
      pointsSide1(:,3), ...
      'Parent', ax, 'FaceColor', 'red', 'FaceAlpha', 0.5);

   % Adjust axes and enable rotation
   axis(ax, 'equal');
   axis(ax, [minX maxX minY maxY minZ maxZ]);
   view(ax, 3);
   rotate3d(ax, 'on');

   % Store area result and update UI
   newRow = {planeNumber, av};
   app.ConvexHullAreas = [app.ConvexHullAreas; newRow];
   app.UITable8.Data = app.ConvexHullAreas;
```

```
   app.PlaneVolume = av;
```

4.2.8 *Planar and Wedge Area*

The function calculates, for each point in 3DPC its distance from the plane selected by the user (Figure 79). This functionality is made possible by the structure of RoDiAn's input data, which provides access to the spatial coordinates of the discontinuity planes.

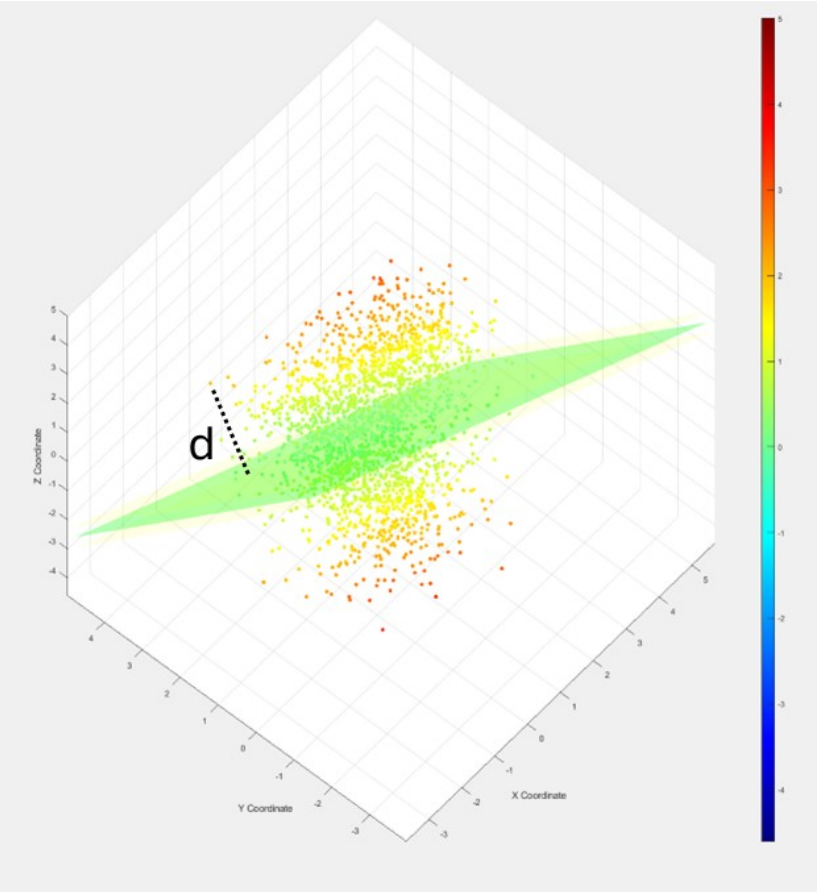


Figure 79: Distance calculation from each point in the 3DPC to the user-selected discontinuity plane. Points are color-coded based on their perpendicular distance d from the plane, with the color scale ranging from blue (farthest) to red (closest). The spatial coordinates of the discontinuity plane are provided by RoDiAn's input data structure

```
%---------------------------------------------------
% PlanarAreaButtonPushed
% Computes the contact area on which the plane slides. Needed
    for
% calculating the Safety Factor
%---------------------------------------------------

screenSize = get(0, 'ScreenSize');

    % Retrieve plane table and initialize result storage
    tableData = app.UITable_3.Data;
    app.Polyarea = {};

    % Get selected plane index
    planeNumber = app.PlaneNumberEditField.Value;

    % Read point cloud data from TXT file
    ptCloud2 = readmatrix(app.txtFilePath);
    points = ptCloud2(:, 1:3);

    % Extract reference point and plane normal from selected
        row
    knownPoint = [tableData{planeNumber, 'Cx'},
        tableData{planeNumber, 'Cy'}, tableData{planeNumber,
        'Cz'}];
    normalVector = [tableData{planeNumber, 'Nx'},
        tableData{planeNumber, 'Ny'}, tableData{planeNumber,
        'Nz'}];

    % Calculate scalar offset 'd' from origin to the plane
    d = -dot(normalVector, knownPoint);
```

The sliding surface area of the discontinuity can be approximated as a 2D polygon obtained from the intersection between the plane and the point cloud. Geometrically, this implies that the plane must be assigned a "thickness," since it is mathematically dimensionless. As a result, it is necessary to define an area of interest around the plane to identify the points affected by the intersection. Computationally, this is achieved by

selecting the points whose distance from the plane falls below a certain threshold. Since the distance of each point from the plane has already been calculated, it is now possible to define a threshold value below which points are considered to belong to the plane (Figure 80). The user can adjust this threshold using the slider available in the interface.

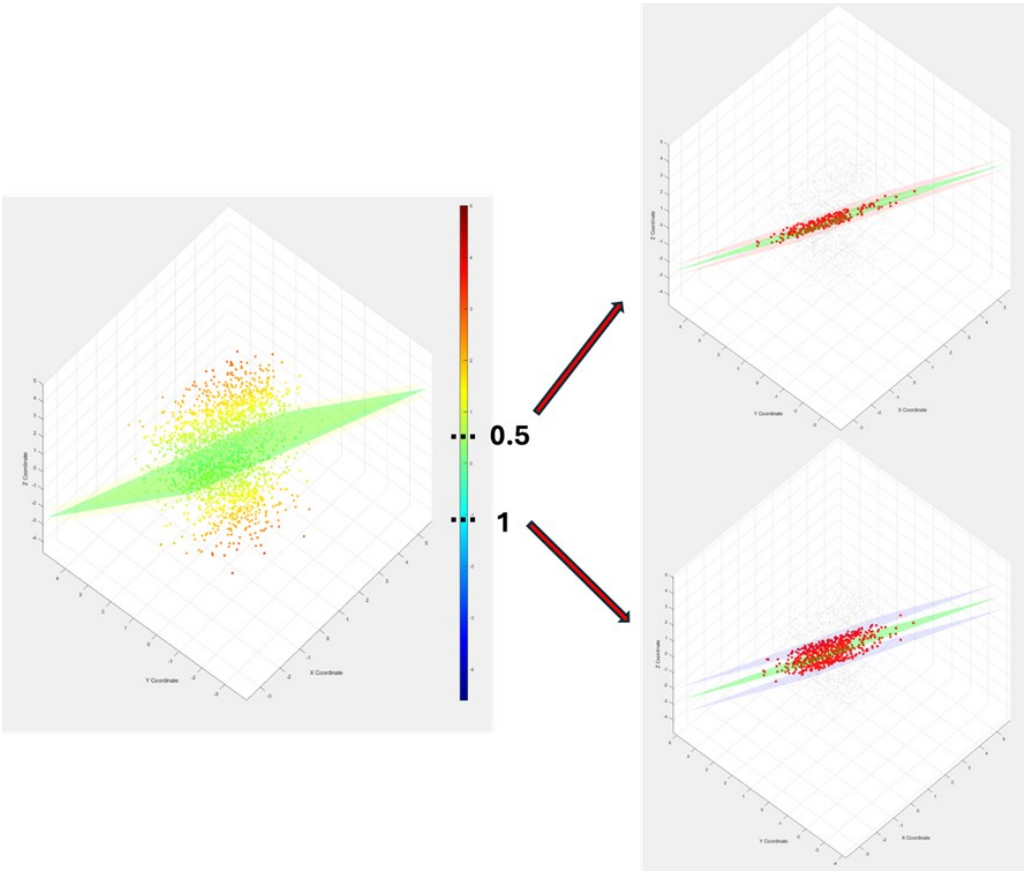


Figure 80: Threshold-based selection of points belonging to the discontinuity plane. Left: Point cloud colored by distance from the plane. Center: User-adjustable threshold slider with values (0.5 and 1 shown as examples). Right: Resulting point selections showing how different threshold values affect the identification of points considered to belong to the plane.

```
% Use slider input to define thickness of planar tolerance
    band
   tolerance = app.AreaPointdensitySlider.Value;
```

```
% Evaluate absolute perpendicular distances from plane for
    each point
distances = abs(normalVector(1) * points(:, 1) + ...
            normalVector(2) * points(:, 2) + ...
            normalVector(3) * points(:, 3) + d) /
               norm(normalVector);

% Keep only points close enough to the plane
onPlaneIndices = find(distances <= tolerance);
planePoints = points(onPlaneIndices, :);

% Construct 2D local coordinates on the plane using SVD
    decomposition
[U, ~, ~] = svd(null(normalVector(:)'));
v1 = U(:, 1)'; % First orthonormal direction on the plane
v2 = U(:, 2)'; % Second orthonormal direction on the plane

% Project in-plane points onto the 2D basis defined by
    {v1, v2}
projectedPoints2D = [dot(planePoints - knownPoint,
    repmat(v1, size(planePoints, 1), 1), 2), ...
                 dot(planePoints - knownPoint, repmat(v2,
                    size(planePoints, 1), 1), 2)];

% Compute convex hull indices for projected polygon
   K = convhull(projectedPoints2D(:,1),
       projectedPoints2D(:,2));

% Create a separate 2D figure to display the hull
fig2d = figure('Name', ['Projected Hull for Plane ',
    num2str(planeNumber)], ...
            'Color', 'w', 'NumberTitle',
               'off','Position',[screenSize(3)*0.366,
               screenSize(3)*0.1, screenSize(3)*0.3,
               screenSize(4)*0.3]);
ax2d = axes('Parent', fig2d);
hold(ax2d, 'on');
axis(ax2d, 'equal');

% Plot polygonal hull and all projected points
```

```
plot(ax2d, projectedPoints2D(K,1), projectedPoints2D(K,2),
    '-r', 'LineWidth', 2);
scatter(ax2d, projectedPoints2D(:,1),
    projectedPoints2D(:,2), '.');

% Compute polygonal area of convex hull
convexHullPoints = projectedPoints2D(K, :);
polygonArea = polyarea(convexHullPoints(:,1),
    convexHullPoints(:,2));
newRow = {planeNumber, polygonArea};

% Store result in app memory and display it in the UI
app.Polyarea = [app.Polyarea; newRow];
app.UITable8_2.Data = app.Polyarea;
app.PlaneArea = polygonArea;
```

Once the "slice" of the plane/point-cloud intersection is obtained, the function repositions the relevant points into the 2D plane to facilitate area computation using standard geometry. To compute the area, it calculates the convex hull of the projected points. To validate whether the hull reasonably covers the sliding contact region, the area is plotted and the user can visually assess the fit (Figure 81).When the function is used to calculate the sliding area of a wedge, the process is repeated for both planes that form the intersection.

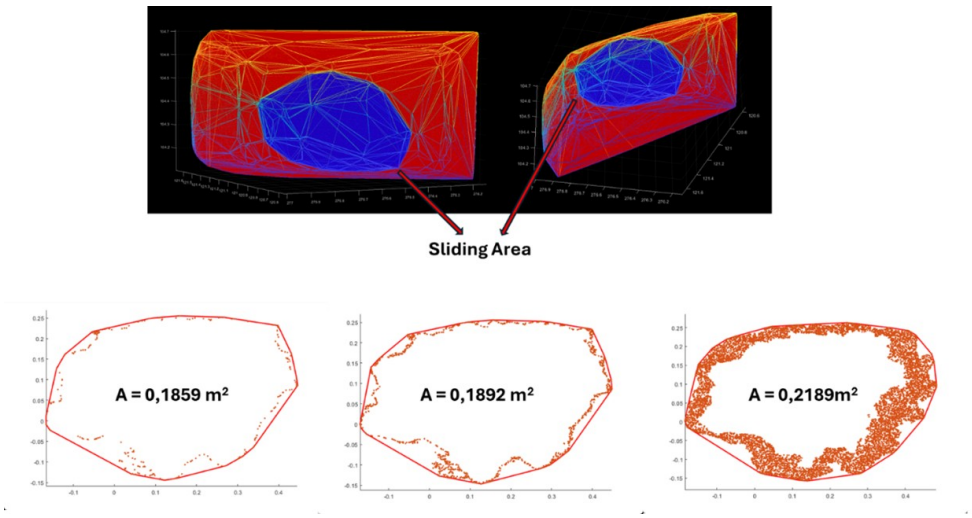


Figure 81: Convex hull computation and area calculation of the discontinuity plane. Top: 3D visualization showing the sliding area (blue) within the point cloud (red) from two perspectives. Bottom: 2D projections of the convex hull onto the plane with computed areas ranging from 0.1859 m^2 to 0.2189 m^2, demonstrating how the threshold selection affects the calculated sliding contact area. The plotted convex hull allows visual validation of whether it reasonably covers the sliding contact region.

4.2.9 *Compute safety factor (planar and wedge)*

This function is used to calculate the Safety Factor (FS) of block moving along a planar or wedge discontinuity. The FS is calculated using Barton's shear strength criterion [13]. The geometric inputs required for the calculation, the block volume and the sliding surface area, are automatically retrieved within the app via the "Planar Volume" and "Planar Area" functions. It is important to note that the model currently accounts only for frictional resistance forces; it does not yet include a cohesive component arising from the infilling material within discontinuities. As a result, cases involving free-fall will not give reasonable results (FS of 0), and safety factors below 1 may be obtained in other kinematic scenarios. The first operation of the function is checking whether the identity (plane or wedge) can fail in freefall. In this case, the safety factor is not calculated (0 is assigned), as there are no frictional resisting forces acting on the block.

```
%--------------------------------------------------
% FSBartonPushed
%
% Computes the Factor of Safety (FS) for planar sliding
% using Barton's shear strength criterion.
%--------------------------------------------------

if app.FreefallMask(planeNumber)
   % This is a check if we have a freefall case - FS = 0, no
      resisting forces
   FS = 0;
   V = app.UITable8.Data{1, 2};       % m^3
   d = app.DensityKgmEditField_4.Value; % D kg/m^3

   % Retrieve the contact area of the plane (m^2)
   mass = V * d;
   W = mass * 9.81;                   % N

   % Load volume and density inputs
   V = app.UITable8.Data{1, 2};       % m^3
   d = app.DensityKgmEditField_4.Value; % D kg/m^3

   % Compute mass and weight of the rock block
```

```
    mass = V * d;
    ResidualD = W;                    % Full weight as driving
        force

    app.FSTextArea_3.Value = {sprintf('%.3f', FS)};
    app.MassKgTextArea_3.Value = {sprintf('%.2f', mass)};
    app.ResidualDrivingForcesNTextArea.Value =
        {sprintf('%.2f', ResidualD)};

    return;
end
```

If the block is not a freefall case, the normal stress on the shear surface can be computed. Barton's shear strength is then calculated, using the cap introduced by Barton (Barton 1973) for the cases of high JCS/Normal stress ratio. The resisting and driving forces are calculated and used to compute FS. In the case of wedge sliding, the calculation follows the same procedure but is applied to both intersecting planes.

```
% Extract selected plane metadata from UI table
tableData1 = app.UITable_2.Data;
planeNumber = app.PlaneNumberEditField.Value;
% Retrieve the contact area of the plane (m^2)
A = app.PlaneArea;
% Load volume and density inputs
V = app.UITable8.Data{1, 2};      % m^3
d = app.DensityKgmEditField_4.Value; % D kg/m^3
% Compute mass and weight of the rock block
mass = V * d;                     % kg
W = mass * 9.81;                  % N
% Retrieve dip and friction angle
psi_p = tableData1{planeNumber, 'Dip'}; % Dip angle (degrees)
phi  = app.EditField_4.Value;     % Friction angle (degrees)
% Retrieve Barton's inputs
JRC = app.JRCEditField_2.Value;   % Joint Roughness
    Coefficient
JCS = app.JCSMPaEditField.Value * 1e6; % Joint Compressive
    Strength (Pa)
% Calculate normal stress on plane (Pa)
sigma_n = (W * cosd(psi_p)) / A;
```

```
% Calculate shear strength (Pa) using Barton's formula or cap
if (JCS / sigma_n) >= 100
   tau = sigma_n * tand(70);      % Maximum allowable shear
      strength
else
   tau = sigma_n * tand(phi + JRC * log10(JCS / sigma_n));
end
% Compute resisting and driving forces
R = A * tau;                      % Resisting force (N)
D = W * sind(psi_p);              % Driving force (N)
% Calculate Factor of Safety
FS = R / D;
ResidualD = D - R;

% Display results in formatted UI fields
app.FSTextArea_3.Value = {sprintf('%.3f', FS)};
app.MassKgTextArea_3.Value = {sprintf('%.2f', mass)};
app.ResidualDrivingForcesNTextArea.Value = {sprintf('%.2f',
   ResidualD)};
```

4.3 VALIDATION AND TESTING

The RoDiAn software has been tested and validated in its computational functions through three distinct approaches:

- Spatial and geometric computation functions were validated using synthetic point clouds with known mathematical properties
- Kinematic analysis functions were validated using point clouds from a real-world case studies, by comparison with one of the industry-standard software tools, Rocscience Dips. It is important to clarify that the functions validated in this section are those involving internal logic beyond the direct application of algebraic formulas from literature. In cases where a function applies a formula directly (e.g., Compute Safety Factor), validation is considered implicit, given the transparency of the code and the explicit formulation of the equations.
- Applicability to real-world failures was demonstrated through retrospective analysis of three possible historical failure events, to confirm that that the kinematic analysis functions could successfully identify the failure mechanisms that occurred in practice.

4.3.1 *Geometrical Validation*

The synthetic point clouds used for validation were designed to replicate the characteristics of those obtained via laser scanning or photogrammetric surveys of historical building facades. These clouds feature an empty backface (the side in contact with the facade), have dimensions on the order of one meter, and are vertically oriented. The geometries were selected to represent three basic morphologies that approximate commonly observed shapes in architectural facades:

- A rectangular parallelepiped with a 1×1 m base and 2×1 m sides
- A square-based pyramid with a 1 m base
- An hemisphere with a 1 m diameter

Discontinuity planes were applied to each 3D point cloud, originating from the geometric center of the respective solid and oriented as follows:

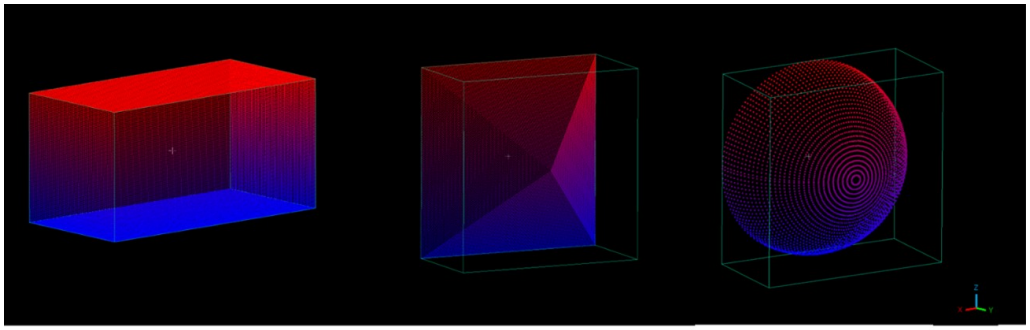


Figure 82: Synthetic 3D point clouds designed for validation. The clouds replicate characteristics of laser scanning or photogrammetric surveys of historical building facades: (left) a rectangular parallelepiped with 1×1 m base and 2×1 m sides, (center) a square-based pyramid with 1 m base, and (right) a hemisphere with 1 m diameter. All geometries have an empty backface (the side in contact with the facade), dimensions on the order of one meter, and are vertically oriented.

Table 1: Orientation data for the validation planes

Plane	**Dip (°)**	**Dip Direction (°)**
Plane 1	45	360
Plane 2	45	180
Plane 3	45	270
Plane 4	45	90

With this planes configuration, the volume and area calculation functions (Planar Volume Side 1/2 and Planar Area) were tested. The numerical outputs from RoDiAn were compared against the theoretical volume and surface values of each solid. The validation results are shown in Figures 83 - 84 - 85 and Tables 2 - 3 - 4.

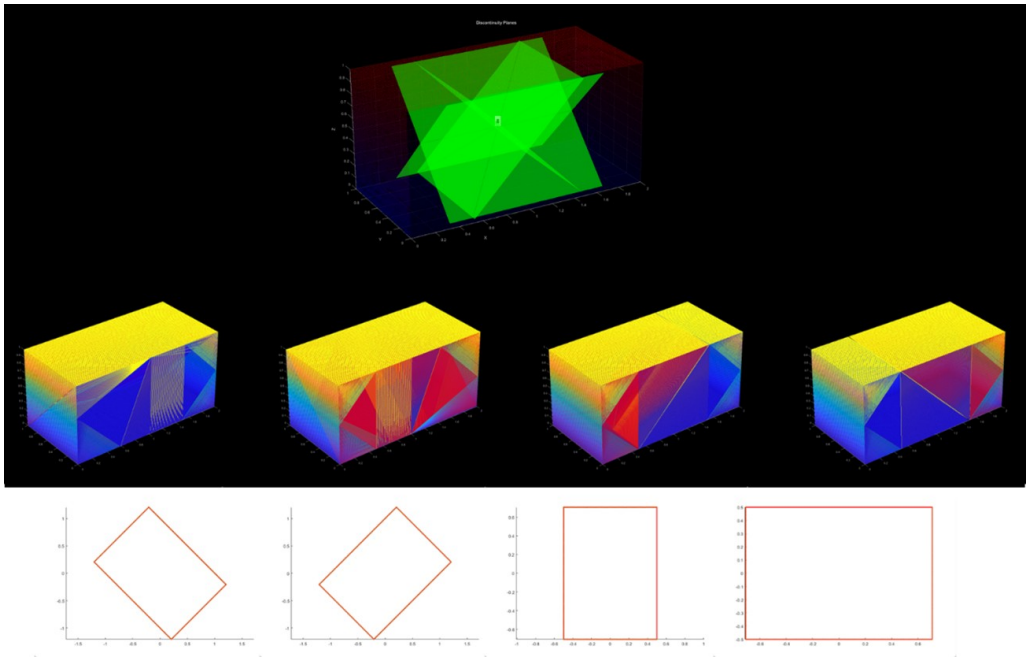


Figure 83: Validation of volume and area calculation functions on the parallepiped point cloud. Top: Configuration showing the planes applied. Bottom: Visual representation of the four planes applied to the parallelepiped along with their 2D 'slice' projections.

Table 2: Comparison of measured (Tot V) and reference volumes (Tot V (ref.)) for the parallepiped point cloud

Plane	**V Side 1**	**V Side 2**	**Tot V**	**Tot V (ref.)**	**Error (%)**
Plane 1	0.995	0.995	1.990	2	0.5
Plane 2	0.995	0.995	1.990	2	0.5
Plane 3	0.9975	0.9975	1.995	2	0.25
Plane 4	0.9975	0.9975	1.995	2	0.25

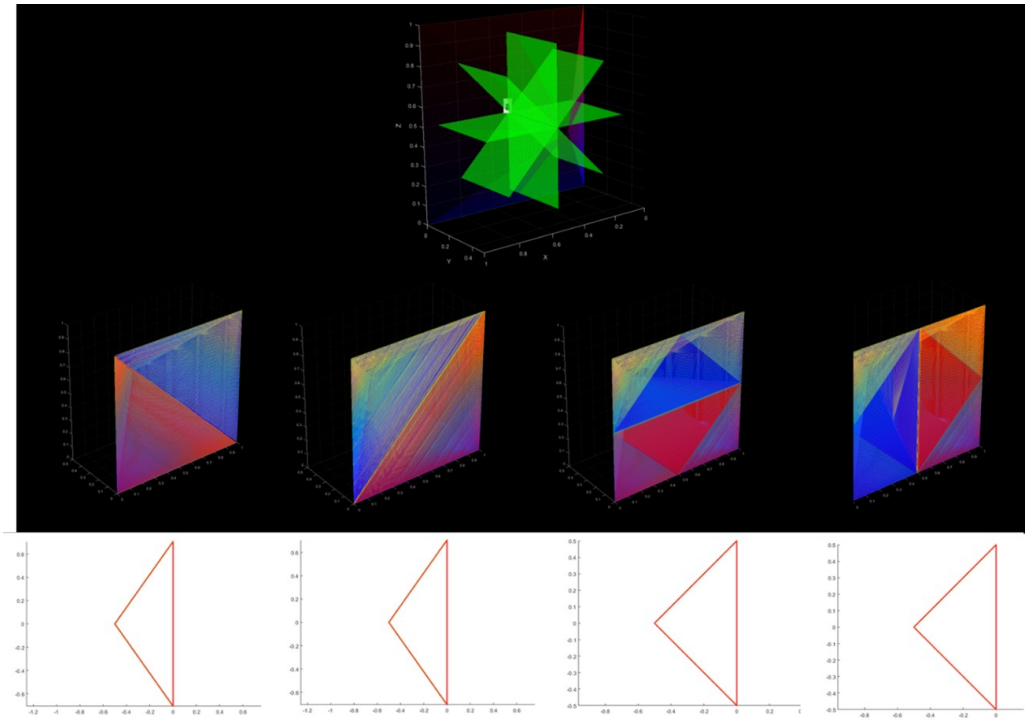


Figure 84: Validation of volume and area calculation functions on the pyramid point cloud. Top: Configuration showing the planes applied. Bottom: Visual representation of the four planes applied to the pyramid along with their 2D 'slice' projections.

Table 3: Comparison of measured (Tot V) and reference volumes (Tot V (ref.)) for the pyramid point cloud

Plane	**V Side 1**	**V Side 2**	**Tot V**	**Tot V (ref.)**	**Error (%)**
Plane 1	0.0896	0.8799	0.9695	1	3.05
Plane 2	0.0896	0.8799	0.9695	1	3.05
Plane 3	0.0839	0.8890	0.9729	1	2.71
Plane 4	0.0839	0.8890	0.9729	1	2.71

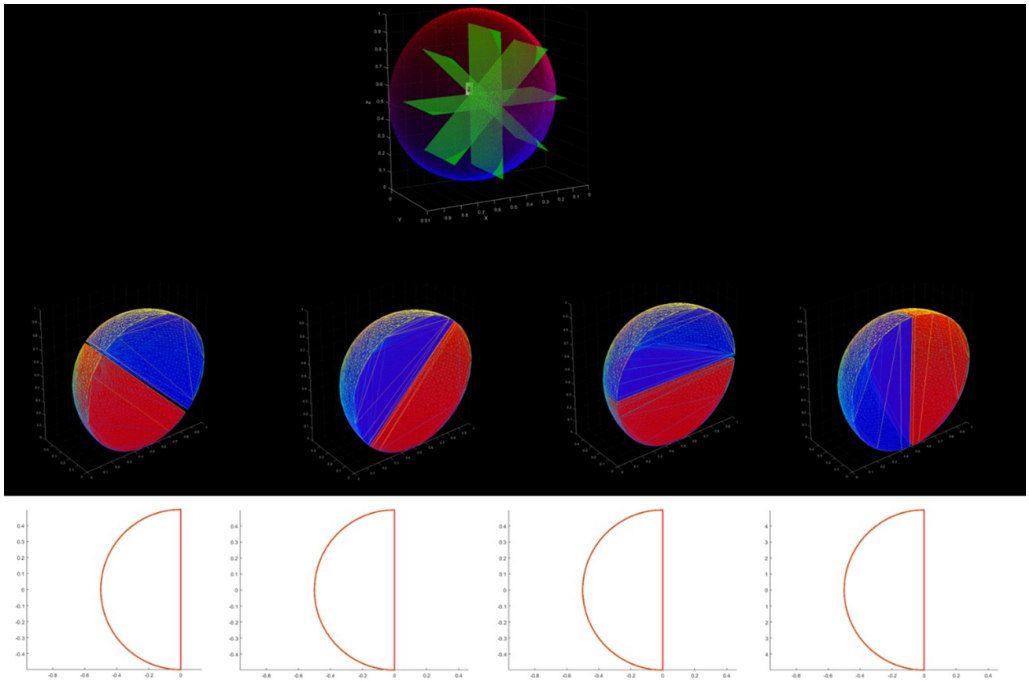


Figure 85: Validation of volume and area calculation functions on the hemisphere point cloud. Top: Configuration showing the planes applied. Bottom: Visual representation of the four planes applied to the hemisphere along with their 2D 'slice' projections.

Overall, the functions demonstrate low relative errors in volume and area calculations, below 4 % in all cases. These discrepancies are primarily due to the limited density of the synthetic point clouds, which introduced minor artifacts in the volume computation.

Table 4: Comparison of measured (Tot V) and reference volumes (Tot V (ref.)) for the hemisphere point cloud

Plane	**Side 1**	**Side 2**	**Tot V**	**Tot V (ref.)**	**Error (%)**
1	0.1307	0.1243	0.2550	0.2615	2.49
2	0.1262	0.1302	0.2564	0.2615	1.95
3	0.1303	0.1261	0.2564	0.2615	1.95
4	0.1230	0.1302	0.2532	0.2615	3.17

Following the same principle, the wedge volume calculation function was also tested. The four volumes resulting from the sector-based decomposition were compared against the total volume of the solid, in order to validate both the partitioning logic and the volumetric fit. To avoid edge-case errors, the planes selected for this verification were modified relative to those used previously.The results are shown in Figures 86 - 87 - 88 and Tables 5 - 6 - 7. This function also shows relatively low errors, with a worst-case deviation of approximately 5%.

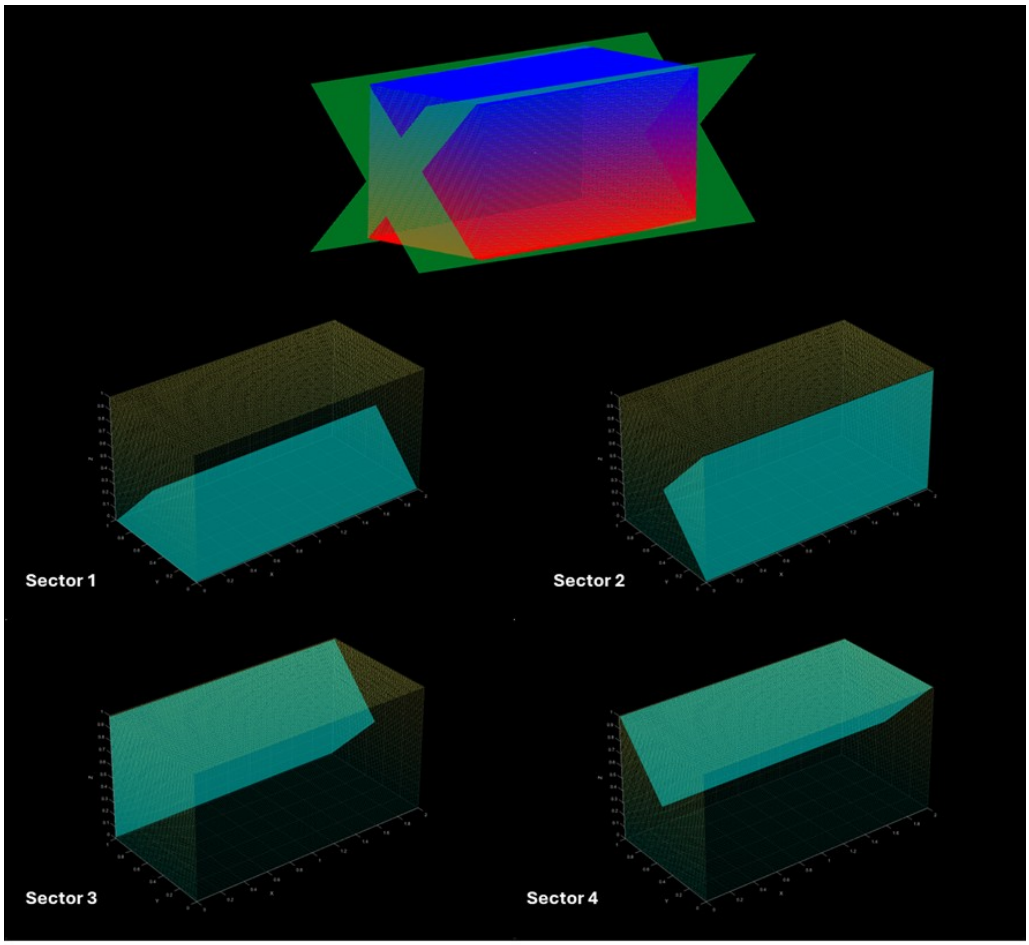


Figure 86: Validation of wedge volume calculation on the parallelepiped point cloud. Top: Configuration showing the planes applied. Bottom: Visual representation of the fours sectors obtained by the wedge intersection.

Table 5: Comparison of measured (Tot V) and reference volumes (Tot V (ref.)) for the hemisphere point cloud

Wedge	$\mathbf{V_1}$	$\mathbf{V_2}$	$\mathbf{V_3}$	$\mathbf{V_4}$	**Tot V**	**Tot V (ref.)**	**Error (%)**
1	0.4886	0.4886	0.4886	0.4886	1.9544	2.0000	2.28

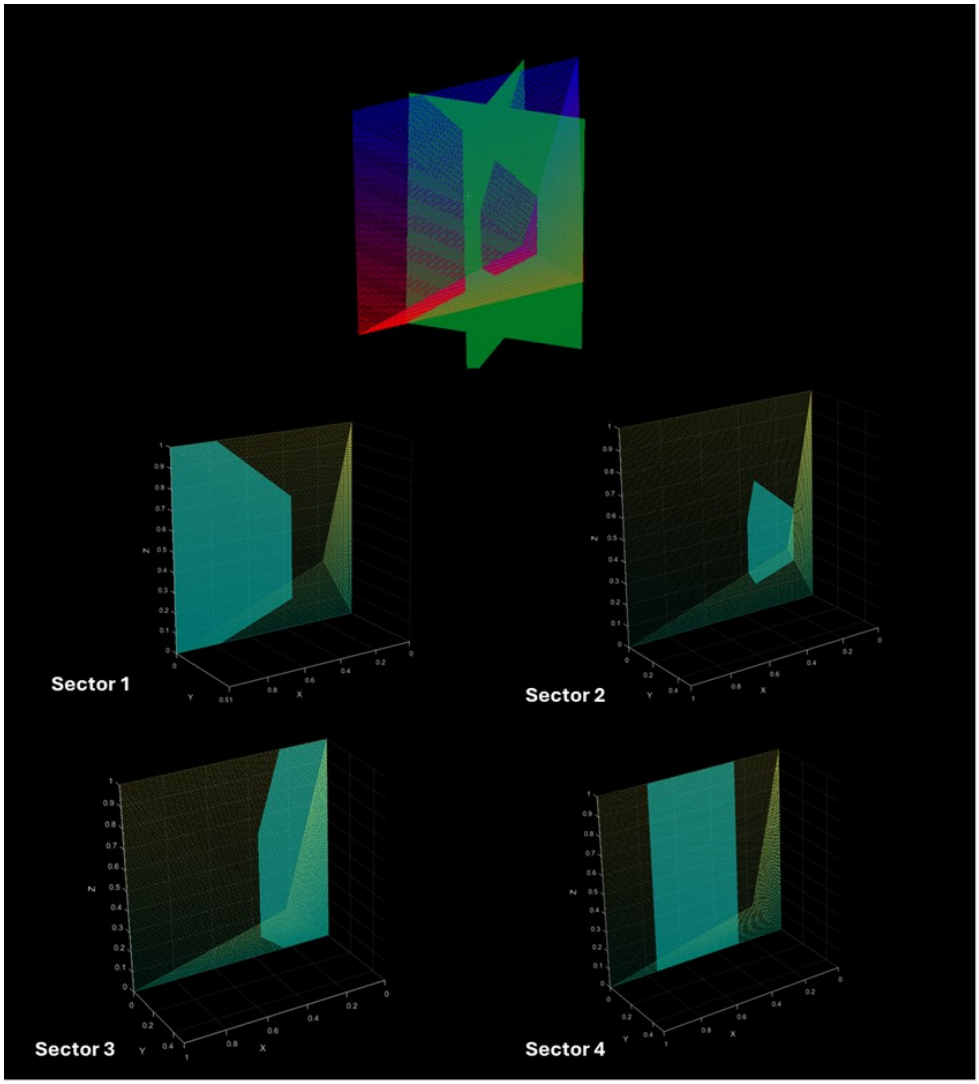


Figure 87: Validation of wedge volume calculation on the pyramid point cloud. Top: Configuration showing the planes applied. Bottom: Visual representation of the fours sectors obtained by the wedge intersection.

Table 6: Comparison of measured (Tot V) and reference volumes (Tot V (ref.)) for the pyramid point cloud

Wedge	$\mathbf{V}_1$	$\mathbf{V}_2$	$\mathbf{V}_3$	$\mathbf{V}_4$	**Tot V**	**Tot V (ref.)**	**Error (%)**
1	0.0069	0.0510	0.0484	0.0510	0.1573	0.1666	5.58

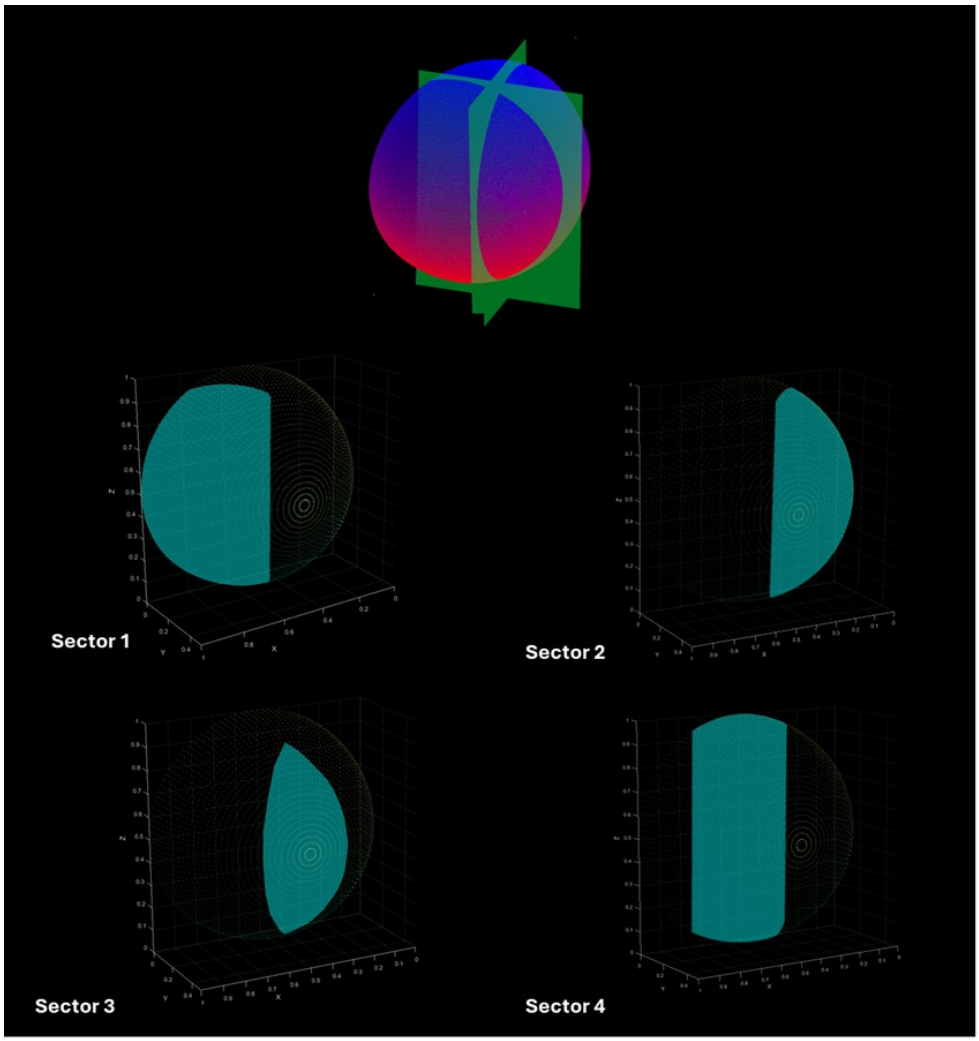


Figure 88: Validation of wedge volume calculation on the hemisphere point cloud. Top: Configuration showing the planes applied. Bottom: Visual representation of the fours sectors obtained by the wedge intersection.

Table 7: Comparison of measured (Tot V) and reference volumes (Tot V (ref.)) for the hemisphere point cloud

Wedge	$\mathbf{V}_1$	$\mathbf{V}_2$	$\mathbf{V}_3$	$\mathbf{V}_4$	**Tot V**	**Tot V (ref.)**	**Error (%)**
1	0.0274	0.0868	0.0594	0.0868	0.2604	0.2618	0.53

4.3.2 *Kinematic Analysis validation*

The kinematic analysis functions were tested by comparing the output generated by RoDiAn with that of Rocscience Dips (Version 8.027, Rocscience Inc., 2024). Dips was selected for this comparison as it is widely regarded as an industry standard and has been used globally for kinematic analysis calculations for nearly twenty years. The functions validated through this approach include: View Wedges, Planar/FreeFall, and Wedge/FreeFall. The selected case study for validation was Palazzo Pitti, which will be discussed in detail in chapter 6. In addition to the analysis performed with RoDiAn, the discontinuities were also analyzed using Dips to validate RoDiAn's kinematic functions. It is important to note that inputting data into Dips using only angular relationships (Dip and Dip Direction) results in the loss of information regarding the spatial position of discontinuity planes within the block, leading to the previously discussed issue of identifying wedges located outside the block. These limitations were disregarded for the purpose of this validation, and Dips was used solely to verify RoDiAn's kinematic output. To carry out the comparison, 49 blocks were analyzed using both software tools, and the kinematic analysis results were compared. As an example, the verification procedure performed on block S1B5 (Figure 89) from the facade of Palazzo Pitti is presented below. The block is affected by three discontinuities with the following orientations:

Table 8: Orientation data of the three planes for the block in example

Plane	**Dip (°)**	**Dip Direction (°)**
Plane 1	83	227
Plane 2	85	67
Plane 3	72	320

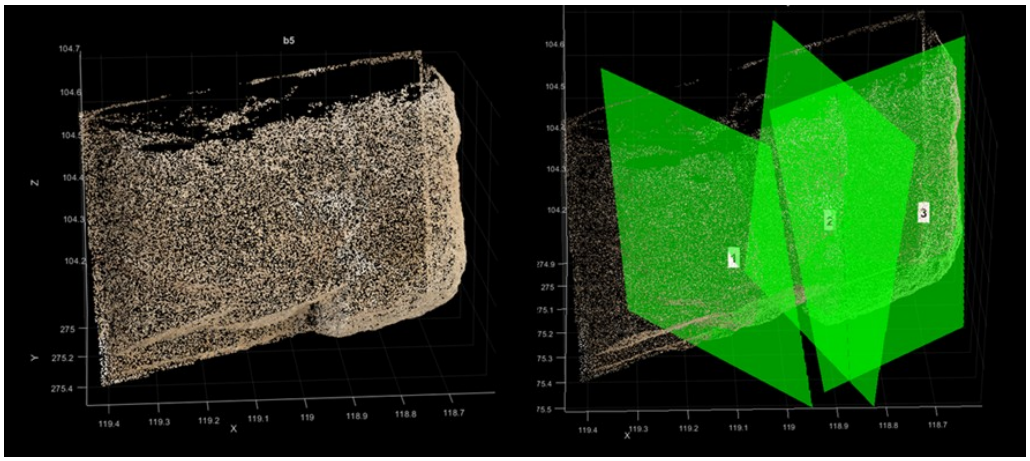


Figure 89: Example block for Kinematic analysis validation. Left: Original point cloud of the block. Right: Three discontinuity planes (labeled 1, 2, and 3) identified within the block for kinematic analysis.

The analysis of the block performed with RoDiAn gives the following results (Figure 90):

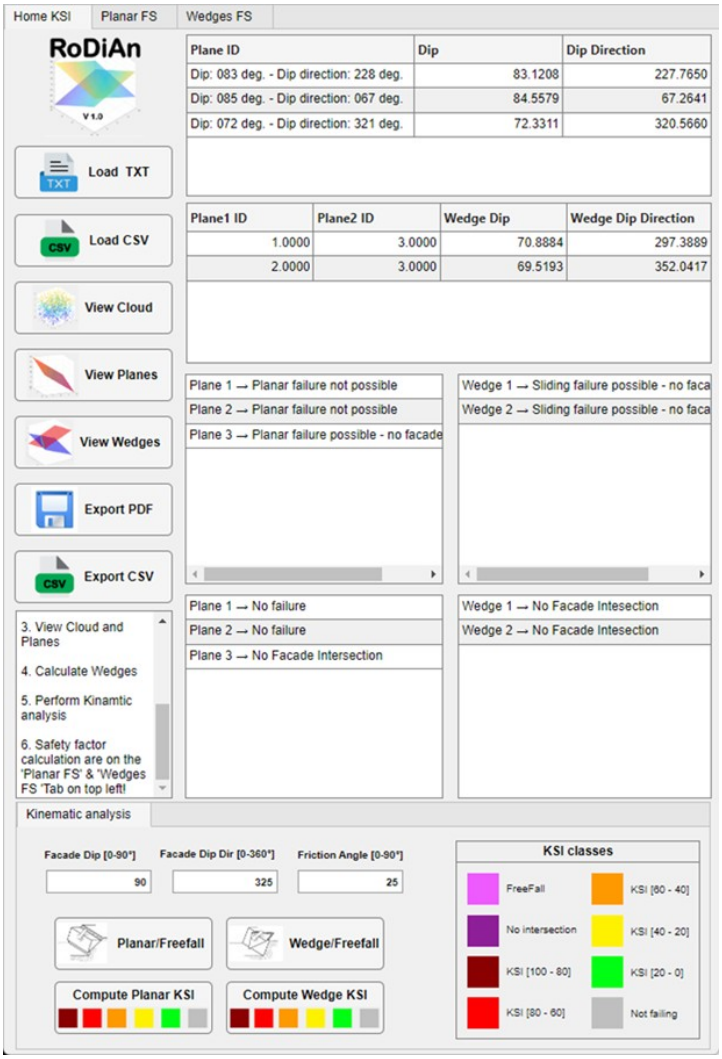


Figure 90: RoDiAn Kinematic analysis results for the example block.

RoDiAn identifies one plane (Plane 3) as being affected by potential planar sliding. This result is confirmed by the analysis performed with Rocscience Dips (Figure 91) , which shows that, of the three planes intersecting the block, only Plane 3 has an orientation that makes it susceptible to planar sliding kinematics.

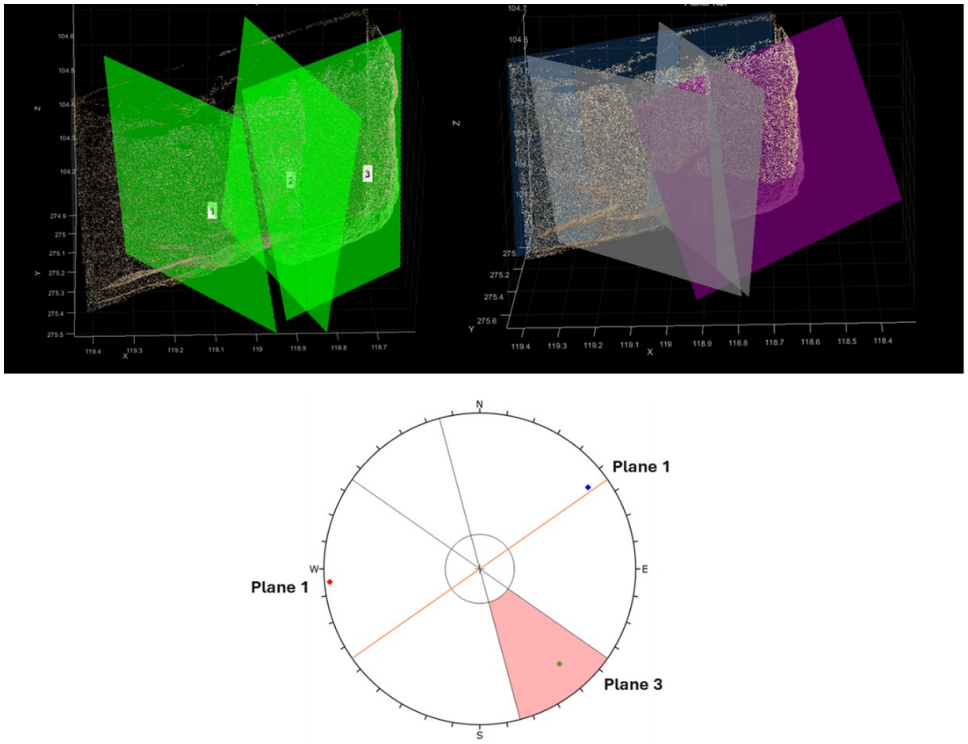


Figure 91: RoDiAn (top) and RocScience Dips (bottom) planar sliding Kinematic analysis results for the example block.

The analysis of the wedges reveals that RoDiAn correctly identifies the two wedges susceptible to sliding (Wedge 1–3 and Wedge 2–3). In addition to accurately detecting the kinematic mechanisms, RoDiAn demonstrates the filtering capability of the View Wedges function, which excludes from the wedge computation all intersections located outside the block, these are instead included in the results produced by Dips. (Figure 92).

The cross-validation procedure presented here for a sample block was carried out across all 49 verification blocks, consistently showing agreement in the results, both in wedge identification and in kinematic classification.

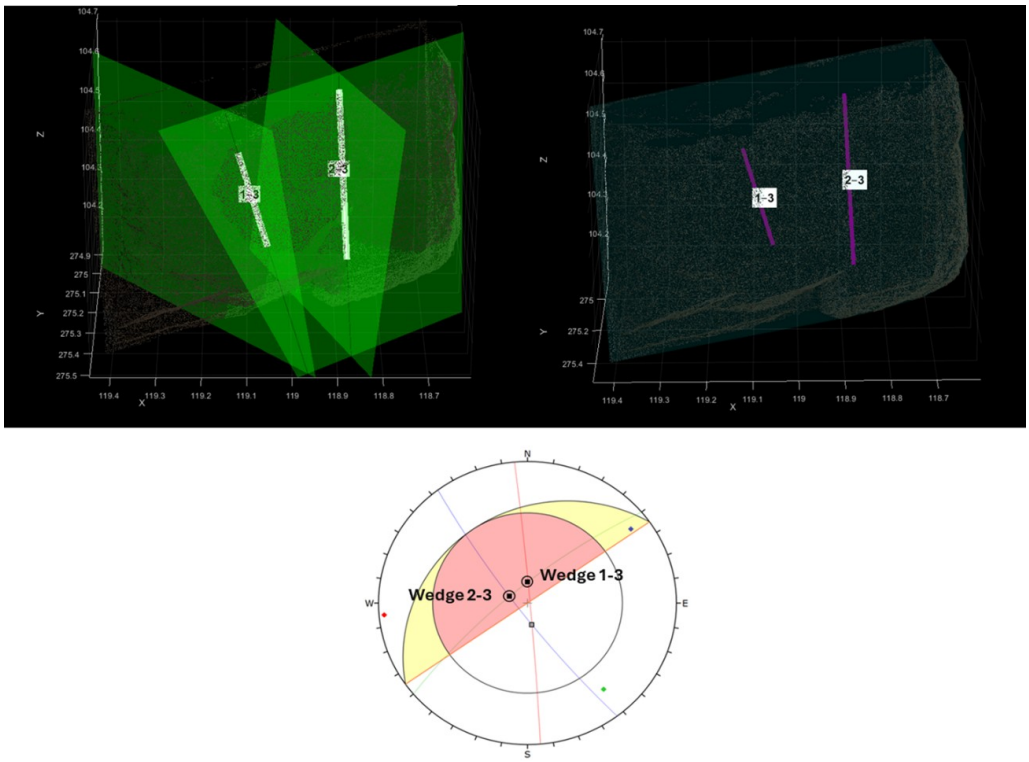


Figure 92: RoDiAn (top) and RocScience Dips (bottom) wedge sliding Kinematic analysis results for the example block.

4.3.3 *Sensitivity and uncertainty analysis of geomechanical assumptions*

To evaluate the impact of the simplifying assumptions inherent in the methodology, a sensitivity analysis was performed on selected representative blocks by varying key geomechanical parameters within the Barton-Bandis shear strength criterion. This approach was necessitated by the fact that, during the investigation campaign, operational constraints made it impractical to fully characterize the internal conditions of the fractures or the weathering state at every point along the block surfaces. As a result, the block strength values and fracture roughness were assumed to be constant and uniform throughout each block and fracture.

Three blocks exhibiting different kinematic mechanisms and geometric configurations were selected: Block P1B16 (planar sliding with facade intersection, Figure 93), Block P2B11 (wedge sliding, Figure 94), and Block P2B17 (planar sliding without facade intersection, Figure 95). The parameters were varied over a range whose variability was determined experimentally during the survey campaign or through variability found in literature data. For each block, the tested parameters are:

- Joint Roughness Coefficient (JRC): tested from 6 to 14, the two extreme values recorded during the survey campaign.
- Joint Wall Compressive Strength (JCS): tested between 40 and 120 MPa. These ranges represent realistic variability for weathered Pietraforte sandstone based on literature values [30] and account for potential spatial heterogeneity within individual blocks and uncertainty in parameter estimation methods.

The representative blocks were analysed by varying the parameters in every possible combination, and in all cases it was observed that the value of the safety factor is not affected by the parameter variation, since in all cases the ratio $J_{CS}/\sigma_n > 100$. In applications where the stress state is orders of magnitude lower than the strength of the rock involved, the Barton criterion may yield results that must be interpreted critically. This observation will be discussed in Section 8.2.

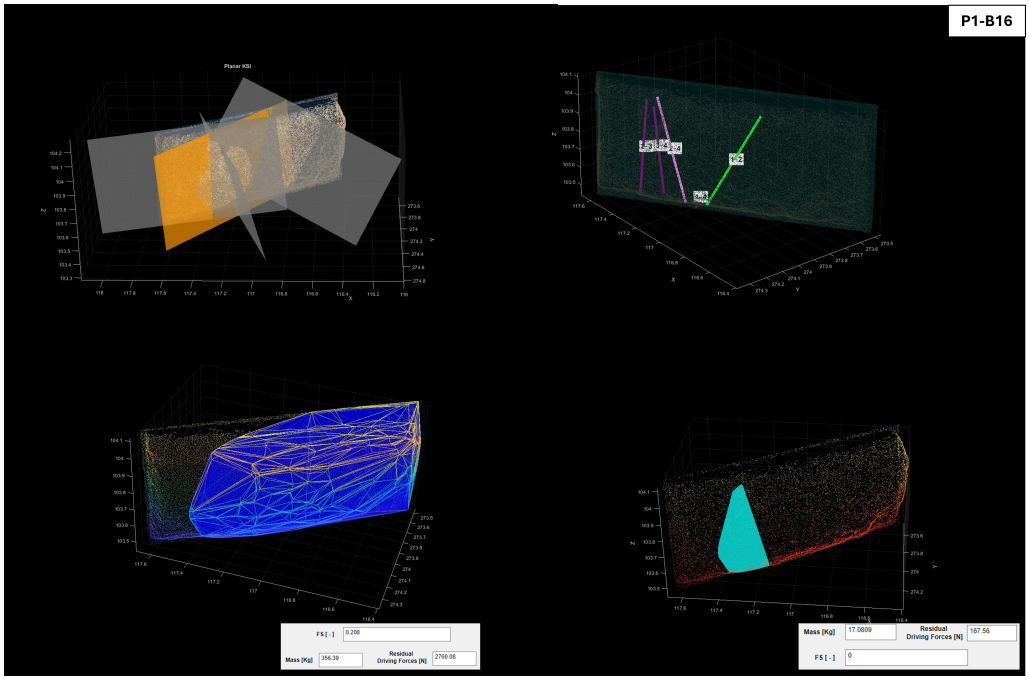


Figure 93: Block P1B16. Example of a case with a discontinuity susceptible to planar slide with an intersection with the facade. Top left: planar susceptibilty; Top right: Wedge susceptibility; Bottom: dynamic analysis results.

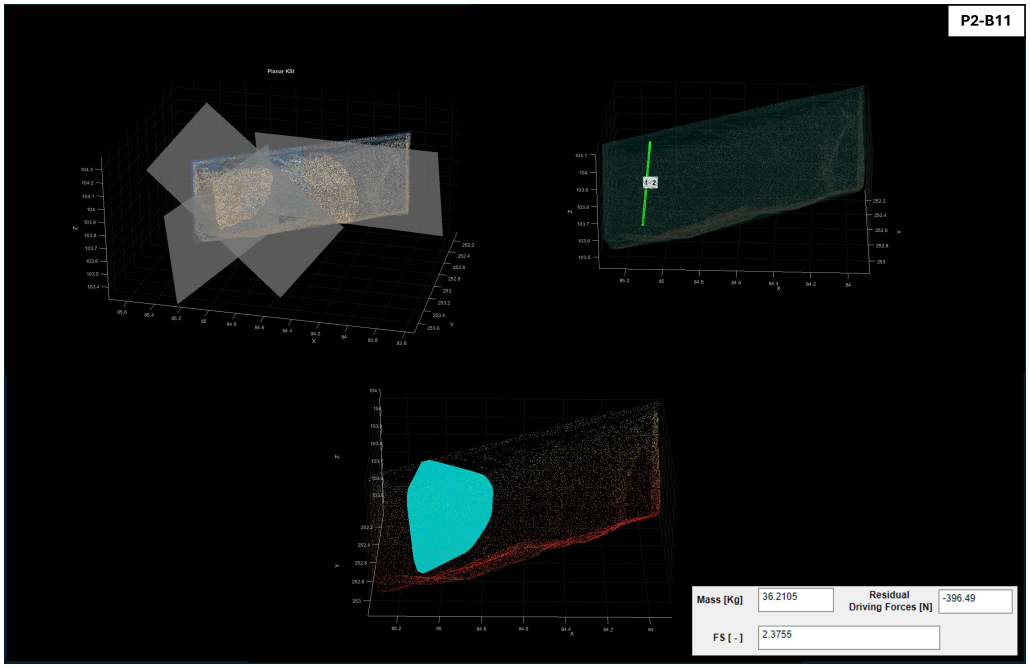


Figure 94: Block P2B11. Example of a case with a wedge susceptible to planar slide. Top left: planar susceptibilty; Top right: Wedge susceptibility; Bottom: dynamic analysis results.

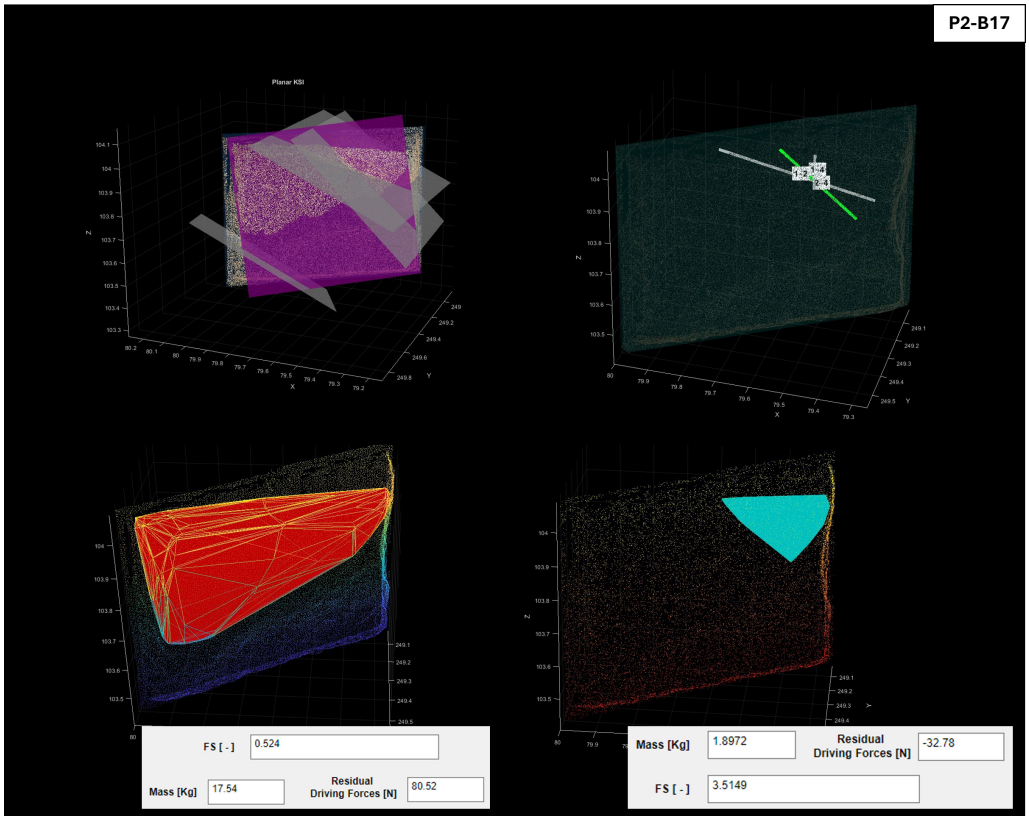


Figure 95: Block P1B17. Example of a case with a discontinuity susceptible to planar slide without an intersection with the facade. Top left: planar susceptibilty; Top right: Wedge susceptibility; Bottom: dynamic analysis results.

4.3.4 *Historical failures validation*

In the context of historical structures built centuries ago, validation against failure events is challenging, as well-documented cases with complete information are unavailable. Direct observation of the failure surfaces at the time of collapse is therefore not possible, and the identification of historical failures must rely on indirect evidence. In the present study, failure surfaces were inferred from the observation of discontinuity geometries and fracture patterns that are still visible on the buildings. These surfaces define blocks whose geometry and orientation are inconsistent with the intact structural elements, as well as with the overall setting and stylistic features of the construction, allowing the inference that these elements must have failed in the past. Although this approach cannot replace systematic validation against a comprehensive database of documented failures, it provides a reasonable basis for retrospective analysis.

Three distinct failure cases were selected for this analysis: one planar sliding failure, one free-fall failure, and one wedge sliding failure. For each case, the current morphology of the structure was documented as observed after the failure events. A plausible reconstruction of the pre-failure geometry was then carried out based on the geometry of adjacent intact blocks and on the stylistic and constructive features of the building. This reconstructed morphology was used as a reasonable approximation of the original configuration for the purposes of the kinematic and dynamic analysis.

- Planar Slide

  For the planar sliding case, a block exhibiting a calcite sliding plane on its frontal surface was selected. The morphology currently observable after the failure event, together with the hypothesized original configuration, is shown in Figure 96. The kinematic analysis performed in RoDiAn indicates that the plane currently observed after detachment would have been identified as kinematically susceptible to planar sliding without contact with the facade (Figure 97). The dynamic analysis further confirms the block's predisposition to failure, yielding a very low safety factor (Figure 97).

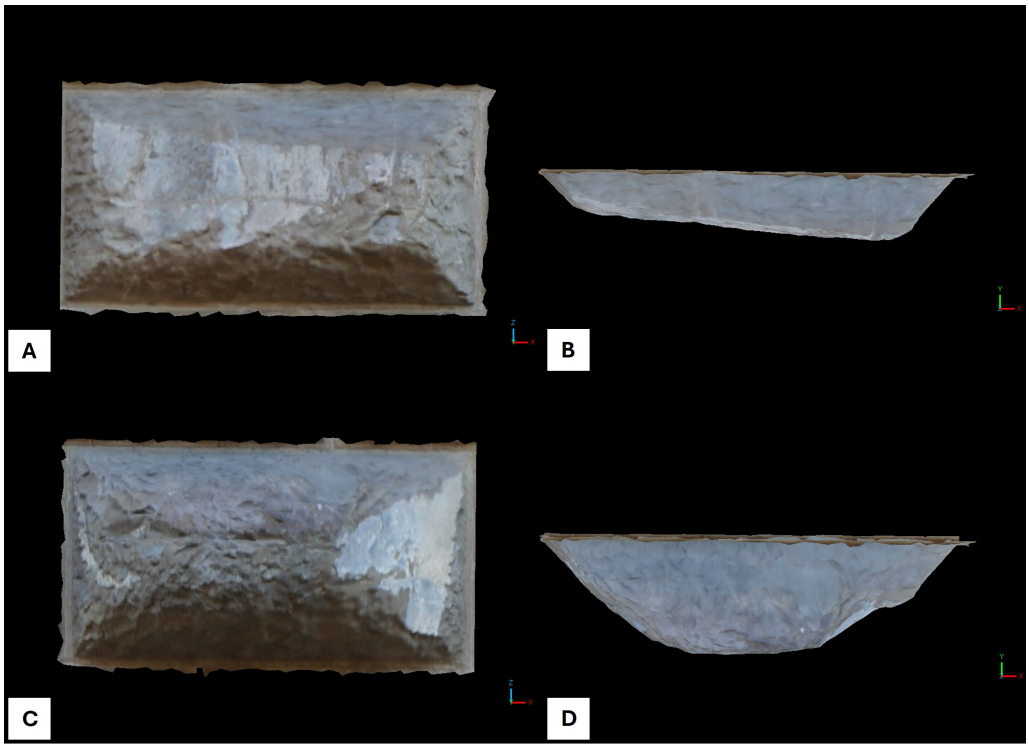


Figure 96: Planar Sliding historical failure. A-B: current post-failure morphology of the selected block, shown in frontal and top views; C-D reconstructed pre-failure morphology based on adjacent intact blocks and architectural stylistic features, shown in the same views.

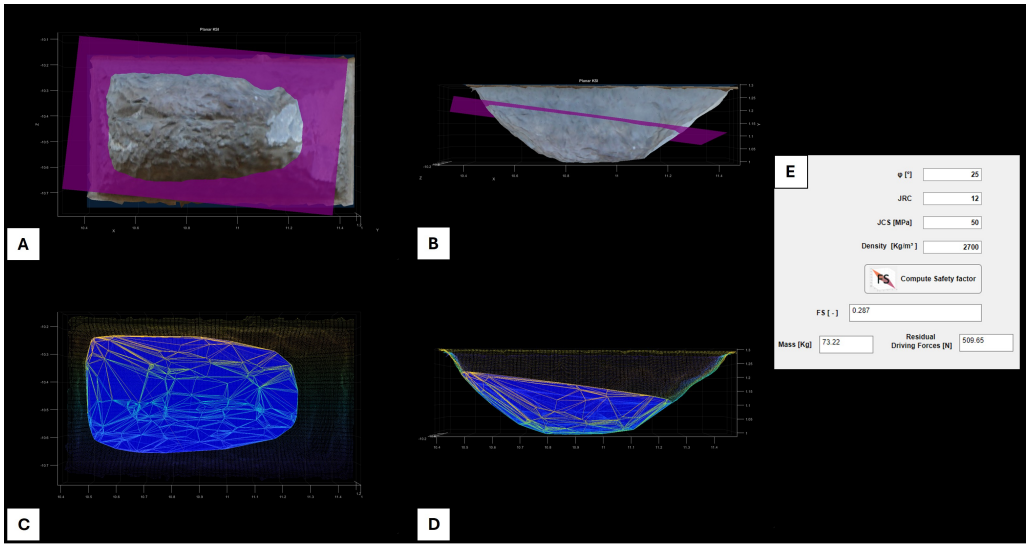


Figure 97: Kinematic and dynamic analysis of the planar sliding case performed in RoDiAn. A-B: results of kinematic analysis in RoDiAn shown in frontal and top views; C-D: potential volume of detachment shown in frontal and top views; E: results of the dynamic analysis in RoDiAn.

- Free Fall

  For the free-fall case, a block showing evidence of sub-vertical collapse was selected. The morphology currently observable after the failure event, together with the hypothesized original configuration, is shown in Figure 98. The kinematic analysis performed in RoDiAn indicates that the block would have been identified as kinematically susceptible to free fall, with no stabilizing contact with the surrounding structure or facade (Figure 99). The dynamic analysis are shown in Figure 99.

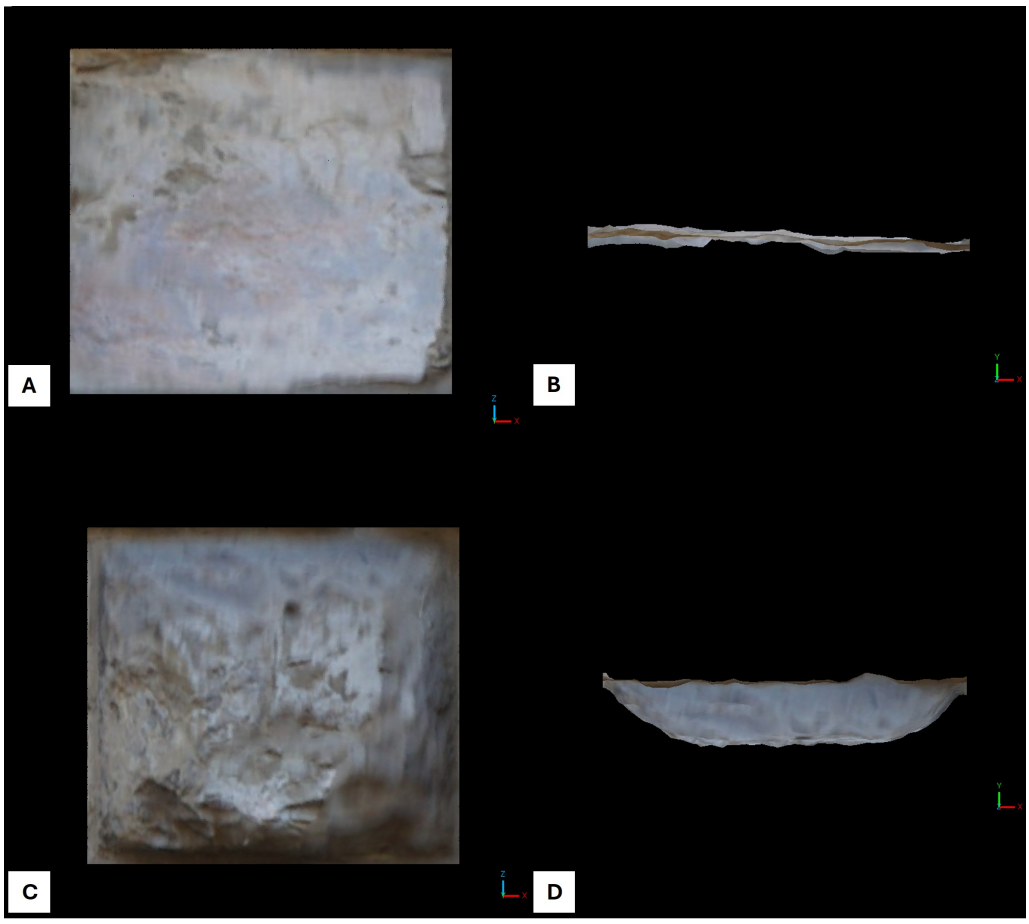


Figure 98: Free Fall historical failure. A-B: current post-failure morphology of the selected block, shown in frontal and top views; C-D reconstructed pre-failure morphology based on adjacent intact blocks and architectural stylistic features, shown in the same views.

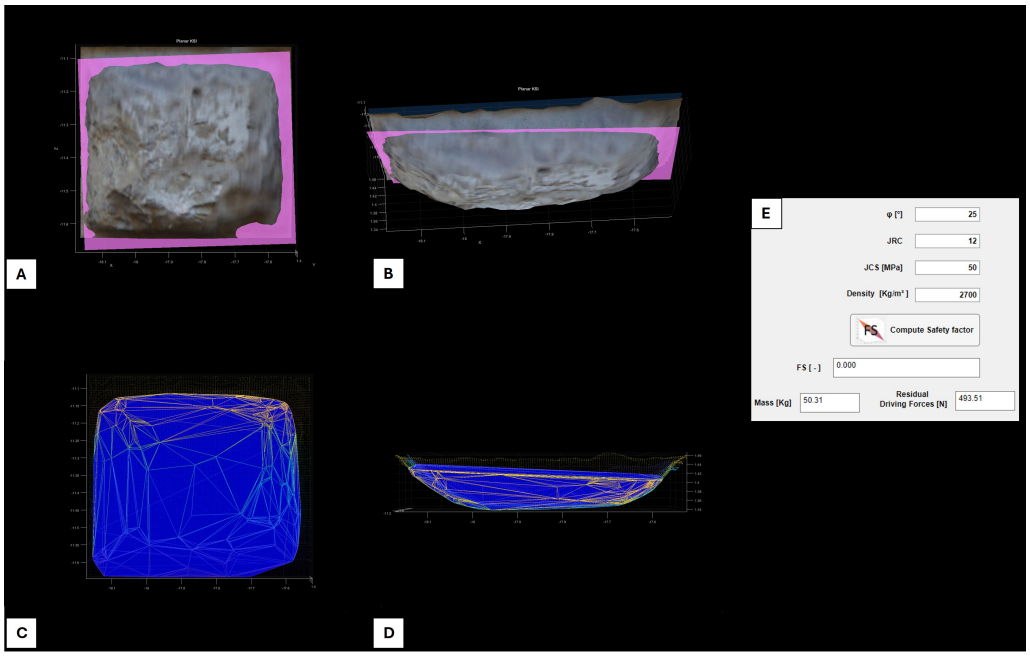


Figure 99: Kinematic and dynamic analysis of the Free Fall case performed in RoDiAn. A-B: results of kinematic analysis in RoDiAn shown in frontal and top views; C-D: potential volume of detachment shown in frontal and top views; E: results of the dynamic analysis in RoDiAn.

- Wedge Sliding

  For the wedge sliding case, a block exhibiting two distinct and intersecting sliding planes was selected. The morphology currently observable after the failure event, together with the hypothesized original configuration, is shown in Figure 100. The kinematic analysis performed in RoDiAn indicates that the plane currently observed after detachment would have been identified as kinematically susceptible to planar sliding without contact with the facade (Figure 101). The dynamic analysis further confirms the block's predisposition to failure, yielding a very low safety factor (Figure 101).

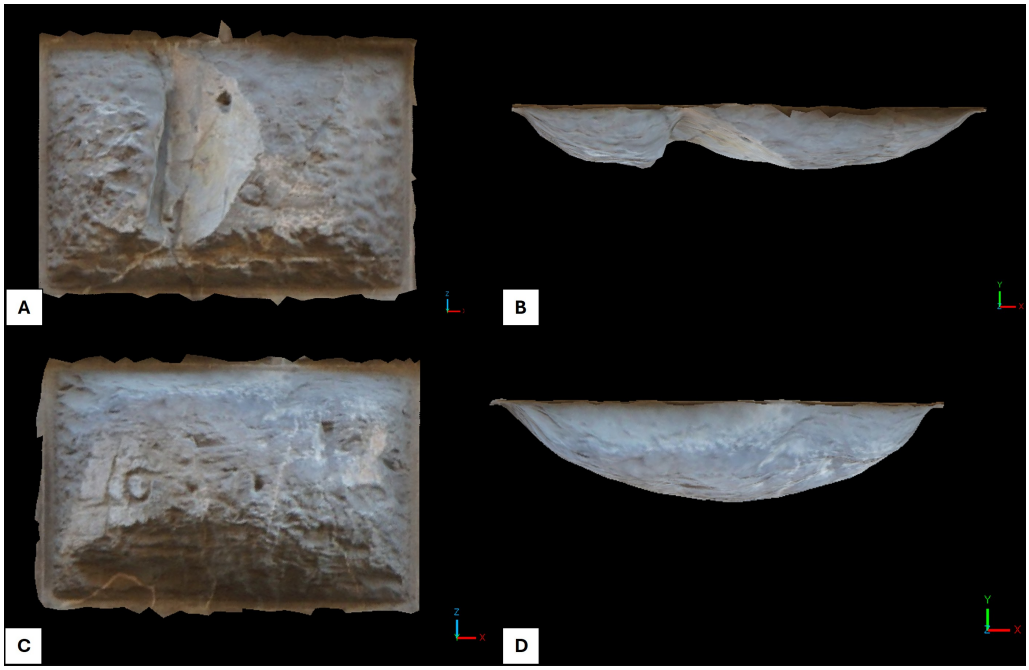


Figure 100: Wedge Sliding historical failure. A-B: current post-failure morphology of the selected block, shown in frontal and top views; C-D reconstructed pre-failure morphology based on adjacent intact blocks and architectural stylistic features, shown in the same views.

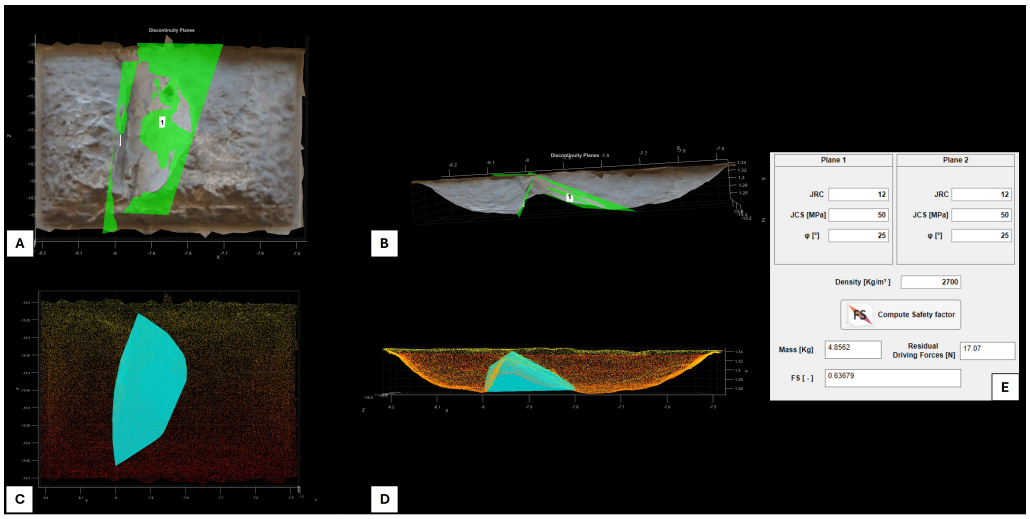


Figure 101: Kinematic and dynamic analysis of the wedge sliding case performed in RoDiAn. A-B: results of kinematic analysis in RoDiAn shown in frontal and top views; C-D: potential volume of detachment shown in frontal and top views; E: results of the dynamic analysis in RoDiAn.

5

SOFTWARE DEVELOPMENT: EZ$_2$JRC

5.1 INTRODUCTION

This chapter presents the development of the software tool named "EZ$_2$JRC " introduced in chapter 3. The primary motivation for developing this software was to create a simple and user-friendly workflow for estimating JRC from 3D point clouds using the Z_2 parameter. The tool automates key steps, including profile extraction, detrending, and JRC computation. The software is designed to reflect the original spirit of the Barton and Choubey [15] JRC chart: an easy and speedy means to assess surface roughness. Like RoDiAn, EZ$_2$JRC is implemented as a MATLAB App Designer application to provide a graphical interface that is as user-friendly as possible. The app is designed around a simple workflow consisting of just four buttons, requiring no code input from the user. All graphical visualization panels are 3D fields, where the user can interact with the data and extract views. The App consists of a small control panel and a dialog window in which the user can read simple user instructions and read the results.

5.2 MAIN FUNCTIONS

This section presents the main functions implemented in EZ$_2$JRC. For each function, the code will be annotated in natural language to clearly explain the underlying logic

5.2.1 *Load Point Cloud*

This function is designed to load and visualize the 3DPC on which the JRC value will be computed. The function begins by cleaning the workspace, closing all open figures except the main application window.

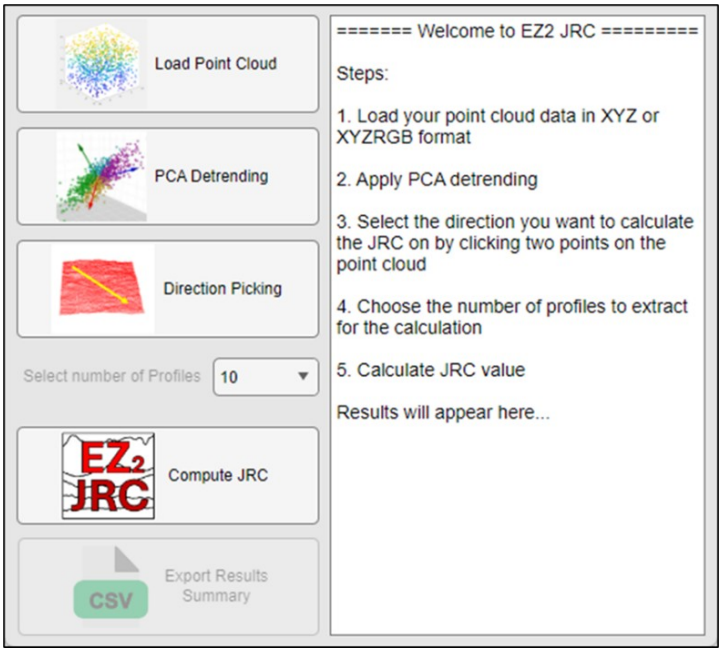


Figure 102: EZ$_2$JRC graphical user interface. The GUI includes: (1) Load Point Cloud button for importing XYZ or XYZ-RGB format data, (2) PCA Detrending, (3) Direction Picking via interactive point cloud selection, (4) profile number selection dropdown, and (5) Compute JRC button. A dialog window on the right provides step-by-step user instructions and displays results. All visualization panels are interactive 3D fields.

This prevents overlapping visualizations if multiple files in a row are processed. The function then opens a file selection dialog in which the user can select the .txt or .csv file. Checks that the input file contains either 3 columns (XYZ) or 6 columns (XYZ + RGB), and that all values are finite. If the file is malformed, an alert is shown and the function exits.

```
%-----------------------------------------------------
% LoadPointCloudButtonPushed - Loads and visualizes a point
    cloud file
% Supports TXT or CSV formats with either XYZ or XYZRGB
    columns.
% Validates input, stores data in app properties, and
    displays the cloud.
%-----------------------------------------------------

    %% Close all figures except the main app window
    allFigures = findall(0, 'Type', 'figure');
    figsToClose = setdiff(allFigures, app.UIFigure);
    close(figsToClose);

    %% Prompt user to select a point cloud file
    [file, path] = uigetfile({'*.txt;*.csv', 'Point Cloud
        Files (*.txt, *.csv)'}, ...
                        'Select Point Cloud File');
    if isequal(file, 0)
        return; % User cancelled
    end

    filePath = fullfile(path, file);
    data = readmatrix(filePath);
    [~, nameOnly, ~] = fileparts(file);
    app.inputFileName = nameOnly;

    %% Validate input dimensions and numeric content
    if ~(size(data, 2) == 3 || size(data, 2) == 6) ||
        any(~isfinite(data), 'all')
        uialert(app.UIFigure, ...
            'File must be either Nx3 (XYZ) or Nx6 (XYZRGB) with
                valid numeric values.', ...
```

```
        'Invalid File');
    return;
end
```

It then extracts the spatial coordinates (X, Y, Z) and, if available, the color channels (R, G, B). If no color data is present, the color array is left empty. It then creates a MATLAB pointCloud object using the file provide. The 3DPC is then plotted in a 3D window.

```
%% Separate XYZ and RGB data
app.pointCloud = data(:, 1:3);
if size(data, 2) == 6
    app.pointCloudColors = data(:, 4:6);
else
    app.pointCloudColors = []; % No color data
end

%% Create MATLAB pointCloud object
ptCloud = pointCloud(app.pointCloud, 'Color',
    uint8(app.pointCloudColors));

%% Display point cloud in a new figure
fig = figure('Name', 'Loaded Point Cloud', ...
          'NumberTitle', 'off', ...
          'Position', [700, 350, 1200, 800]);
ax = axes('Parent', fig);
pcshow(ptCloud, 'Parent', ax);
view(ax, 3);
xlabel(ax, 'X');
ylabel(ax, 'Y');
zlabel(ax, 'Z');
title(ax, 'Loaded Point Cloud');

%% Enable PCA detrending button
app.PCADetrendingButton.Enable = 'on';
```

5.2.2 *PCA Detrending*

The purpose of this function is to flatten the 3DPC along the Z axis. This step is necessary to perform the JRC calculation based on the Z_2 value, as any trend in the profiles would distort the derivative computation. The function validates and loads the input. The points in the 3D point cloud are cleaned to avoid overlapping along the Z axis. A spatial tolerance of 1 mm is applied to homologous points on the plane, this same value is later used as the sampling size for JRC calculation along the profiles.

```
function PCADetrendingButtonPushed(app, event)
% Ensure point cloud data is loaded
if isempty(app.pointCloud)
   uialert(app.UIFigure, 'No point cloud data loaded. Please
      load a file first.', 'Error');
   return;
end

% Extract original XYZ points
originalPoints = app.pointCloud;
tolerance = 1e-4; % rounding tolerance for XY coordinates
   (100 microns)

% Round XY coordinates to reduce noise and group close points
XY = originalPoints(:, 1:2);
Z = originalPoints(:, 3);
XY_rounded = round(XY / tolerance) * tolerance;

% Find unique XY points and compute average Z for each group
[uniqueXY, ~, idx] = unique(XY_rounded, 'rows', 'stable');
meanZ = accumarray(idx, Z, [], @mean);
roundedPoints = [uniqueXY, meanZ];
```

To perform the PCA detrending, it first subtracts the mean of the point cloud from each point to center the data around the origin as shown in Figure 103.

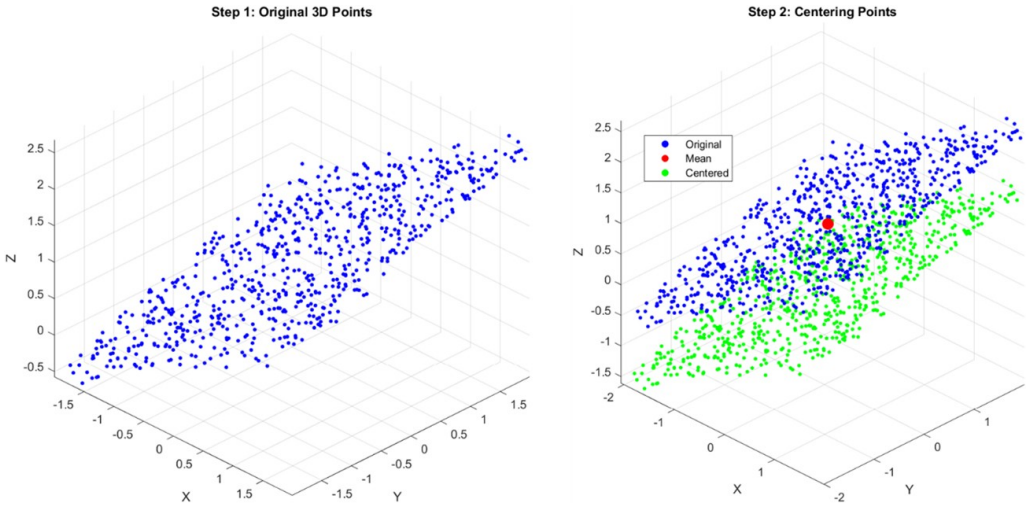


Figure 103: PCA detrending process in EZ^{2}JRC. Visualization of the detrending process showing Step 1 (original 3D points) and Step 2 (centered points around the origin) before rotation and flattening.

Then it calculates the covariance matrix of the centered points and extract eigenvectors (V) and eigenvalues (D), finding the principal directions of variation in the data (Figure 104). The eigenvector with the smallest eigenvalue represents the direction with least variation: it's the normal vector to the best-fit plane.

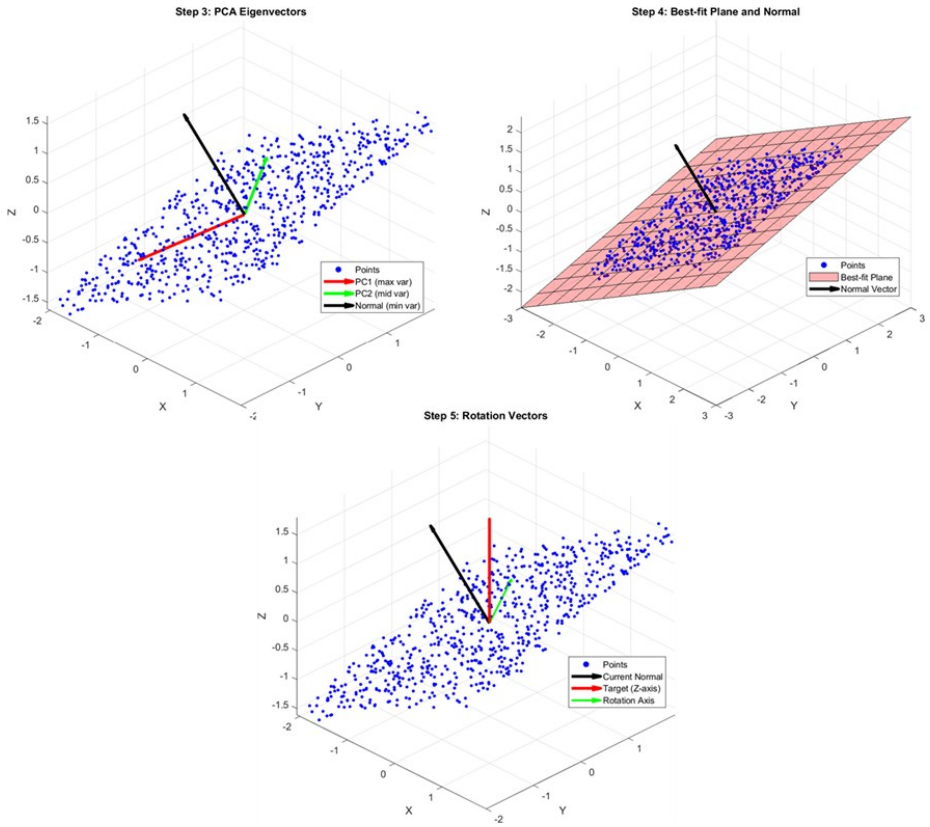


Figure 104: PCA eigenvector analysis and point cloud alignment. Step 3 (top left): PCA eigenvectors overlaid on the centered point cloud, where the eigenvector with the smallest eigenvalue (black arrow) represents the normal vector to the best-fit plane with least variation. Step 4 (top right): Best-fit plane visualization that shows the alignment of its normal vector with the relative Z-axis. Step 5 (bottom): Rotation vector in green, used to make the current normal (black arrow) and target normal (red arrow) coincide.

To flatten the cloud on the Z axis, it aligns the normal vector with the Z-axis. In order to do that a rotation matrix is calculated using Rodrigues formula [90], ash shown in Figure 105. This matrix is used to flatten the point cloud, that is stored for later use.

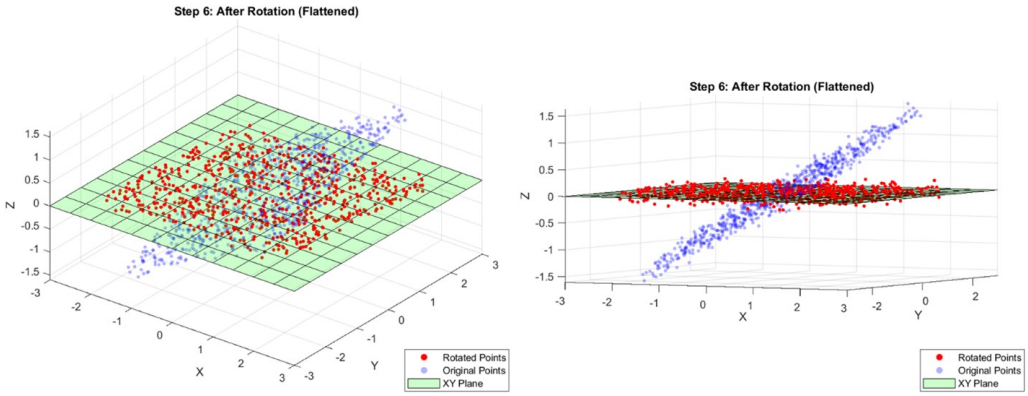


Figure 105: Final flattened point cloud after PCA rotation (Step 6). Left: 3D view showing the rotated points (red) aligned with the XY plane (green), with original points (blue) shown for reference. Right: Side view demonstrating that the rotated points now lie approximately on the XY plane ($Z \approx 0$).

```
% Perform PCA on centered points to find normal direction
centeredPoints = roundedPoints - mean(roundedPoints, 1);
covMat = cov(centeredPoints);
[V, D] = eig(covMat);
[~, sortIdx] = sort(diag(D), 'ascend');
normal = V(:, sortIdx(1)); % eigenvector with smallest
    eigenvalue = normal to best-fit plane

% Calculate rotation matrix to align normal vector with
    Z-axis ([0;0;1])
target = [0; 0; 1];
axis_rot = cross(normal, target);
if norm(axis_rot) < 1e-6
    R = eye(3); % already aligned
else
    axis_rot = axis_rot / norm(axis_rot);
    angle = acos(dot(normal, target));
    K = [  0, -axis_rot(3), axis_rot(2);
         axis_rot(3),  0, -axis_rot(1);
        -axis_rot(2), axis_rot(1), 0];
    R = eye(3) + sin(angle)*K + (1 - cos(angle))*(K*K);
end

% Rotate the points to flatten them
rotatedPoints = (R * roundedPoints')';

% Store rotated points and rotation matrix in app properties
    for later use
app.rotatedPoints = rotatedPoints;
app.PCARotationMatrix = R;
```

5.2.3 *Calculate JRC*

The function computes the JRC on the flattened cloud alongside the chosen direction selected by the user. The number of profiles extracted and used for the calculation is determined by the value selected by the user in the dropdown menu.

Firstly the interpolation parameters are initialized: the grid spacing is the most important one, as it determines the effective resolution on which the JRC calculation will be performed. The value of 1mm is chosen as it reflects the original sampling of Barton profiles (Marsch 2021). The profiles are selected by calculating their distance to the lines traced on the XY plane following the direction selected by the user (Figure 106). The selected points are trimmed at the extremities to reduce edge artifacts, that can often happen when cutting planar sections of 3DPCs. The profiles are considered valid only if they are made of at least 100 points, meaning that they must be full length (100mm) to be used. This is made to ensure that when selecting some directions that may interact with the cloud edges, the edge profiles are excluded.

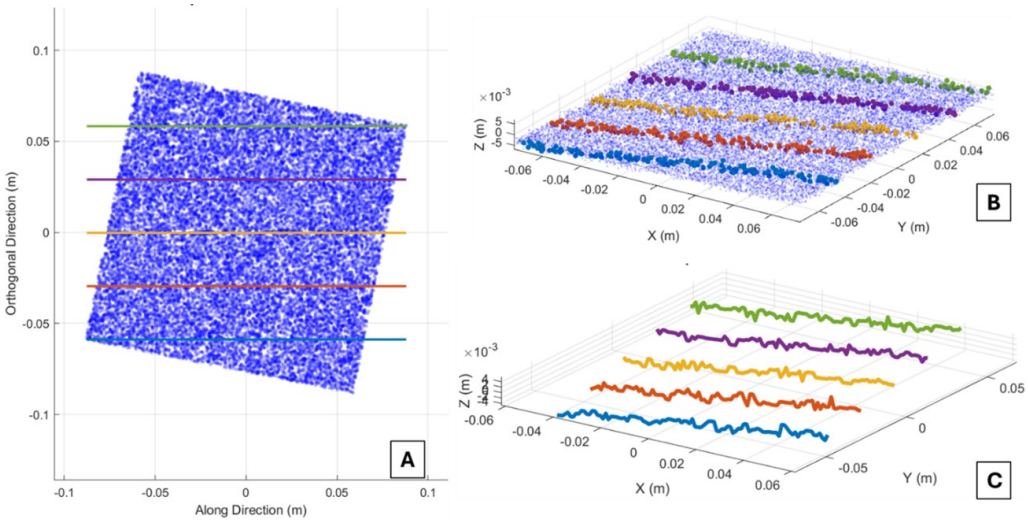


Figure 106: Profile selection and extraction for JRC calculation. (A) Flattened point cloud on the XY plane with user-selected direction line traced across the surface. (B) 3D view showing the points selected for the profile extraction. (C) 2D representation of the extracted profiles.

```
% Interpolation parameters
gridSpacing = 0.001; % 1 mm resolution
```

```
epsilon = 1e-6;
s_center = mean(proj_along);
profileLength = 0.1; % 100 mm
s = (-profileLength/2 : gridSpacing : profileLength/2)';

% Iterate through each profile
for p = 1:numProfiles
   orthCoord = profileSpacing(p);

   % Construct profile line in XY plane
   ux = app.customDirectionVector(1);
   uy = app.customDirectionVector(2);
   x = s * ux + orthCoord * -uy + s_center * ux;
   y = s * uy + orthCoord * ux + s_center * uy;

   % Define profile width tolerance (orthogonal distance from
      centerline)
   profileWidth = 0.0005;

   % Select points close to the current profile in 2D
   centerVec = [ux; uy] * s_center + [-uy; ux] * orthCoord;
   relativeXY = rotatedPoints(:, 1:2) - centerVec';
   distanceToLine = abs((relativeXY * [-directionVec(2);
      directionVec(1)]));
   inProfile = distanceToLine < profileWidth;

   if sum(inProfile) < 100
      JRC_values(p) = NaN;
      numPointsUsed(p) = sum(inProfile);
      continue;
   end

   % Interpolate Z using only points in the current profile
      window
   localPoints = rotatedPoints(inProfile, :);
   F = scatteredInterpolant(localPoints(:,1),
      localPoints(:,2), localPoints(:,3), ...
                     'nearest', 'none');

   z = F(x, y);
```

```
% Filter valid data
valid = ~isnan(z);
xValid = x(valid);
yValid = y(valid);
zValid = z(valid);
nValid = numel(zValid);
numPointsUsed(p) = nValid;

% Optional trimming for correcting edge artifacts (e.g. 2%
    ends)
trimCount = floor(0.02 * nValid);
if nValid > 2 * trimCount
   xValid = xValid(trimCount+1:end-trimCount);
   yValid = yValid(trimCount+1:end-trimCount);
   zValid = zValid(trimCount+1:end-trimCount);
end
```

The JRC value is calculated on each profile using the correlation from Tatone and Grasselli (Tatone and Grasselli 2010):

$$\mathrm{JRC} = 55.03 \cdot (Z_2)^{0.74} - 6.1 \tag{6}$$

where Z_2 is defined as:

$$Z_2 = \sqrt{\frac{1}{(N-1)\cdot(dx)^2}\sum_{i=1}^{N-1}(y_{i+1}-y_i)^2} \tag{7}$$

To exclude degenerate values the results are cut-off at both the extremes. The results for each profile are stored for later export and shown in the dialogue window. Statistics for the overall analysis (Number of profiles, Mean JRC, Standard Deviation, Range) are calculated and printed.

```
% Compute JRC using Z2 parameter
if numel(zValid) >= 2
   dx = mean(sqrt(diff(xValid).^2 + diff(yValid).^2));
   slope = diff(zValid);
   Z2 = sqrt(1 / ((numel(zValid)-1) * dx^2) *
      sum(slope.^2));
```

```
        if Z2 < epsilon
            JRC_temp = 0;
        else
            JRC_temp = 55.03 * Z2^0.74 - 6.1;
            JRC_temp = max(0, min(JRC_temp, 20)); % Clamp to
                realistic JRC range
        end
        JRC_values(p) = JRC_temp;
    else
        JRC_values(p) = NaN;
    end
end

hold(ax3D, 'off');

%% === Report Summary ===

valid_JRC = JRC_values(~isnan(JRC_values));
mean_JRC = mean(valid_JRC);
std_JRC = std(valid_JRC);
num_valid = numel(valid_JRC);

resultString = sprintf('=== EZ2 JRC ===\n\n');
resultString = sprintf('%sProcessed %d profiles (%d
    valid)\n\n', resultString, numProfiles, num_valid);
resultString = sprintf('%s- Mean JRC: %.4f\n', resultString,
    mean_JRC);
resultString = sprintf('%s- Standard Deviation: %.4f\n',
    resultString, std_JRC);
resultString = sprintf('%s- Range: [%.4f - %.4f]\n',
    resultString, ...
                  min(valid_JRC), max(valid_JRC));
resultString = sprintf('%sAnalysis performed on: %s\n\n', ...
                  resultString,
                     datetime('now','Format','yyyy-MM-dd
                     HH:mm:ss'));

% Append per-profile results
if num_valid > 0
```

```
    resultString = sprintf('%sProfile Results:\n',
        resultString);
    for p = 1:numProfiles
        if ~isnan(JRC_values(p))
            resultString = sprintf('%s| %-7d | %8.4f | (%d
                pts)\n', ...
                resultString, p, JRC_values(p), numPointsUsed(p));
        else
            resultString = sprintf('%s| %-7d | (invalid) | (%d
                pts)\n', ...
                resultString, p, numPointsUsed(p));
        end
    end
end
app.JRC_values = JRC_values;
app.numPointsUsed = numPointsUsed;
% Output to UI text area
app.ResultsTextArea.Value = resultString;
```

5.3 VALIDATION AND TESTING

EZ2JRC has been tested and validated using both synthetic data and real examples of rock profiles. The validation process involved both the PCA detrending function and the JRC calculation routine.

5.3.1 *Synthetic data validation*

To test the app's ability to compute the JRC value from the Z_2 parameter, a series of synthetic point clouds was generated with the following characteristics:

- Known Z_2 value, defined a priori through their generation equation with a target JRC value
- Point spacing below 1 mm, to test the accuracy of interpolation and sampling routines
- Random inclination with respect to the Z axis, to verify the correct functioning of the PCA detrending procedure

Ten point clouds were generated, one for each original JRC class. For each class, the selected Z_2 value corresponds to the median value.

Table 9: JRC classes and corresponding Z_2 values

JRC Class	Z_2 (median)
0–2	0.0628
2–4	0.0879
4–6	0.1149
6–8	0.1438
8–10	0.1742
10–12	0.2061
12–14	0.2393
14–16	0.2738
16–18	0.3094
18–20	0.3462

The generated 3DPC are visible in Figure 107. The clouds are represented as flattened only for plotting purposes, each cloud has a random orientation.

The results obtained in the original output from the EZ2JRC analysis are shown in Table 10.

Table 10: EZ_2JRC Analysis results for the 10 validation syntethic point clouds

Sample	Profiles	Mean JRC	Std Dev	Range
1	20 (20)	1.1889	0.1335	[0.897 - 1.358]
2	20 (20)	3.0701	0.1812	[2.698 - 3.426]
3	20 (18)	5.1706	0.1912	[4.798 - 5.388]
4	20 (20)	6.7630	0.3514	[6.510 - 7.651]
5	20 (20)	8.7554	0.1363	[8.537 - 9.004]
6	20 (20)	10.7085	0.2986	[10.469 - 11.472]
7	20 (20)	12.7052	0.3131	[12.286 - 13.740]
8	20 (20)	14.5862	0.1241	[14.305 - 14.675]
9	20 (20)	16.3941	0.1515	[16.355 - 16.874]
10	20 (20)	18.4420	0.1723	[18.155 - 18.671]

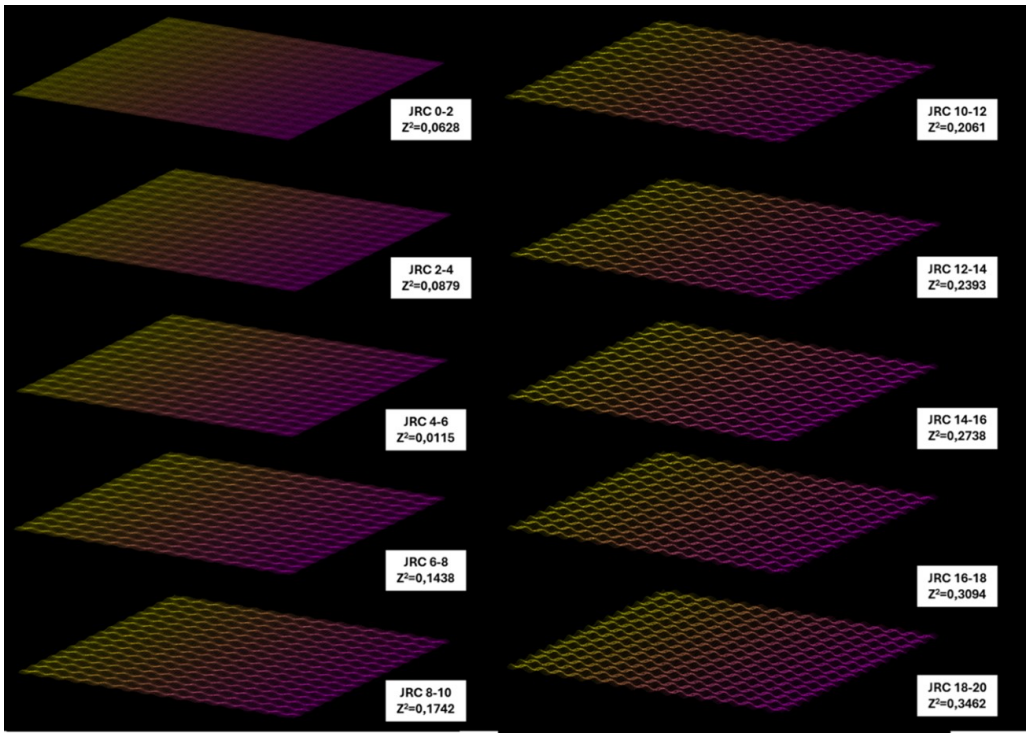


Figure 107: Synthetic point clouds generated for JRC validation. Each cloud corresponds to one JRC class. The surfaces are shown flattened for visualization purposes, while in the actual dataset each cloud has a random inclination with respect to the Z axis.

A summary of the results is shown in Table 11. Overall, the method demonstrates a good ability to predict the JRC value, with a slight underestimation starting from class 6–8. This underestimation, although minimal (approximately 1σ), is conservative and therefore considered acceptable.

Table 11: Summary of the EZ_2JRC validation results

Expected JRC	**EZ_2JRC results** $\pm\sigma$
1	1.2 ± 0.13
3	3.1 ± 0.18
5	5.2 ± 0.19
7	6.8 ± 0.36
9	8.8 ± 0.13
11	10.7 ± 0.29
13	12.7 ± 0.31
15	14.6 ± 0.12
17	16.5 ± 0.15
19	18.4 ± 0.17

5.3.2 *Field data validation*

The app was also tested on real rock samples acquired through photogrammetry. Several lithotypes with varying apparent roughness were analyzed, and selected examples are shown in Figure 108.

The samples were collected from accessible surfaces and analyzed manually using the traditional Barton profilometer method. The profiles were processed with EZ_2JRC, and the results were compared against Barton's standard profile charts. An example of the steps of the EZ_2JRC workflow on these samples is shown in Figure 109.

Overall the comparison with manual calculation of JRC via the Barton profilometer, despite the inherently subjective nature of this method, gave consistently matching results. To illustrate this convergence, four representative samples are presented below. For each sample, in addition to the EZ_2JRC results (Figures 110, 112, 114, 116), the extracted profiles have also been included to allow visual comparison with Barton's standard reference profiles (Figures 111, 113, 115, 117).

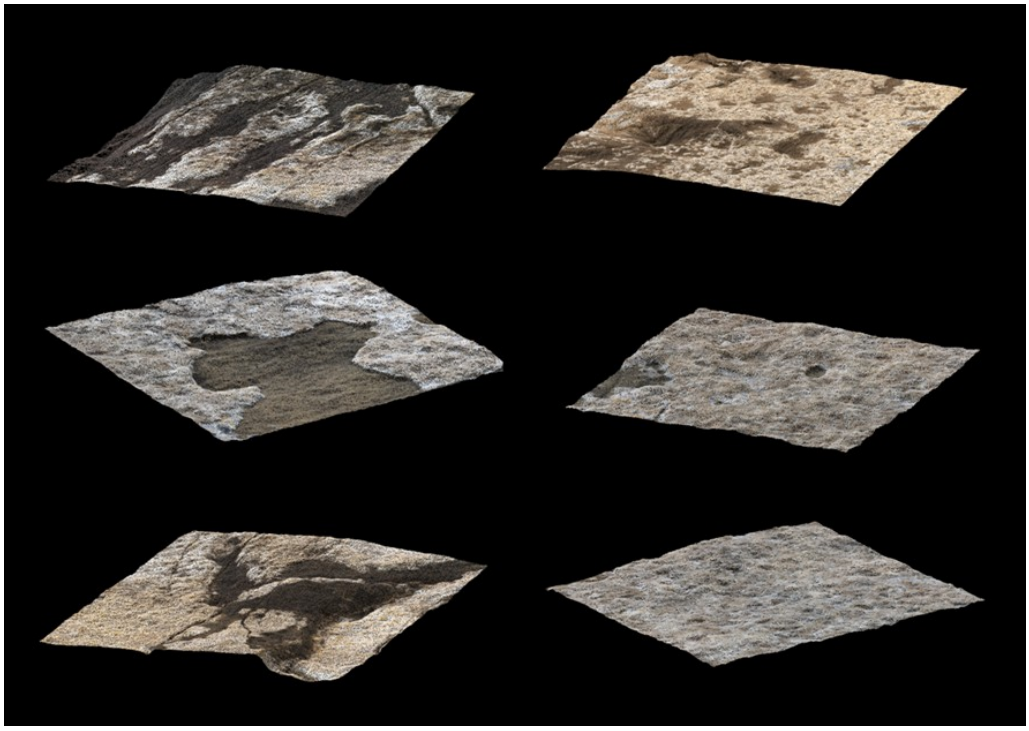


Figure 108: Examples of real rock surface models acquired through photogrammetry. The selected lithotypes exhibit varying degrees of apparent roughness, and were used to validate the app's performance on natural samples.

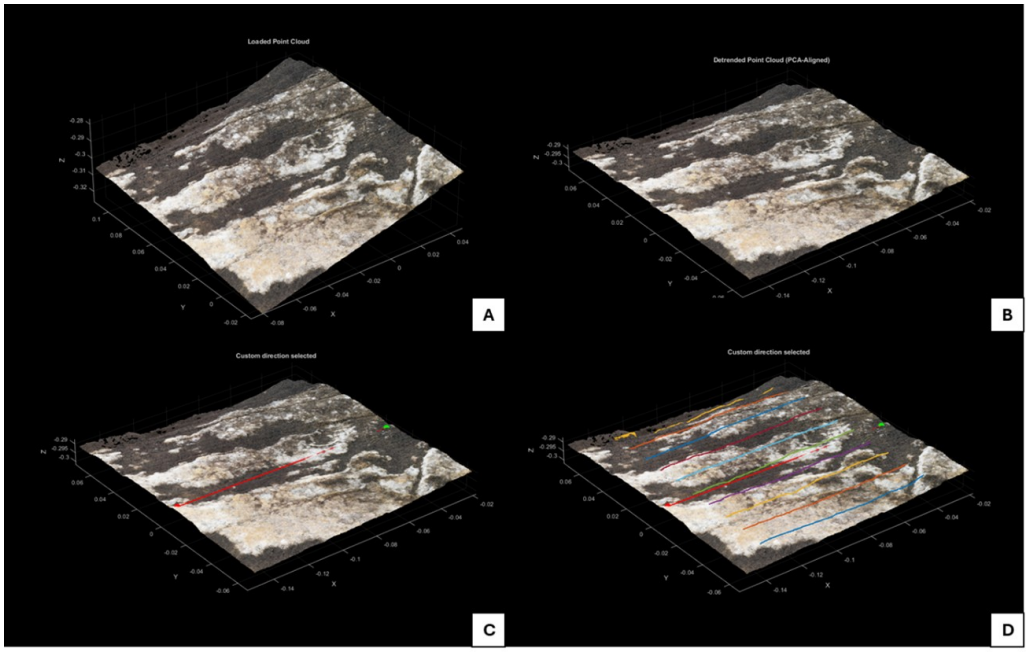


Figure 109: Example of the EZ_2JRC workflow applied to a real rock surface model. A: Loaded point cloud; B: Detrended point cloud after PCA alignment; C: Custom direction selection for profile extraction; D: Generated profiles used for JRC estimation and comparison with Barton's standard charts.

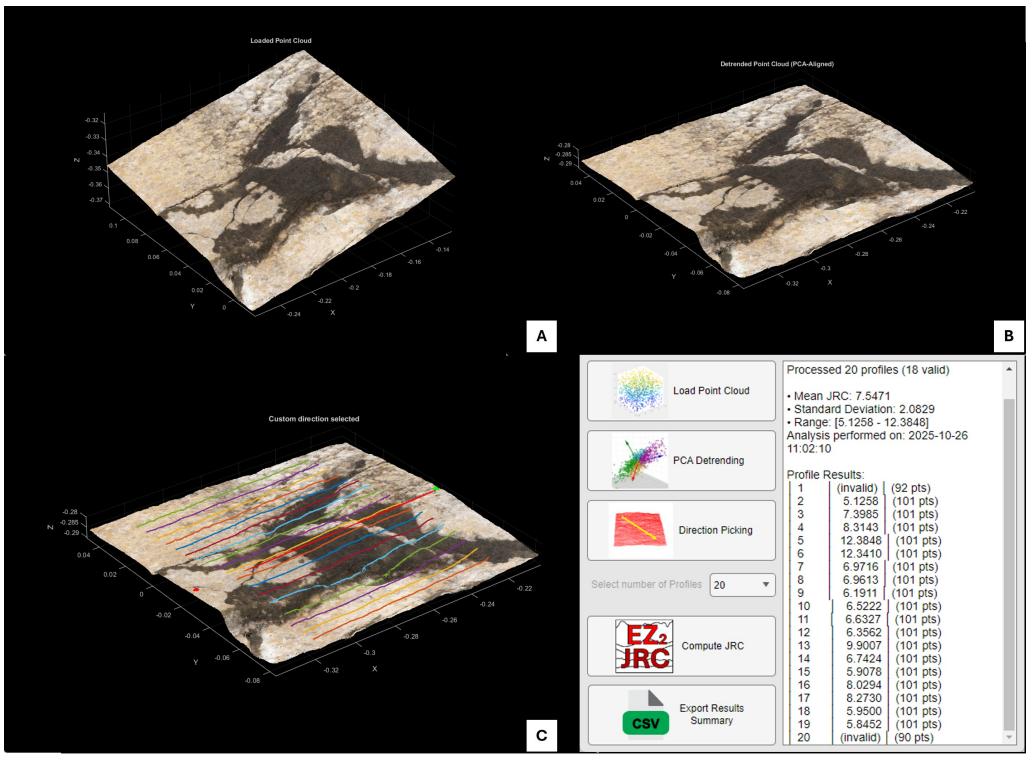


Figure 110: Example of the EZ$_2$JRC workflow applied to a real rock surface model. Results of Sample 1. A: Loaded point cloud; B: Detrended point cloud after PCA alignment; C: Custom direction selected for profile extraction.

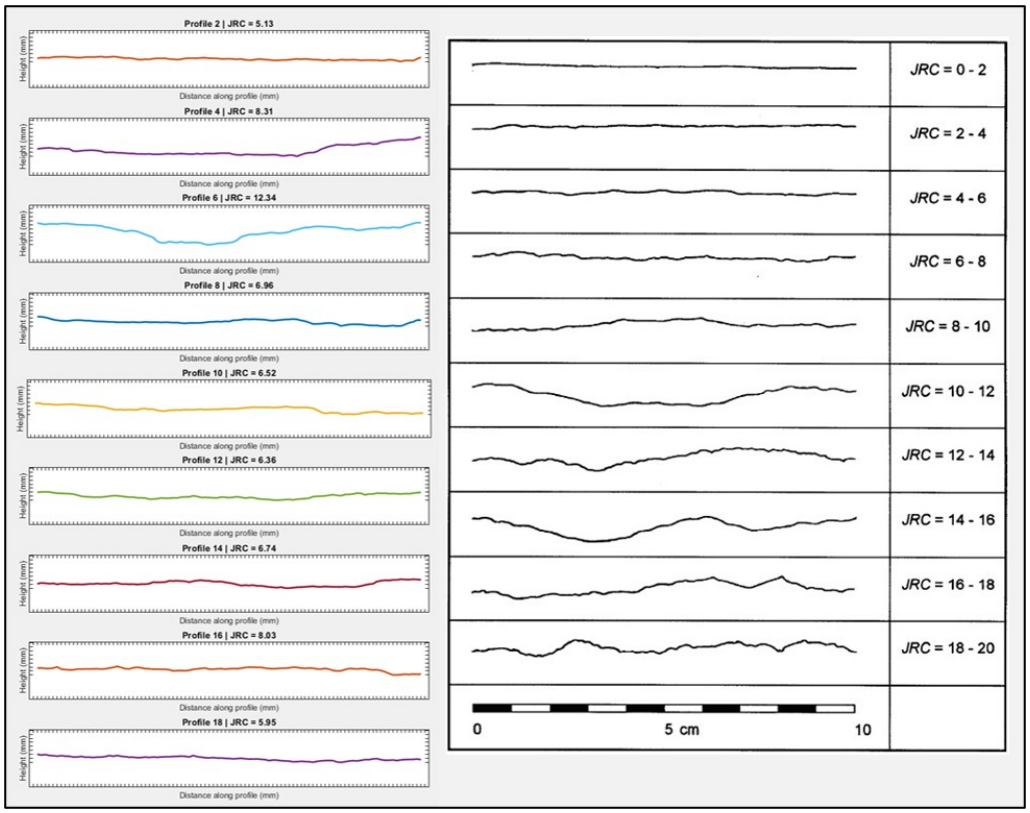


Figure 111: Example profiles from Sample 1 extracted to show the comparison with Barton standard profiles chart.

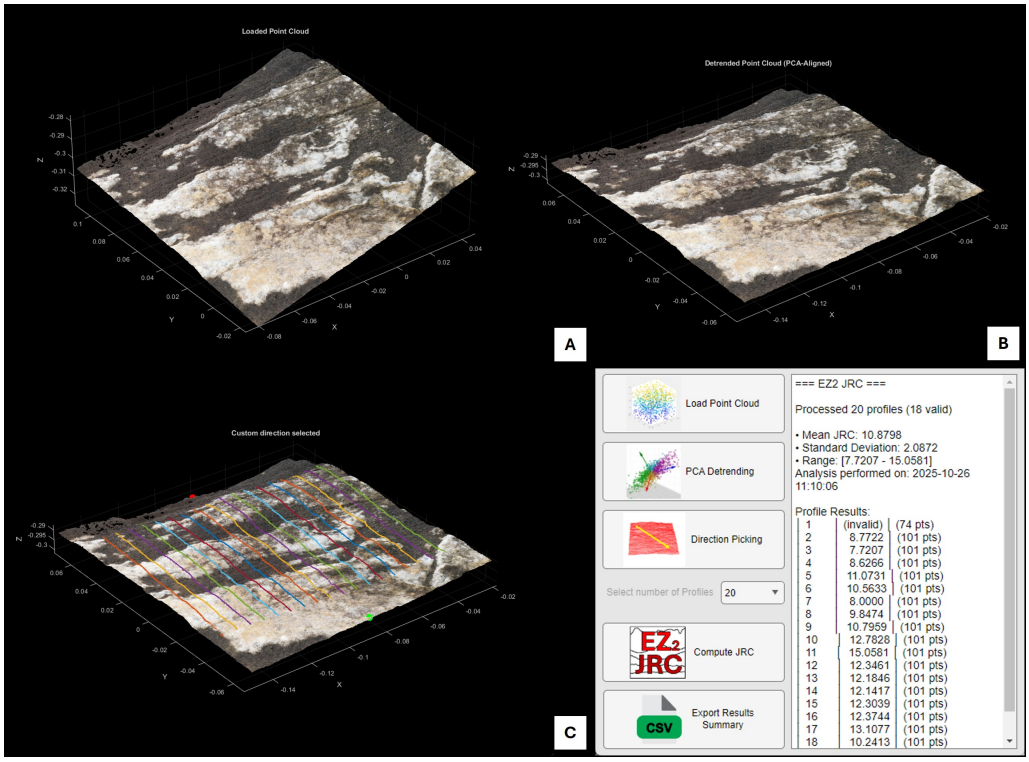


Figure 112: Example of the EZ$_2$JRC workflow applied to a real rock surface model. Results of Sample 2. A: Loaded point cloud; B: Detrended point cloud after PCA alignment; C: Custom direction selected for profile extraction.

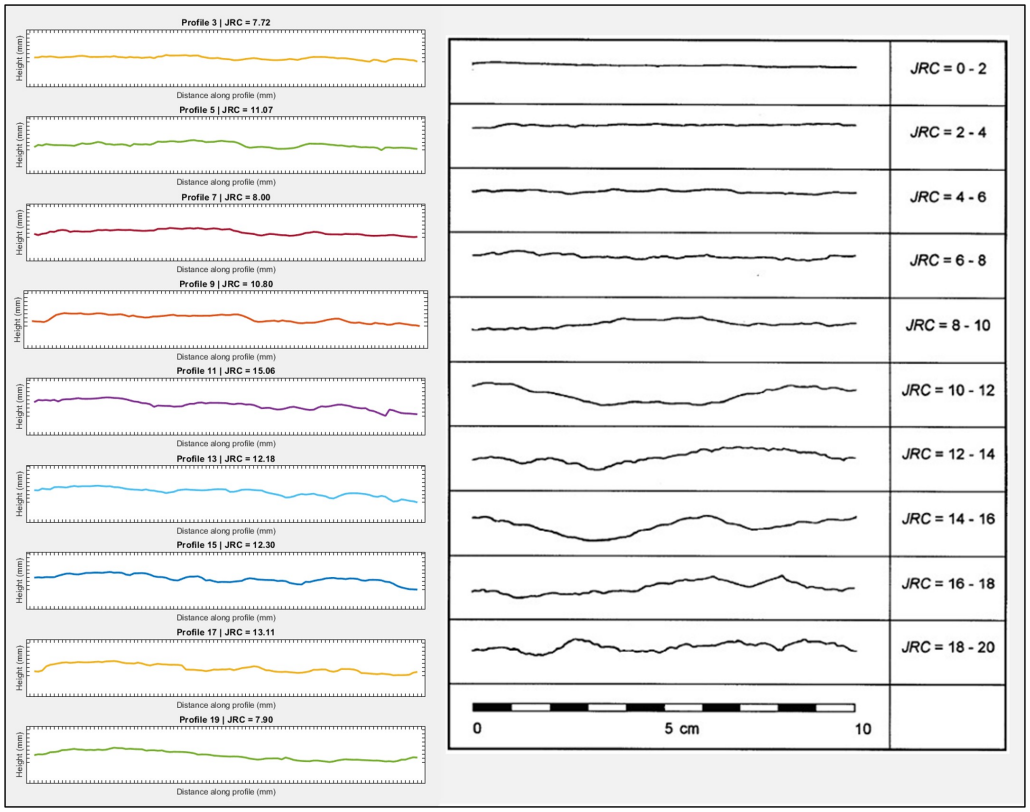


Figure 113: Example profiles from Sample 2 extracted to show the comparison with Barton standard profiles chart.

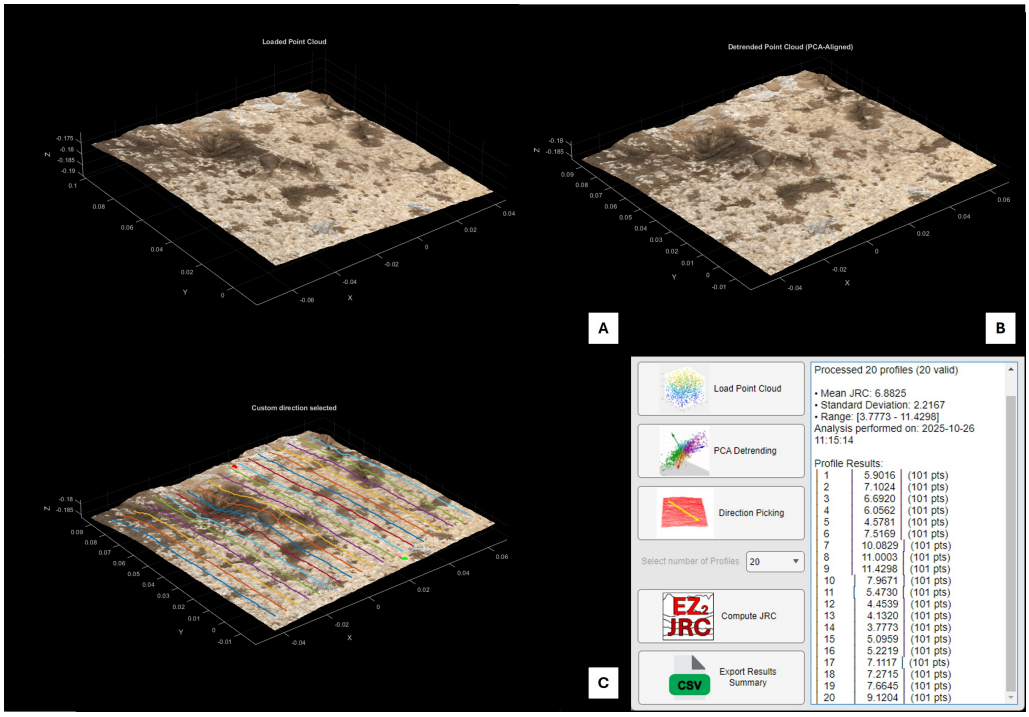


Figure 114: Example of the EZ$_2$JRC workflow applied to a real rock surface model. Results of Sample 3. A: Loaded point cloud; B: Detrended point cloud after PCA alignment; C: Custom direction selected for profile extraction.

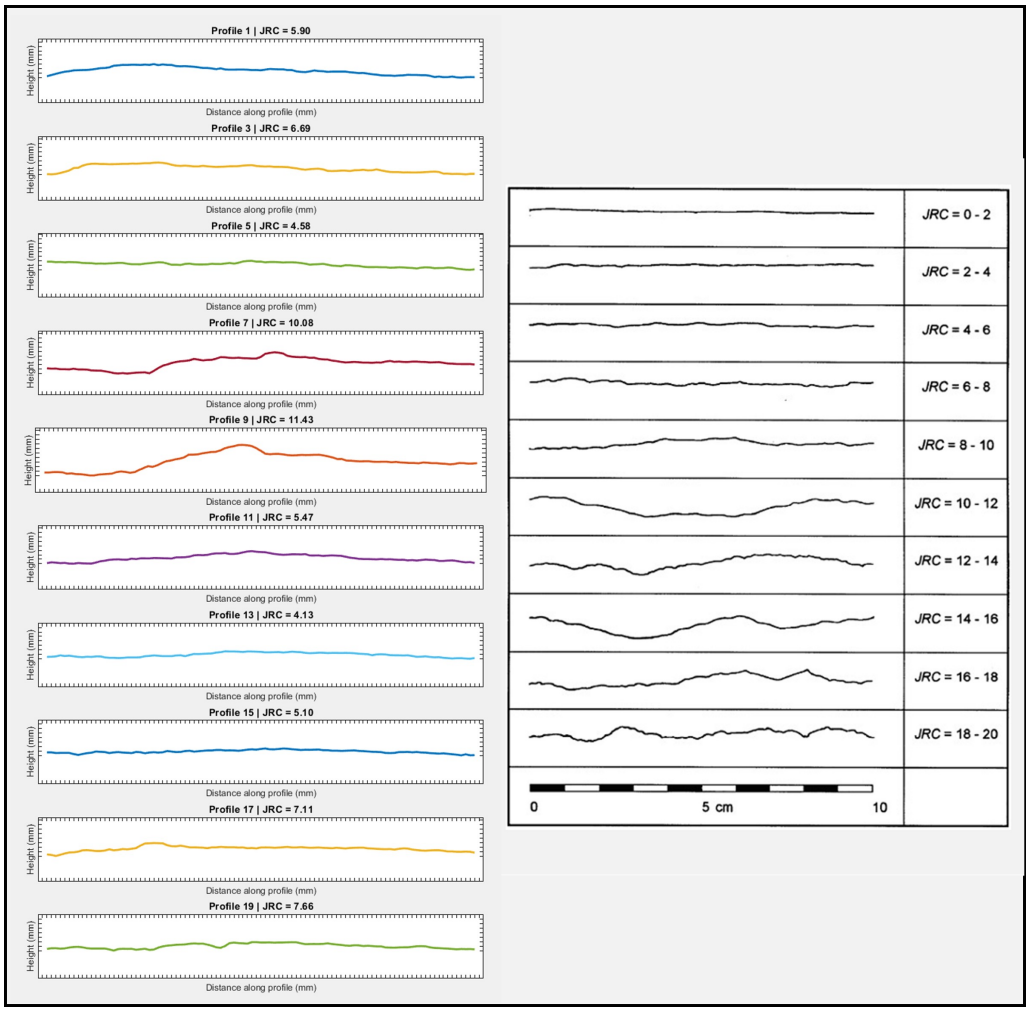


Figure 115: Example profiles from Sample 3 extracted to show the comparison with Barton standard profiles chart.

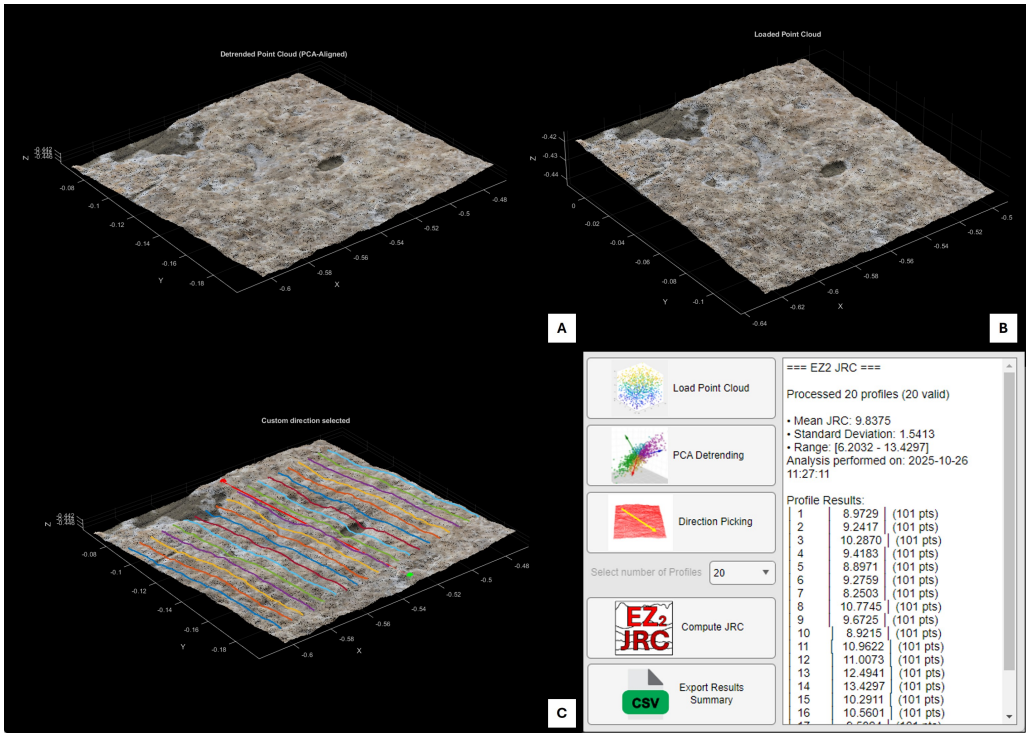


Figure 116: Example of the EZ$_2$JRC workflow applied to a real rock surface model. Results of Sample 4. A: Loaded point cloud; B: Detrended point cloud after PCA alignment; C: Custom direction selected for profile extraction.

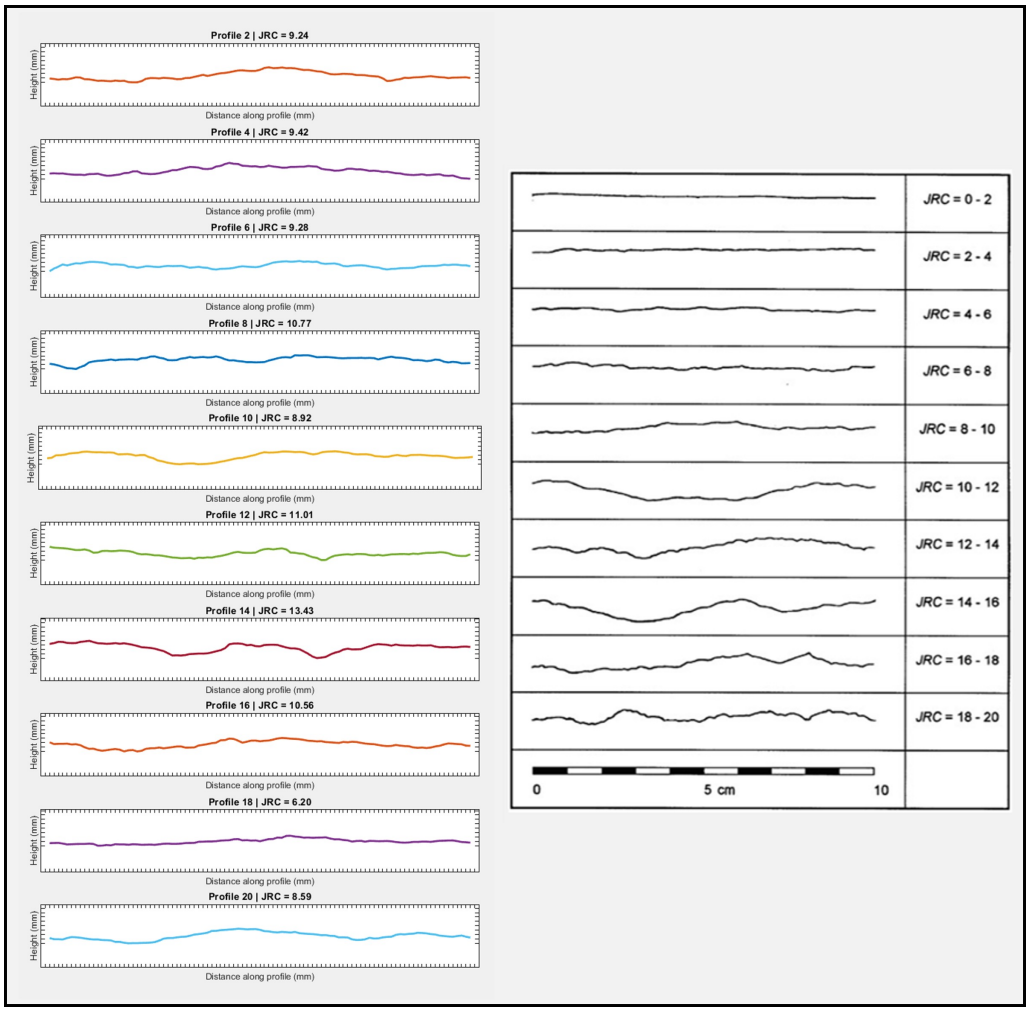


Figure 117: Example profiles from Sample 4 extracted to show the comparison with Barton standard profiles chart.

6

CASE STUDIES

The methodology described in this work was applied to case studies involving historic buildings located in the historic center of Florence. The case studies were selected based on operational requirements (e.g., permission from site managers to conduct analyses, accessibility of the work areas) and the lithological and morphological characteristics of the architectural elements under investigation. The selected case studies are:

- Palazzo Pitti
- Palazzo Medici Riccardi
- Palazzo Zuccari

The different case studies were analyzed with distinct objectives: some were selected for a full characterization of the architectural elements (Palazzo Pitti, Palazzo Medici Riccardi), while others involved partial application of the methodology, for example, volume estimation and calculation of stabilization forces (Palazzo Zuccari, Palazzo Medici Riccardi), or testing the applicability of the functions on various types of architectural elements. The locations of the case studies is reported in the map in Figure 118.

6.1 PALAZZO PITTI

The case study of Palazzo Pitti served as the "pilot" study for this work and has been object of diagnostic investigations by the LAM laboratory since 2020. These extensive studies are justified by the fact that the palace, both in terms of size and historical significance, stands as one of the city's iconic landmarks. It hosts five nationally significant museums and a national museum. From an architectural standpoint, the palace represents a case study in the evolution of Florentine palatial architecture across four



Figure 118: Map of the three buildings selected for methodological application: Palazzo Pitti, Palazzo Medici Riccardi, Palazzo Zuccari

centuries of construction and modification. Commissioned in 1457 by the banker Luca Pitti, the palace was designed by Luca Fancelli according to plans originally conceived by Filippo Brunelleschi [19] [49] . Financial difficulties forced the Pitti family to halt construction after completing only the central portion of the building. The palace's architectural development resumed in 1549 when Eleonora di Toledo, wife of Cosimo I de' Medici, purchased the property and initiated extensive renovation work under Bartolomeo Ammannati's direction [26]. In the early seventeenth century, Giulio Parigi added two wings to complete the central structure's three-floor configuration, while Pasquale Poccianti designed the vestibule and supervised completion of the two Rondò buildings in the 1840s [32]. The palace's main facade (Figure 119), measuring 36 meters in height and 170 meters in width, features three intersecting arched planes with rusticated ashlar masonry. The building materials reflect different construction phases: the original sixteenth-century sections utilized Pietraforte from quarries in the Boboli Gardens, while the later south and north wings incorporated stone from the Monteripaldi quarry [95].

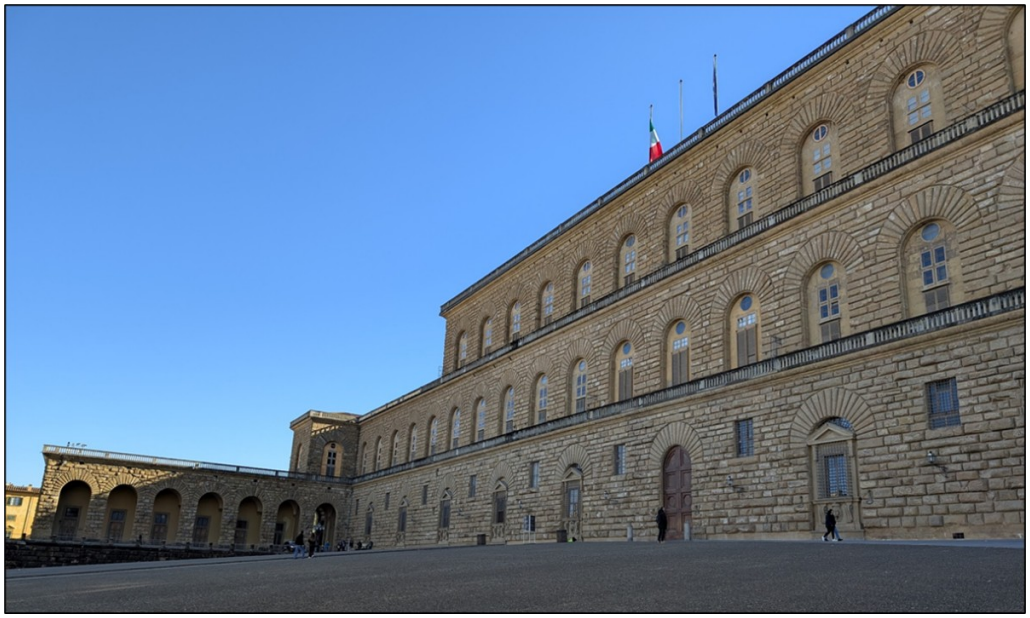


Figure 119: Palazzo Pitti main facade

In this study, a sector of the facade was selected as the test area. Two scans were performed in this zone: one using laser scanning technology with the Microgeo GeoSLAM device, a Mobile Laser Scanner (MLS) system, and the other using photogrammetric techniques (Figure 120).



Figure 120: Documentation of facade survey using MLS and photogrammetric techniques: left, operator with Microgeo GeoSLAM device (Mobile Laser Scanner); right, operator with tripod-mounted camera for photogrammetric acquisition.

The MLS scan was georeferenced using ground control points (Figure 121) and served as a general reference for the photogrammetric scans of selected sectors. The point cloud obtained from the laser scanner was also used to georeference the individual 3D point clouds of the selected blocks by matching homologous points.



Figure 121: Ground control point location for the MLS acquisition.

Photogrammetric scans were carried out on selected sectors accessible from ground level and processed using Agisoft Metashape Pro software (Figure 122).

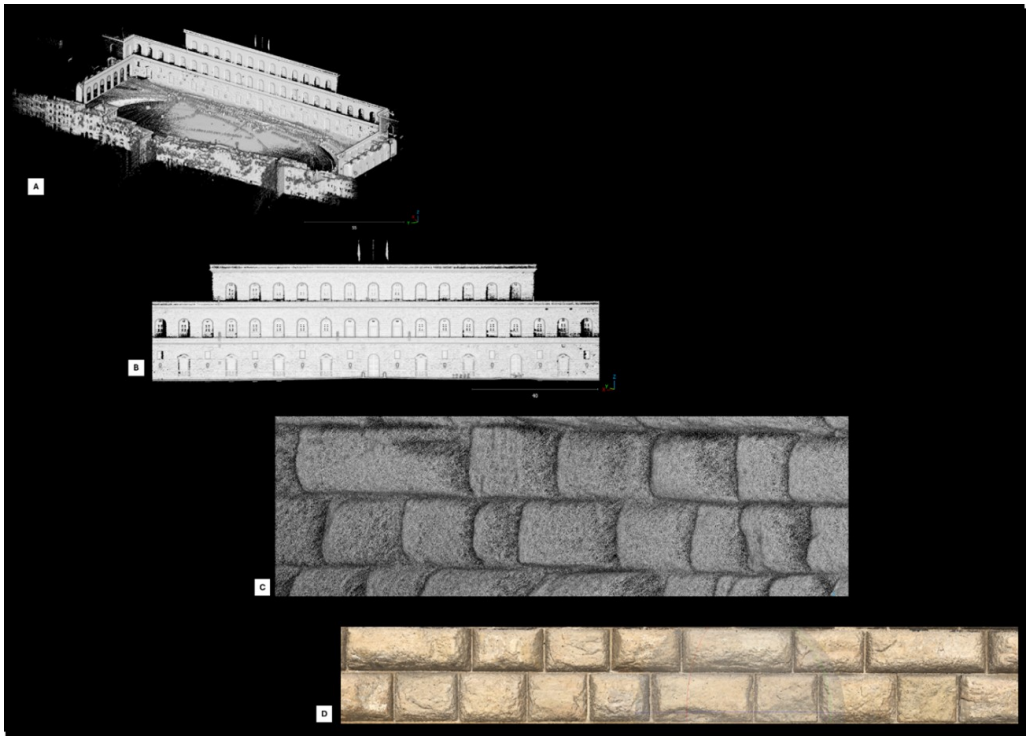


Figure 122: Outputs from the survey of ground-accessible facade sectors. A-C: progressive detail levels from Mobile Laser Scanner (MLS) acquisition using the Microgeo GeoSLAM device; D: high-density point cloud generated via photogrammetry using Agisoft Metashape Pro.

6.2 PALAZZO MEDICI RICCARDI

Palazzo Medici Riccardi is the prime example of early Renaissance civil architecture in Florence, and represents all the architectural principles that would influence subsequent palatial construction throughout the fifteenth and sixteenth centuries. Commissioned around 1444 by Cosimo the Elder, patriarch of the Medici family, the palace was designed by the architect Michelozzo di Bartolomeo and constructed on Via Larga (now Via Cavour), near the Church of San Lorenzo. The building, completed between 1444 and 1464, demonstrates a systematic approach to rustication across its three stories, progressing from heavy, rough stone on the ground floor to smooth ashlar masonry on the upper levels, culminating in a prominent cornice [17]. While the rusticated masonry and cornice had precedents in Roman architectural practice, the palace's overall composition created a distinctly Florentine architectural language that differed from any known Roman building. The structure served as the primary residence of the Medici family until 1540, when they relocated to the Palazzo Vecchio following political changes in the city's governance [92]. In 1659, the palace was sold to the Riccardi family, who expanded the structure and occupied it for approximately 150 years. The building underwent significant extension during the seventeenth century, with the Riccardi family lengthening the original block-like structure [3]. Pecchioni et al. [95] suggest that the Pietraforte employed in the facade construction, particularly during the initial building phase prior to the Riccardi family's expansion, was likely extracted from the Boboli quarries.

The Palace has been the subject of numerous investigation campaigns by the LAM laboratory starting from 2018, which covered the entire extension of the two facades of the Palace, that of Via Gori and that of Via Cavour. During the 2019-2021 investigation campaign, a total 3D scan of the palace was carried out through drone. The aerial photogrammetry activity was carried out using the Saturn Mini drone, exclusively designed, manufactured, and patented by DST-UNIFI. This 3D model (Figure 124) was used to investigate a portion of rusticated blocks of the facade, which had been reported as being in critical conservation conditions during the 2019-2021 investigation campaign.

In addition to the facade blocks, other various architectural elements of the palace were analyzed such as dentils of the first level cornice (Figure 125) and portions of the summit cornice (Figure 126).



Figure 123: Palazzo Medici Riccardi main facade

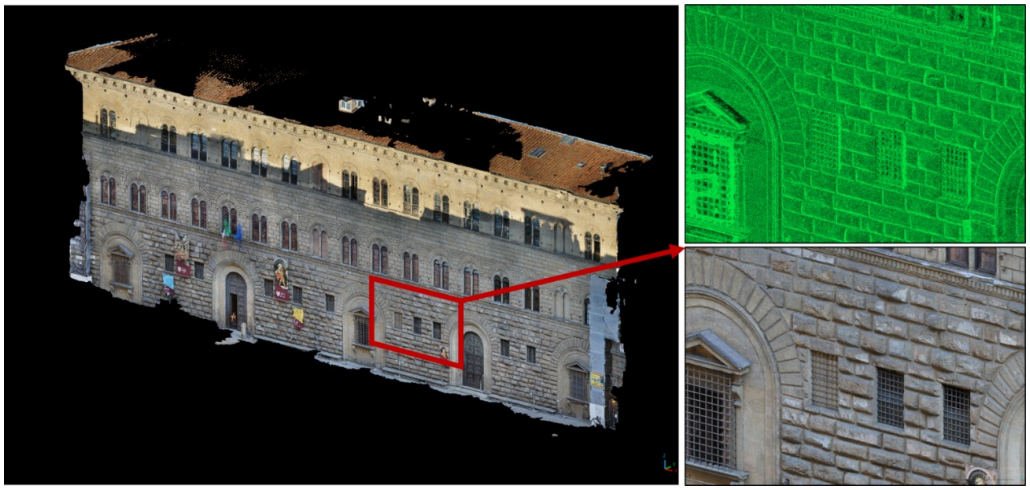


Figure 124: Outputs from the 2019–2021 investigation campaign conducted by LAM laboratory using the Saturn Mini drone (DST-UNIFI): left, full 3D model of the palace facade along Via Cavour; right, detailed view of the portion of rusticated blocks studied in this research

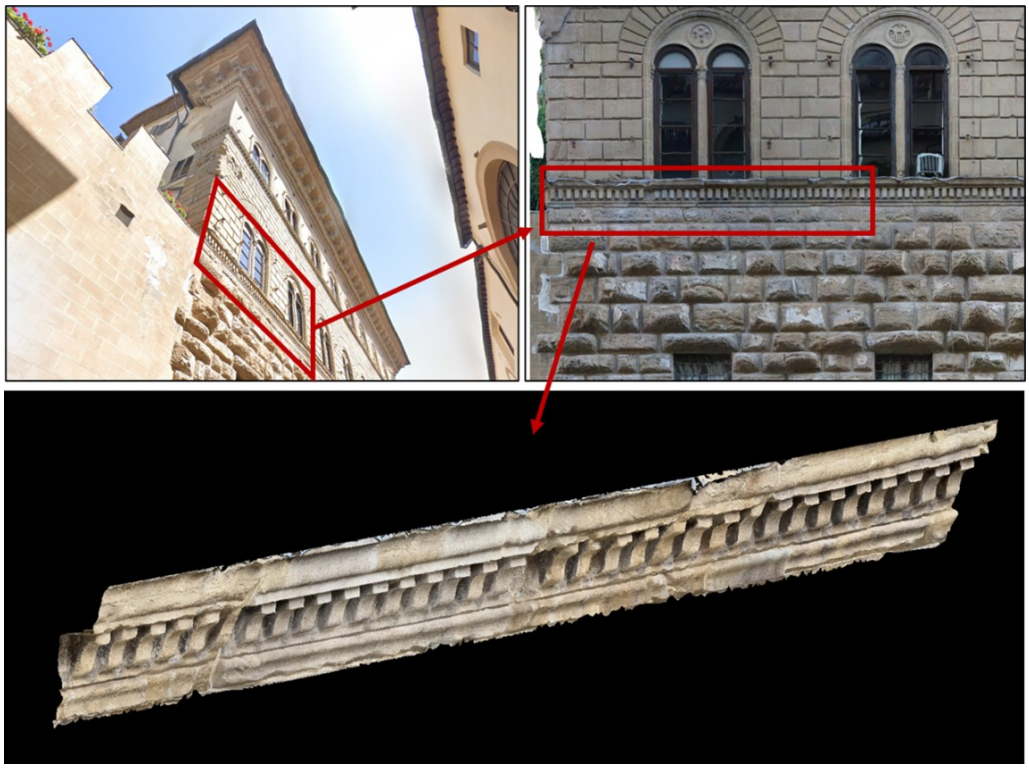


Figure 125: Dentils of the first level cornice of Palazzo Medici Riccardi along Via Gori

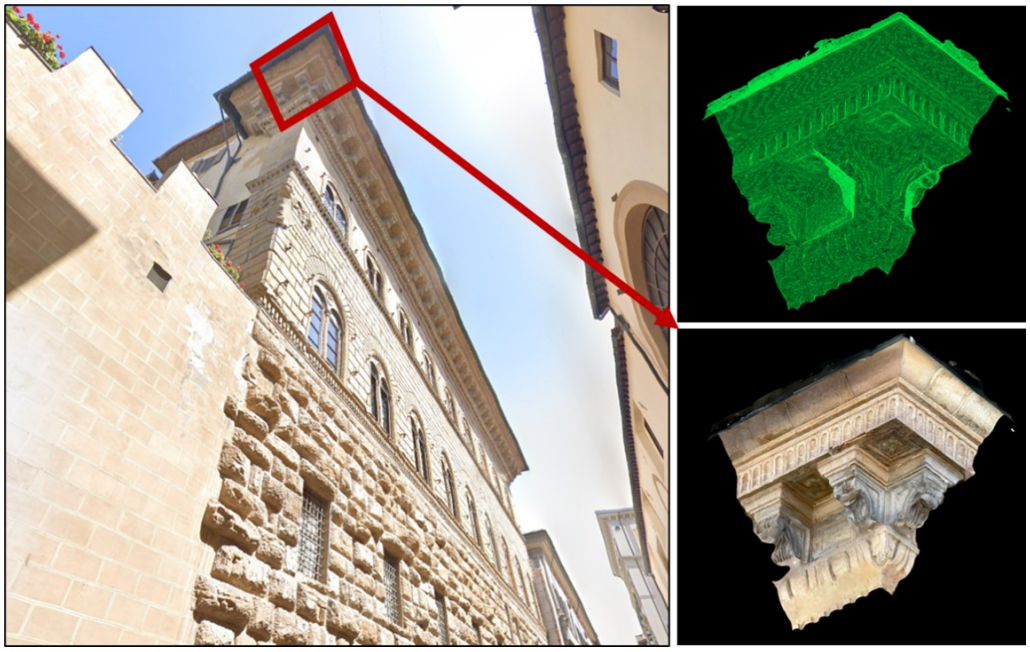


Figure 126: Summit cornice of Palazzo Medici Riccardi along via Gori and Via Ginori

6.3 PALAZZO ZUCCARI

Palazzo Zuccari represents a rare example of mannerist architecture in the late 500's Florence. It was commissioned by the painter Federico Zuccari in 1577 following his acquisition of Andrea del Sarto's former residence on via San Sebastiano. The building was constructed as a purpose-built studio on via del Mandorlo, replacing earlier modest structures including del Sarto's original workshop [62] [139]. The facade (Figure 127), designed ex novo as Zuccari's first architectural work, functioned as a theoretical manifesto of the central themes of sixteenth-century aesthetics including the relationship between art and nature, the hierarchy of the arts, and the social position of the artist [2] [63]. The building's three-story elevation uses an experimental rustication system that departs from the florentine conventions of the palaces presented earlier (Palazzo Pitti, Palazzo Medici Riccardi) reducing rough stone elements to fragments applied against a smooth ground and integrated in a geometric framework of smooth parts [115]. The building materials consists primarily of bigia stone, a locally sourced argillaceous sandstone, but also incorporates an unusual

combination of materials for Florence, like exposed brick in the upper section.



Figure 127: Palazzo Zuccari facade

The palace was the subject of an important restoration project completed in 2023 in which the LAM Laboratory was involved in the diagnostic phase, which included numerous investigations conducted with various techniques. Among these, 3D scanning with photogrammetry of the main projecting element of the facade, the stone coat of arms placed above the entrance portal, was also integrated (Figure 128).

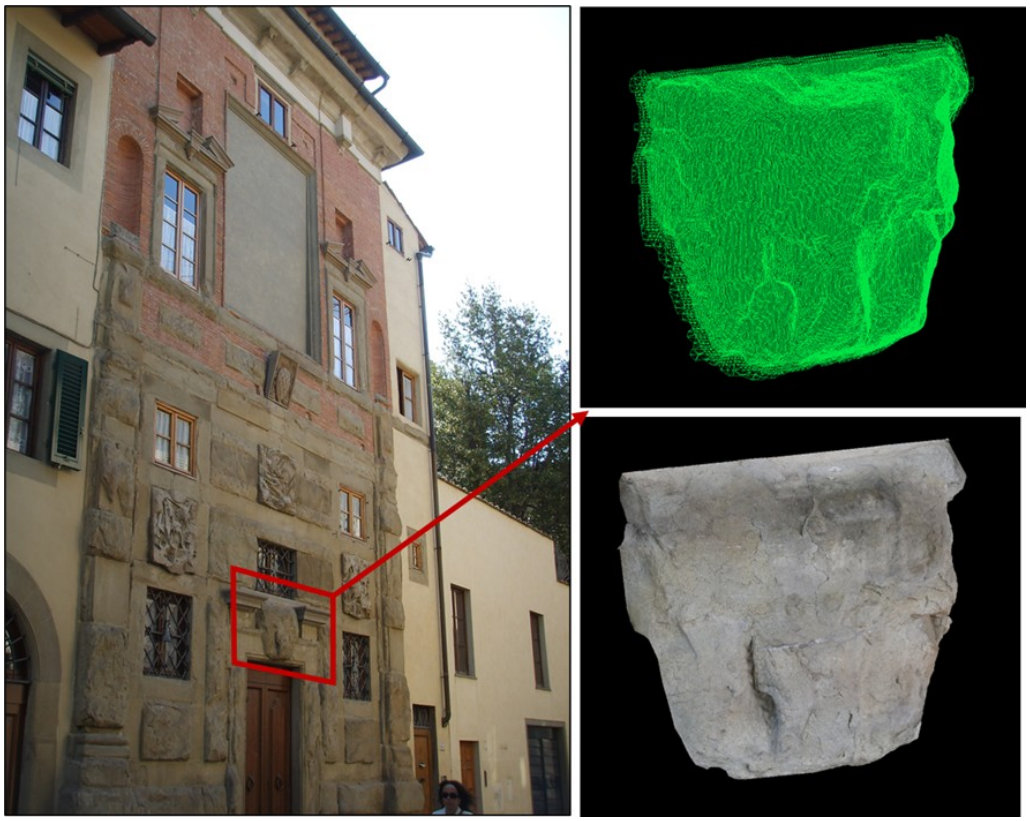


Figure 128: Stone coat of arms on the facade of Palazzo Zuccari

7

RESULTS AND DISCUSSION

The results are structured to provide both quantitative statistical summaries and qualitative interpretative discussions of representative examples. Individual rusticated blocks are documented in detail in Appendix 9, while this chapter focuses on patterns, trends, and cases that serve as an example of the applicability and limitations of the RoDiAn approach.

7.1 PALAZZO PITTI

Palazzo Pitti The RoDiAn workflow was applied to the three test areas is visible in Figure 129. The results of individual rusticated blocks are reported in Appendix 9. The graphical data sheets corresponding to each block display the direct output generated by RoDiAn's kinematic susceptibility index (KSI) computation functions, where each discontinuity plane is coded according to the scale embedded in the software interface (Figure 37). Additionally, both the chapter and the appendix include the results of the dynamic analysis for the most susceptible plane or wedge within each block. It should be noted that, for the purposes of this work, the graphical outputs have been constrained to a two-dimensional format. However, these are inherently three-dimensional datasets, and their interpretation is more effectively conducted within the RoDiAn software environment, where their full 3D interactivity is preserved. The parameters used for the kinematic and dynamic analysis are:

- $\varphi = 25^{\circ}$
- JRC $= 12$
- JCS $= 50$ MPa
- $\rho = 2700$ kg/m^3

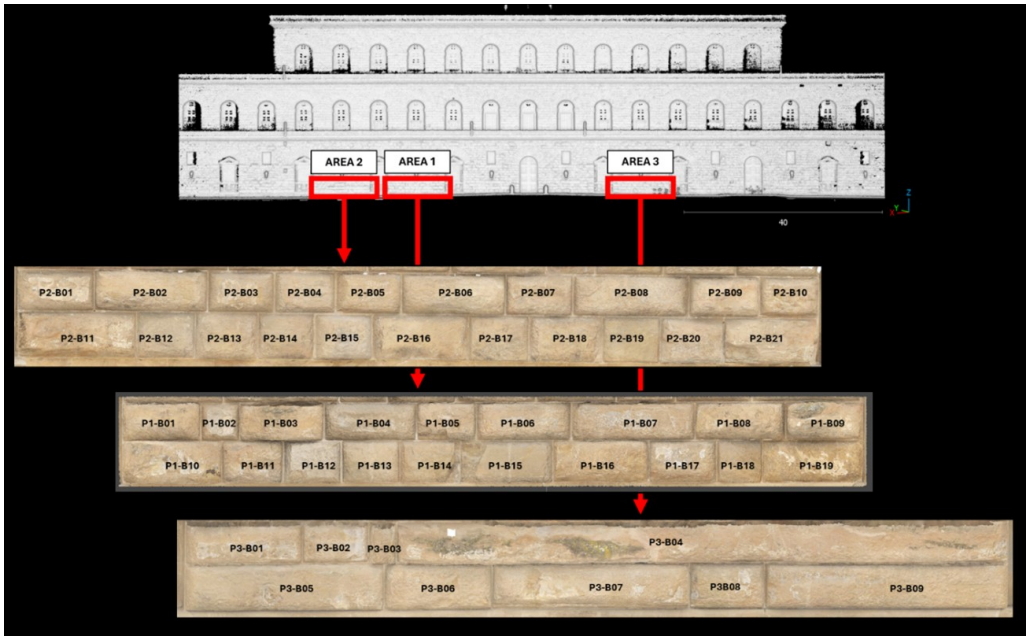


Figure 129: Test areas on Palazzo Pitti

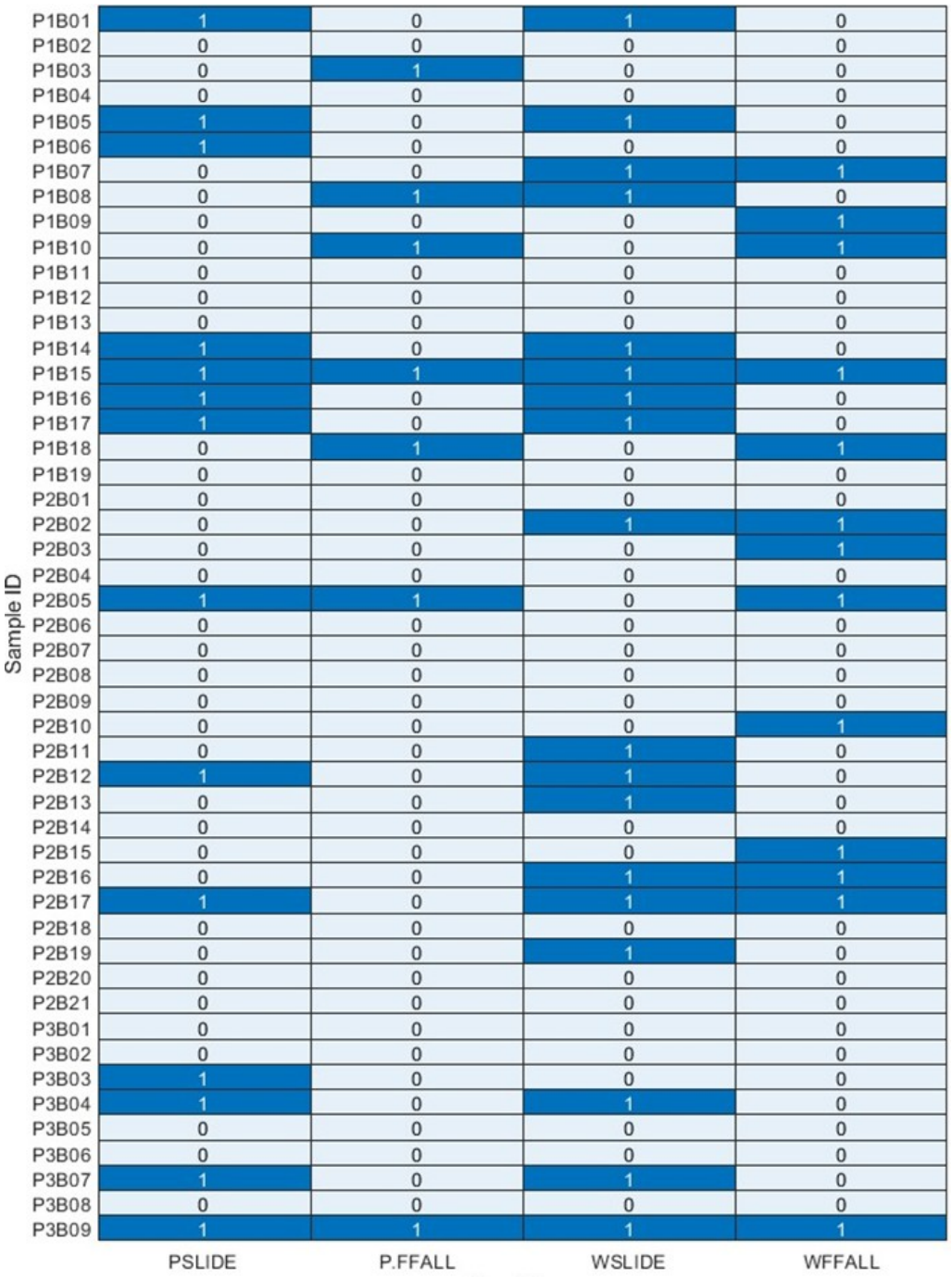
Figure 130 provides a general graphical summary of the results obtained for the individual blocks, highlighting the type of kinematic mechanism identified in each block.

As shown by the results in Figure 130, the majority of blocks (56%) are affected by potential kinematic mechanisms. Figure 131 reports the number of mechanisms identified for each individual sample. It is evident that, in cases where any possible failure is present, the most common scenario involves the simultaneous occurrence of multiple failure modes, typically Planar Slide and Wedge Slide.

Figure 132 illustrates the distribution of the different kinematic mechanisms: the most common is Wedge Sliding, followed by Planar Slide.

7.1.1 *Test Area 1*

Figures 133, 134, and 135 show summary maps of the results obtained for the calculation of the Kinematic Susceptibility Index (KSI): for planar sliding (Figure 133), wedge sliding (Figure 134), and the combined assessment of both mechanisms (Figure 135).



Sample ID	PSLIDE	P.FFALL	WSLIDE	WFFALL
P1B01	1	0	1	0
P1B02	0	0	0	0
P1B03	0	1	0	0
P1B04	0	0	0	0
P1B05	1	0	1	0
P1B06	1	0	0	0
P1B07	0	0	1	1
P1B08	0	1	1	0
P1B09	0	0	0	1
P1B10	0	1	0	1
P1B11	0	0	0	0
P1B12	0	0	0	0
P1B13	0	0	0	0
P1B14	1	0	1	0
P1B15	1	1	1	1
P1B16	1	0	1	0
P1B17	1	0	1	0
P1B18	0	1	0	1
P1B19	0	0	0	0
P2B01	0	0	0	0
P2B02	0	0	1	1
P2B03	0	0	0	1
P2B04	0	0	0	0
P2B05	1	1	0	1
P2B06	0	0	0	0
P2B07	0	0	0	0
P2B08	0	0	0	0
P2B09	0	0	0	0
P2B10	0	0	0	1
P2B11	0	0	1	0
P2B12	1	0	1	0
P2B13	0	0	1	0
P2B14	0	0	0	0
P2B15	0	0	0	1
P2B16	0	0	1	1
P2B17	1	0	1	1
P2B18	0	0	0	0
P2B19	0	0	1	0
P2B20	0	0	0	0
P2B21	0	0	0	0
P3B01	0	0	0	0
P3B02	0	0	0	0
P3B03	1	0	0	0
P3B04	1	0	1	0
P3B05	0	0	0	0
P3B06	0	0	0	0
P3B07	1	0	1	0
P3B08	0	0	0	0
P3B09	1	1	1	1

Figure 130: Summary of kinematic mechanisms identified in individual blocks at Palazzo Pitti. Each row corresponds to a sample ID, with binary indicators for four kinematic mechanisms: Planar slide (PSLIDE), Planar FreeFall (P.FFALL), Wedge slide (WSLIDE), Wede FreeFall (W.FFALL). Cells marked in blue denote presence of the respective mechanism.

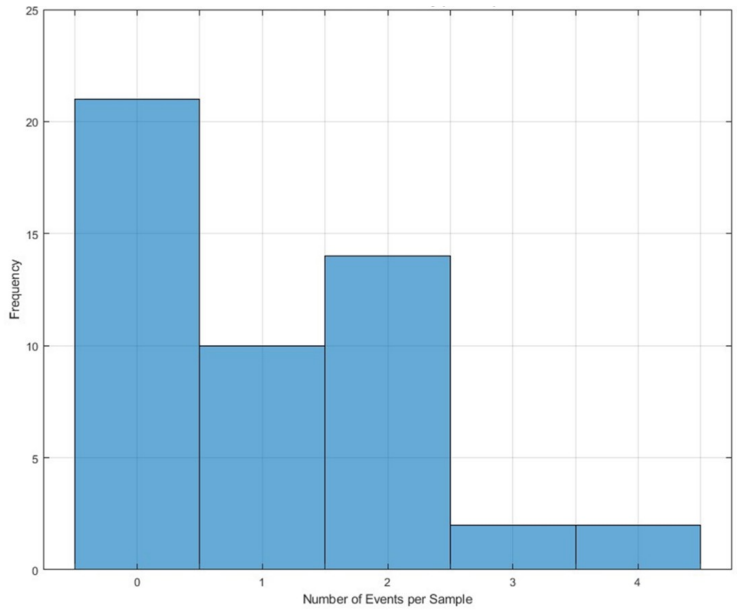


Figure 131: Distribution of kinematic mechanisms per sample at Palazzo Pitti.

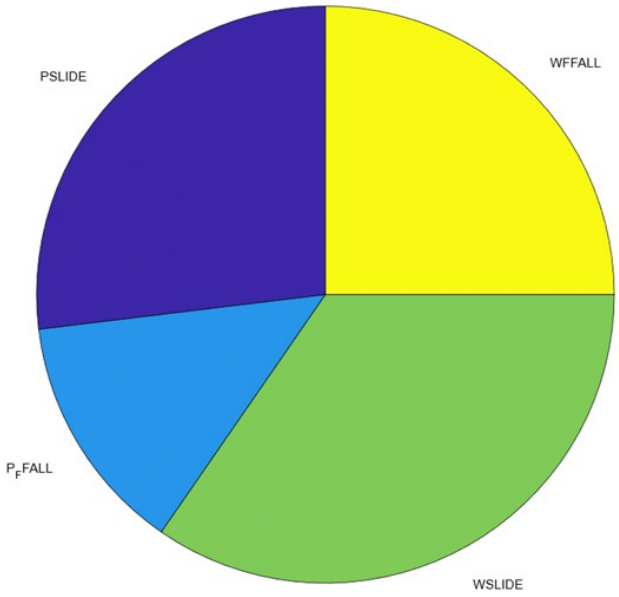


Figure 132: Pie chart illustrating the relative frequency of failure modes at Palazzo Pitti: Planar slide (PSLIDE), Planar FreeFall (P.FFALL), Wedge slide (WSLIDE), Wede FreeFall (W.FFALL)



Figure 133: Planar susceptibility map on Area Test 1 - Palazzo Pitti. The blocks are color coded using RoDiAn KSI legend (Figure 37)



Figure 134: Wedge susceptibility map on Area Test 1 - Palazzo Pitti. The blocks are color coded using RoDiAn KSI legend (Figure 37)

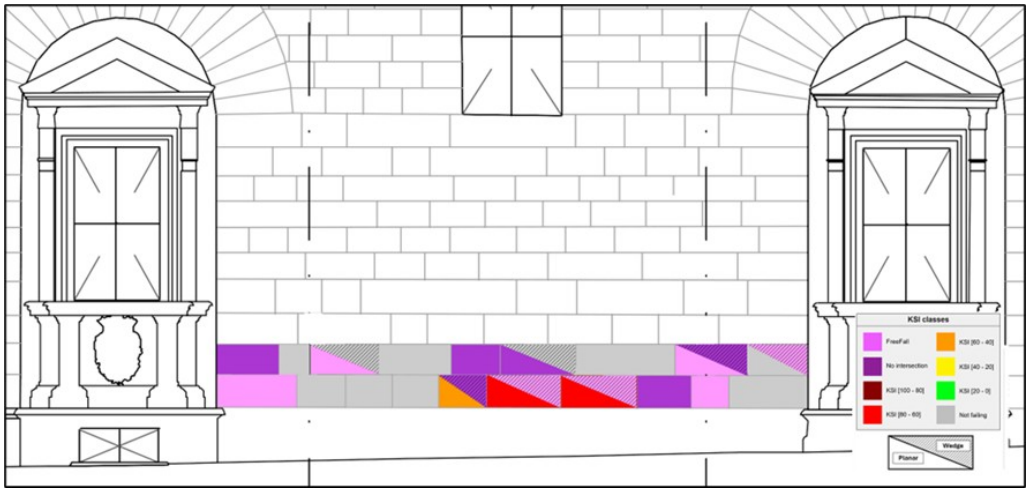


Figure 135: Planar (bottom left of each block) and Wedge (top right of each block) susceptibility map on Area Test 1 - Palazzo Pitti. The blocks are color coded using RoDiAn KSI legend (Figure 37)

Figure 136 presents a summary map of the results, indicating the total number of discontinuities that exhibit susceptibility to any of the analyzed kinematic mechanisms.

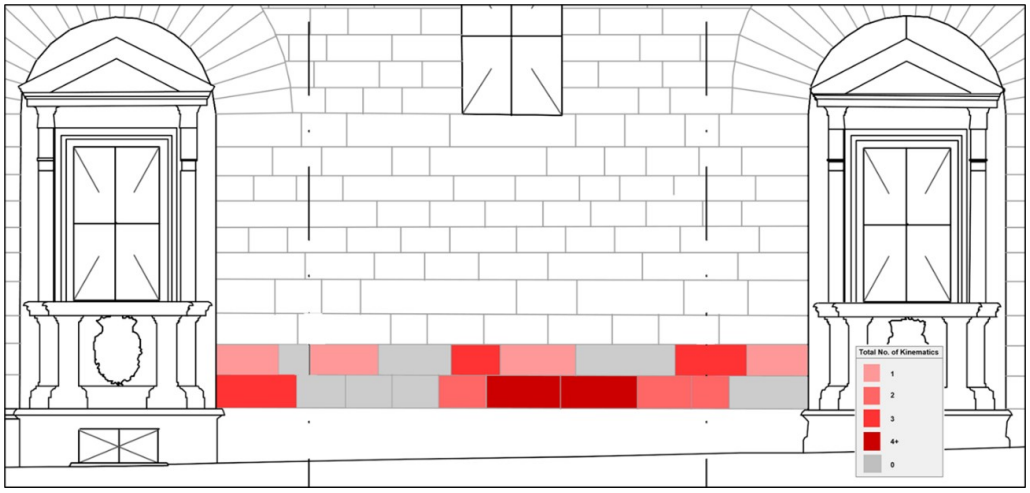


Figure 136: Map of total number of discontinuities that exhibit susceptibility to any kinematic mechanism on Area Test 1 - Palazzo Pitti

In the Test Area 1, all possible scenarios were identified, from blocks with no kinematic mechanisms to those susceptible to all four types. Cases of null susceptibility can be grouped into two distinct categories:

- Absence of visible discontinuities, e.g. P1B2 (Figure 137)
- Presence of discontinuities whose orientation does not activate kinematic mechanisms due to their dip or dip direction, e.g. P1B13 (Figure 138)

The second category is more common when the dip direction of the discontinuity is perpendicular to the facade. In such cases, the geometry prevents sliding, even if the dip angle is much bigger than the friction angle limit. By contrast, when the dip direction aligns with a potential sliding path but the inclination remains below the friction angle, susceptibility is still considered null, though these instances are less frequent.

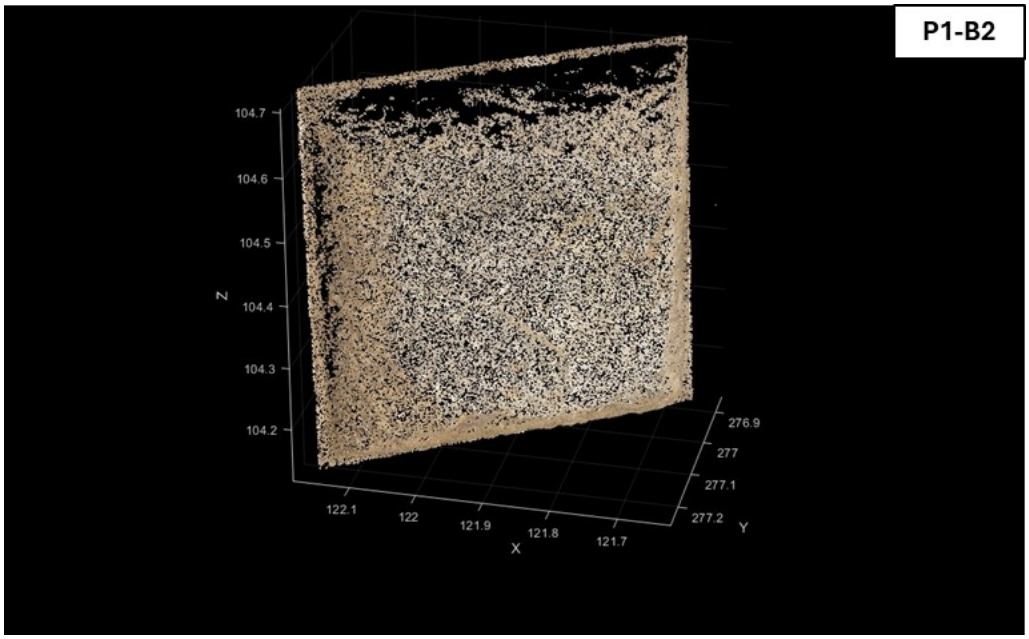


Figure 137: Block P1B2. Example of cases with null susceptibility due to the absence of visibile discontinuities.

There are instances in which a single kinematic mechanism is identified, as exemplified by Block P1B3 (Figure 139), which exhibits a potential planar free fall. In the cases where a free-fall kinematic is identified, the output of the dynamic analysis reports exclusively the residual driving forces, given that frictional resistance forces are null under free fall

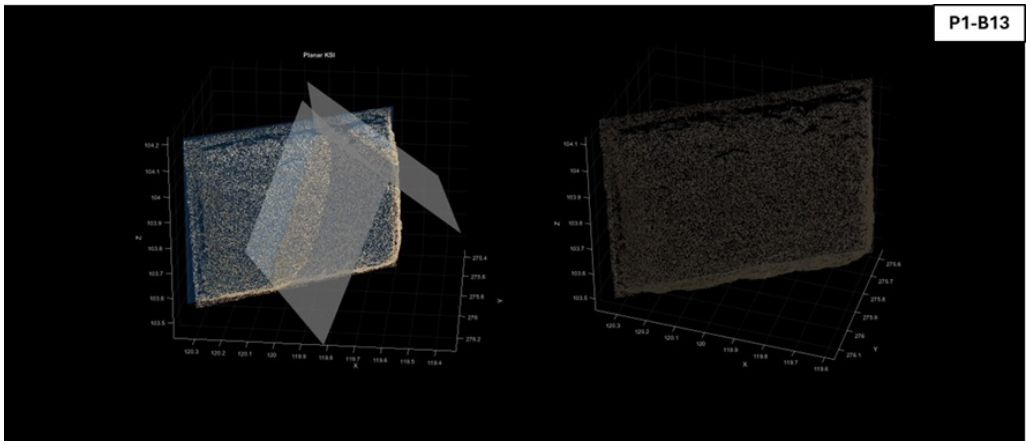


Figure 138: Block P1B13. Example of cases with discontinuities oriented in stable configurations

conditions. In free fall cases the residual driving forces correspond to the weight of the block.

There are also cases, such as block P1B5 (Figure 140), where two sliding mechanisms are present, like a planar and a wedge sliding. In this case, the results of the dynamic analysis show a value lower than 1 for the planar sliding scenario. As specified in paragraph 3.4, the only resisting force considered is friction, while the cohesion of the discontinuity infill is neglected. For the wedge sliding case observed in block P1B5, the safety factor is greater than 1, and the negative Residual Driving Forces indicate the excess of resisting forces.

Block P1B15 (Figure 141) is an example of a sample affected by all four identifiable kinematic mechanisms. The complete analysis of complex samples like this one, where multiple detachment scenarios are possible, is presented here in a reduced form, reporting the dynamic analysis of one mechanism per type (one planar and one wedge).

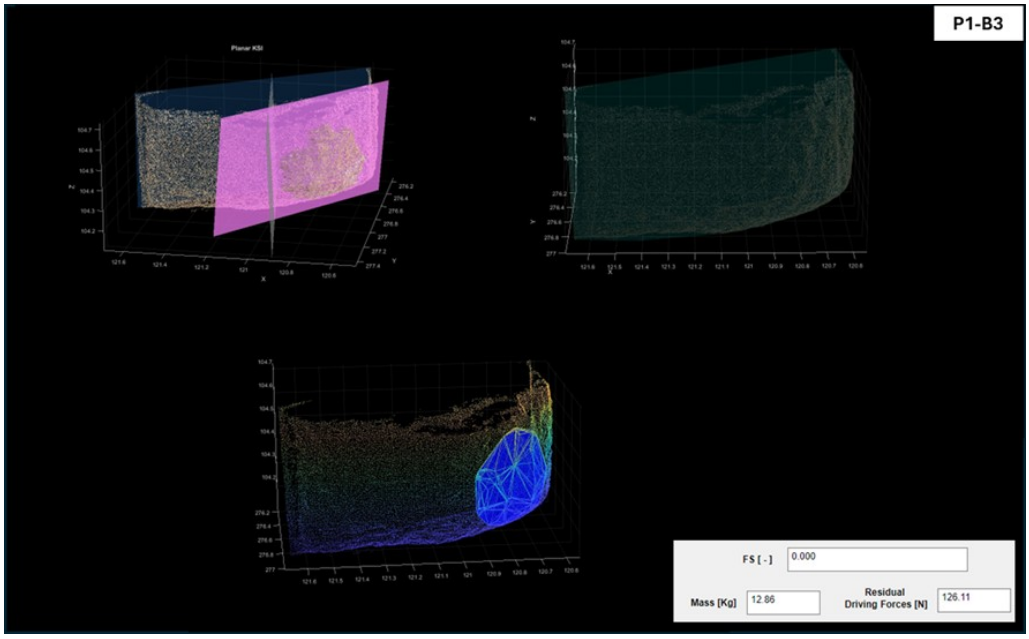


Figure 139: Block P1B3. Example of cases with free fall susceptibile discontinuities. Top left: planar susceptibilty; Top right: Wedge susceptibility; Bottom: dynamic analysis results.

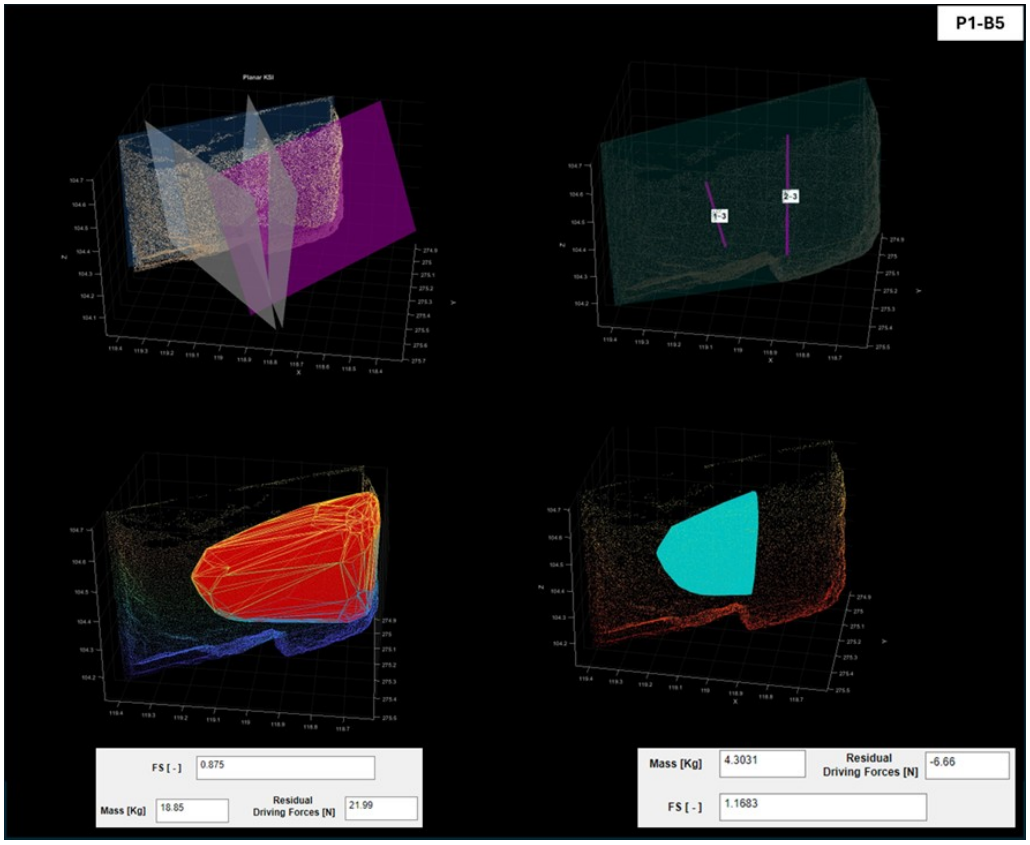


Figure 140: Block P1B5. Example of cases with multiple possible kinematic mechanisms. Top left: planar susceptibilty; Top right: Wedge susceptibility; Bottom: dynamic analysis results.

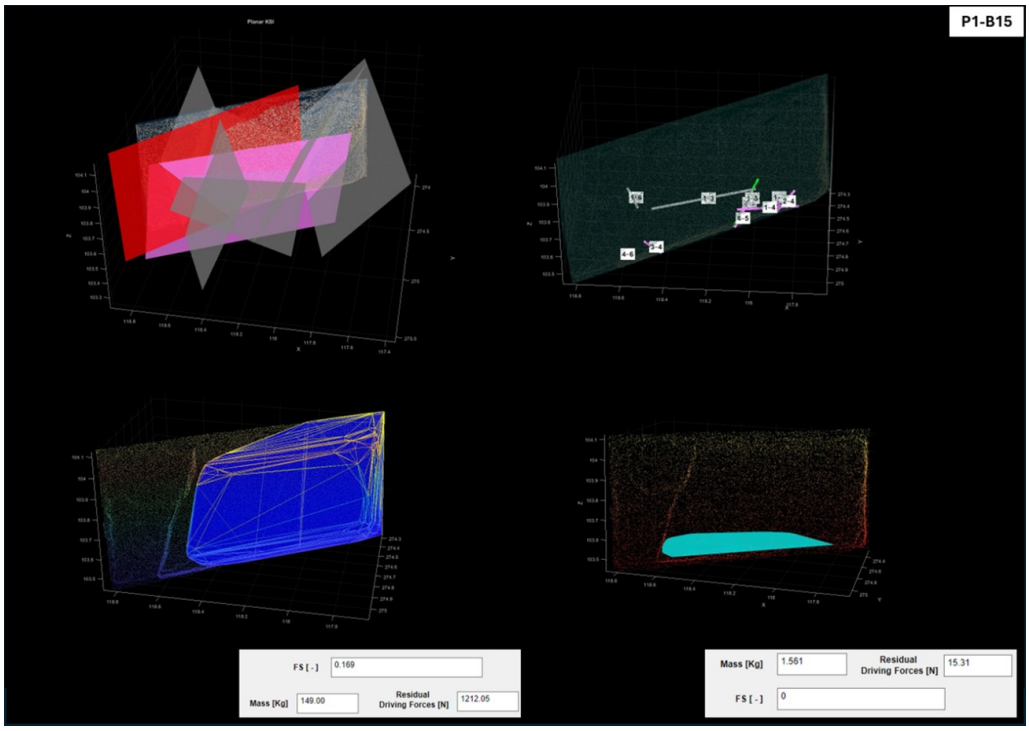


Figure 141: Block P1B15. Example of cases with all possible kinematic mechanisms identified. Top left: planar susceptibilty; Top right: Wedge susceptibility; Bottom: dynamic analysis results.

7.1.2 *Test Area 2*

Figures 142, 143, and 144 present summary maps of the results for the calculation of the Kinematic Susceptibility Index (KSI): for planar sliding (Figure 142), wedge sliding (Figure 143), and the combined assessment of both mechanisms (Figure 144).

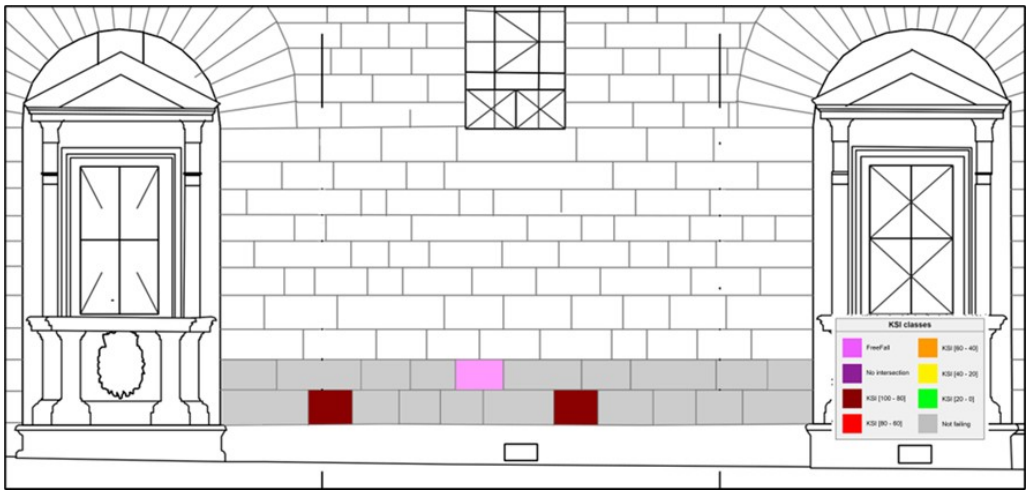


Figure 142: Planar susceptibility map on Area Test 2- Palazzo Pitti. The blocks are color coded using RoDiAn KSI legend (Figure 37)

Figure 145 presents a summary map of the results, indicating the total number of discontinuities that show susceptibility to any of the analyzed kinematic mechanisms.

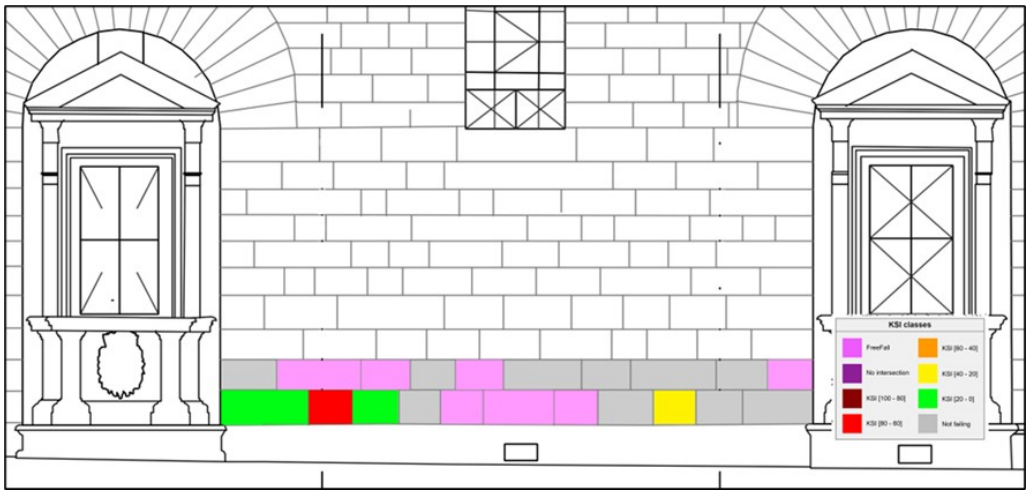


Figure 143: Wedge susceptibility map on Area Test 2- Palazzo Pitti. The blocks are color coded using RoDiAn KSI legend (Figure 37)

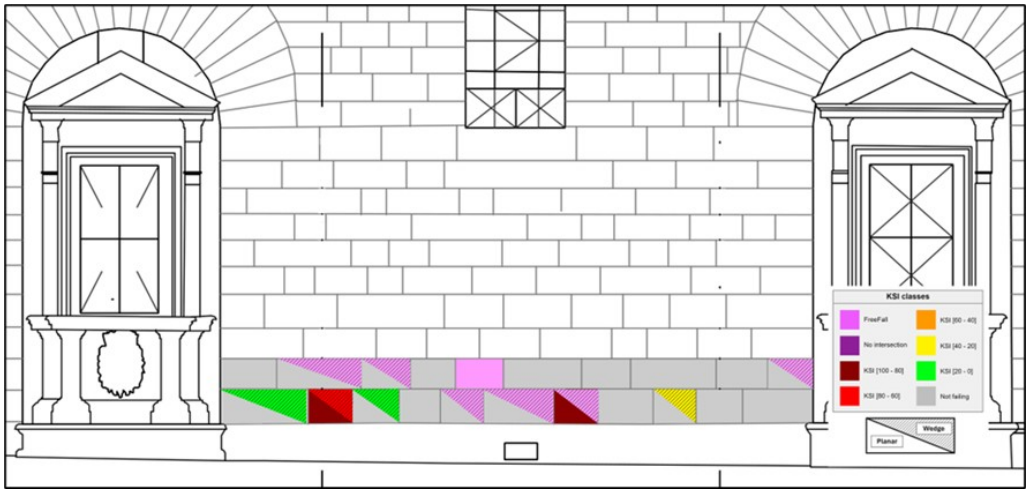


Figure 144: Planar (bottom left of each block) and Wedge (top right of each block) susceptibility map on Area Test 2- Palazzo Pitti. The blocks are color coded using RoDiAn KSI legend (Figure 37)

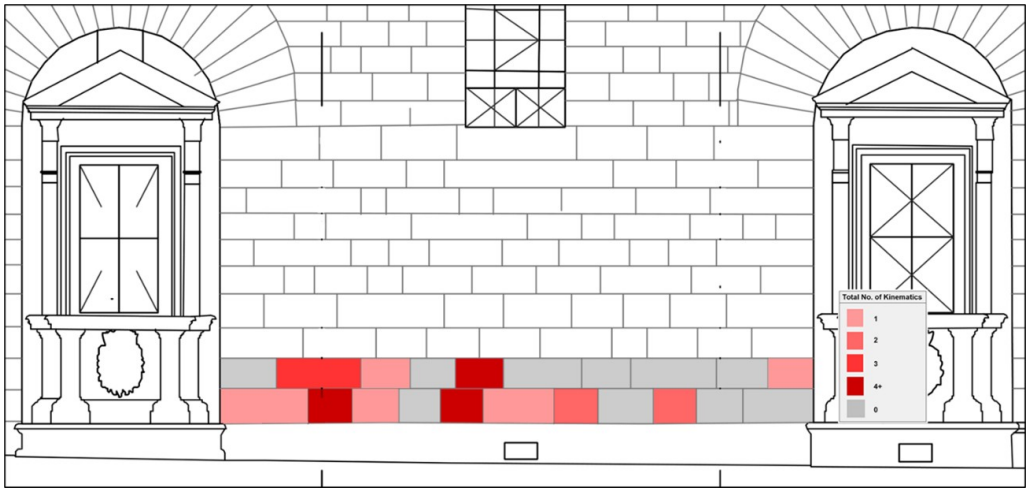


Figure 145: Map of total number of discontinuities that exhibit susceptibility to any kinematic mechanism on Area Test 2 - Palazzo Pitti

In Test Area 2, cases of planar and wedge sliding were identified in proportions that differ significantly from those observed in Area 1. Many blocks are affected exclusively by wedge sliding and not by planar sliding, indicating the presence of discontinuities that, individually, are not favorably oriented for sliding, but whose intersections form wedges with geometries that can fail. Among the cases with no potential kinematic mechanisms, we again observe blocks with no visible discontinuities (e.g., Block P2-B21, Figure 146). However, there are also examples of blocks that do not exhibit any possible failure mechanisms despite having numerous discontinuities, both planar, as seen in Area 1, and wedge-forming (e.g., Blocks P2-B04 and B14, Figures 147 and 148).

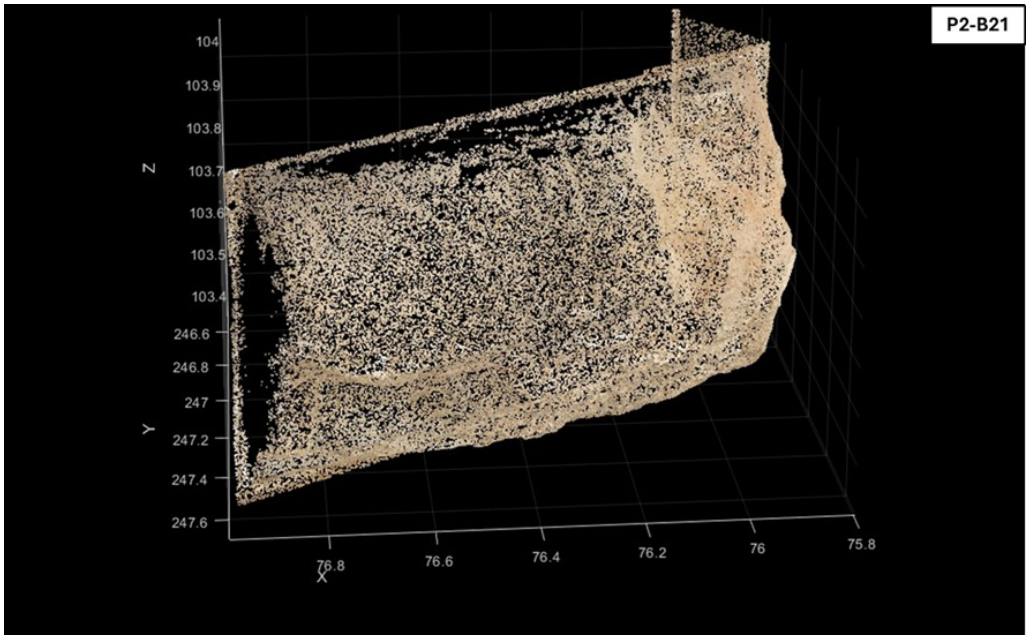


Figure 146: Block P2B21. Example of cases with no visibile discontinuities.

Several cases (8 blocks), show no possible planar sliding, but an high susceptibility to wedge sliding (e.g., blocks P2-B11 and B15, Figures 149 and 150). This scenario typically occurs in the presence of sub-vertical planes, with dip angles greater than 75° and dip directions of approximately ±90° relative to the facade. These planes, which are stable from a planar kinematic perspective, intersect to form wedges with steep sliding directions parallel to the facade, making them susceptible to detachment.

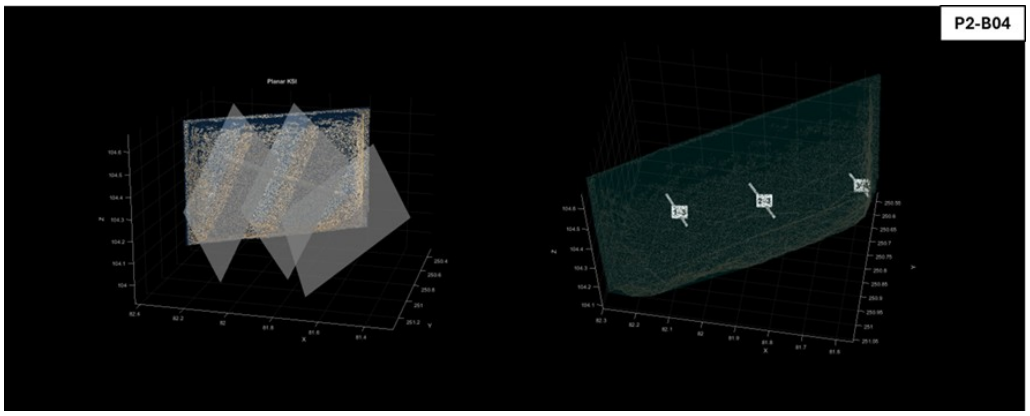


Figure 147: Block P2B04. Example of cases with discontinuities oriented in stable configurations that form stable wedges.

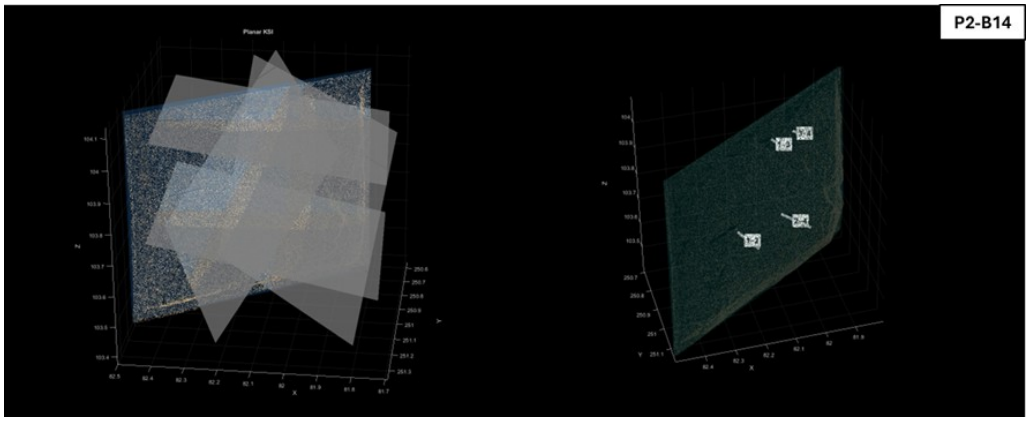


Figure 148: Block P2B14. Example of cases with discontinuities oriented in stable configurations that form stable wedges.

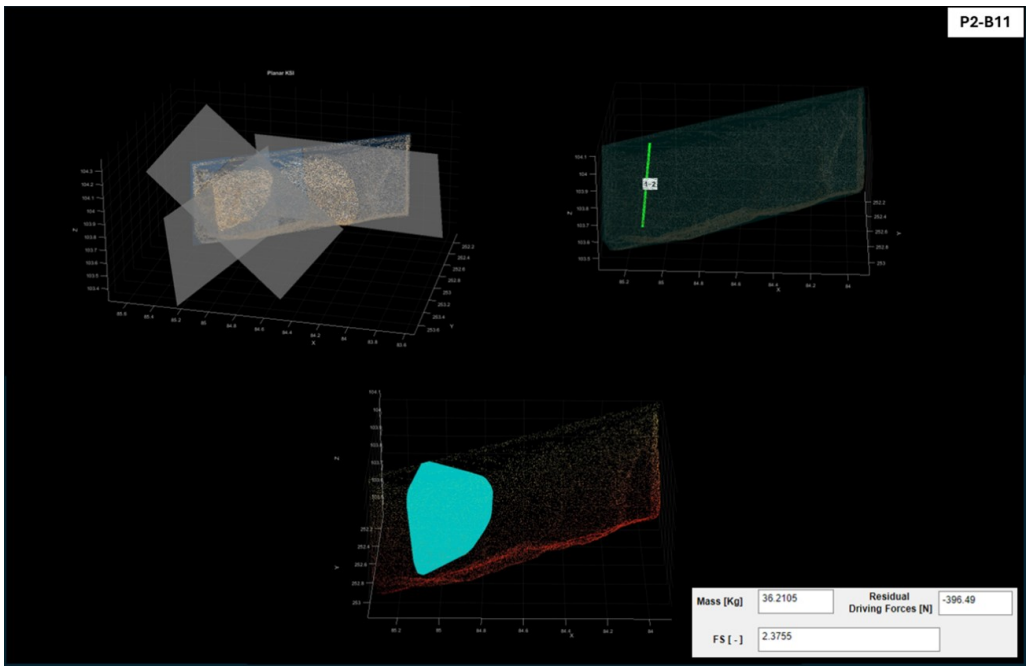


Figure 149: Block P2B11. Example of cases with discontinuities oriented in stable configurations relative to planar sliding that form unstable wedges.

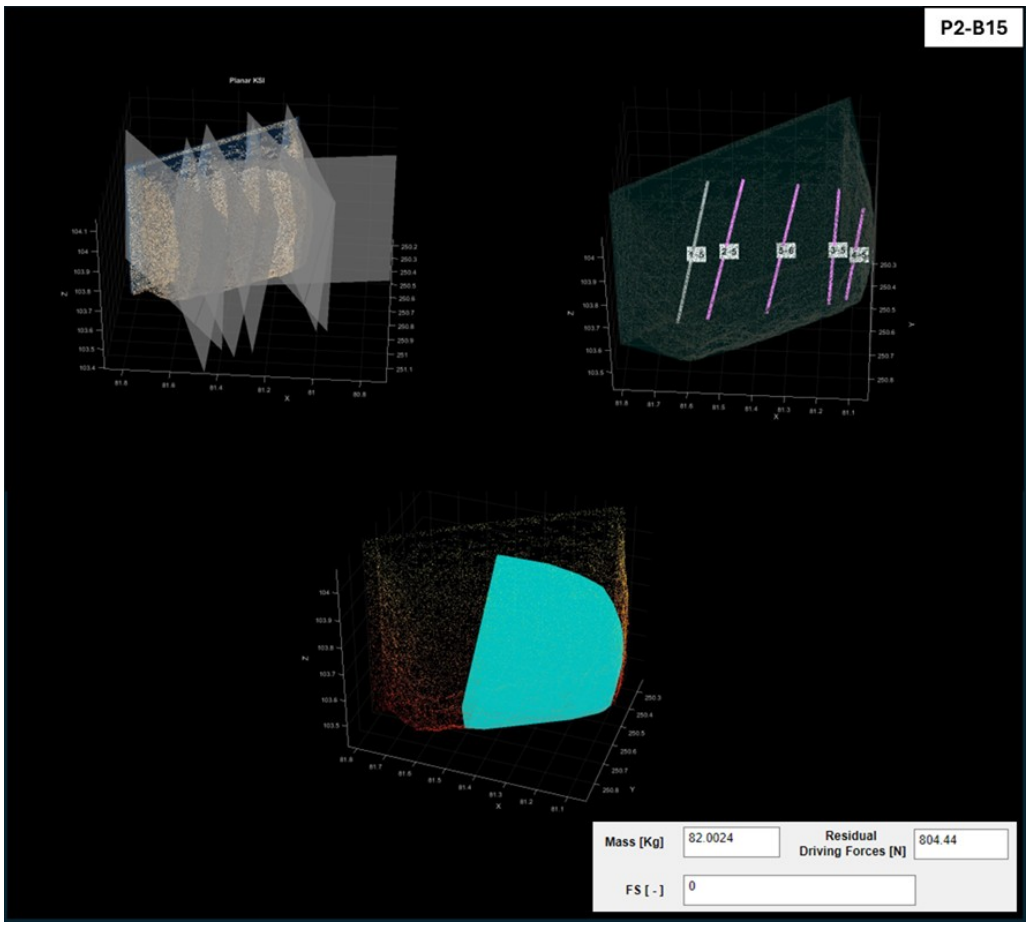


Figure 150: Block P2B15. Example of cases with discontinuities oriented in stable configurations relative to planar sliding that form unstable wedges.

7.1.3 *Test Area 3*

Figures 151, 152, and 153 present summary maps of the results for the calculation of the Kinematic Susceptibility Index (KSI): for planar sliding (Figure 151), wedge sliding (Figure 152), and the combined assessment of both mechanisms (Figure 153).



Figure 151: Planar susceptibility map on Area Test 3- Palazzo Pitti. The blocks are color coded using RoDiAn KSI legend (Figure 37)

Figure 154 presents a summary map of the results, showing the total number of discontinuities that exhibit susceptibility to any of the analyzed kinematic mechanisms.

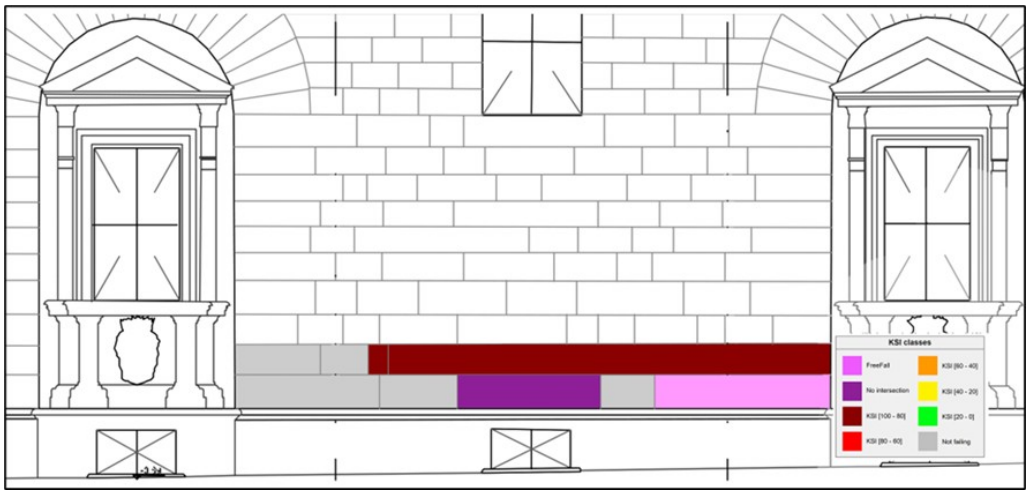


Figure 152: Wedge susceptibility map on Area Test 3- Palazzo Pitti. The blocks are color coded using RoDiAn KSI legend (Figure 37)

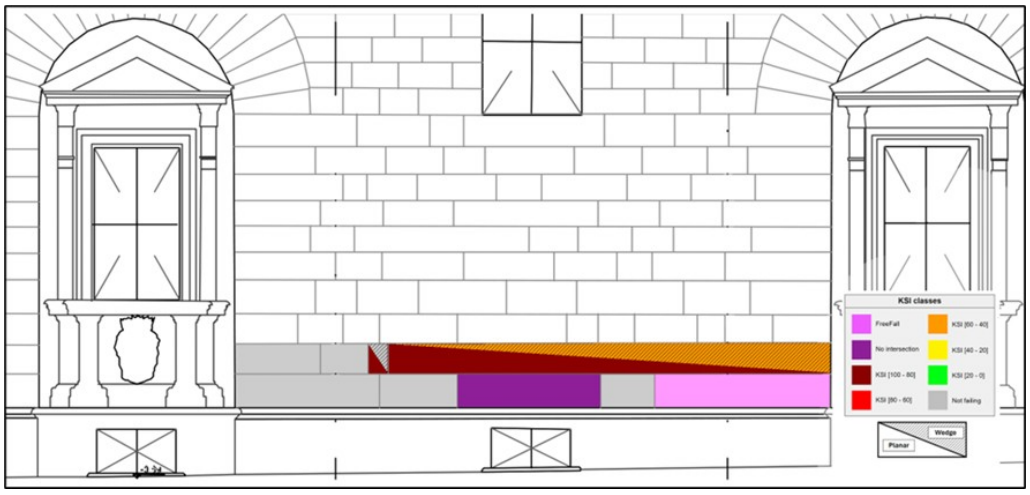


Figure 153: Planar (bottom left of each block) and Wedge (top right of each block) susceptibility map on Area Test 3- Palazzo Pitti. The blocks are color coded using RoDiAn KSI legend (Figure 37)

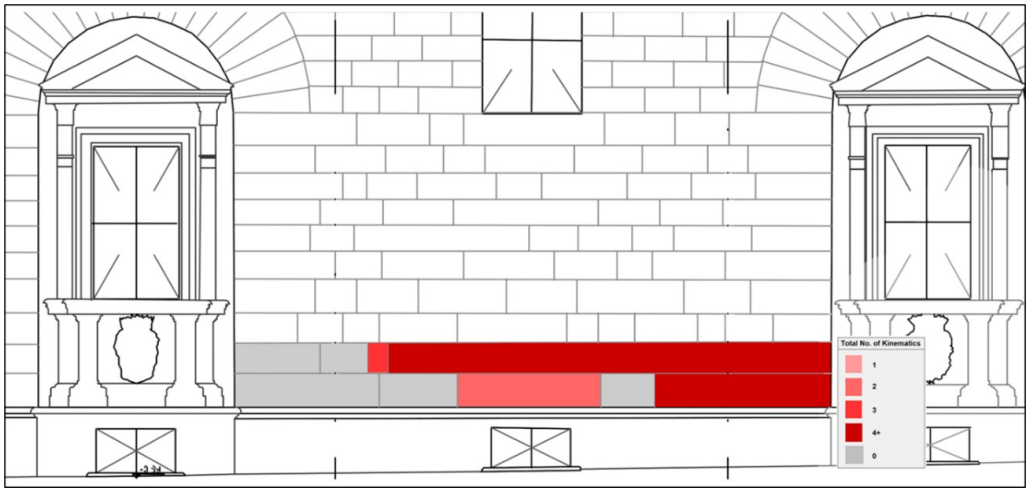


Figure 154: Map of total number of discontinuities that exhibit susceptibility to any kinematic mechanism on Area Test 3 - Palazzo Pitti

The blocks in Test Area 3 exhibit the same kinematic scenarios observed in Areas 1 and 2, with no significant differences. These range from blocks with no identified kinematic mechanisms (e.g., Block P3-B6, Figure 155) to those affected by multiple mechanisms (e.g., Block P3-B9, Figure 156).

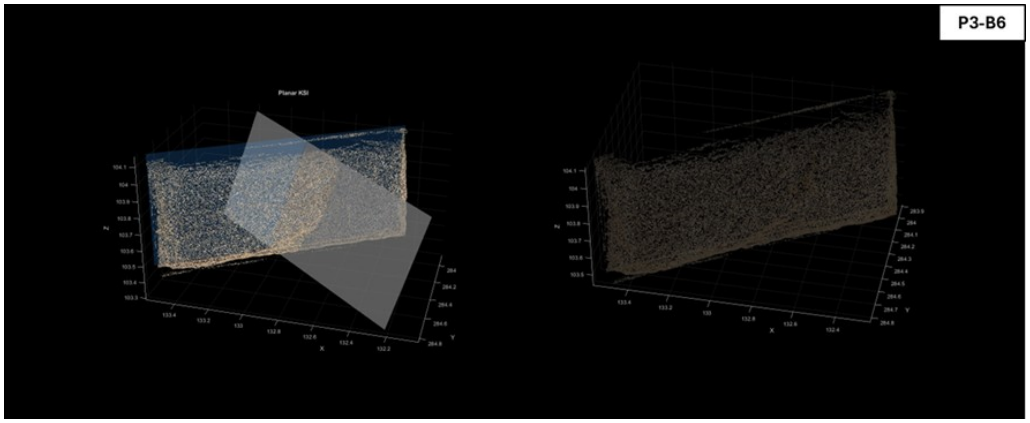


Figure 155: Block P3B06. Example of cases with discontinuities oriented in stable configurations.

A particular configuration is represented by block P3-B03 (Figure 157), which was installed rotated by 90° compared to the other blocks in the facade. The block exhibits rock lamination perpendicular to that observed in the surrounding blocks, and this rotation is reflected in its distinctive susceptibility to planar sliding. Specifically, the block exhibits a set of discontinuities that are also present in other blocks, but arranged orthogonally with respect to the configuration observed in the block under analysis. Due to this rotation, the vertical discontinuities observed in the adjacent blocks assume a horizontal orientation, becoming potentially susceptible to sliding.

7.2 PALAZZO MEDICI RICCARDI

The analyses conducted on Palazzo Medici Riccardi involved multiple architectural elements, and the methodology was successfully adapted to the specific characteristics of each. The rusticated blocks of the facade were subjected to a complete characterization, making full use of RoDiAn's functionalities. For the dentils, a simpler assessment was tested, focused solely on the potential for planar sliding and free fall. For the corbels and the upper cornice, the volume calculation functions were pri-

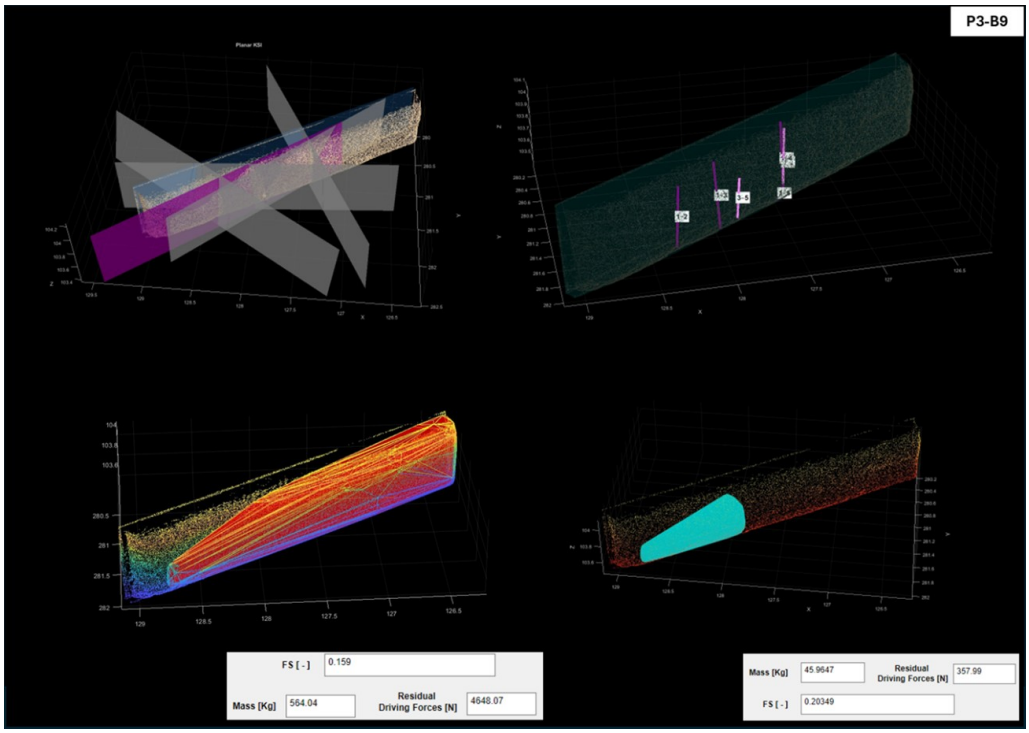


Figure 156: Block P3B09. Example of cases that exhibit susceptibility many kinematic mechanism.

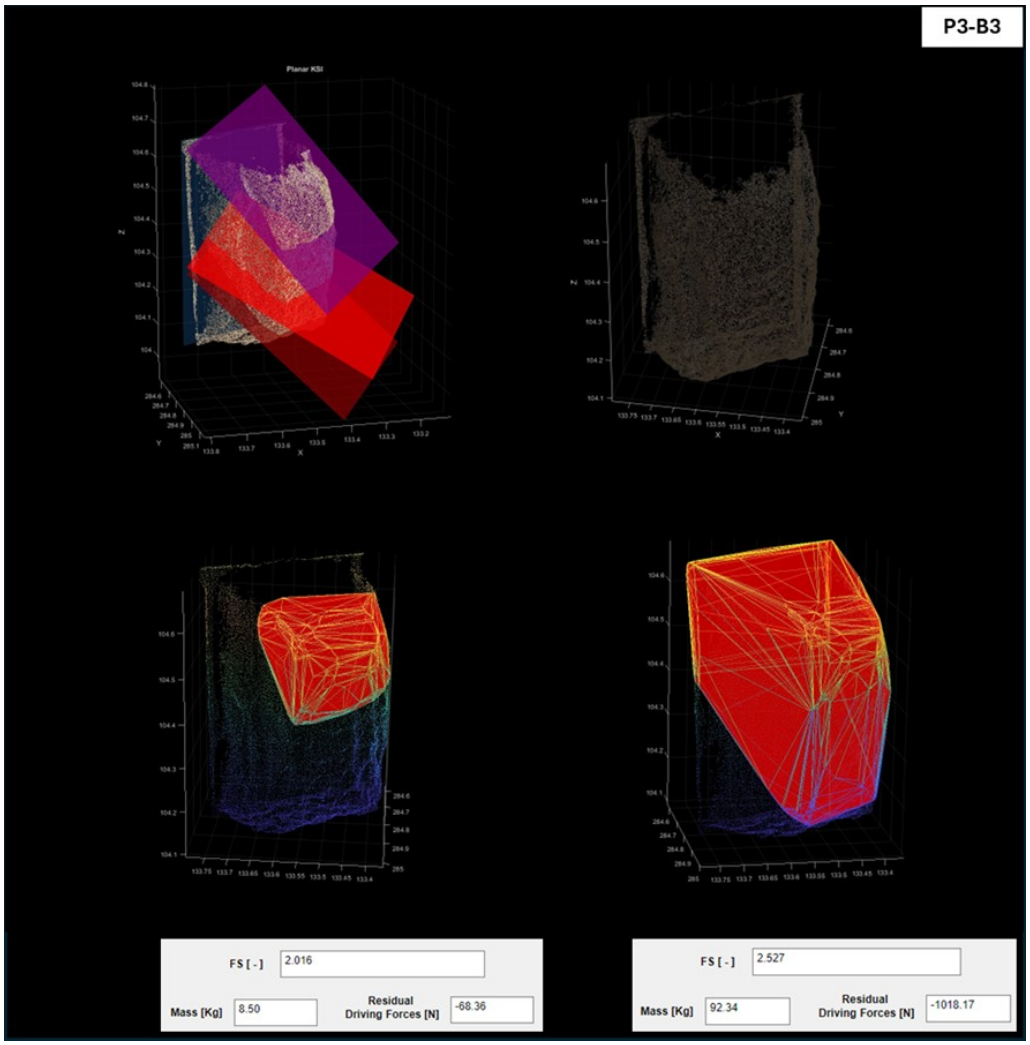


Figure 157: Block P3B03. Example of a block that was installed rotated by 90° compared to other blocks on the facade and shows a distinctive susceptibility to planar sliding

marily employed to estimate the extent of potential detachments observed during the ongoing restoration works.

7.2.1 *Rusticated block of the facade*

The analyses conducted on the facade blocks revealed, as in the case study of Palazzo Pitti, all the possible different kinematic mechanisms identifiable through the use of RoDiAn. The test area from which the blocks were selected is shown in Figure 158, while Figure 159 highlights the blocks that were investigated. The results for each rusticated block are reported in Appendix 9; in both the chapter and the appendix, each block's datasheet includes the dynamic analysis output for the most susceptible plane or wedge. This chapter presents statistical summaries of the results and selected individual cases used for discussion.

The parameters used for the kinematic and dynamic analysis are:

- $\varphi = 25°$
- JRC $= 12$
- JCS $= 50$ MPa
- $\rho = 2700$ kg/m^3

Figure 160 provides a general graphical summary of the results obtained for the individual blocks, highlighting the type of kinematic mechanism identified in each block.

As shown by the results in Figure 160, the majority of blocks (67%) are affected by at least one potential kinematic mechanism. Figure 161 reports the number of mechanisms identified for each individual sample. Among the blocks exhibiting susceptibility, the most common configuration is that of a single mechanism, unlike the case of Palazzo Pitti, where the coexistence of multiple mechanisms was more frequent. Another notable difference from the aforementioned case study is the absence of blocks exhibiting all four possible kinematic mechanisms.

Figure 162 illustrates the distribution of the different kinematic mechanisms: the most common is Wedge Sliding, followed by Planar Slide and Wedge Freefall. This distribution closely resembles that observed in the Palazzo Pitti case study.

Figures 163, 164, and 165 present summary maps of the results for the calculation of the Kinematic Susceptibility Index (KSI): for planar sliding

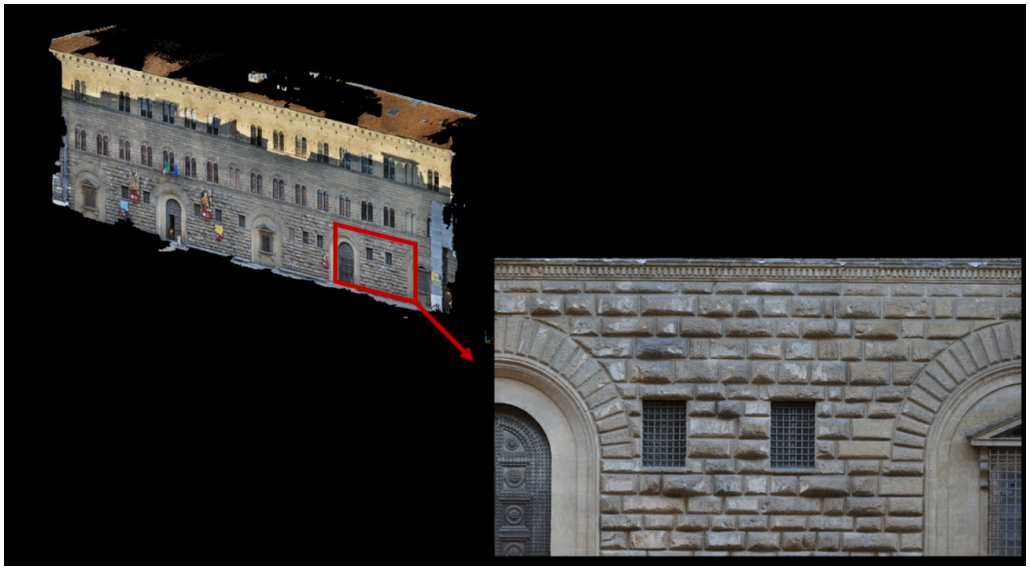


Figure 158: Test area selected for this research on the facade of Palazzo Medici Riccardi

(Figure 163), wedge sliding (Figure 164), and the combined assessment of both mechanisms (Figure 165)

Figure 166 presents a summary map of the results, indicating the total number of discontinuities that exhibit susceptibility to any of the analyzed kinematic mechanisms.

Cases without discontinuities susceptible to detachment all fall within the category of block with the presence of discontinuities whose orientation does not activate kinematic mechanisms due to their dip or dip direction. It is observed that in nearly all such cases, the factor contributing to the kinematic stability of these discontinuities is not a dip angle lower than the friction angle, but rather a dip direction typically of ± 90° relative to the facade. Cases of this type (e.g., blocks CL1-12, 39; Figures 167 and 168) support the hypothesis of a deliberate choice by the builders to position the blocks in the facade with consideration of the geological features of the material.

Cases of potential planar sliding are characterized by a relative abundance (9 out of 11 total) of discontinuities that do not intersect the facade surface, resulting in possible planar sliding without contact (blocks in Figure 169 and 170) and free fall scenarios (Figure 171). Both mechanisms are particularly critical, as they tend to involve the detachment of large blocks. The results of the dynamic analysis for this block show a negligi-

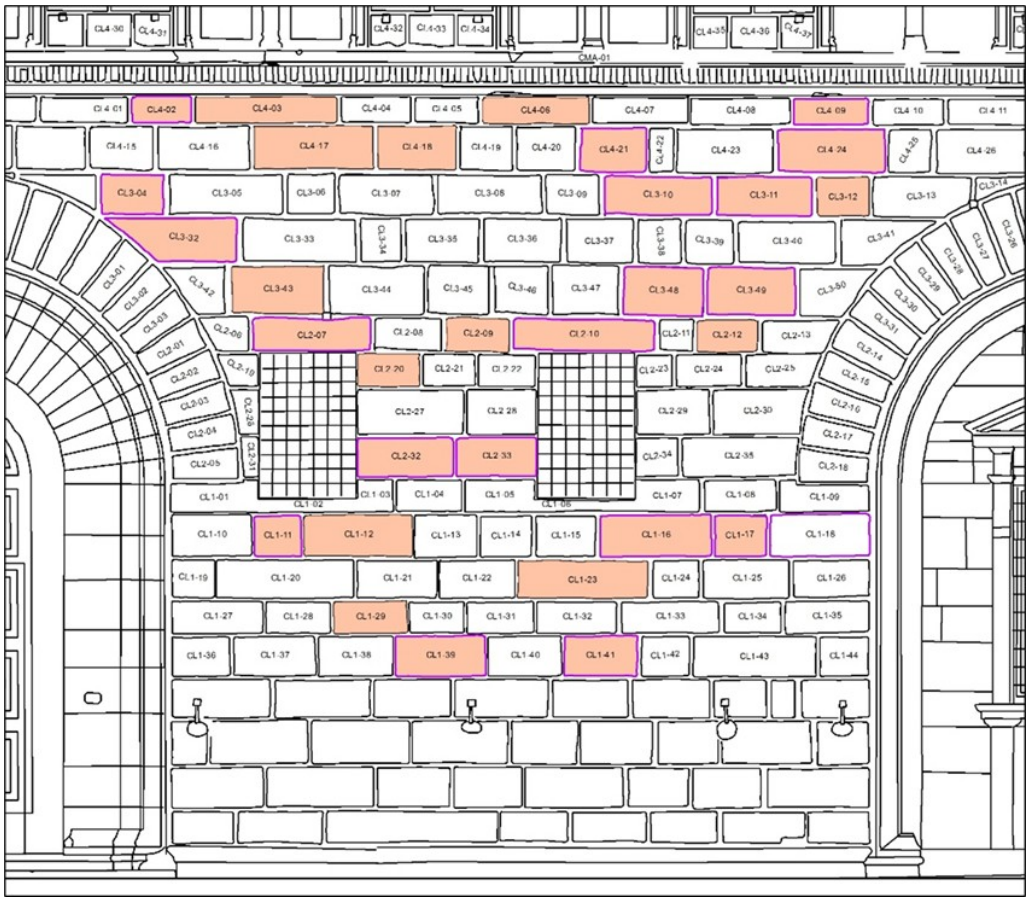


Figure 159: Map of the selected block (in red) for the analysis

Sample ID	PSLIDE	P.FFALL	WSLIDE	WFFALL
CL1-11	0	0	0	0
CL1-12	0	1	0	1
CL1-16	0	0	0	1
CL1-17	0	0	0	0
CL1-23	0	0	1	0
CL1-29	0	0	1	0
CL1-39	0	0	0	0
CL1-41	0	0	0	0
CL2-07	0	0	1	0
CL2-09	0	0	0	0
CL2-10	1	0	1	0
CL2-12	0	1	0	1
CL2-20	1	0	1	0
CL2-32	1	0	1	1
CL2-33	1	0	1	1
CL3-04	0	0	0	0
CL3-10	1	0	1	0
CL3-11	1	0	0	1
CL3-12	0	0	0	0
CL3-32	1	0	1	1
CL3-43	0	0	0	1
CL3-48	0	0	0	0
CL3-49	0	0	1	0
CL4-02	0	1	1	0
CL4-09	0	0	0	0
CL4-17	0	0	1	0
CL4-18	0	0	0	0
CL4-21	0	0	0	0
CL4-24	1	0	0	0

Figure 160: Summary of kinematic mechanisms identified in individual blocks at Palazzo Medici Riccardi. Each row corresponds to a sample ID, with binary indicators for four kinematic mechanisms: Planar slide (PSLIDE), Planar FreeFall (P.FFALL), Wedge slide (WSLIDE), Wede FreeFall (W.FFALL). Cells marked in blue denote presence of the respective mechanism.

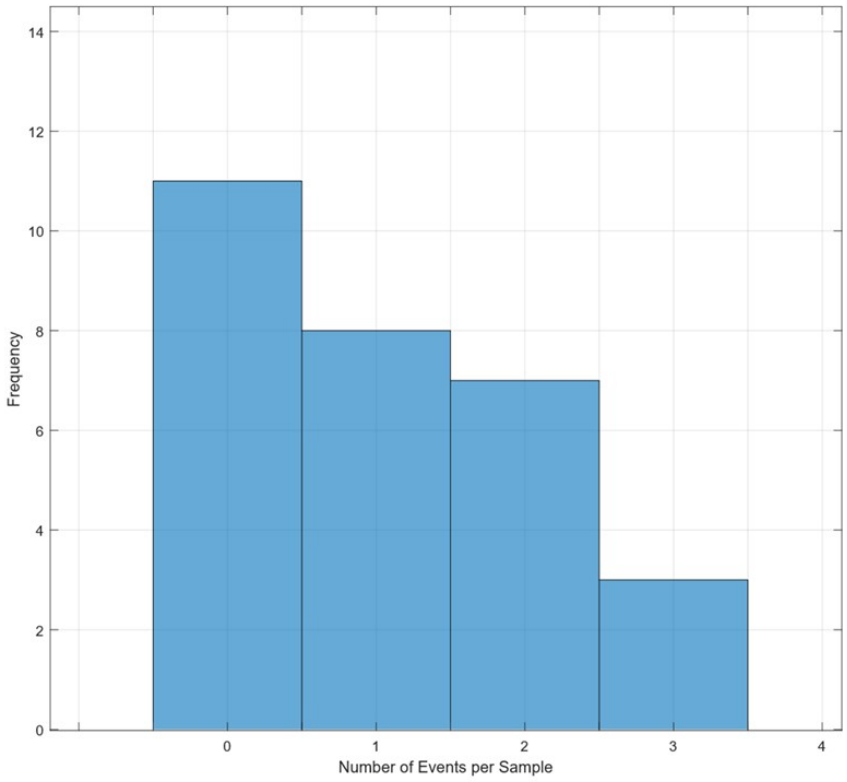


Figure 161: Distribution of kinematic mechanisms per sample at Palazzo Medici Riccardi

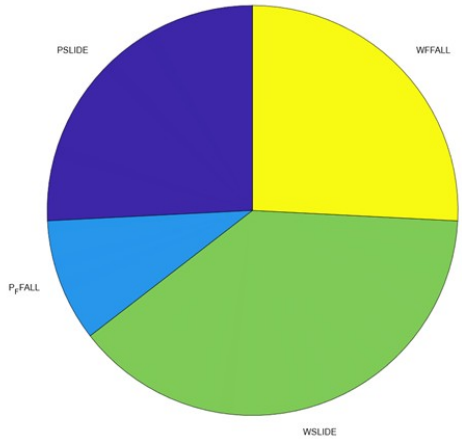


Figure 162: Pie chart illustrating the relative frequency of failure modes at Palazzo Medici Riccardi: Planar slide (PSLIDE), Planar FreeFall (P.FFALL), Wedge slide (WSLIDE), Wede FreeFall (W.FFALL)

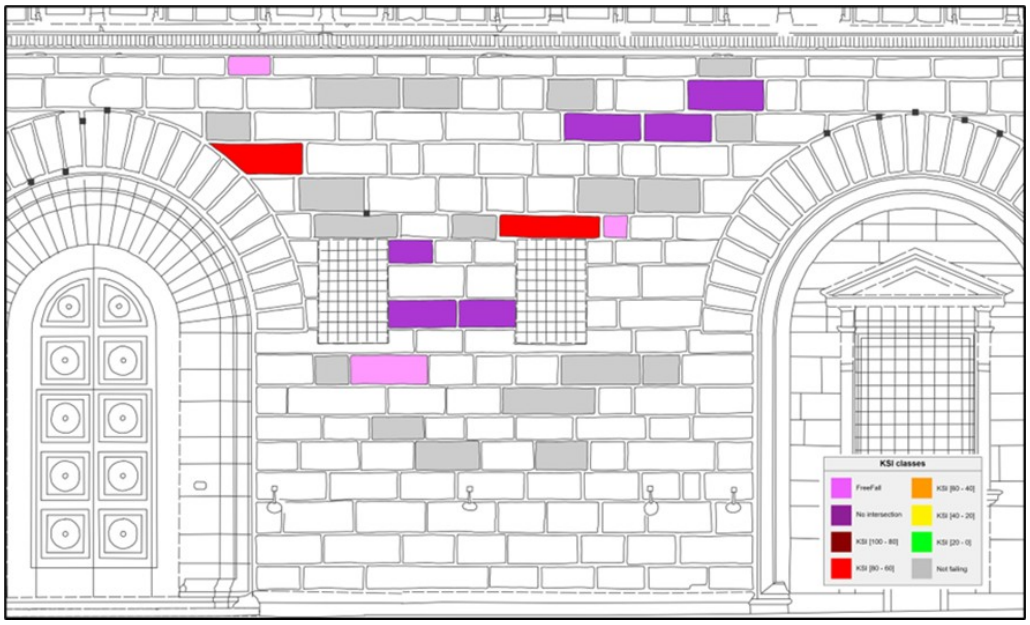


Figure 163: Planar susceptibility map on Palazzo Medici Riccardi. The blocks are color coded using RoDiAn KSI legend (Figure 37)

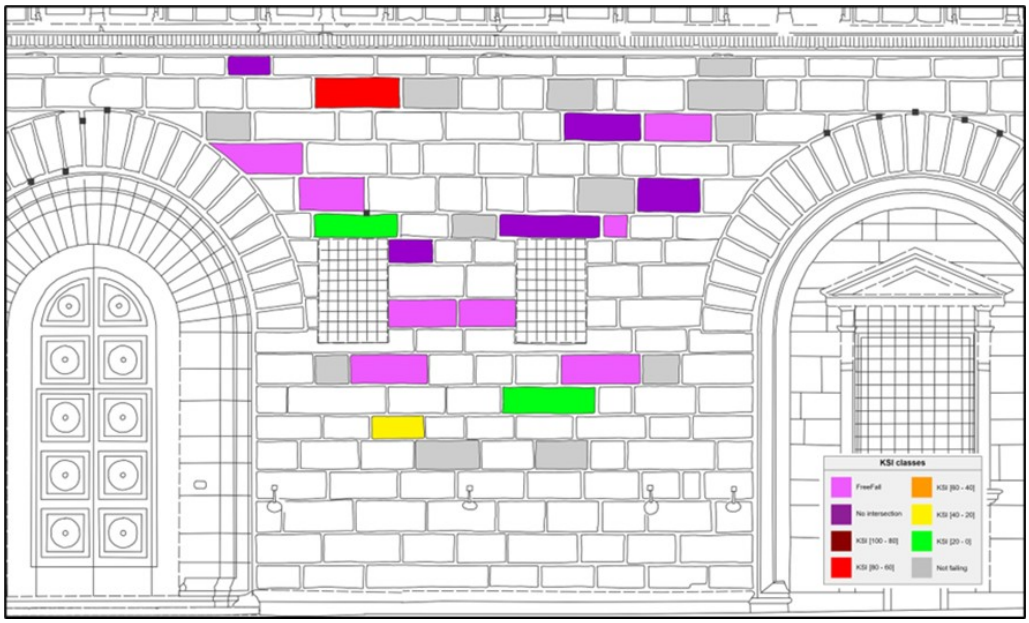


Figure 164: Wedge susceptibility map on Palazzo Medici Riccardi. The blocks are color coded using RoDiAn KSI legend (Figure 37)

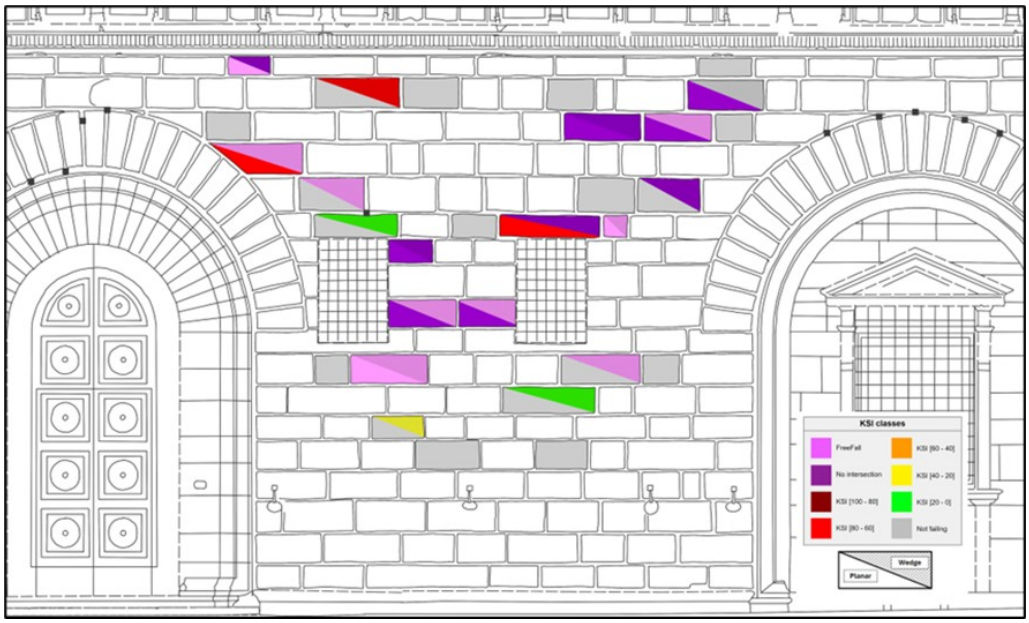


Figure 165: Planar (bottom left of each block) and Wedge (top right of each block) susceptibility map on APalazzo Medici Riccardi. The blocks are color coded using RoDiAn KSI legend (Figure 37)

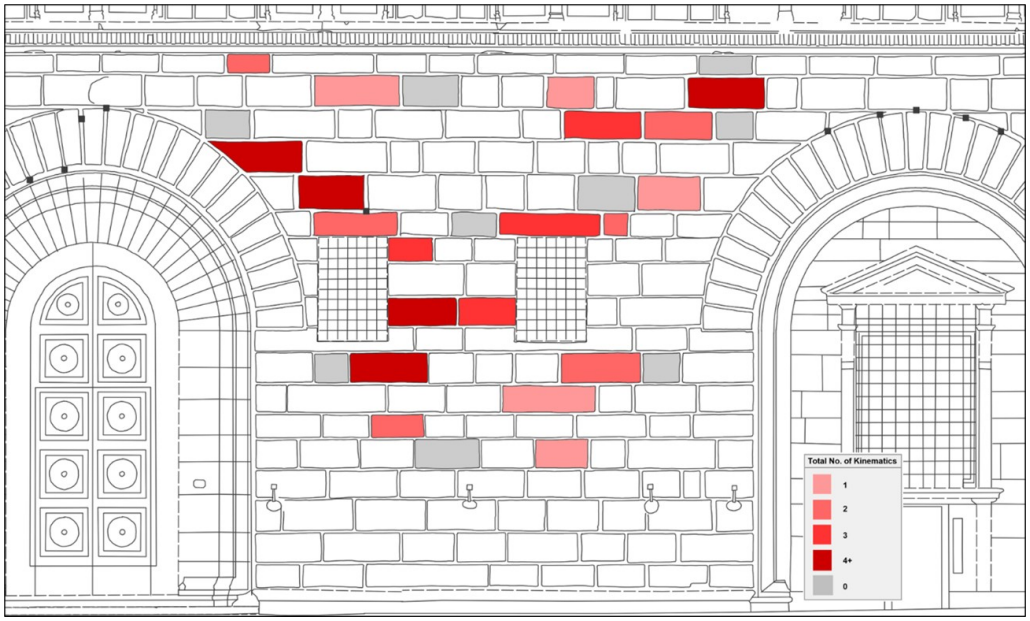


Figure 166: Map of total number of discontinuities that exhibit susceptibility to any kinematic mechanism on Palazzo Medici Riccardi

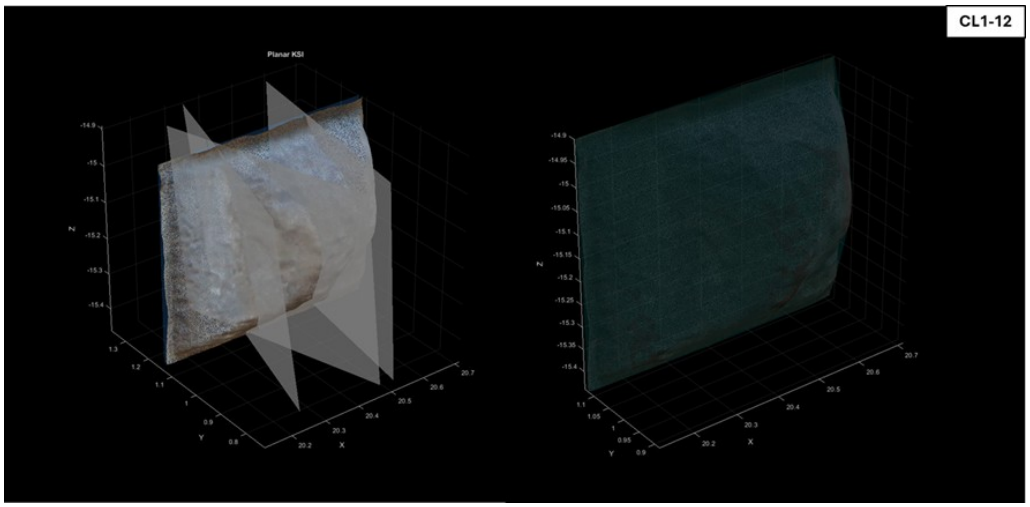


Figure 167: Block CL1-12. Example of cases with discontinuities oriented in stable configurations due to their dip direction

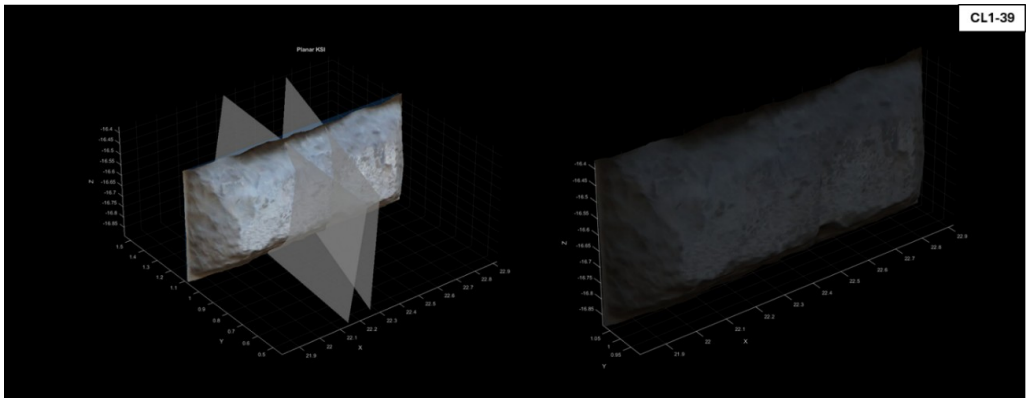


Figure 168: Block CL1-39. Example of cases with discontinuities oriented in stable configurations due to their dip direction

ble contribution from frictional resistance in planar sliding cases (null in free fall scenarios), where the large mass and extremely high dip angle lead to a very low safety factors.

Numerous cases were also observed in which the block is susceptible to wedge sliding but not to planar sliding. Many of these instances occur when a family of discontinuities is oriented perpendicularly to the facade, with individual planes considered kinematically stable, yet their intersections forming potentially unstable wedges. These wedges may exhibit a sliding direction facing outward and be susceptible to planar sliding (e.g., blocks CL1-29, CL4-17; Figures 172 and 173), or face inward and be susceptible to free fall (e.g., blocks CL3-43, CL4-06; Figures 174 and 175).

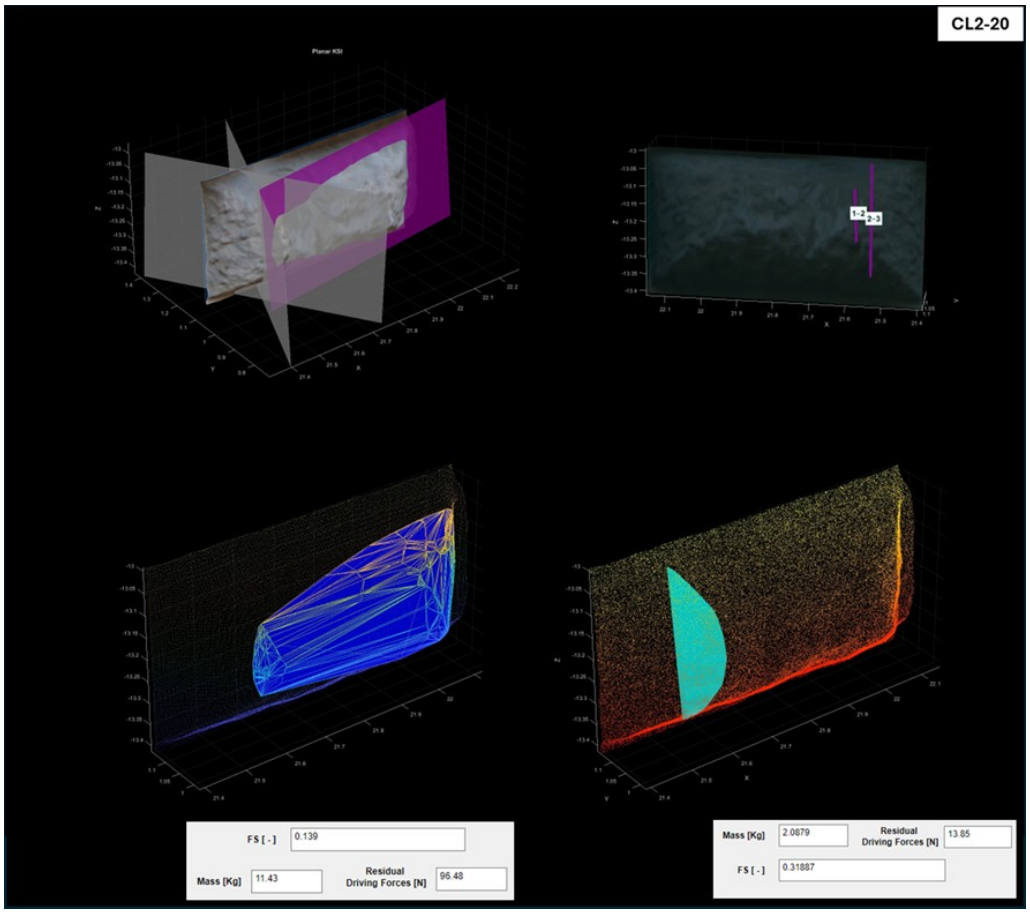


Figure 169: Block CL2-20. Example of discontinuities susceptible to planar sliding with no facade intersection

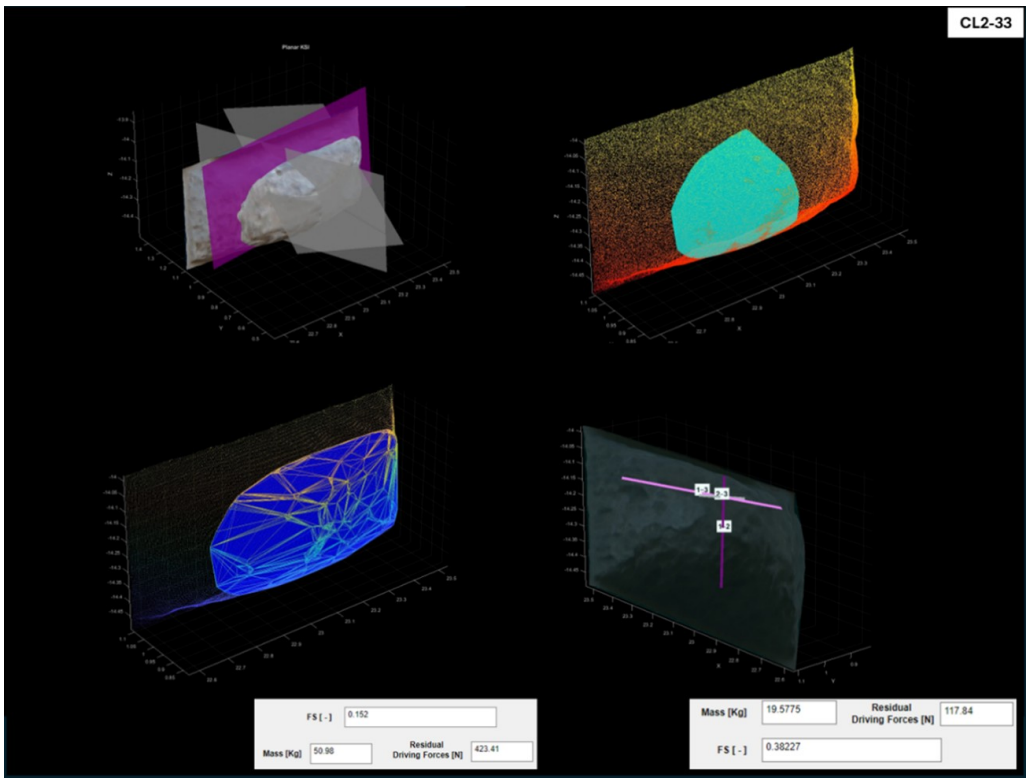


Figure 170: Block CL2-33. Example of discontinuities susceptible to planar sliding with no facade intersection

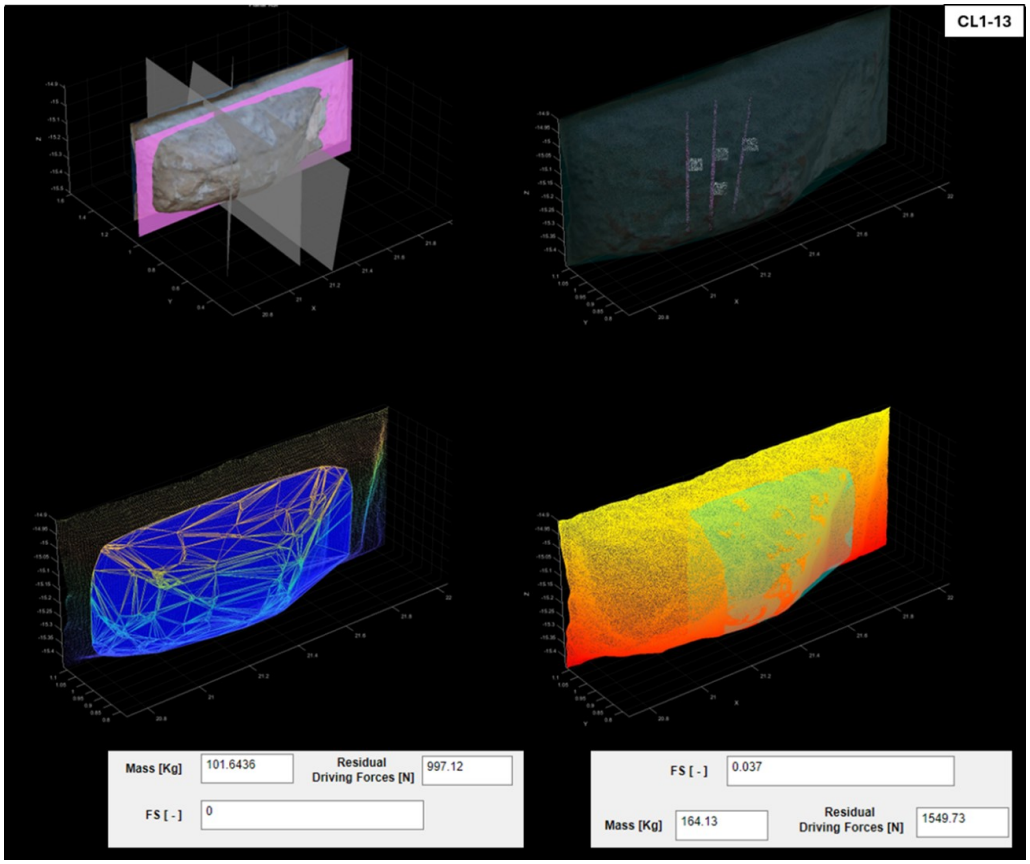


Figure 171: Block CL1-13. Example of cases with discontinuities susceptible to free fall failure

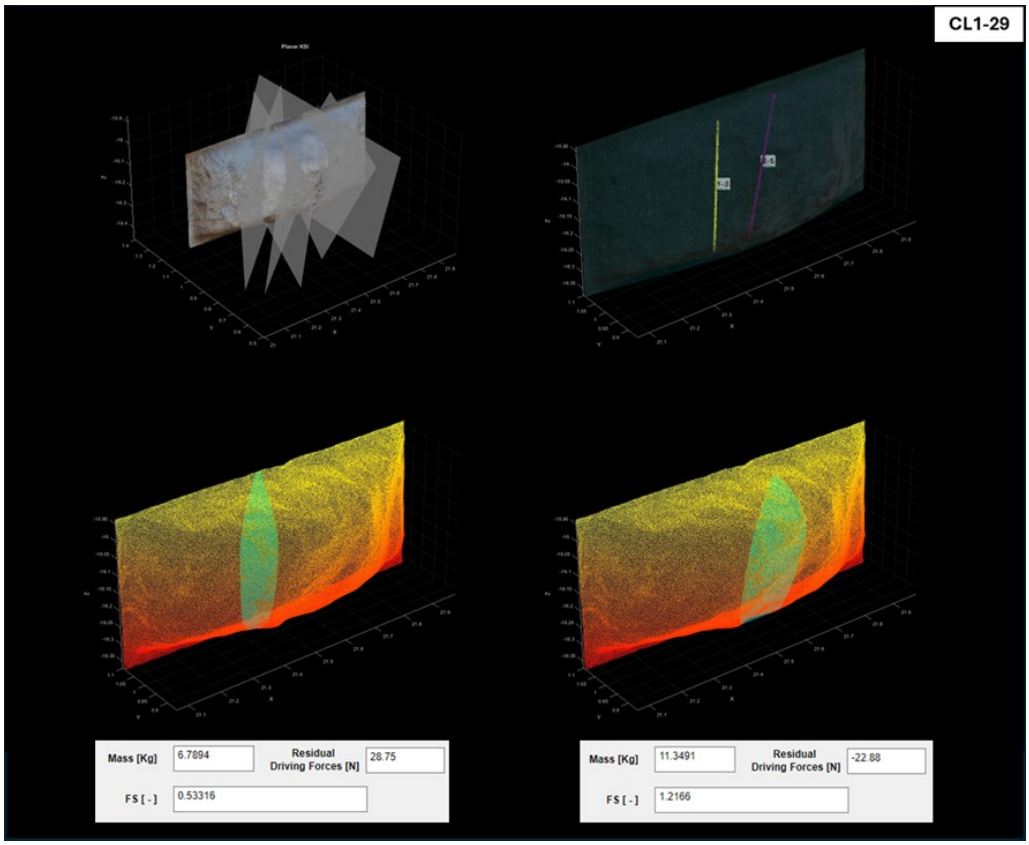


Figure 172: Block CL2-20. Example of discontinuities not susceptible to planar sliding that form wedges which could fail.

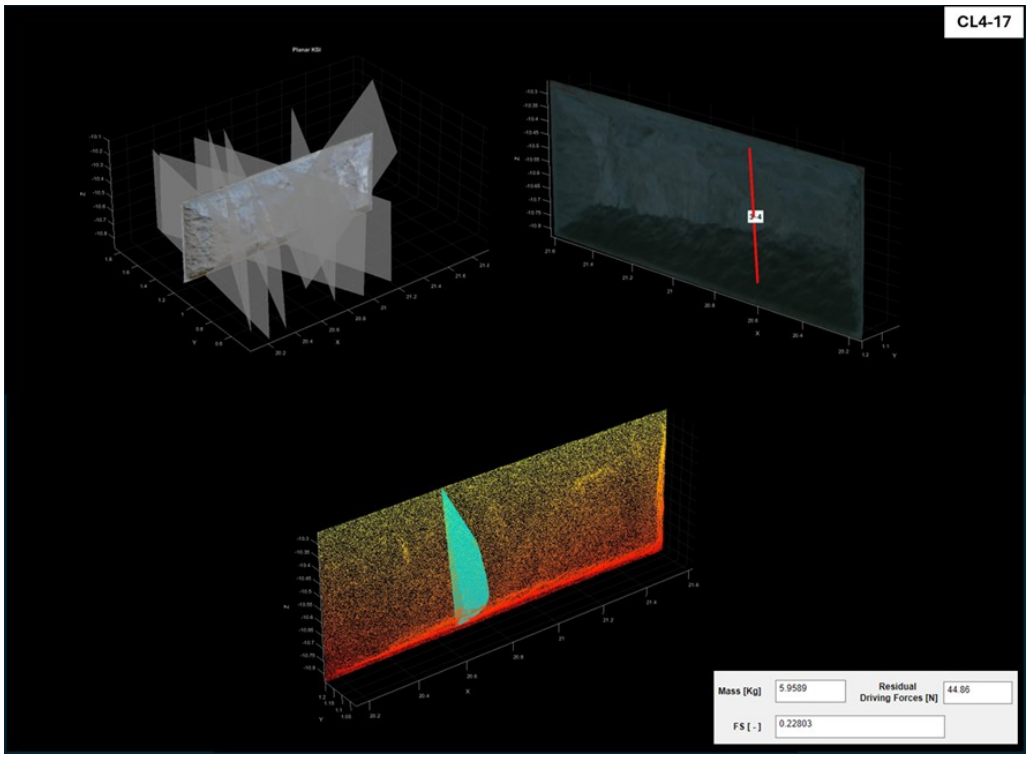


Figure 173: Block CL2-33. Example of discontinuities not susceptible to planar sliding that form wedges which could fail.

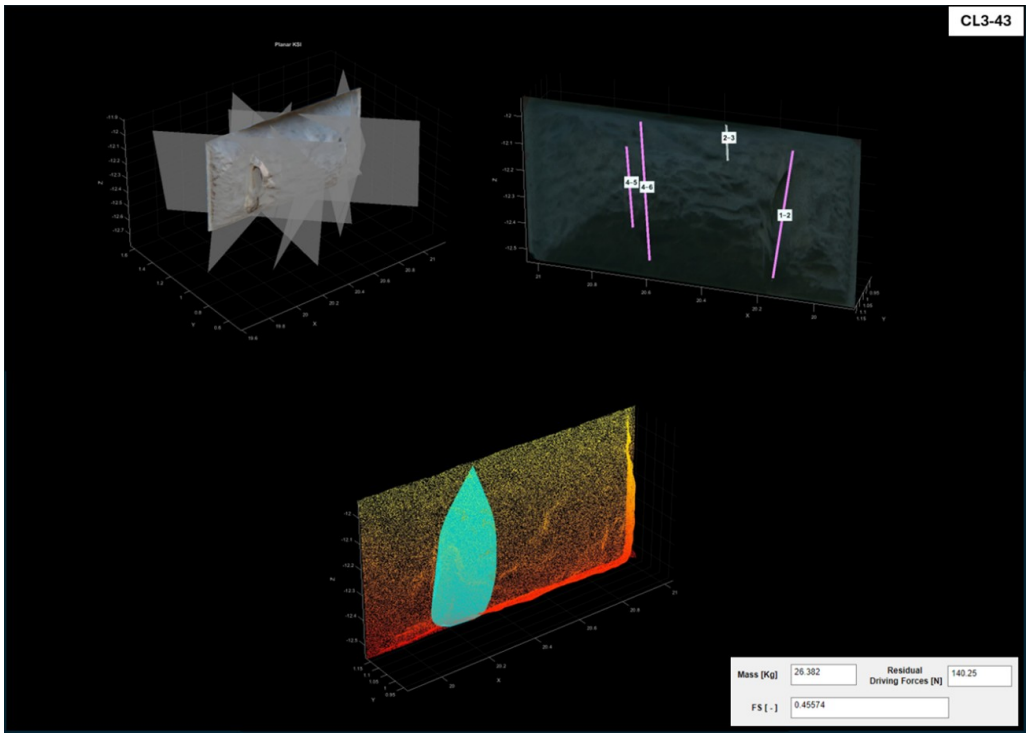


Figure 174: Block CL1-13. Example of discontinuities not susceptible to planar sliding that form wedges which could fail via free fall.

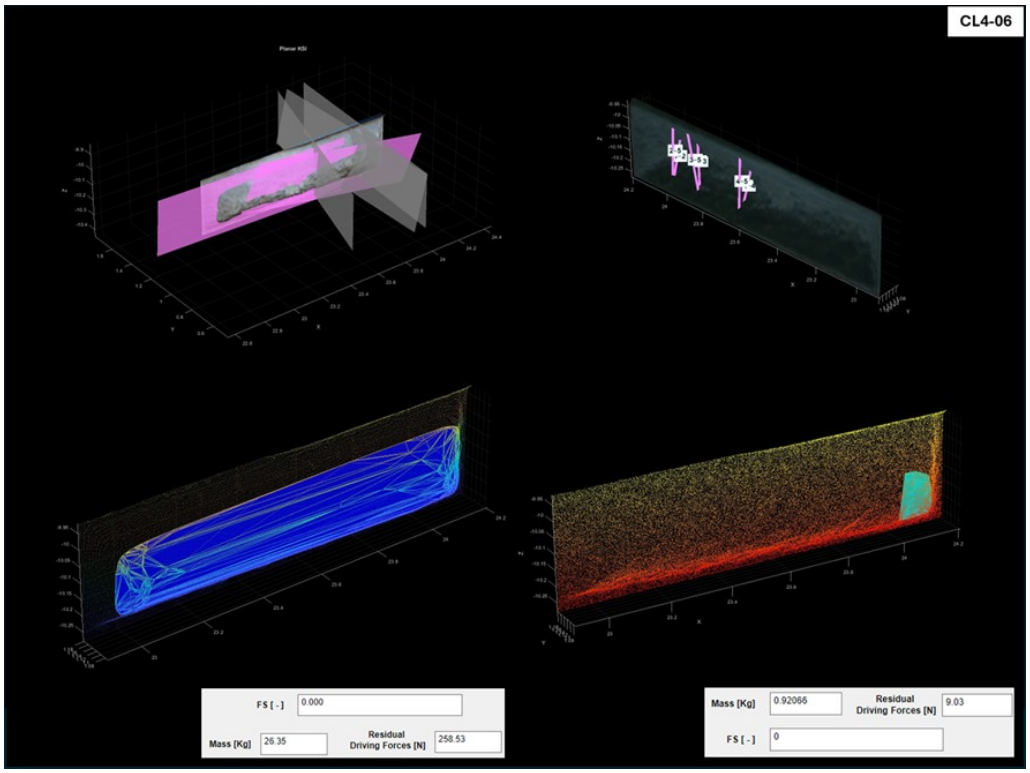


Figure 175: Example of discontinuities not susceptible to planar sliding that form wedges which could fail via free fall.

7.2.2 *Dentils of the cornice*

Investigations on the dentils of the cornice were carried out following the detachment of an element (Figure 176) along a calcite vein in February 2025. The detachment had no consequences, as the palace facade was undergoing restoration and was covered by scaffolding at the time. Nevertheless, it triggered a series of diagnostic investigations, including the one presented here.



Figure 176: Dentil of the cornice at Palazzo Medici Riccardi that detached along two calcite veins in February 2025.

To assess other potentially unstable areas, a simplified analysis was carried out using RoDiAn, employing only the functions related to the calculation of possible kinematic mechanisms. For this purpose, the cornice was subdivided into four blocks, each corresponding to a single rock element. This subdivision was necessary based on the assumption that calcite veins propagate within the same block but are not structurally

connected to adjacent ones. The four analyzed blocks are shown in Figure 177.

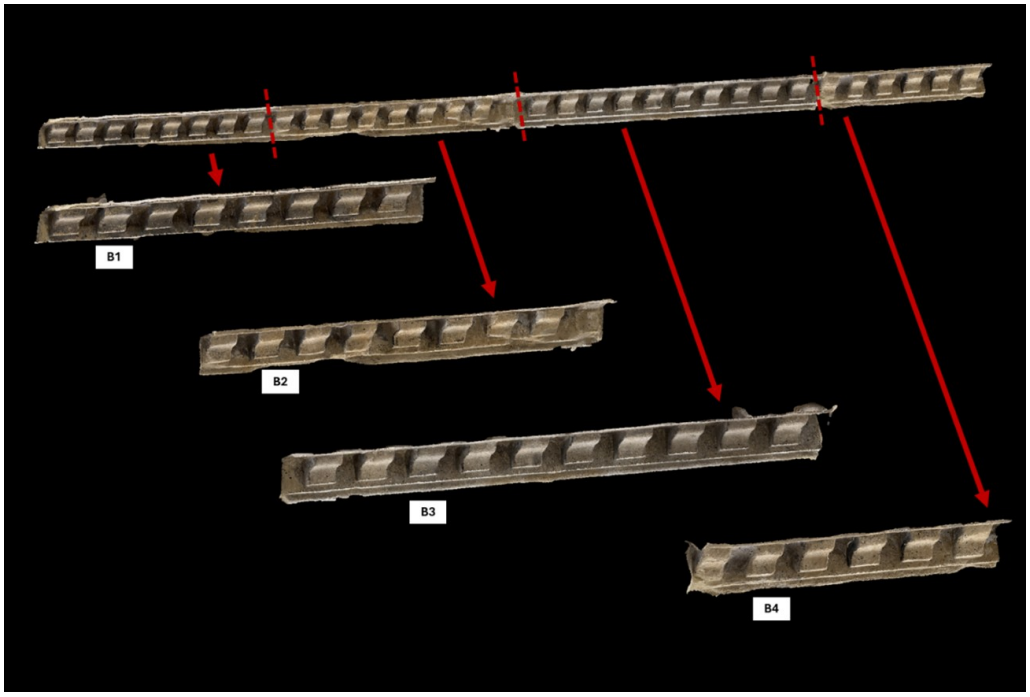


Figure 177: Blocks that form the portion of the cornice analyzed at Palazzo Medici Riccardi.

The analyses of the four blocks (Figure 178, 179, 180, 181)did not reveal any critical issues, except for the formation of a wedge susceptible to free fall in block 2.

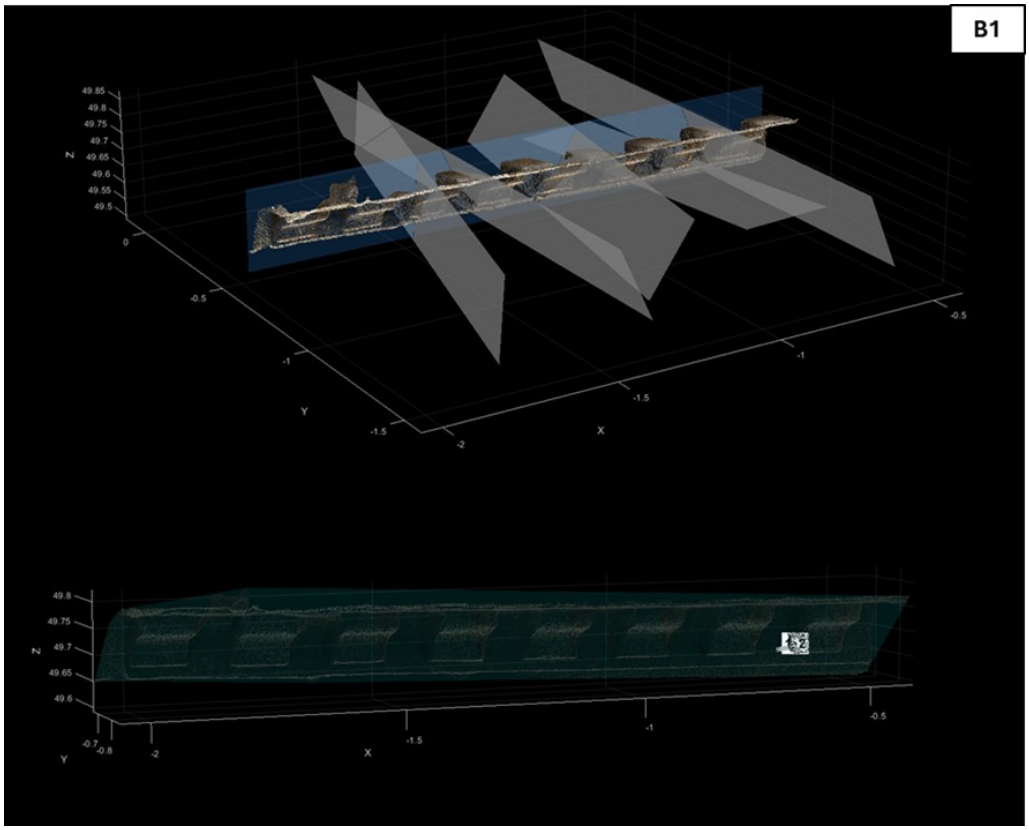


Figure 178: Block 1 of the cornice at Palazzo Medici Riccardi. RoDiaN susceptibility results for planar (top) and wedge (bottom) kinematic.

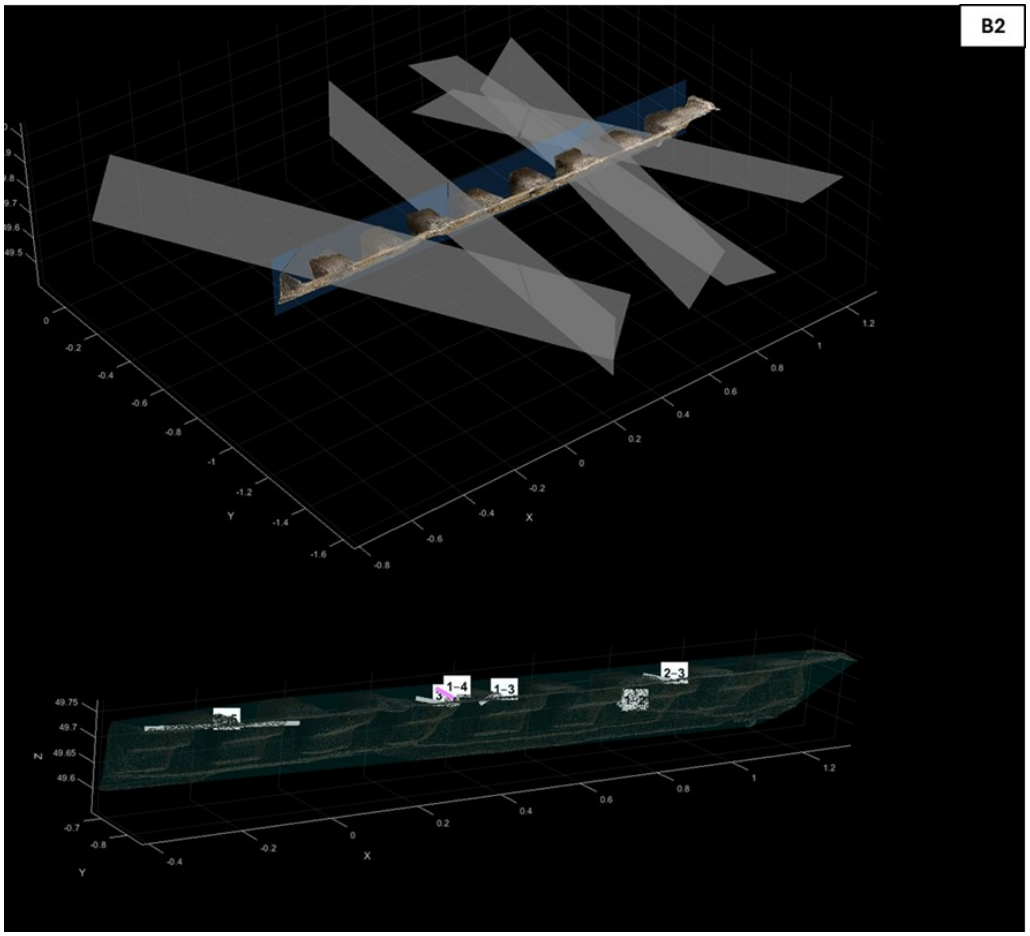


Figure 179: Block 1 of the cornice at Palazzo Medici Riccardi. RoDiaN susceptibility results for planar (top) and wedge (bottom) kinematic.

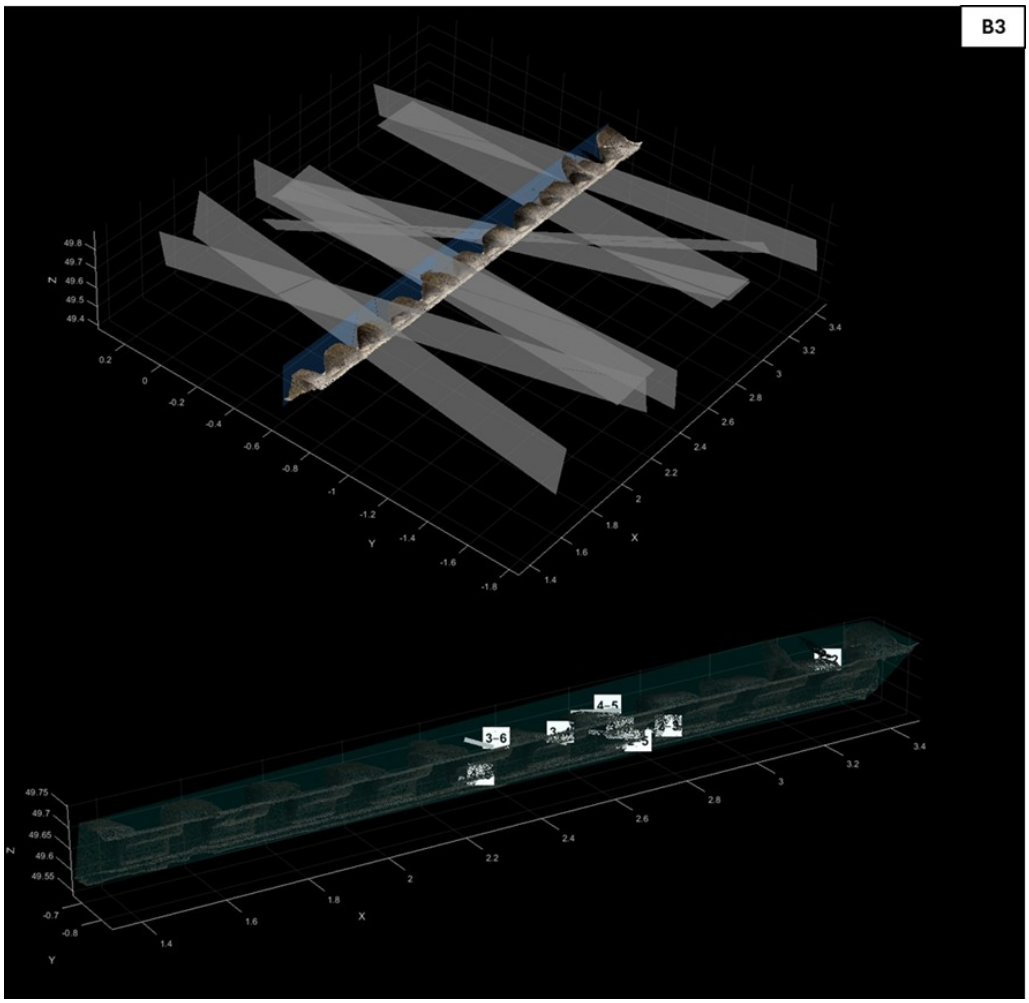


Figure 180: Block 1 of the cornice at Palazzo Medici Riccardi. RoDiaN susceptibility results for planar (top) and wedge (bottom) kinematic.

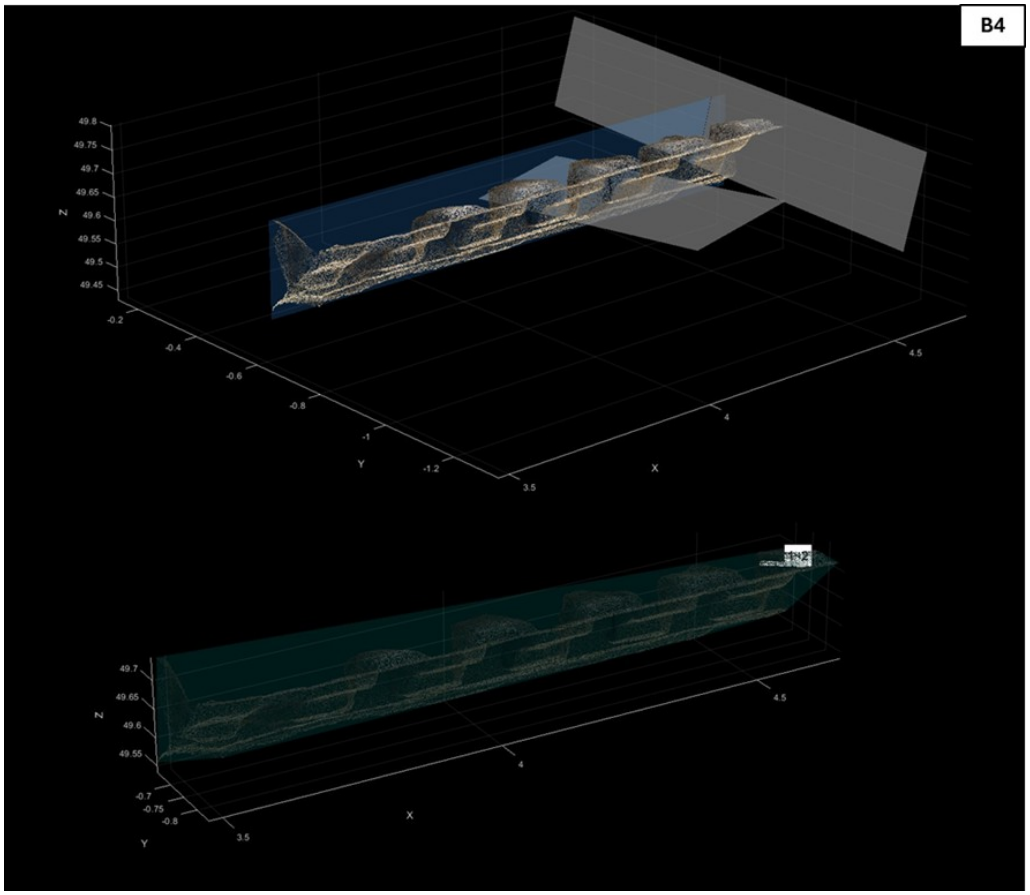


Figure 181: Block 1 of the cornice at Palazzo Medici Riccardi. RoDiaN susceptibility results for planar (top) and wedge (bottom) kinematic.

7.2.3 *Summit Cornice*

The summit cornice between Via dei Gori and Via Ginori is affected by an angular discontinuity that cuts across the block, as shown in Figure 182.



Figure 182: Portion of the summit cornice at Palazzo Medici Riccardi analyzed in this research

The element exhibits a geometry and morphological features that make it poorly suited for a full analysis using RoDiAn. In particular, the point cloud presents a configuration that hinders the accurate identification of intersections between discontinuities and the facade surface. Consequently, this block was selected to test specific functionalities of the software, such as the calculation of detachment volumes and the estimation of driving forces to be considered for potential stabilization interventions.

Figure 183 shows the result of the kinematic analysis for planar sliding. As evident in the figure, all discontinuities, including those with orientations that would normally be considered stable, are flagged as susceptible to free fall. This outcome is due to the interaction between the discontinuity planes and the reference plane that RoDiAn identifies as the facade surface (highlighted in blue in Figure 183). Since this interaction is influenced by the geometry of the point cloud, it is essential to verify that the software correctly identifies the facade plane. For this reason,

the automatic tracing of the blue reference plane is included in every analysis.

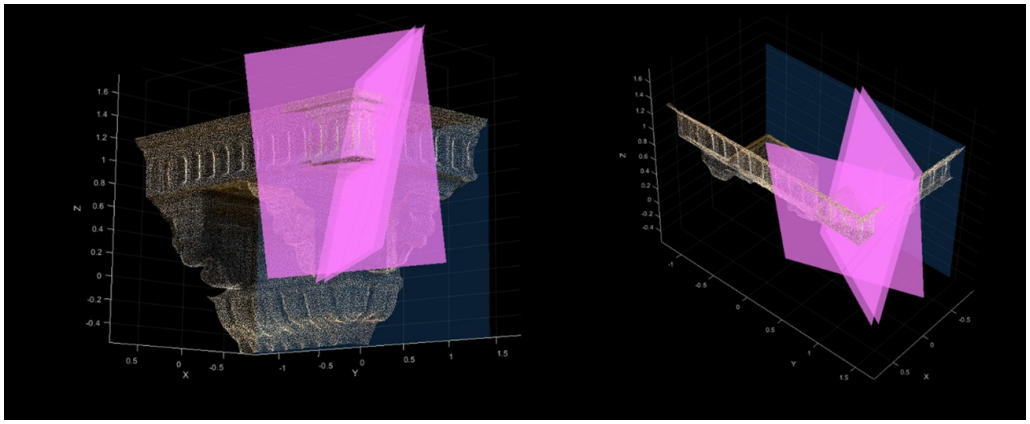


Figure 183: Portion of the summit cornice at Palazzo Medici Riccardi analyzed in this research

Figure 184 illustrates a possible application of RoDiAn in cases such as the one presented. Through its volume calculation functions, it is possible to obtain useful information for the potential stabilization of the unstable block. The software computes the block's mass and the associated driving forces. These values allow precise dimensioning of the support devices required to ensure structural safety.

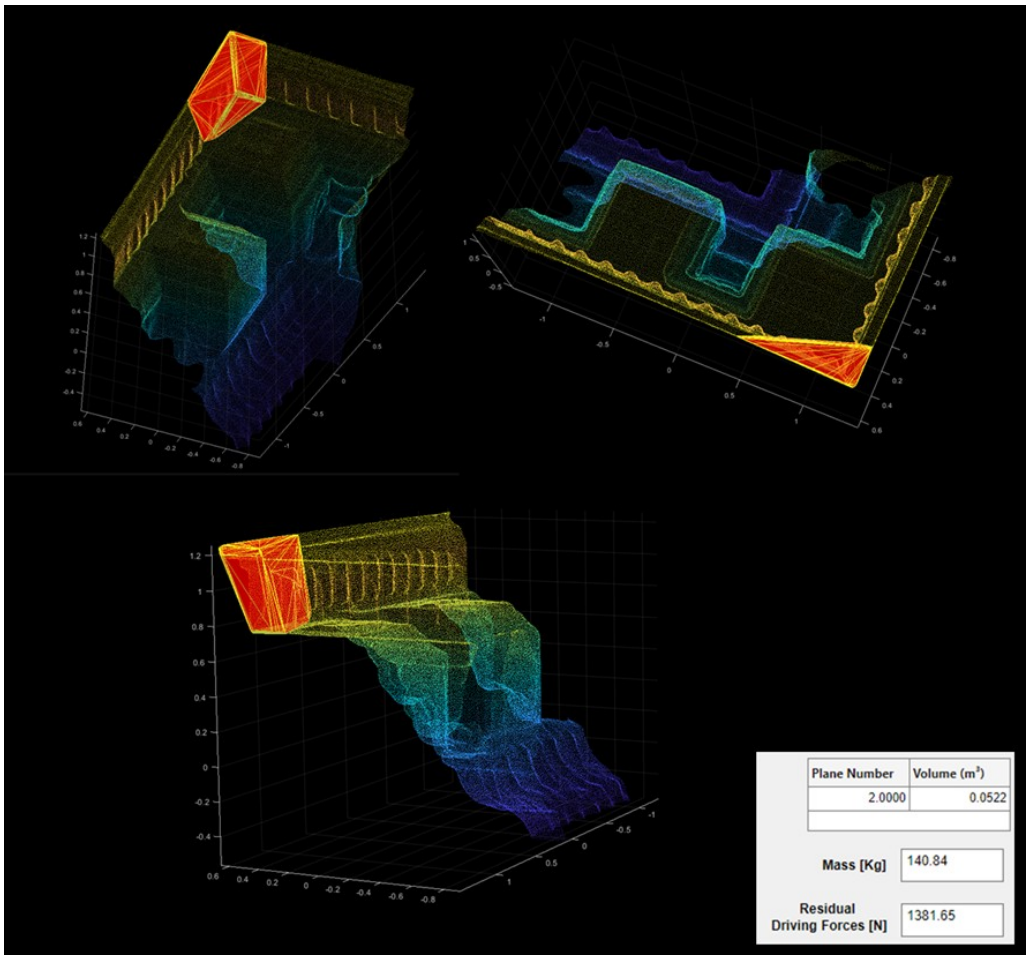


Figure 184: RoDiAn results for the summit cornice at Palazzo Medici Riccardi. The computed mass and volume values can help decide the dimensioning of stabilization devices based on driving force.

7.3 PALAZZO ZUCCARI

The analyzed element in the case study of Palazzo Zuccari is the stone coat of arms positioned above the main portal. The shield appears in poor conservation condition and reveal a complex system of fractures (Figure 185). The parameters used for the kinematic and dynamic analysis are:

- $\varphi = 25°$
- JRC $= 10$
- JCS $= 40$ MPa
- $\rho = 2650$ kg/m^3



Figure 185: Stone coat of arms of Palazzo Zuccari (left) showing three discontinuities in the rock matrix.

Kinematic analysis was performed on the element, revealing the presence of a potential instance of planar sliding, wedge sliding, and wedge free fall (Figure 186).

Dynamic analysis was performed on the discontinuity identified as susceptible to planar sliding. The volume of the block is shown in Figures

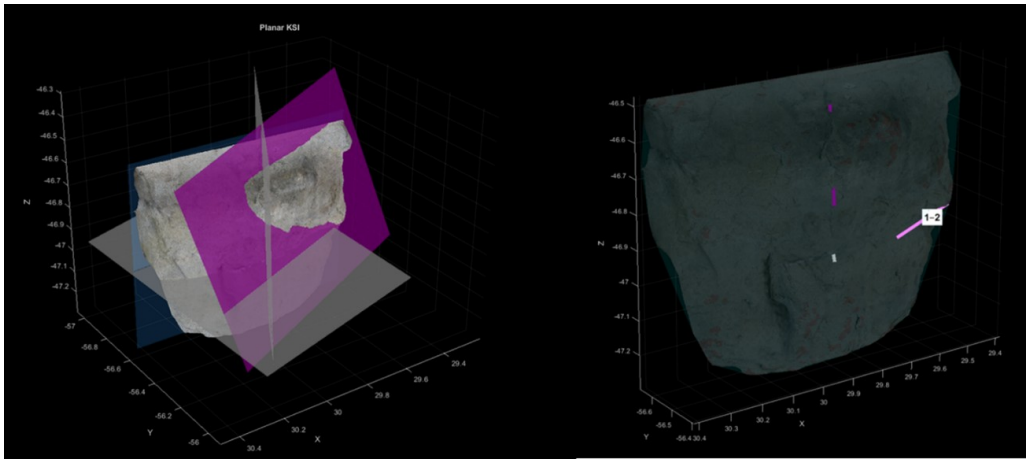


Figure 186: Stone coat of arms of Palazzo Zuccari. RoDiaN susceptibility results for planar (left) and wedge (right) kinematic.

187A and 187B, while the sliding area is illustrated in Figure 187C. The results of the dynamic analysis indicate a safety factor lower than 1, which, it should be noted, is due to the fact that the model accounts only for frictional resistance forces and excludes cohesive contributions.

Dynamic analysis was also performed on the wedge identified as susceptible to planar sliding. The volume of the block is shown in Figures 188A and 188B, while the sliding area across both discontinuities is illustrated in Figure 188C. As with the previously analyzed plane, the results of the dynamic analysis indicate a safety factor lower than 1.

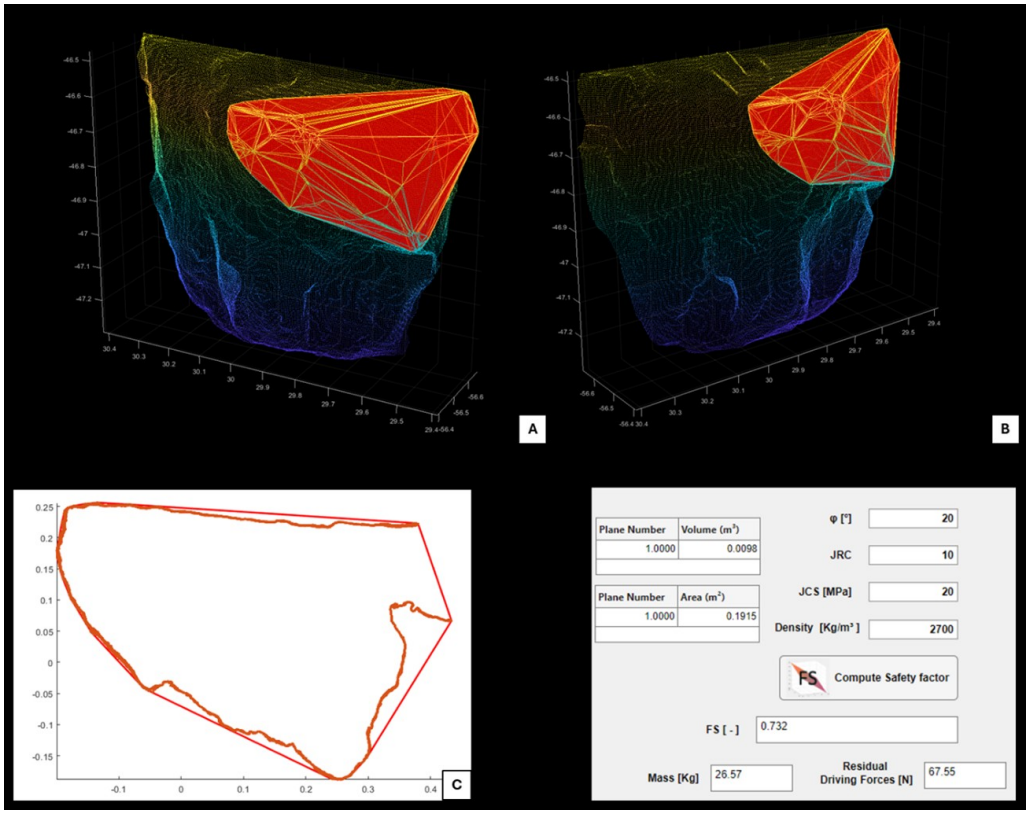


Figure 187: Stone coat of arms of Palazzo Zuccari, RoDiaN dynamic analysis results for planar sliding (A, B) and sliding area (C)

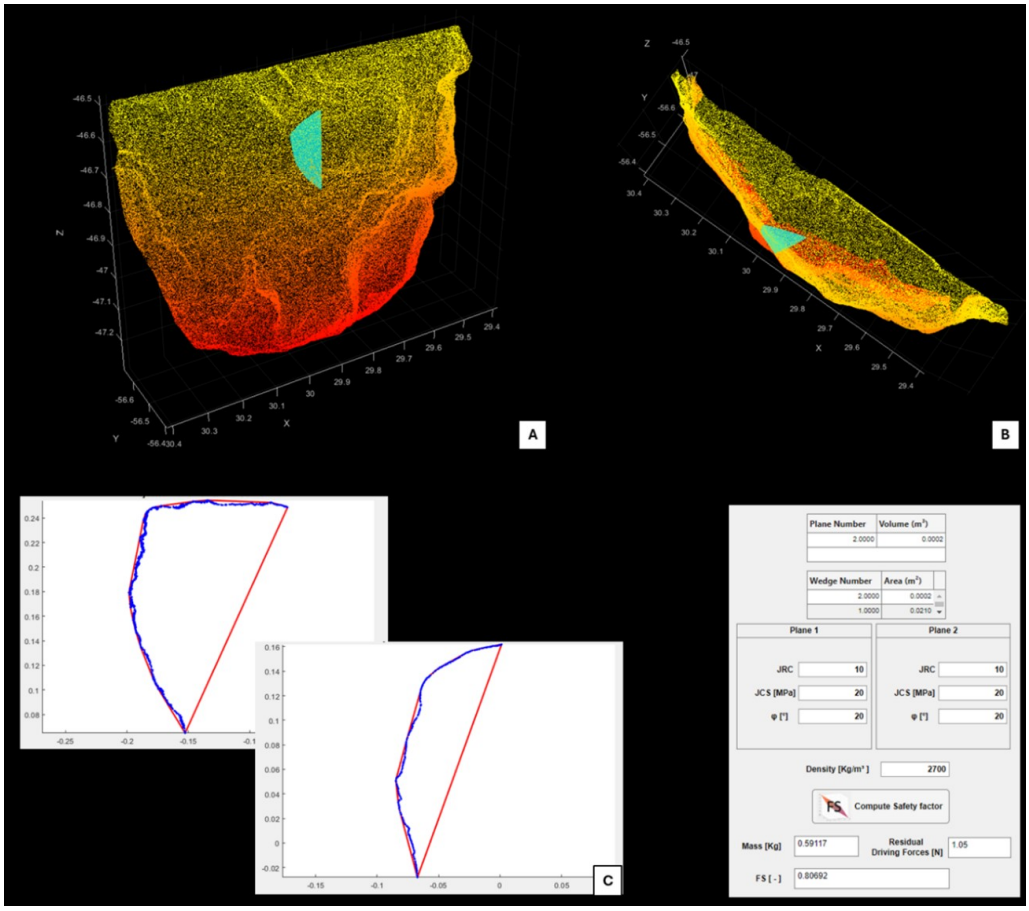


Figure 188: Stone coat of arms of Palazzo Zuccari, RoDiaN dynamic analysis results for wedge sliding (A, B) and sliding area (C)

7.4 DISCUSSION

The application of the methodology to the three historical case studies demonstrates its versatility and effectiveness in assessing kinematic susceptibility in architectural elements on historical facades. RoDiAn's modular structure proved capable of delivering meaningful partial results even in cases where its full application was not feasible or not necessary. The methodology successfully identified all possible kinematic mechanisms across different architectural contexts. The results confirm that the approach can be effectively adapted to various architectural elements, as demonstrated by the expedited analysis applied to the dentils at Palazzo Medici Riccardi and the volumetric calculations performed on cornices. This flexibility makes RoDiAn a valuable tool for diverse types of assessment in the context of historical buildings.

The three case studies also provided an opportunity to evaluate the methodology's performance across different 3D data acquisition techniques. Palazzo Pitti was analyzed using mobile laser scanning combined with photogrammetry; Palazzo Medici Riccardi was scanned using iPad LiDAR technology and drone-based photogrammetry; Palazzo Zuccari was acquired through manual photogrammetry.

The methodology is capable of processing diverse 3D input formats while maintaining consistent analytical capabilities, although each acquisition method presents specific advantages and limitations in terms of precision and data management. The need to visualize discontinuity traces on the surface requires an RGB point cloud with a resolution at least equal to the size of the trace to be identified. In cases such as Palazzo Pitti, where traces are millimetric, this requires working with extremely dense point clouds. Even disregarding the need for high-density point clouds, file management alone becomes problematic. As an indicative reference, each 3DPC block from Palazzo Pitti occupies approximately 2GB of storage. For a project like Palazzo Pitti, involving thousands of blocks, this results in a complex data management scenario. To address this, hybrid approaches were tested, such as at Palazzo Medici Riccardi, where point clouds were generated by sampling textured meshes. This approach allows discontinuities to be traced directly on RGB textures, where traces visibility is optimal. Mesh files are significantly lighter than dense 3DPCs and can be sampled at custom densities. The advantages are numerous, and the main drawback (the reduced volumetric precision of point clouds sampled from lower resolution meshes) is mitigated by RoDiAn's computational logic. While sampling meshes that do not

precisely replicate the morphology of the sample leads to some loss of volumetric accuracy, it is important to note that all RoDiAn functions involving volume calculations (e.g., wedge computation and dynamic analysis) do not operate directly on point cloud entities but instead compute a mesh. This mesh, specifically a convex hull mesh, renders the spatial accuracy advantage of high-resolution 3DPCs debatable. In the absence of computational constraints, a workflow based entirely on 3DPCs remains superior; however, the results obtained at Palazzo Medici Riccardi demonstrate that the methodology performs effectively even with lower-resolution mesh-based data. The analysis also revealed geometric limitations inherent to the approach in cases where the element exhibits specific complex three-dimensional geometry. These limitations mainly produce two kind of errors:

- A block with unusual dimensions (Block P3-B04, Figure 189) generated a false wedge when the intersection between Plane 1 and Plane 3 was considered. This error is due to the block's length, nearly 10 meters (tipical block size is 1-2m), which leads to the identification of an intersection that does not actually occur (Planes 1 and 3 do not intersect in reality), resulting in a wedge that is geometrically invalid. This issue is limited to this specific block, whose morphology is particularly atypical.

- Wedge calculations occasionally produce unrealistic volumes or geometries. This error typically occurs in irregular blocks where the convex hull does not tightly conform to the point cloud. As a result, the volume of the convex hull, used for wedge computations due to computational constraints, is slightly larger than that of the actual point cloud. If a plane intersection occurs precisely within this buffer volume, RoDiAn may identify a wedge that would not actually form within the block. This issue, which generates a false positive (an overly conservative alert), is easily recognizable by the user, as the line representing the wedge appears on the surface of the point cloud, as shown in the example in Figure 190. These boundary cases involve negligible potential falling volumes, but can skew the results if not critically evaluated.

A critical observation across all case studies is that dynamic analyses frequently yielded safety factors below 1.0. This systematic outcome requires careful interpretation within the framework of the model's assumptions and limitations. The current implementation of RoDiAn

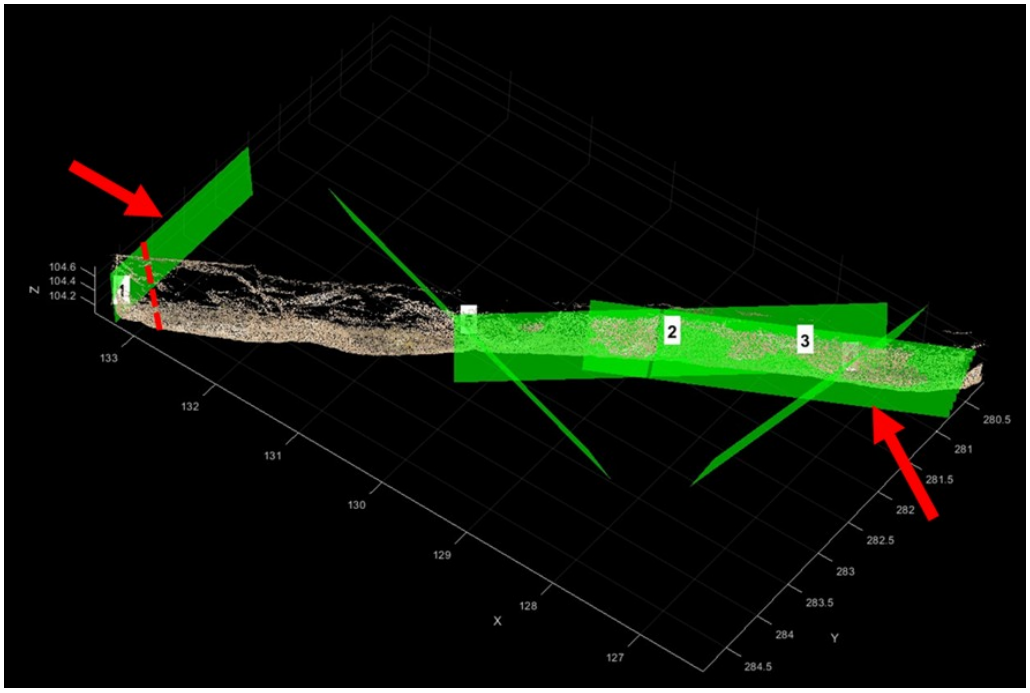


Figure 189: Example of error arising from the analysis in Block P3-B04: the intersection between Plane 1 and Plane 3 generates a wedge that is not physically valid due to the block's elongated morphology.

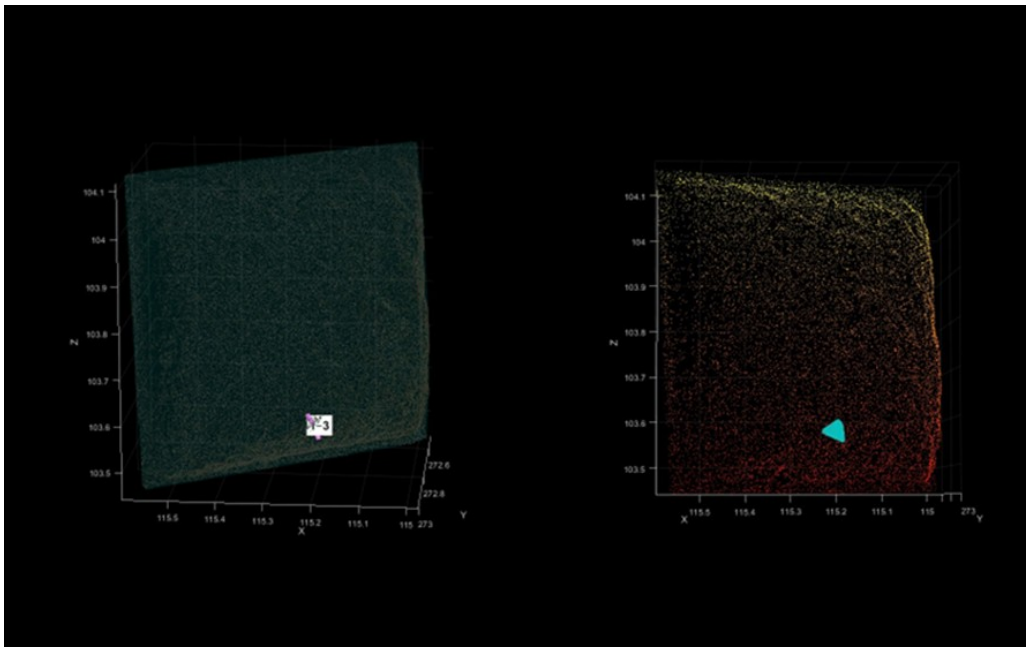


Figure 190: Example of boundary case error in RoDiAn analysis: the convex hull used for wedge computation slightly exceeds the actual point cloud, leading to identification of a wedge that does not physically form within the block. This conservative false positive is recognizable by the wedge line appearing on the surface of the point cloud.

accounts solely for frictional resistance forces, neglecting the cohesive contribution of discontinuity infill materials or mortar joints, which in real-world scenarios provide significant additional resistance. This conservative approach, which tends to overestimate instability, is intended as a screening tool to identify potentially problematic areas that warrant further investigation through traditional structural analysis methods or non-destructive testing techniques. Low safety factors should therefore be interpreted as indicators of relative instability rather than immediate failure predictions; nonetheless, the method allows for prioritization of interventions based on the obtained values. Alternatively, safety factors can be used in the form of Residual Driving Forces to support the design of stabilization systems.

The analysis reveals distinct patterns in kinematic mechanism distribution across the different case studies. Palazzo Pitti exhibits a higher frequency of multiple simultaneous kinematic mechanisms per block (56% affected blocks), while Palazzo Medici Riccardi shows a different pattern with single kinematic mechanisms being more common (67% affected blocks). Wedge sliding emerges as the most common kinematic mechanism across all case studies, followed by planar sliding. This distribution pattern suggests that intersection-controlled instabilities are more frequent than single-plane controlled failures possibly due to the inherent joint network geometry in cut stone construction.

Cases identified as susceptible to free fall mechanisms represent the most critical findings from a conservation perspective. These scenarios typically involve large block volumes with minimal restraint, creating significant safety hazards. The prevalence of such cases at Palazzo Medici Riccardi (9 out of 11 total kinematism involving a planar discontinuity) indicates that this failure mode requires priority attention in conservation planning. The occurrence of blocks that have already experienced this type of detachment, as observed during the analysis, validates the methodology's capability to identify genuine instability conditions. However, the temporal aspect of failure progression cannot be determined through kinematic analysis alone.

The results also provide compelling evidence of intentional construction practices designed to minimize kinematic instability. The predominance of discontinuities oriented perpendicular to facade planes (dip direction ±90°) suggests that medieval and Renaissance builders possessed empirical understanding of stone stability principles. This pattern is particularly evident at Palazzo Medici Riccardi, where blocks without kinematic susceptibility consistently exhibit perpendicular discontinuity

orientations. The case of block P3-B03 (Figure 157) at Palazzo Pitti, which was installed rotated 90° relative to adjacent blocks, demonstrates how deviation from optimal orientation significantly increases kinematic susceptibility. This observation reinforces the hypothesis that stone placement was carefully considered during construction, with geological features serving as primary determinants for block orientation.

8

CONCLUSIONS AND FUTURE DEVELOPMENTS

8.1 KEY FINDINGS AND PRACTICAL APPLICATIONS IN CONSERVATION

This research has successfully demonstrated the feasibility and effectiveness of adapting geomechanical methodologies from rock slope stability analysis to assess detachment susceptibility in architectural heritage elements. The development and application of the RoDiAn software, together with the supporting EZ_2JRC tool, represents a significant methodological advancement in the field of heritage conservation. The primary methodological contribution of this work lies in the successful adaptation of kinematic analysis principles to architectural heritage contexts. The research demonstrates that fundamental rock mechanics concepts like kinematic susceptibility and dynamic analysis can be modified to address the geometric and analytical needs of stone-made heritage structures.

The use of the Kinematic Susceptibility Index (KSI) provides a quantitative criterion for prioritizing architectural elements based on their geometric predisposition to failure. This makes it possible to sistematically assess large building facades , an impractical feat using conventional detailed analysis approaches. The validation of the methodology through application to three distinct case studies (Palazzo Pitti, Palazzo Medici Riccardi, and Palazzo Zuccari), confirms its versatility across different contexts.

The methodology developed in this research offers several practical advantages for heritage conservation practice that address current operational limitations. Traditional conservation approaches struggle with buildings with extensive stone surfaces made of hundreds or thousands of single elements. The workflow presented here can be applied ad systematic preliminary screening of entire facades. With the results of the RoDiAn workflow, such as the susceptibility maps presented in chapter 7, high-priority areas requiring detailed investigation can be identified.

This capability is particularly valuable for major monuments like Palazzo Pitti, where a traditional element-by-element assessment would be prohibitively time consuming and expensive. This traditional assessments usually also require access to the elements, while the presented workflow relies primarily on 3D point cloud data. The compatibility with various acquisition methods (terrestrial/mobile laser scanning, photogrammetry) also ensures adaptability to different site conditions, accessibility constraints, and budget limitations. The color-coded visual outputs of RoDiAn and the numerical susceptibility index provide intuitive communication tools for stakeholders who may lack technical backgrounds. The ability to present results as 3D models or facade maps facilitates discussions among conservators, engineers, building managers and regulatory authorities.

The modular nature of the methodology makes it possible to adapt its tools to different needs. In cases where a full kinematic and dynamic analysis is not required or feasible, individual components like volume calculation can be applied independently. This flexibility makes the approach accessible to conservation projects with varying technical capabilities and budget limitations. The volume and mass calculations generated by RoDiAn directly support engineering design of conservation interventions. Traditional conservation practice often employs empirically based anchoring systems or protective measures without rigorous quantitative design. The ability to calculate precise loads and force requirements optimize the intervention designs, potentially reducing both costs and visual impact on heritage structures.

8.2 CURRENT LIMITATIONS AND CRITICAL CONSIDERATIONS

Despite the demonstrated effectiveness of the developed methodology, several limitations must be acknowledged regarding the current implementation and interpretation of results. RoDiAn's current implementation considers only frictional resistance, neglecting cohesive forces from discontinuity infill or mortar joints. This intentionally conservative approach systematically underestimates safety factors (frequently below 1 even for stable elements), meaning results should be interpreted as relative indicators rather than absolute failure predictions. The residual driving forces provide more meaningful quantitative outputs for practical applications than safety factors alone. Volume and area calculations rely on convex hull approximations, which can overestimate actual values for elements with concave geometries. This means that the wedge calculation

algorithm occasionally produces artifacts in blocks with unusual geometries or when plane intersections occur near point cloud boundaries, though these are generally identifiable through visual inspection. Sliding area can also be overestimated, in cases where the contact surface of the discontinuity presents many concavities. This is easily identified by the operator as the area fitted is plotted against the point cloud slice for this specific reason. The reliance on manual discontinuity identification and characterization represents another significant limitation that affects both efficiency and consistency of analysis. The requirement to identify and fit planes to discontinuity traces introduces subjective elements into an otherwise quantitative methodology and represents the most time-intensive workflow component. The assumption of planar discontinuities also excludes irregular or curved failure surfaces that may occur in different materials.

Another critical consideration that occurred during the research is that the current dynamic analysis module of RoDiAn employs Barton's shear strength criterion. However, the architectural elements analyzed in this research exist in an essentially tensional stress domain with near-zero confining pressure. In such low-stress conditions, the Barton criterion's dependence on normal stress (particularly the J_{CS}/σ_n ratio) may not accurately represent actual shear resistance mechanisms. At very low normal stresses, discontinuity behavior is also influenced by surface interlocking and asperity contact rather than only stress-dependent shear resistance. Future development of failure criteria specifically calibrated for low-stress contexts will significantly improve quantitative prediction accuracy, though the kinematic susceptibility assessments remain valid as they depend on geometric relationships. The JRC determination methodology trough the development of EZ_2JRC still requires careful validation against established reference methods. The preliminary validation conducted in this research using synthetic data and limited field samples demonstrates proof-of-concept functionality, but represents only a first step in a broader ongoing research program. Critical questions remain regarding the influence of different 3D data acquisition methods (laser scanning versus photogrammetry) on JRC estimation accuracy, optimal sampling parameters for different rock surface types, and systematic comparison with traditional profiling techniques across diverse lithologies and weathering states. The current implementation should therefore be considered a research tool requiring further calibration rather than a fully validated measurement instrument.

8.3 FUTURE DEVELOPMENTS

The first future development of the methodology should prioritize automation of discontinuity identification and characterization processes. Geological features recognition and discontinuity detection from 3D point clouds or high-resolution imagery is a developing field and many methodologies could be adapted to this research [58] [97] [85] [39]. This could reduce the reliance on subjective judgement and cut the total time cost of the workflow. Another priority is the implementation of failure criteria specifically appropriate for the near-zero confining stress conditions characterizing the architectural stone elements analyzed in the research. Incorporating cohesive resistance from discontinuity infill materials would also provide more realistic safety factor estimates. The modular nature of the software allows for future integration of methods to calculate the effects of conservation interventions and to determine optimal angles for anchor installation. It should also be noted that, since the software is still in its alpha stage, it could benefit from further optimization and refinement of its functional structure to improve maintainability and facilitate future extensions. In preparation for deployment, several enhancements will be implemented, like input validation,a more robust error handling and user feedback mechanisms to improve the user experience.

8.4 CONCLUDING REMARKS

This research demonstrates that the disciplinary boundary between rock mechanics and heritage conservation is artificial and that architectural elements, regardless of their cultural significance, remain rock masses subject to the same physical principles governing natural rock slopes. However, the unique geometric configurations of architectural elements, such as limited block dimensions, complex surfaces, and confined spatial contexts, impose constraints that prevent the direct application of traditional rock mechanics software, thereby creating specific research needs that must be addressed through adapted methodologies and dedicated tools. The development of accessible software (RoDiAn and EZ_2JRC) and their successful application to major Florentine monuments demonstrates the feasibility and practical value of the methodology in addressing these issues. The ability to identify potentially unstable elements across large building facades and prioritize intervention areas addresses an operation need in conservation practice. Being able to provide quantitative data

supporting stabilization design for architectural elements is also a big improvement in a field that regularly employ empirical judgment. The tragic 2017 fatality at Santa Croce and numerous near-miss incidents in Florence underscore the urgency of developing better assessment methods for stone detachment risk. While no methodology can eliminate all uncertainty, this research provides conservation professionals with a systematic tool identifying and prioritizing potentially hazardous conditions. The tools presented here should be taken as research instruments aiming at an improved understanding of the subject rather than definitive predictive models, with quantitative outputs best interpreted as relative indicators supporting prioritization decisions rather than absolute failure predictions.

BIBLIOGRAPHY

[1] L. W. Abramson, T. S. Lee, S. Sharma, and G. M. Boyce. *Slope Stability and Stabilization Methods*. John Wiley & Sons, New York, NY, 2nd edition, 2002.

[2] C. Acidini. Un episodio fiorentino: le formelle dello studio zuccari nella facciata-manifesto. In C. Acidini and E. Capretti, editors, *Innocente e calunniato. Federico Zuccari (1539/40–1609) e le vendette d'artista*, pages 164–171. Giunti, Firenze, 2009. Catalogo della mostra, Gabinetto Disegni e Stampe degli Uffizi, 6 dicembre 2009–28 febbraio 2010.

[3] C. Acidini Luchinat. *I restauri nel Palazzo Medici Riccardi: Rinascimento e barocco*. Banca Toscana, Firenze, 1992.

[4] C. Alonso, C. Andrade, J. Rodriguez, and J. M. Diez. Factors controlling cracking of concrete affected by reinforcement corrosion. *Materials and Structures*, 31:435–441, 1998.

[5] C. Alves, C. A. M. Figueiredo, J. Sanjurjo-Sánchez, and A. C. Hernández. Effects of Water on Natural Stone in the Built Environment—A Review. *Geosciences*, 11(11):459, November 2021.

[6] G. Amoroso and V. Fasina. Stone decay and conservation; Atmospheric pollution, cleaning; and consolidation. 1983. Publisher: Elsevier Science Pub., New York, NY.

[7] C. Arrighi, M. Tanganelli, M. T. Cristofaro, V. Cardinali, A. Marra, F. Castelli, and M. De Stefano. Multi-risk assessment in a historical city. *Natural Hazards*, 119:1041–1072, January 2023. Open access.

[8] M. Askaripour, A. Saeidi, P. Mercier-Langevin, and A. Rouleau. A review of relationship between texture characteristic and mechanical properties of rock. *Geotechnics*, 2(1):262–296, 2022.

[9] P. G. Asteris, M. P. Chronopoulos, C. Z. Chrysostomou, H. Varum, V. Plevris, N. Kyriakides, and V. Silva. Seismic vulnerability assessment of historical masonry structural systems. *Engineering Structures*, 62–63:118–134, March 2014.

[10] Australia ICOMOS. The burra charter: The australia icomos charter for places of cultural significance 1999. Australia ICOMOS Inc., with associated guidelines and code on the ethics of co-existence, 1999.

[11] A. Banchelli, F. Fratini, M. Germani, P. Malesani, and C. Manganelli Del Fà. The sandstones of the florentine historic buildings: individuation of the marker and determination of the supply quarries of the rocks used in some florentine monuments. *Science and Technology for Cultural Heritage*, 6(1):13–22, 1997.

[12] S. Bandis. *Experimental Studies of Scale Effects on Shear Strength, and Deformation of Rock Joints*. PhD thesis, University of Leeds, Leeds, UK, 1980.

[13] N. Barton. Review of a new shear-strength criterion for rock joints. *Engineering Geology*, 7(4):287–332, January 1973.

[14] N. Barton and V. Choubey. The shear strength of rock joints in theory and practice. In *Proceedings of the International Symposium on Rock Mechanics*, pages 1–10, Lisbon, Portugal, 1976.

[15] N. Barton and V. Choubey. The shear strength of rock joints in theory and practice. *Rock Mechanics*, 10(1-2):1–54, 1977.

[16] A. J. Beer, D. Stead, and J. S. Coggan. Estimation of the joint roughness coefficient (jrc) by visual comparison. *Rock Mechanics and Rock Engineering*, 35:65–74, February 2002. Technical Note.

[17] G. Belli. *Paramenti bugnati e architettura nella Firenze del Quattrocento*. Firenze University Press, 2019. Formato: e-book.

[18] V. Bonora, I. Centauro, L. Fiorini, A. Conti, T. Salvatici, S. Calandra, R. Raffa, E. Intrieri, C. A. Garzonio, and G. Tucci. Virtual inspection based on 3d survey supporting risks detachment analysis in pietraforte stone built heritage. *The International Archives of the Photogrammetry, Remote Sensing and Spatial Information Sciences*, XLVIII-M-2-2023:273–280, 2023.

[19] E. Borsook. *Ecco Firenze: Guida ai luoghi e nel tempo*. Ugo Mursia Editore, 1 edition, 1972. Edizione n. 189.

[20] V. Bosiljkov, M. Uranjek, R. Žarnić, and V. Bokan-Bosiljkov. An integrated diagnostic approach for the assessment of historic masonry structures. *Journal of Cultural Heritage*, 11(3):239–249, July 2010.

[21] P. Brimblecombe, editor. *The Effects of Air Pollution on the Built Environment*, volume 2 of *Air Pollution Reviews*. Imperial College Press, London, UK, 2003.

[22] E. T. Brown and E. Hoek. *Underground Excavations in Rock*. CRC Press, Boca Raton, FL, first edition edition, 1980.

[23] S. Calandra, I. Centauro, T. Salvatici, E. Pecchioni, and C. A. Garzonio. Monitoring and Evaluation of Pietra Serena Decay Adopting NDT Techniques: Application on Building Stones in Situ. In Furferi R., Governi L., Volpe Y., Gherardini F., and Seymour K., editors, *The Future of Heritage Science and Technologies*, pages 292–304. Springer International Publishing, Cham, 2023. Series Title: Lecture Notes in Mechanical Engineering.

[24] I. Centauro, J. G. Vitale, S. Calandra, T. Salvatici, C. Natali, M. Coppola, E. Intrieri, and C. A. Garzonio. A multidisciplinary methodology for technological knowledge, characterization and diagnostics: Sandstone facades in florentine architectural heritage. *Applied Sciences*, 12(9):4266, 2022. Received: 22 Mar 2022; Revised: 20 Apr 2022; Accepted: 21 Apr 2022; Published: 23 Apr 2022.

[25] N. Chen, X. Cai, S. Li, X. Zhang, and Q. Jiang. Automatic extraction of rock mass discontinuity based on 3d laser scanning. *Quarterly Journal of Engineering Geology and Hydrogeology*, 54(1):187–198, February 2021.

[26] M. Chiarini. *Pitti Palace, Art and History*. Becocci Editore, 1973. Guide to the history and artistic heritage of Palazzo Pitti, Florence.

[27] M. Chigira and T. Oyama. Mechanism and effect of chemical weathering of sedimentary rocks. *Developments in Geotechnical Engineering*, 84:267–278, 2000.

[28] C. Coletti. Climate Change Threats to Stone Cultural Heritage: State of the Art of Quantitative Damage Functions and New Challenges for a Sustainable Future. *Heritage*, 7(6):3276–3290, June 2024.

[29] M Coli. The boboli garden, firenze (italy): from quarryscape to place of delights. In *Natural Stone for Cultural Heritage: Local Resources with a Global Impact, International Conference on "Natural Stone for Cultural Heritage: Local Resources with a Global Impact", Abstract Book*, pages 1–13, 2021.

[30] M. Coli, T. Donigaglia, M. T. Cristofaro, M. Tanganelli, and S. Viti. Assessments on the material properties of the Pietraforte stone of Florence (Italy) in conservation, restoration and construction. *Case Studies in Construction Materials*, 16:e00986, June 2022.

[31] V. Comite, M. Ricca, S. A. Ruffolo, S. F. Graziano, N. Rovella, C. Rispoli, C. Gallo, L. Randazzo, D. Barca, P. Cappelletti, and M. F. La Russa. Multidisciplinary approach for evaluating the geochemical degradation of building stone related to pollution sources in the historical center of naples (italy). *Applied Sciences*, 10(12):4241, June 2020.

[32] C. Cresti. *Firenze, capitale mancata: Architettura e città dal piano Poggi a oggi*. Electa, 1995. Brossura. Digitized by the University of Virginia, 24 Mar 2010.

[33] J. Delgado Rodrigues. Defining, mapping and assessing deterioration patterns in stone conservation projects. *Journal of Cultural Heritage*, 16(3):267–275, May 2015.

[34] C. Di Benedetto, P. Cappelletti, M. Favaro, S. F. Graziano, A. Langella, D. Calcaterra, and A. Colella. Porosity as key factor in the durability of two historical building stones: Neapolitan yellow tuff and vicenza stone. *Engineering Geology*, 193:1–10, 2015.

[35] İ. Dinçer, A. Orhan, P. Frattini, and G. B. Crosta. Rockfall at the heritage site of the Tatlarin Underground City (Cappadocia, Turkey). *Natural Hazards*, 82(2):1075–1098, June 2016.

[36] J. M. Duncan. *Soil Strength and Slope Stability*. New York Academy of Sciences Series. John Wiley & Sons, Incorporated, Newark, 1st ed edition, 2014.

[37] J. Michael Duncan. State of the art: Limit equilibrium and finite-element analysis of slopes. *Journal of Geotechnical Engineering*, 122(7):577–596, 1996.

[38] S. N. Emery and A. E. Charola. Coatings on brick masonry: Are they protective or can they enhance deterioration? *Journal of the American Institute for Conservation*, 46(1):39–52, 2007.

[39] M. Esmaeili, T. Beni, G. Gigli, and V. Tofani. Rock mass exposure fracture detection through 2D close-range images using image processing techniques: a review. *Earth Science Informatics*, 18(3):494, September 2025.

[40] F. Faccini, E. Raso, C. Malgarotto, and G. Antonielli. Rockfall risk assessment and management along the "via dell'amore" (lovers' lane) in the cinque terre national park (italy). In G. Lollino, A. Manconi, J. Clague, W. Shan, and M. Chiarle, editors, *Engineering Geology for Society and Territory – Volume 2*, pages 2015–2019.

[41] R. Fanti, G. Gigli, L. Lombardi, D. Tapete, and P. Canuti. Terrestrial laser scanning for rockfall stability analysis in the cultural heritage site of Pitigliano (Italy). *Landslides*, 10(4):409–420, August 2013.

[42] F. Fratini and S. Rescic. The stone materials of the historical architecture of Tuscany, Italy. *Geological Society, London, Special Publications*, 391(1):71–92, January 2014.

[43] D. M. Freire-Lista and R. Fort. Causes of scaling on bush-hammered heritage ashlars: a case study—Plaza Mayor of Madrid (Spain). *Environmental Earth Sciences*, 75(10):932, May 2016.

[44] D. M. Freire-Lista, L. Sousa, R. Carter, and F. Al-Na'īmī. Petrographic and petrophysical characterisation and structural function of the heritage stones in fuwairit archaeological site (ne qatar): implications for heritage conservation. *Episodes*, 44(1):43–58, March 2021.

[45] W. Frodella, M. Elashvili, D. Spizzichino, G. Gigli, A. Nadaraia, G. Kirkitadze, L. Adikashvili, C. Margottini, N. Antidze, and N. Casagli. Applying Close Range Non-Destructive Techniques for the Detection of Conservation Problems in Rock-Carved Cultural Heritage Sites. *Remote Sensing*, 13(5):1040, March 2021.

[46] W. Frodella, L. Lombardi, M. Nocentini, and G. Gigli. Ground based remote sensing techniques for the san leo (northern italy) rock cliff monitoring. In *Proceedings of the X Congresso dei Giovani Ricercatori di Geologia Applicata*, Bologna, Italy, February 2016. University of Florence, Department of Earth Sciences.

[47] G. Gigli and N. Casagli. Semi-automatic extraction of rock mass structural data from high resolution lidar point clouds. *International Journal of Rock Mechanics and Mining Sciences*, 48(2):187–198, 2011.

[48] G. Gigli, W. Frodella, F. Mugnai, D. Tapete, F. Cigna, R. Fanti, E. Intrieri, and L. Lombardi. Instability mechanisms affecting cultural heritage sites in the maltese archipelago. *Natural Hazards and Earth System Sciences*, 12:1883–1903, June 2012.

[49] L. Ginori Lisci. *I palazzi di Firenze nella storia e nell'arte, Volume 2*. Giunti, G. Barbèra, 1972. Digitized by the University of Michigan, 16 Nov 2009. Total length: 886 pages.

[50] F. Giuliani, A. De Falco, V. Cutini, and M. Di Sivo. A simplified methodology for risk analysis of historic centers: the world heritage site of San Gimignano, Italy. *International Journal of Disaster Resilience in the Built Environment*, 12(3):336–354, May 2021.

[51] R. E. Goodman and J. W. Bray. Toppling of rock slopes. In *Proceedings of the Specialty Conference on Rock Engineering for Foundations and Slopes*, volume 2, pages 201–234, University of California, Berkeley, 1976. ASCE.

[52] V. K. Gopinath and R. Ramadoss. Review on structural health monitoring for restoration of heritage buildings. *Materials Today: Proceedings*, 43:1534–1538, October 2021.

[53] M. Groh, J. Orlowsky, and R. Schulte Holthausen. Analysing the porosity distribution in stone surfaces by means of unilateral nmr after long-term outdoor weathering. *Materials*, 15(13):4604, 2022.

[54] D. Guha Roy and T. N. Singh. Fracture and tensile properties of the layered crystalline rocks. In *Proceedings of the 7th Indian Rock Conference (INDOROCK-2017)*, Delhi, India, October 2017.

[55] J. Guo, Y. Liu, L. Wu, S. Liu, T. Yang, W. Zhu, and Z. Zhang. A geometry- and texture-based automatic discontinuity trace extraction method for rock mass point cloud. *International Journal of Rock Mechanics and Mining Sciences*, 124:104132, December 2019.

[56] J. Guo, L. Wu, M. Zhang, S. Liu, and X. Sun. Towards automatic discontinuity trace extraction from rock mass point cloud without triangulation. *International Journal of Rock Mechanics and Mining Sciences*, 112:226–237, December 2018.

[57] J. Guo, Z. Zhang, Y. Mao, S. Liu, W. Zhu, and T. Yang. Automatic extraction of discontinuity traces from 3d rock mass point clouds considering the influence of light shadows and color change. *Remote Sensing*, 14(21):5314, 2022.

[58] J. Guo, Z. Zhang, Y. Mao, S. Liu, W. Zhu, and T. Yang. Automatic Extraction of Discontinuity Traces from 3D Rock Mass Point Clouds Considering the Influence of Light Shadows and Color Change. *Remote Sensing*, 14(21):5314, October 2022.

[59] S. Guo, H. Pu, M. Yang, and X. Junce. Study of the influence of clay minerals on the mechanical and percolation properties of weakly cemented rocks. *Geofluids*, 2022.

[60] B. Guru and S. D. Santha. People-centred early warning systems and disaster risk reduction: A scoping study of public participatory geographical information systems (ppgis) in india. Technical report, Tata Institute of Social Sciences (TISS), December 2013. Prepared for the Global Assessment Report on Disaster Risk Reduction 2015.

[61] K. Hall. Evidence for freeze–thaw events and their implications for rock weathering in northern canada. *Earth Surface Processes and Landforms*, 2003.

[62] D. Heikamp. Federico zuccari a firenze: 1575–1579. ii. federico a casa sua. *Paragone Arte*, 18(207):3–34, 1967.

[63] D. Heikamp. Le case di federico zuccari a firenze: aggiornamento sulla loro storia e significato. *Dialoghi di Storia dell'Arte*, 3:4–31, 1996.

[64] K. F. B. Hempel. Notes on the conservation of sculpture, stone, marble and terracotta. *Studies in conservation*, 13(1):34–44, 1968. Publisher: Taylor & Francis.

[65] E. Hoek and J. Bray. *Rock slope engineering*. Published for the Institution of Mining and Metallurgy by E & FN Spon, London, 3rd rev. ed edition, 1981. OCLC: 1100420287.

[66] International Council on Monuments and Sites. International charter for the conservation and restoration of monuments and sites (the venice charter 1964). Adopted at the IInd International Congress of Architects and Technicians of Historic Monuments, Venice, 1964, 1964. Adopted by ICOMOS in 1965.

[67] International Society for Rock Mechanics. *Suggested Methods for the Quantitative Description of Discontinuities in Rock Masses*. International Society for Rock Mechanics, Lisbon, Portugal, 1978. Commission on Standardization of Laboratory and Field Tests.

[68] Y. Israeli and S. Emmanuel. Impact of grain size and rock composition on simulated rock weathering. *Earth Surface Dynamics*, 6(2):319–327, 2018.

[69] J. C. Jaeger. Shear failure of anistropic rocks. *Geological Magazine*, 97(1):65–72, 1960.

[70] S.-H. Jiang, J.-D. Chen, and J. Huang. Stability analysis of jointed rock slopes based on the universal elliptical disc model. In *Geo Shanghai International Conference 2024 – Volume 2: Rock Mechanics and Rock Engineering*, volume 1331 of *IOP Conference Series: Earth and Environmental Science*, page 012002, Shanghai, China, May 2024. IOP Publishing. Published under licence by IOP Publishing Ltd.

[71] J. Kundu, K. Sarkar, A. K. Verma, and T. N. Singh. Novel methods for quantitative analysis of kinematic stability and slope mass rating in jointed rock slopes with the aid of a new computer application. *Bulletin of Engineering Geology and the Environment*, 81(1), January 2022. Publisher: Springer Science and Business Media LLC.

[72] S. Lagomarsino. On the vulnerability assessment of monumental buildings. *Bulletin of Earthquake Engineering*, 4:445–463, 2006.

[73] A. Langella, D. Calcaterra, P. Cappelletti, S. Ciarcia, M. D'Amore, D. Di Martire, S. F. Graziano, and M. De Gennaro. An Example of Integrated Geological Survey of Geomaterials and their Weathering Forms: the *Reggia di Caserta* Main Façade. *Studies in Conservation*, 68(4):432–444, May 2023.

[74] A. Langella, D. Calcaterra, P. Cappelletti, S. Ciarcia, M. D'Amore, D. Di Martire, S. F. Graziano, and M. De Gennaro. An Example of Integrated Geological Survey of Geomaterials and their Weathering Forms: the *Reggia di Caserta* Main Façade. *Studies in Conservation*, 68(4):432–444, May 2023.

[75] L. Lazzarini and M.L. Tabasso. *Il restauro della pietra*. CEDAM, 1986.

[76] Y.-H. Lee, J. R. Carr, D. J. Barr, and C. J. Haas. The fractal dimension as a measure of the roughness of rock discontinuity profiles. *International Journal of Rock Mechanics and Mining Sciences & Geomechanics Abstracts*, 27(6):453–464, December 1990.

[77] F. Lemy and J. Hadjigeorgiou. Discontinuity trace map construction using photographs of rock exposures. *International Journal of Rock Mechanics and Mining Sciences*, 40(6):903–917, September 2003.

[78] Y. Li and Y. Zhang. Quantitative estimation of joint roughness coefficient using statistical parameters. *International Journal of Rock Mechanics and Mining Sciences*, 77:27–35, July 2015.

[79] Ugo Losacco. *Osservazioni geologiche sulla Pietraforte dei dintorni di Firenze*. Arti grafiche Pacini Mariotti, 1963.

[80] Feilden B. M. *Conservation of Historic Buildings*. Butterworth Scientific, London; Boston, 1982. Internet Archive collection.

[81] P. Malesani, E. Pecchioni, E. Cantisani, and F. Fratini. Geolithology and provenance of materials of some historical buildings and monuments in the centre of Florence (Italy). *Episodes*, 26(3):250–255, September 2003.

[82] J. T. Markland. A useful technique for estimating the stability of rock slopes when the rigid wedge slide type of failure is expected. Technical report, Imperial College of Science and Technology, London, UK, 1972.

[83] K. Marsch and T. M. Fernandez-Steeger. Comparative Evaluation of Statistical and Fractal Approaches for JRC Calculation Based on a Large Dataset of Natural Rock Traces. *Rock Mechanics and Rock Engineering*, 54(4):1897–1917, April 2021.

[84] D. M. McCann and M. C. Forde. Review of ndt methods in the assessment of concrete and masonry structures. *NDT & E International*, 34(2):71–84, March 2001.

[85] S. Mehrishal, J. Kim, Y. Shao, and J. J. Song. Artificial intelligence-aided semi-automatic joint trace detection from textured three-dimensional models of rock mass. *Journal of Rock Mechanics and Geotechnical Engineering*, 17(4):1973–1985, April 2025.

[86] N. Menegoni, D. Giordan, R. Inama, and C. Perotti. Dice: An open-source matlab application for quantification and parametrization of digital outcrop model-based fracture datasets. *Journal of Rock Mechanics and Geotechnical Engineering*, 15(5):1090–1110, May 2023. Open access under a Creative Commons license.

[87] N. Menegoni, D. Giordan, and C. Perotti. An open-source algorithm for 3d rock slope kinematic analysis (roka). *Applied Sciences*, 11(4):1698, 2021. Published: 14 Feb 2021. Special Issue: 3D Jointed Rock Mass Structural Analysis and Evaluation of Rockfall Potential.

[88] F. Meng, Y. Zhai, Y. Li, R. Zhao, Y. Li, and H. Gao. Research on the effect of pore characteristics on the compressive properties of sandstone after freezing and thawing. *Engineering Geology*, 286:106088, 2021.

[89] S. Mineo and G. Pappalardo. Sustainable Fruition of Cultural Heritage in Areas Affected by Rockfalls. *Sustainability*, 12(1):296, December 2019.

[90] R. M. Murray, Z. Li, and S. S. Sastry. *A mathematical introduction to robotic manipulation*. CRC, Boca Raton [etc.], 1994.

[91] A. Palamidessi, E. Intrieri, T. Salvatici, I. Centauro, and C. A. Garzonio. Risk of falling stone material on the ramps of piazzale michelangelo in florence. In *EGU General Assembly 2024*, Vienna, Austria and Online, April 2024.

[92] Palazzo Medici Riccardi. *Palazzo Medici Riccardi - guida*. Officina libraria, Milano, 2021.

[93] G. Pappalardo, R. Punturo, S. Mineo, and L. Contrafatto. The role of porosity on the engineering geological properties of 1669 lavas from mount etna. *Engineering Geology*, 221:16–28, 2017.

[94] E. Pecchioni, F. Fratini, E. Pandeli, E. Cantisani, and S. Vettori. Pietraforte, the Florentine building material from the Middle Ages to contemporary architecture. *Episodes*, 44(3):259–271, September 2021.

[95] E. Pecchioni, F. Fratini, E. Pandeli, E. Cantisani, and S. Vettori. Pietraforte, the Florentine building material from the Middle Ages to contemporary architecture. *Episodes*, 44(3):259–271, September 2021.

[96] L. Peck, C. C. Barton, and R. B. Gordon. Microstructure and the resistance of rock to tensile fracture. *Journal of Geophysical Research: Solid Earth*, 90(B13):11533–11541, 1985.

[97] X. Peng, P. Lin, H. Sun, and M. Wang. A Semi-automatic Method to Recognize Discontinuity Trace in 3D Point Clouds Based on Stacking Learning. *Mining, Metallurgy & Exploration*, 42(1):433–448, February 2025.

[98] H. Phillips. The capacity to adapt to climate change at heritage sites—the development of a conceptual framework. *Environmental Science & Policy*, 47:118–125, March 2015.

[99] D. M. Potts and L. Zdravković. *Finite element analysis in geotechnical engineering: theory*. Telford ; Distributed by ASCE Press, London : Reston, VA, 1999.

[100] D. Priest Stephen. *Discontinuity Analysis for Rock Engineering*. Chapman & Hall, London, UK, 1993.

[101] T. Ramamurthy, Rao G. Venkatappa, and J. Singh. A strength criterion for anisotropic rocks. In *Proceedings of the Fifth Australia-New Zealand Conference on Geomechanics*, Sydney, Australia, August 1988. Australia-New Zealand Conference on Geomechanics.

[102] M. Ravan, M. J. Revez, I. V. Pinto, P. Brum, and J. Birkmann. A Vulnerability Assessment Framework for Cultural Heritage Sites: The Case of the Roman Ruins of Tróia. *International Journal of Disaster Risk Science*, 14(1):26–40, February 2023.

[103] T.R. Reid and J.P. Harrison. A semi-automated methodology for discontinuity trace detection in digital images of rock mass exposures. *International Journal of Rock Mechanics and Mining Sciences*, 37(7):1073–1089, October 2000.

[104] Repubblica Italiana. Decreto legislativo 22 gennaio 2004, n. 42: Codice dei beni culturali e del paesaggio, ai sensi dell'articolo 10 della legge 6 luglio 2002, n. 137. Gazzetta Ufficiale n. 45 del 24 febbraio 2004, Supplemento Ordinario n. 28, 2004.

[105] Adrián J. Riquelme, A. Abellán, R. Tomás, and M. Jaboyedoff. A new approach for semi-automatic rock mass joints recognition from 3d point clouds. *Computers & Geosciences*, 68:38–52, July 2014.

[106] Rocscience Inc. *Dips: Stereographic Projection Software for the Analysis of Orientation Data*. Rocscience Inc., Toronto, Canada, 2021. User Manual and Technical Documentation. Available at: https://www.rocscience.com/software/dips.

[107] Rocscience Inc. *RocSlope2:3D Stability Analysis Software*. Rocscience Inc., Toronto, Canada, 2021. User Manual and Technical Documentation. Available at: https://www.rocscience.com/software/rocslope2.

[108] Rocscience Inc. *RocSlope3: 3D Limit Equilibrium Slope Stability Analysis for Rock Slopes*. Rocscience Inc., Toronto, Canada, 2021. User Manual and Technical Documentation. Available at: https://www.rocscience.com/software/rocslope3.

[109] F. Rodolico. *Le pietre delle città d'Italia*. F. Le Monnier, 1953.

[110] C. Rodriguez-Navarro and E. Doehne. Salt weathering: Influence of evaporation rate, supersaturation and crystallization pattern. *Earth Surface Processes and Landforms*, 24(3):191–209, 1999.

[111] M. Romana. A geomechanical classification for slopes: Slope mass rating. In *Rock Testing and Site Characterization: Principles, Practice and Projects*, pages 575–600. 1993.

[112] M. Romana, R. Tomás, and J. B. Serón. Slope mass rating (smr) geomechanics classification: thirty years review. 2015.

[113] N. Rosser, M. Lim, D. Petley, S. Dunning, and R. Allison. Patterns of precursory rockfall prior to slope failure. *Journal of Geophysical Research: Earth Surface*, 112, December 2007.

[114] L. G. F. Salazar, X. Romão, and R. Figueiredo. A hybrid approach for the assessment of flood vulnerability of historic constructions and their contents. In *Structural Analysis of Historical Constructions (SAHC 2023)*, volume 46 of *RILEM Bookseries*, pages 1117–1133. Springer, 2023.

[115] S. Salomone. Il «capriccio regolato». l'interpretazione della natura nella architettura di federico zuccari. In M. Fagiolo, editor, *Natura e artificio*. Officina, Roma, 1981.

[116] T. Salvatici, S. Calandra, I. Centauro, E. Pecchioni, E. Intrieri, and C. A. Garzonio. Monitoring and Evaluation of Sandstone Decay

Adopting Non-Destructive Techniques: On-Site Application on Building Stones. *Heritage*, 3(4):1287–1301, November 2020.

[117] T. Salvatici, I. Centauro, S. Calandra, E. Segabinazzi, E. Intrieri, and C. A. Garzonio. Non-destructive methods applied for in situ mechanical
Heritage Science, 11:116, 2023. Received: 13 Dec 2022; Accepted: 20 May 2023; Published: 30 May 2023. Licensed under CC BY 4.0.

[118] T. Salvatici, I. Centauro, E. Segabinazzi, S. Calandra, E. Intrieri, and C. A. Garzonio. Multi-analytical methodology to indagate the pietraforte sandstone risk assessment. In *EGU General Assembly 2023*, Vienna, Austria and Online, April 2023. Abstract ID: EGU-14744. Published: May 2023.

[119] T. Salvatici, I. Centauro, E. Segabinazzi, S. Calandra, E. Intrieri, and C. A. Garzonio. Multi-analytical methodology to indagate the Pietraforte sandstone risk assessment, May 2023.

[120] T. Salvatici, I. Centauro, E. Segabinazzi, S. Calandra, F. Pilati, C. A. Garzonio, and E. Intrieri. An integrated methodology of ndts for the characterization of stone pillars and columns. *Restauro Archeologico*, 32(2):200, 2024.

[121] T. Salvatici, M. V. de Mitri, I. Centauro, S. Calandra, E. Segabinazzi, G. Curatella, C. A. Garzonio, and A. P. Santo. A conservation study of sandstone: The church of orsanmichele in florence (italy). In *Lecture Notes in Mechanical Engineering*, pages 93–104. Springer, 2026.

[122] S. Scrivano, L. Gaggero, and J. Gisbert Aguilar. Micro-porosity and minero-petrographic features influences on decay: Experimental data from four dimension stones. *Construction and Building Materials*, 173:342–349, 2018.

[123] E. Segabinazzi, T. Salvatici, I. Centauro, S. Calandra, and C. A. Garzonio. Assessing weathering damage in arenitic rock using non-destructive testing: The case study of the stone coats of arms of palazzo ricasoli in florence. In *EGU General Assembly 2023*, Vienna, Austria and Online, April 2023. Abstract ID: EGU-13699. Published: May 2023.

[124] E. Segabinazzi, T. Salvatici, I. Centauro, E. Intrieri, S. Calandra, and C. A. Garzonio. Applying a geomechanical approach to mitigate rockfall risk from stone heritage buildings. In *New Challenges in Rock Mechanics and Rock Engineering*, pages 1–6. CRC Press, 1st edition, 2024.

[125] E. Sesana, A. S. Gagnon, C. Ciantelli, J. Cassar, and J. J. Hughes. Climate change impacts on cultural heritage: A literature review. *Wiley Interdisciplinary Reviews: Climate Change*, 2021.

[126] T. Siddique. Rock mass classification in slope engineering with special emphasis on Slope mass rating: Current status and future projections. *Geological Journal*, 59(9):2472–2486, September 2024. Publisher: Wiley.

[127] S. Siegesmund, T. Weiss, and A. Vollbrecht. Natural stone, weathering phenomena, conservation strategies and case studies: Introduction. *Geological Society, London, Special Publications*, 205:1–7, 01 2002.

[128] B. J. Smith, M. Gomez-Heras, and S. McCabe. Understanding the decay of stone-built cultural heritage. *Progress in Physical Geography: Earth and Environment*, 32(4):439–461, August 2008.

[129] R. Tomás, J. Delgado, and J.B. Serón. Modification of slope mass rating (SMR) by continuous functions. *International Journal of Rock Mechanics and Mining Sciences*, 44(7):1062–1069, October 2007. Publisher: Elsevier BV.

[130] Roberto Tomás, editor. *New Challenges in Rock Mechanics and Rock Engineering proceedings of the ISRM Rock Mechanics Symposium 2024 EUROCK 2024, 15-19 July 2024, Alicante, Spain*. CRC Press, Boca Raton, first edition edition, 2024.

[131] R. Tse and D.M. Cruden. Estimating joint roughness coefficients. *International Journal of Rock Mechanics and Mining Sciences & Geomechanics Abstracts*, 16(5):303–307, October 1979.

[132] A. Tugrul and I. H. Zarif. The influence of mineralogical textural and chemical characteristics on the durability of selected sandstones in istanbul, turkey. *Bulletin of Engineering Geology and the Environment*, 57(2):185–190, 1998.

[133] N. Turk, M. J. Greig, W. R. Dearman, and F. F. Amin. Characterization of rock joint surfaces by fractal dimension. In *Proceedings of the 28th U.S. Symposium on Rock Mechanics (USRMS)*, Tucson, Arizona, USA, June 1987. American Rock Mechanics Association. Paper Number: ARMA-87-1223. Published: June 29, 1987.

[134] A. Valagussa, P. Frattini, G. Crosta, D. Spizzichino, G. Leoni, and C. Margottini. Multi-risk analysis on european cultural and natural unesco heritage sites. *Natural Hazards*, 105:2659–2676, 2021.

[135] M. J. Varas-Muriel, E. M. Pérez-Monserrat, C. Vázquez-Calvo, and R. Fort. Effect of conservation treatments on heritage stone. characterisation of decay processes in a case study. *Construction and Building Materials*, 95:611–622, October 2015.

[136] V. Vergès-Belmin. *ICOMOS-ISCS: illustrated glossary on stone deterioration patterns*. Number 15 15 in Monuments and sites. ICOMOS, Paris, english-french version edition, 2008.

[137] H. A. Viles. Linking weathering and rock slope instability: nonlinear perspectives. *Earth Surface Processes and Landforms*, 2012.

[138] Z. Vojinovic, M. Hammond, D. Golub, S. Hirunsalee, S. Weesakul, V. Meesuk, N. Medina, A. Sanchez, S. Kumara, and Abbott M. Holistic approach to flood risk assessment in areas with cultural heritage: a practical application in ayutthaya, thailand. *Natural Hazards*, 81:589–616, December 2016. Open access.

[139] Z. Waźbiński. Lo studio – la scuola fiorentina di federico zuccari. *Mitteilungen des Kunsthistorischen Institutes in Florenz*, 29(2–3):275–346, 1985.

[140] H. Weber. Conservation and restoration of natural stone in europe. *Bulletin of the Association for Preservation Technology*, 17(2):15–23, 1985. Publisher: JSTOR.

[141] X. Wu, F. Wang, M. Wang, X. Zhang, Q. Wang, and S. Zhang. A new method for automatic extraction and analysis of discontinuities based on tin on rock mass surfaces. *Remote Sensing*, 13(15):2894, 2021.

[142] J. Yan, J. Chen, C. Tan, Y. Zhang, Y. Liu, X. Zhao, and Q. Wang. Rockfall source areas identification at local scale by integrating

discontinuity-based threshold slope angle and rockfall trajectory analyses. *Engineering Geology*, 313:106993, February 2023.

[143] O. C. Zienkiewicz, R. L. Taylor, and J. Zhu, editors. *The finite element method: its basis and fundamentals*. Elsevier Butterworth-Heinemann, Amsterdam Boston, 6th ed edition, 2005.

9

APPENDIX

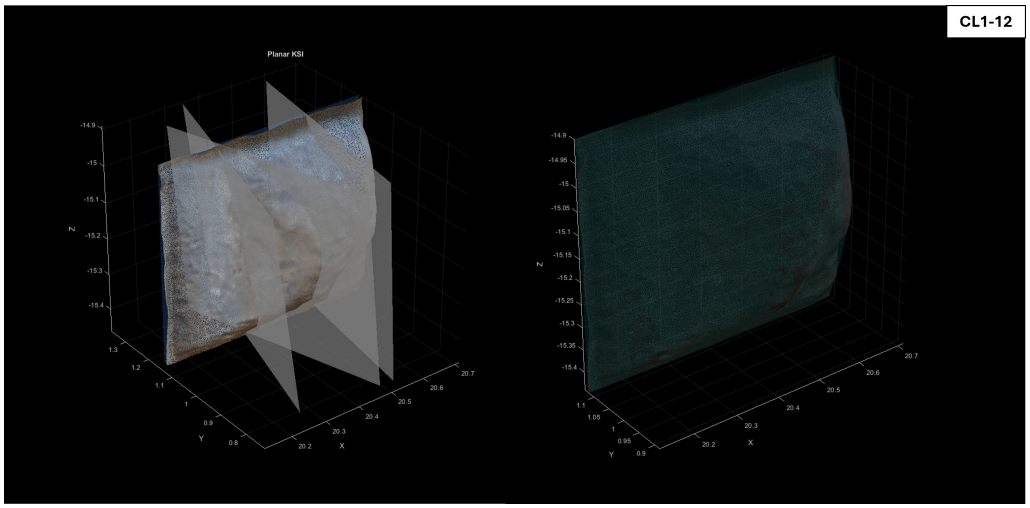


Figure 191

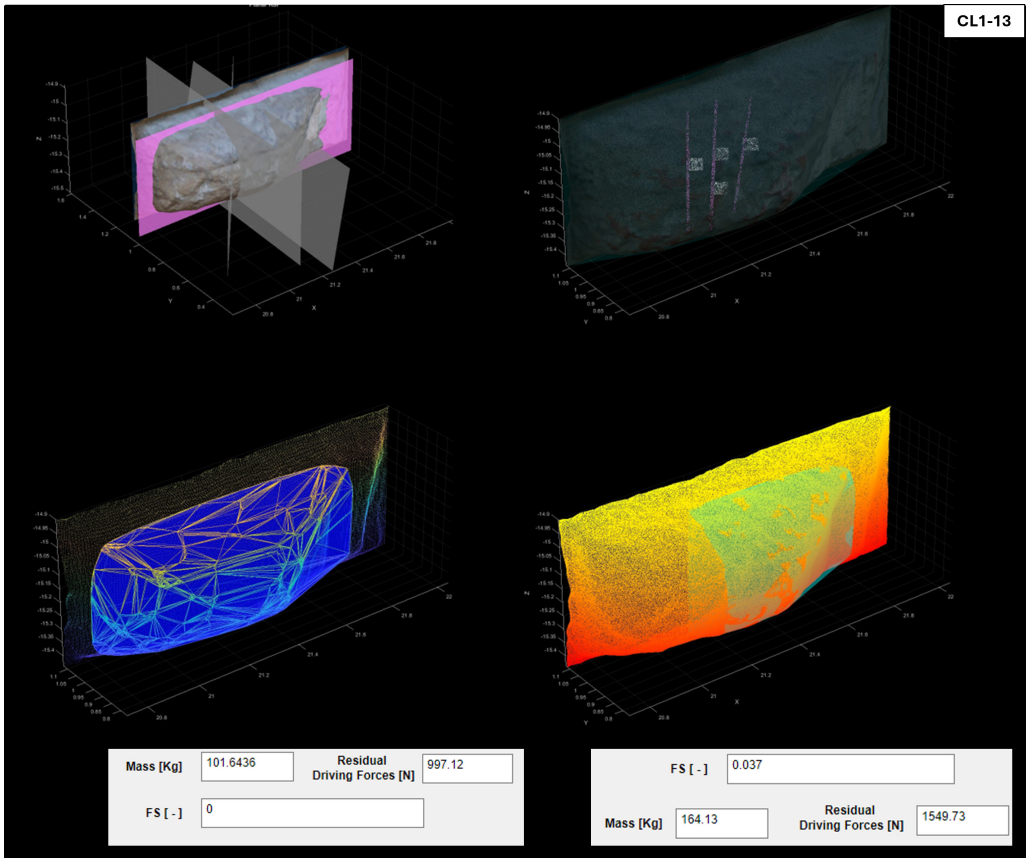

CL1-13
Mass [Kg]
101.6436
Residual
Driving Forces [N]
997.12
FS [-]
0
FS [-]
0.037
Mass [Kg]
164.13
Residual
Driving Forces [N]
1549.73

Figure 192

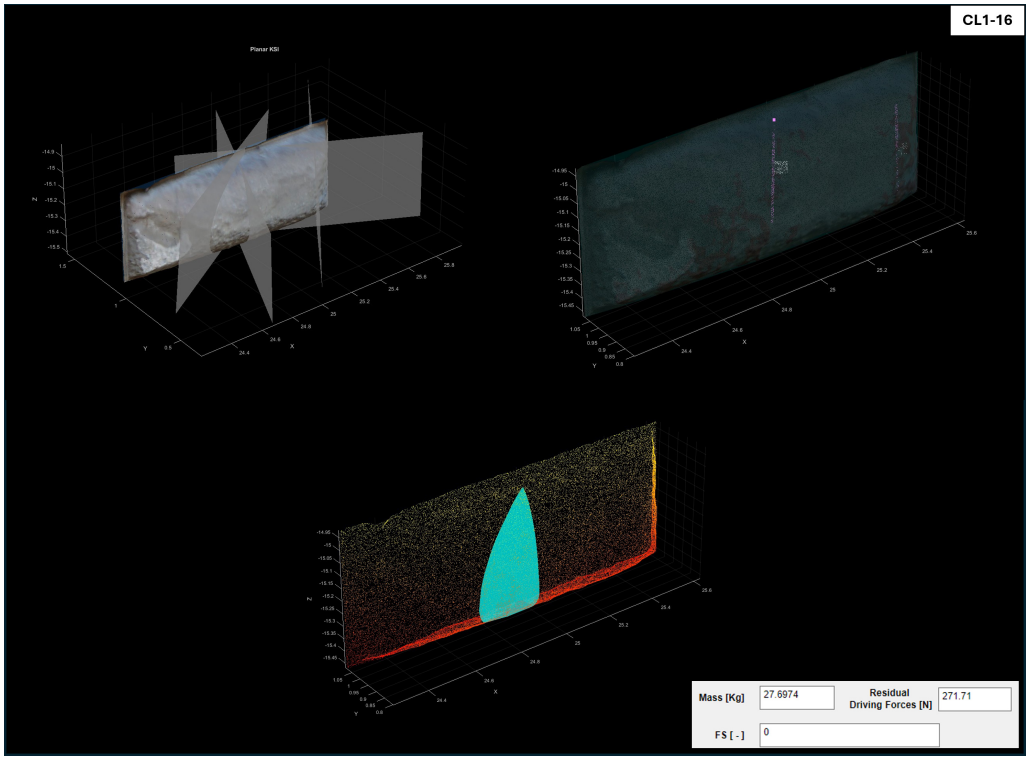


Figure 193

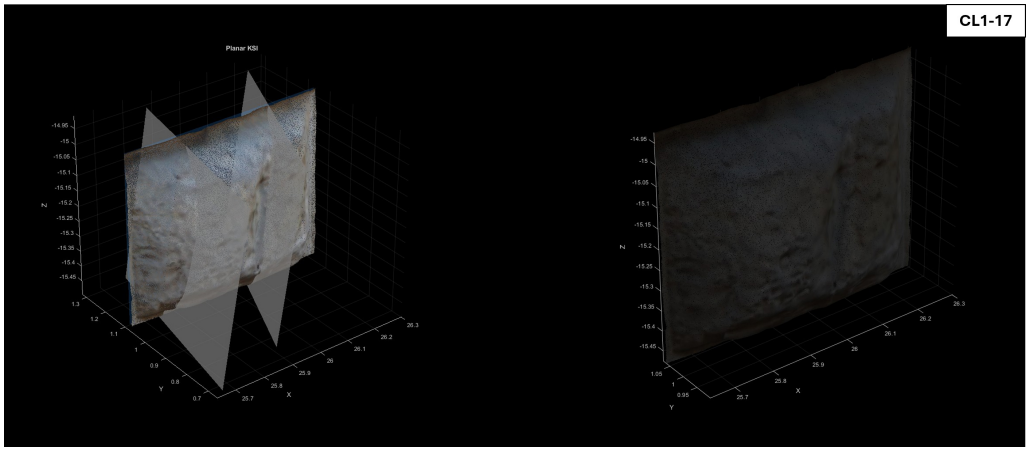


Figure 194

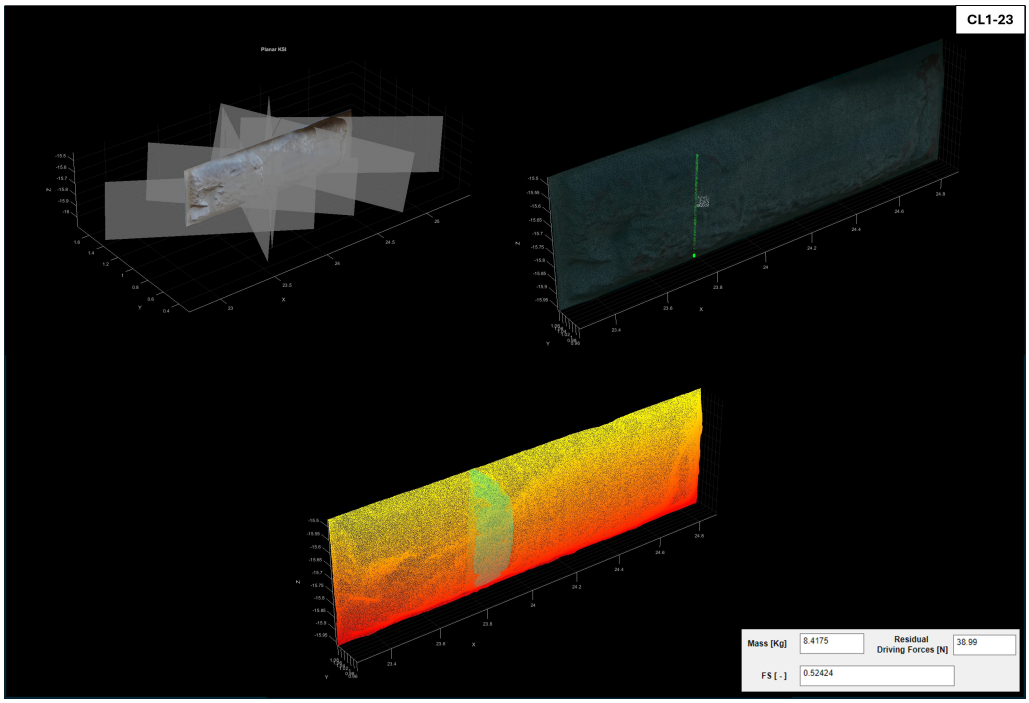

CL1-23
Planar KSI
Mass [Kg]
8.4175
Residual Driving Forces [N]
38.99
FS [-]
0.52424

Figure 195

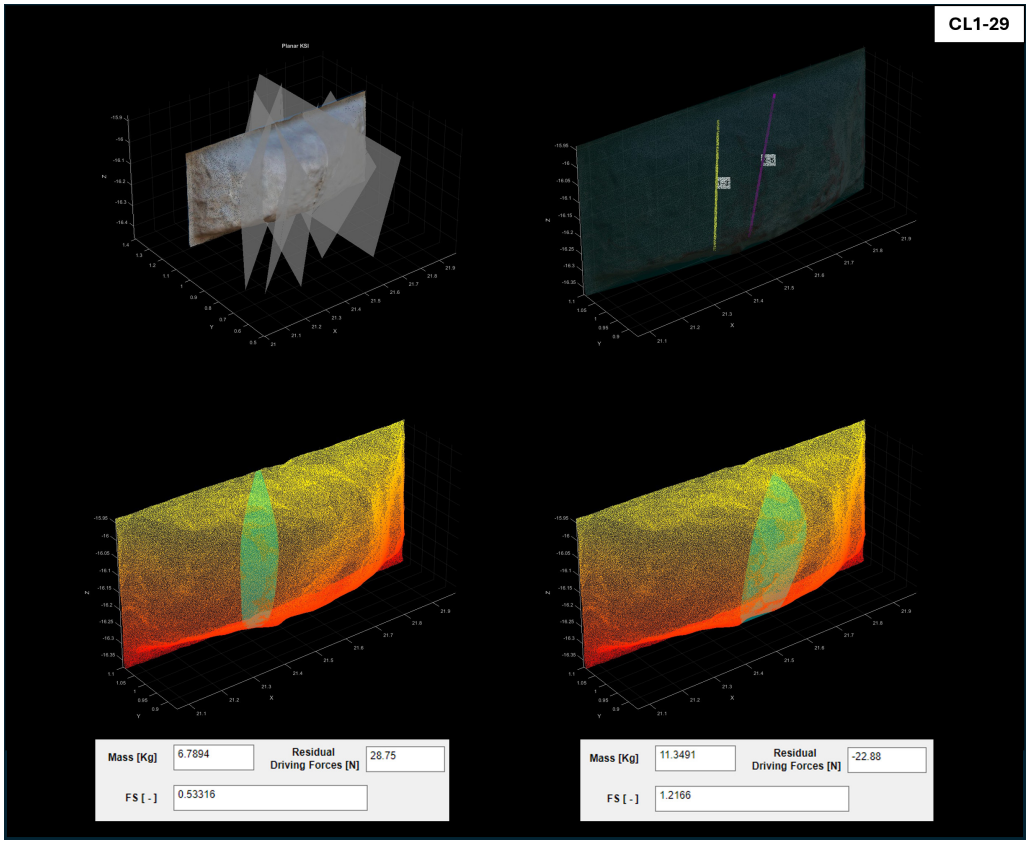

CL1-29
Planar KSI
Mass [Kg]
6.7894
Residual Driving Forces [N]
28.75
FS [-]
0.53316
Mass [Kg]
11.3491
Residual Driving Forces [N]
-22.88
FS [-]
1.2166

Figure 196

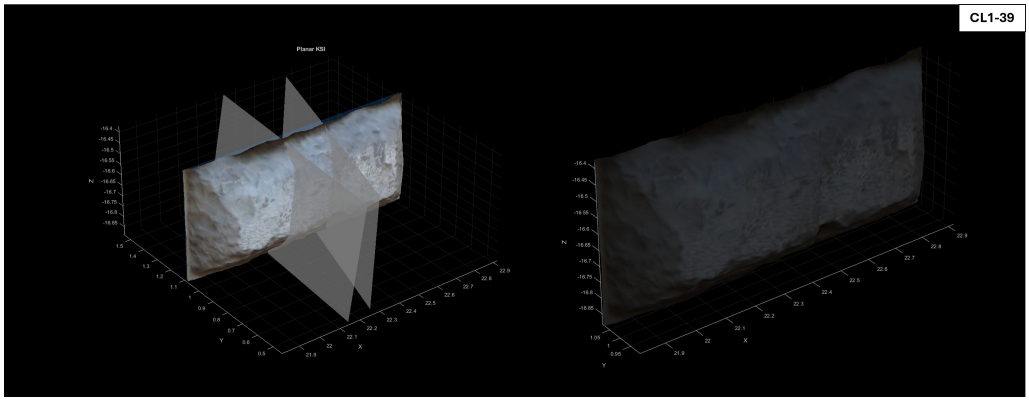


Figure 197

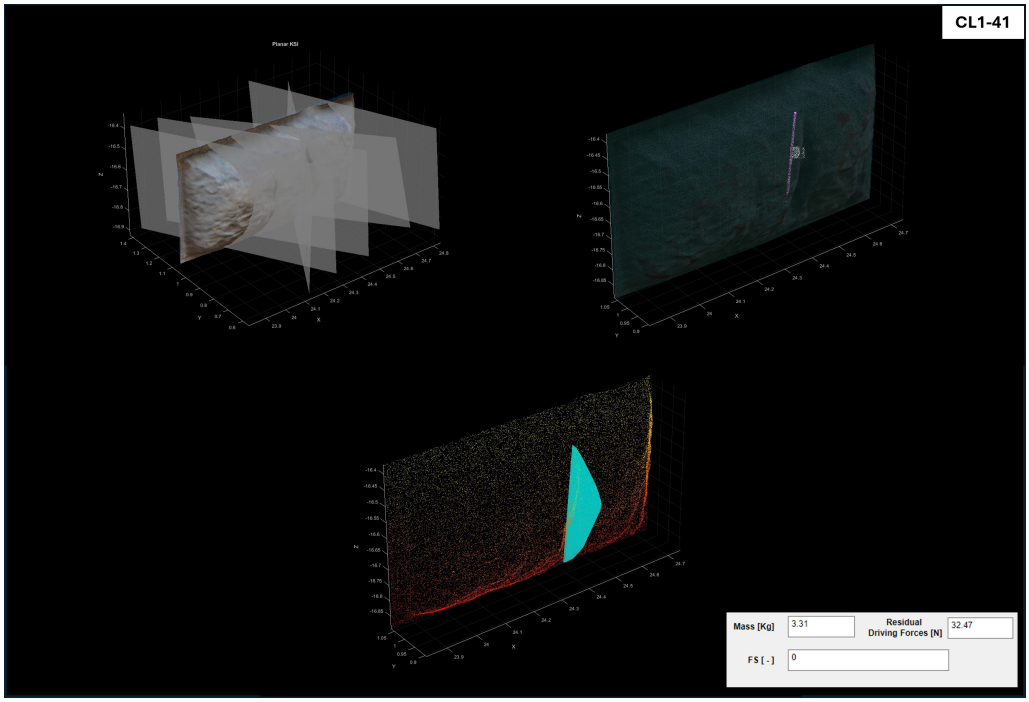


Figure 198

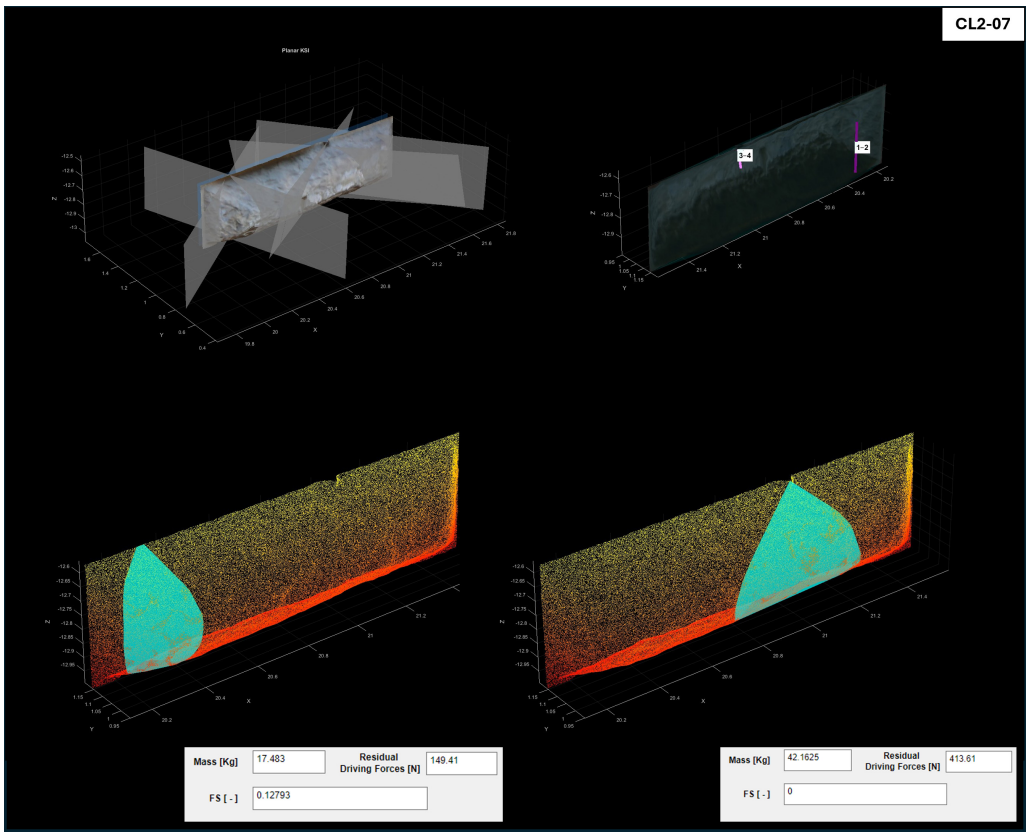


Figure 199

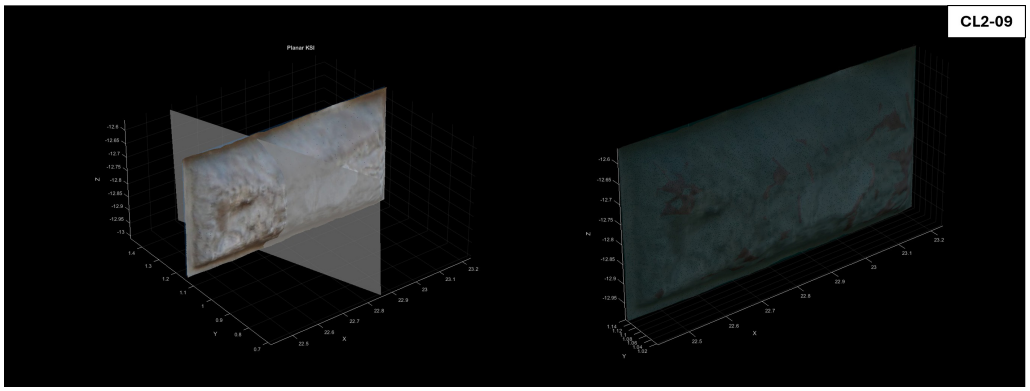


Figure 200

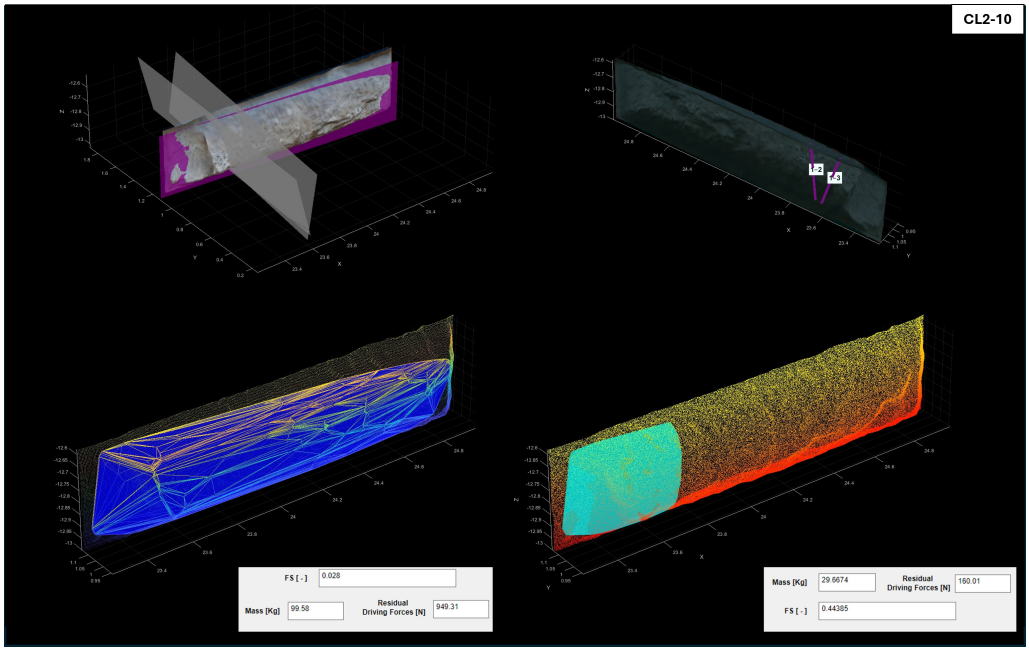

CL2-10
FS [-]
0.028
Mass [Kg]
99.58
Residual Driving Forces [N]
949.31
Mass [Kg]
29.6674
Residual Driving Forces [N]
160.01
FS [-]
0.44385

Figure 201

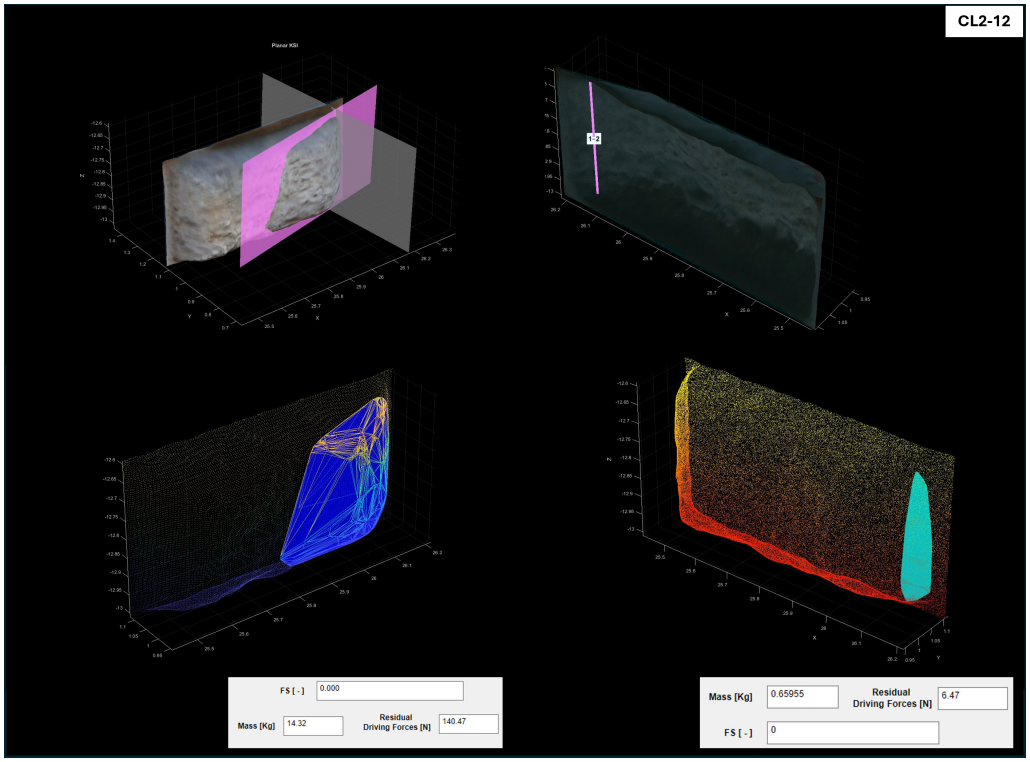

CL2-12
Planar KSI
1-2
FS [-]
0.000
Mass [Kg]
14.32
Residual
Driving Forces [N]
140.47
Mass [Kg]
0.65955
Residual
Driving Forces [N]
6.47
FS [-]
0

Figure 202

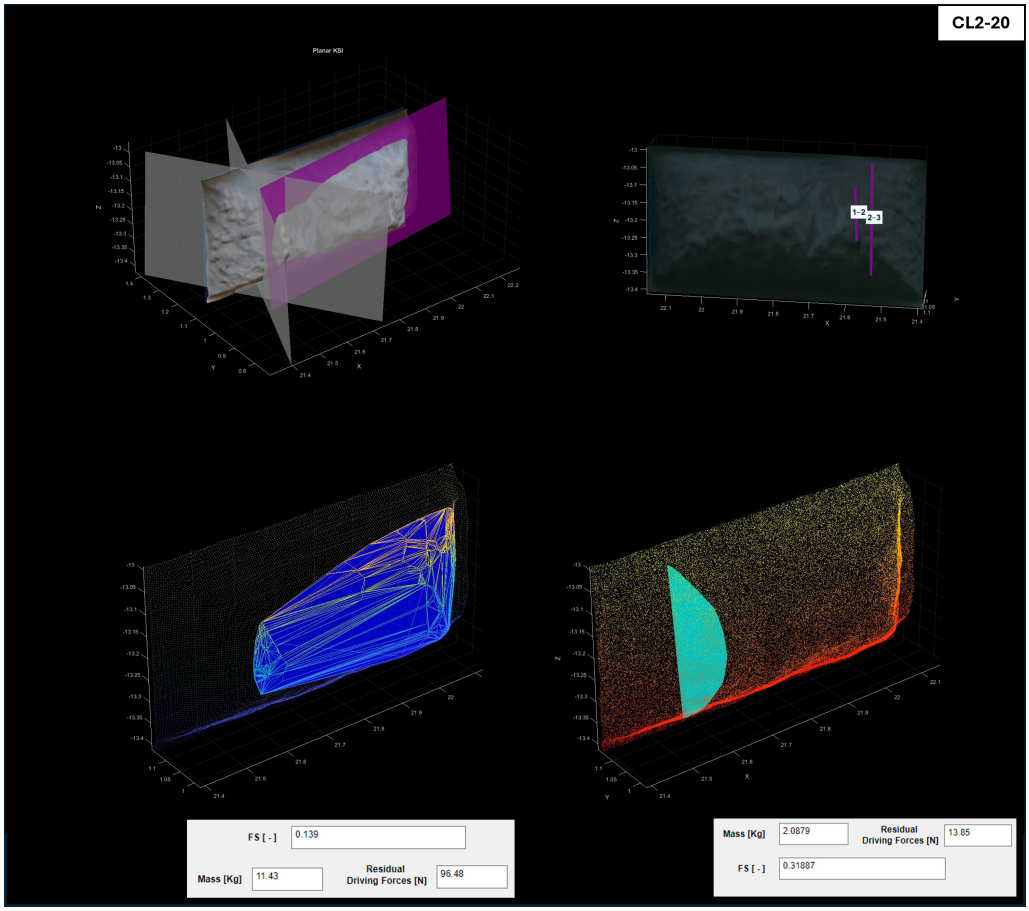

CL2-20
Planar KSI
1-2
2-3
FS [-]
0.139
Mass [Kg]
11.43
Residual Driving Forces [N]
96.48
Mass [Kg]
2.0879
Residual Driving Forces [N]
13.85
FS [-]
0.31887

Figure 203

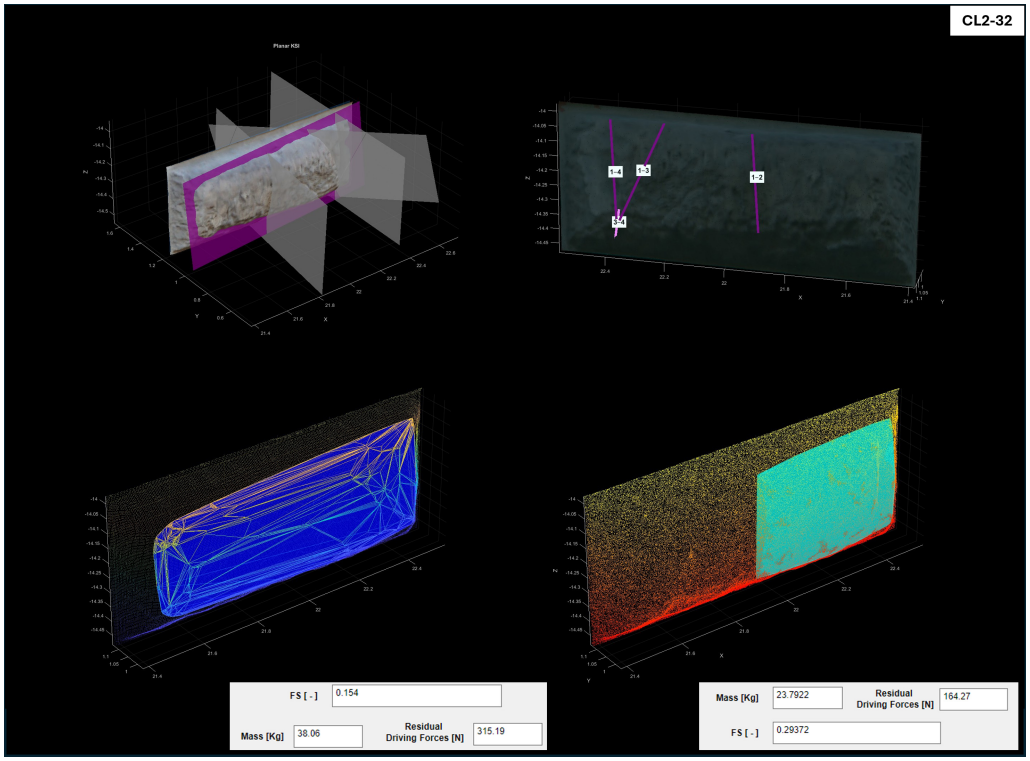

CL2-32
Planar KSI
1-4
1-3
1-2
3-4
FS [-]
0.154
Mass [Kg]
38.06
Residual
Driving Forces [N]
315.19
Mass [Kg]
23.7922
Residual
Driving Forces [N]
164.27
FS [-]
0.29372

Figure 204

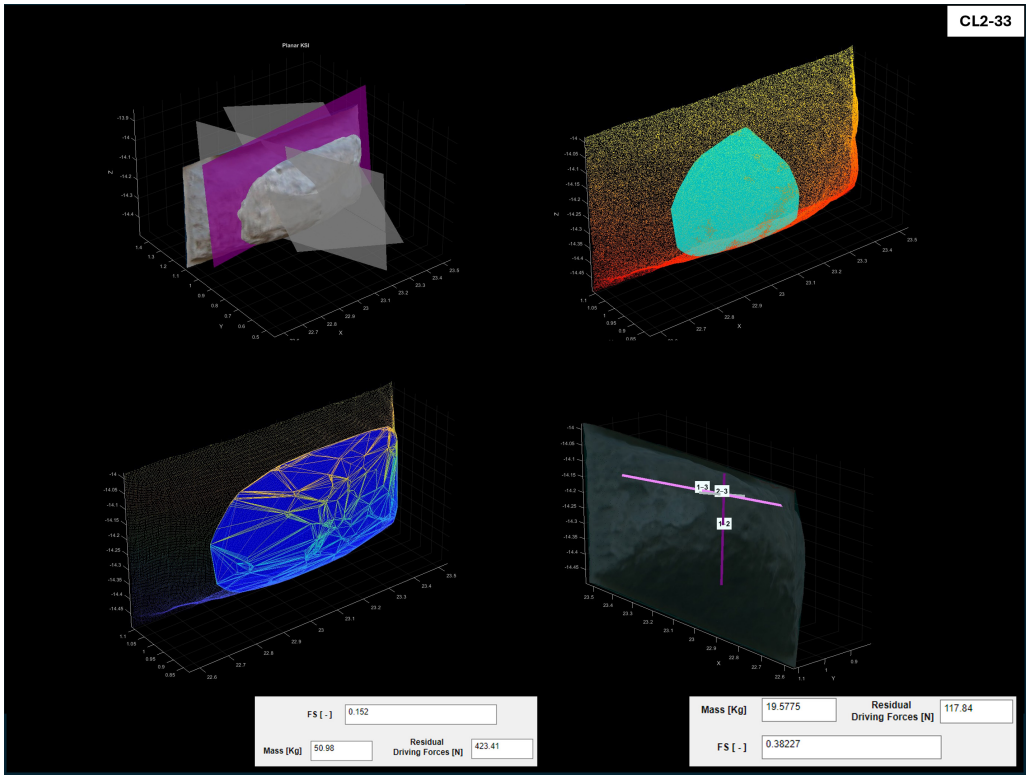

CL2-33
Planar KSI
FS [-] 0.152
Mass [Kg] 50.98
Residual Driving Forces [N] 423.41
Mass [Kg] 19.5775
Residual Driving Forces [N] 117.84
FS [-] 0.38227

Figure 205

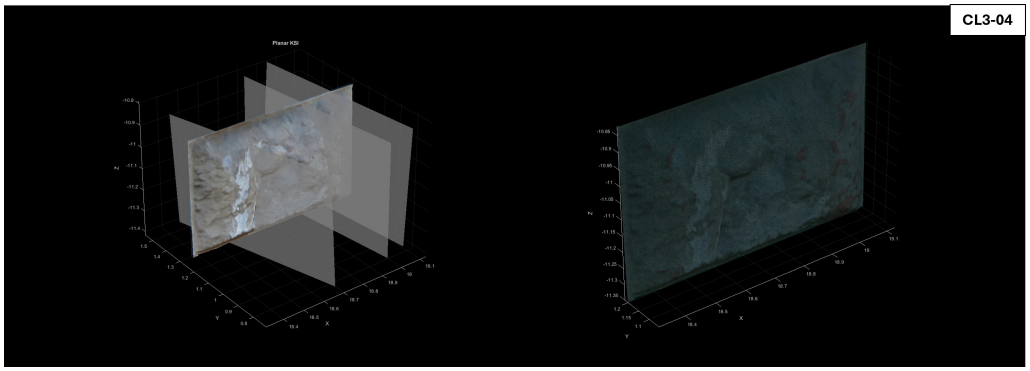


Figure 206

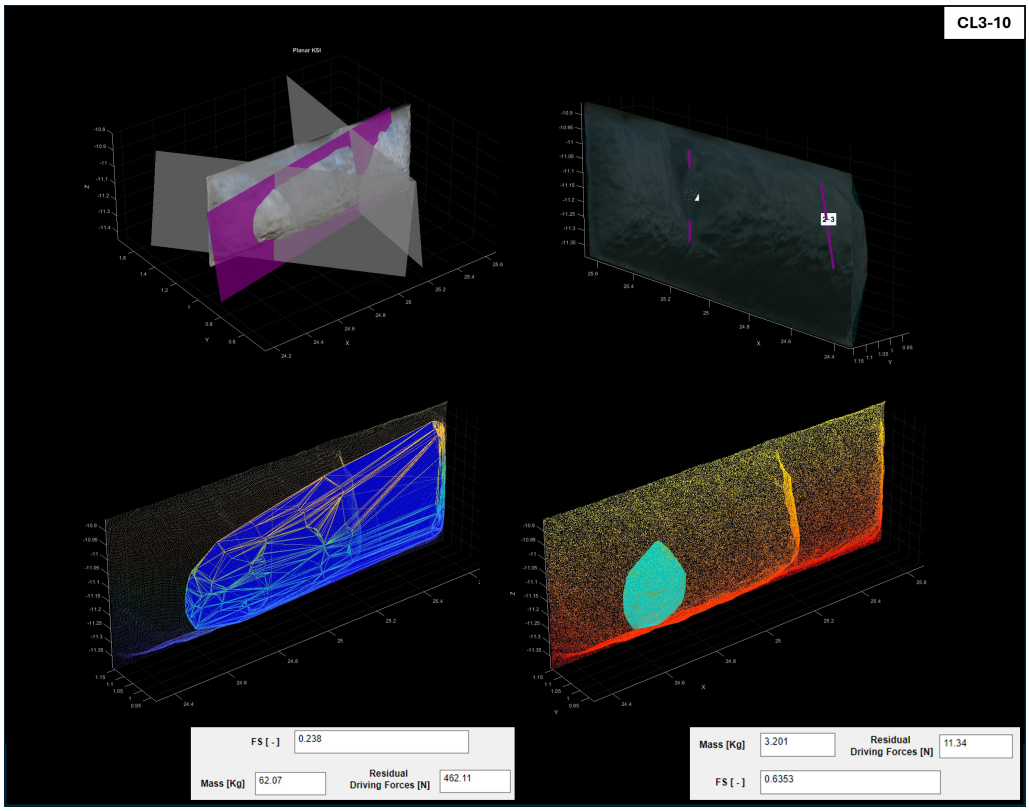

CL3-10
Planar KSI
FS [-] 0.238
Mass [Kg] 62.07
Residual Driving Forces [N] 462.11
Mass [Kg] 3.201
Residual Driving Forces [N] 11.34
FS [-] 0.6353

Figure 207

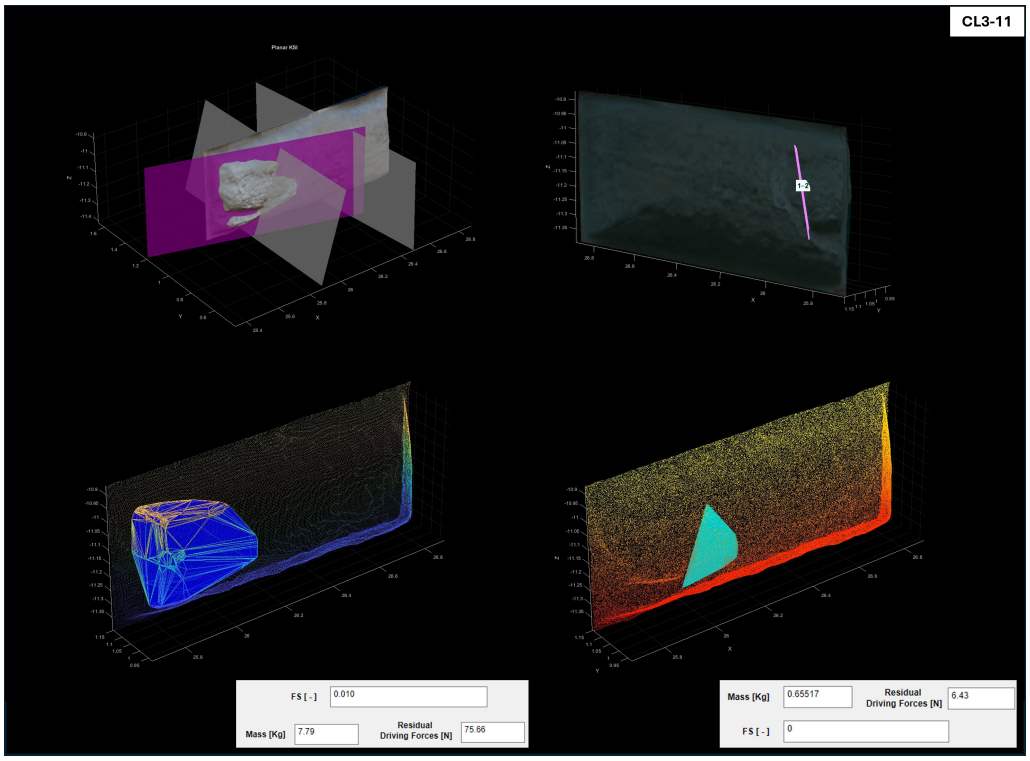


Figure 208

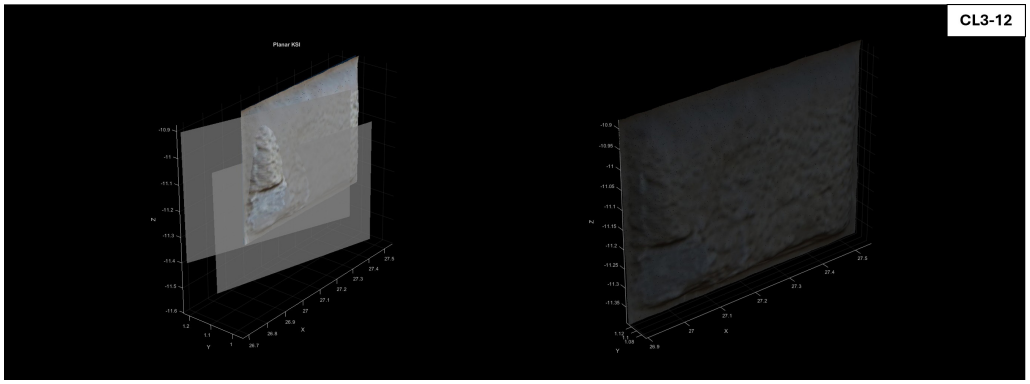


Figure 209

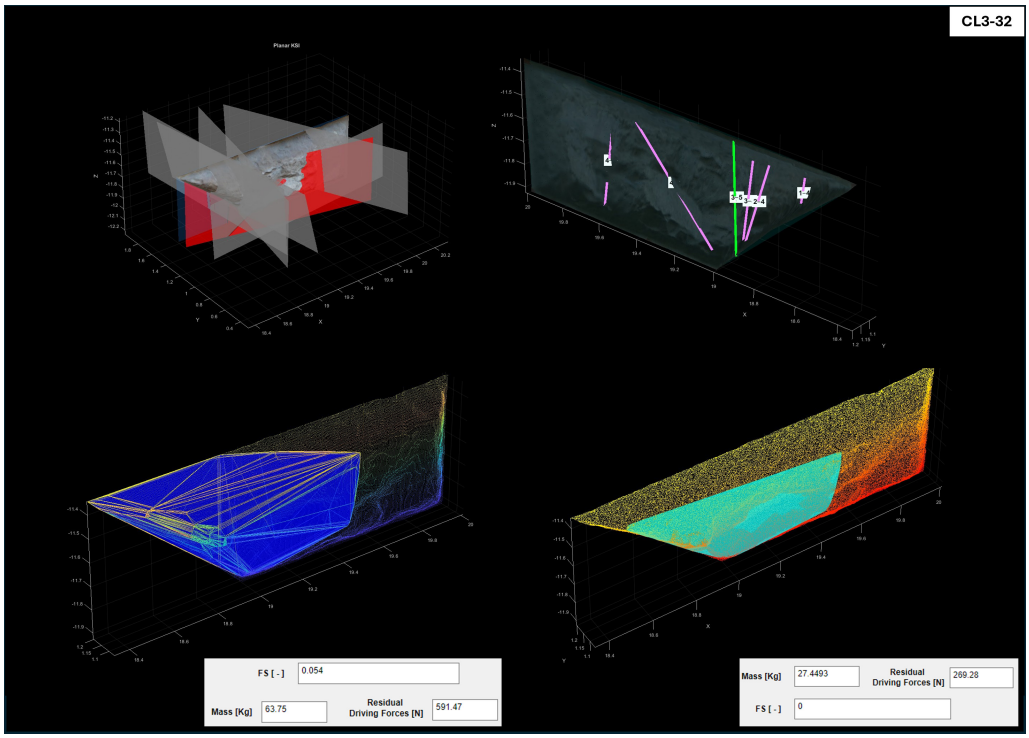

CL3-32
Planar KSI
FS [-] 0.054
Mass [Kg] 63.75
Residual Driving Forces [N] 591.47
Mass [Kg] 27.4493
Residual Driving Forces [N] 269.28
FS [-] 0

Figure 210

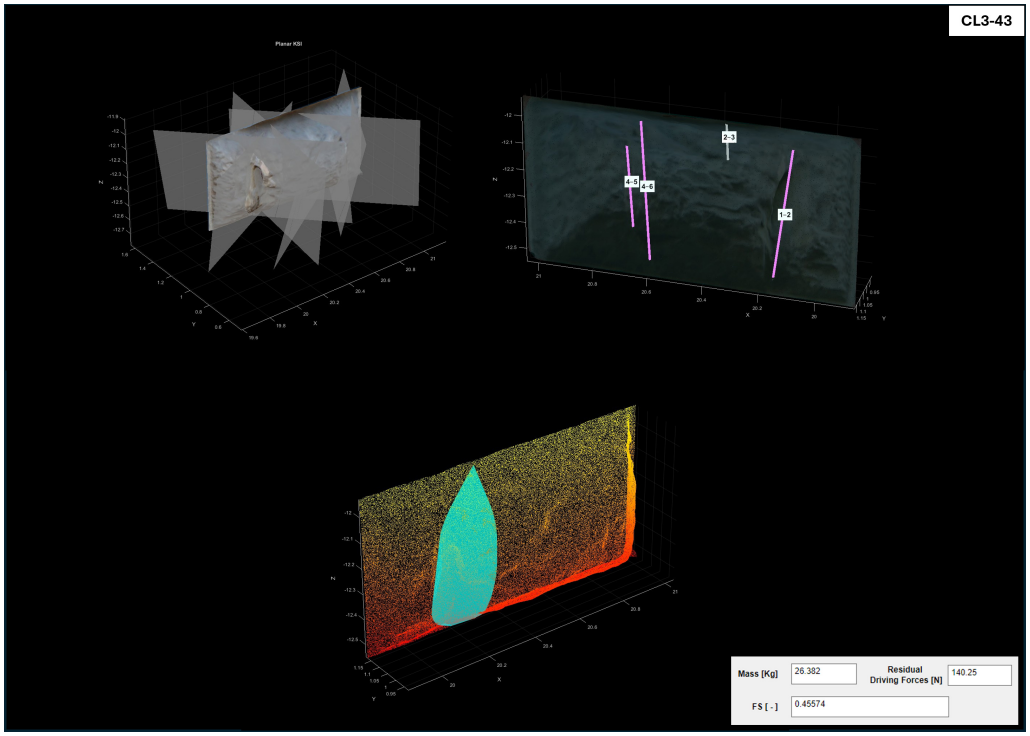

CL3-43
Planar KSI
2-3
4-5
4-6
1-2
Mass [Kg]
26.382
Residual Driving Forces [N]
140.25
FS [-]
0.45574

Figure 211

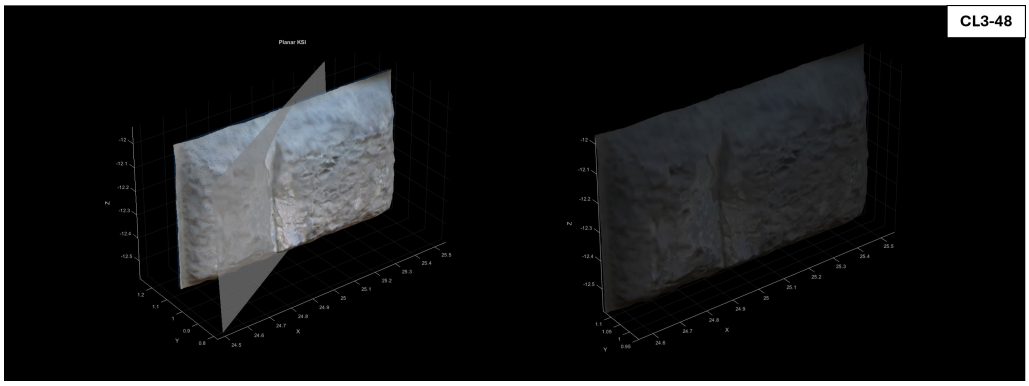


Figure 212

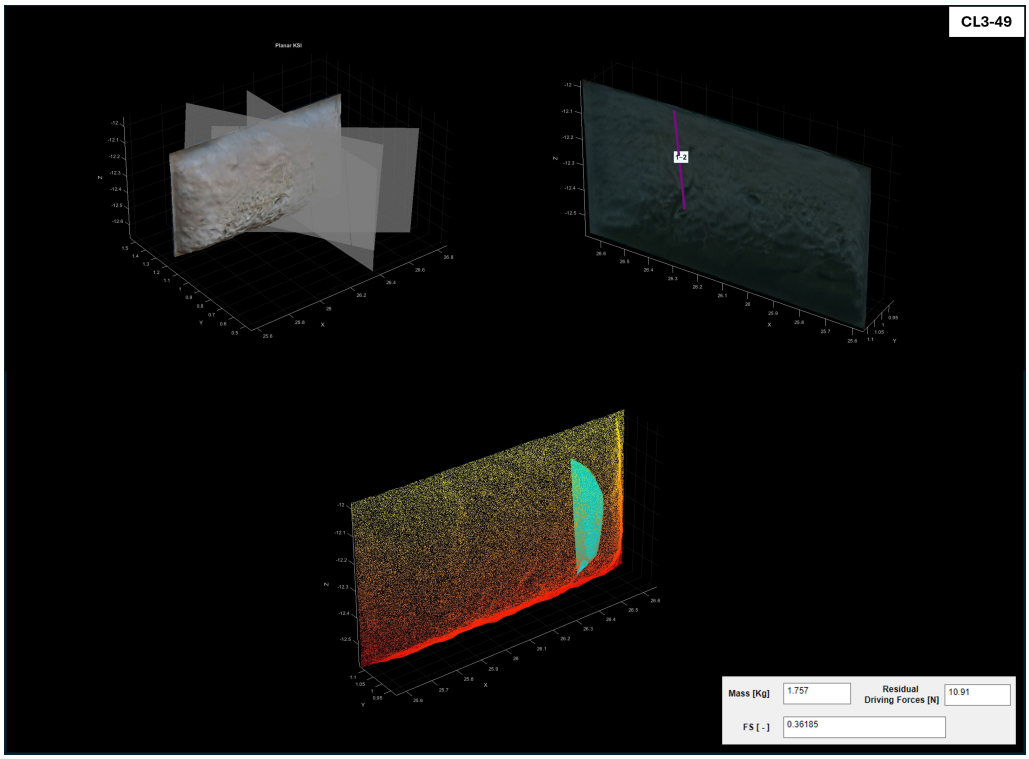


Figure 213

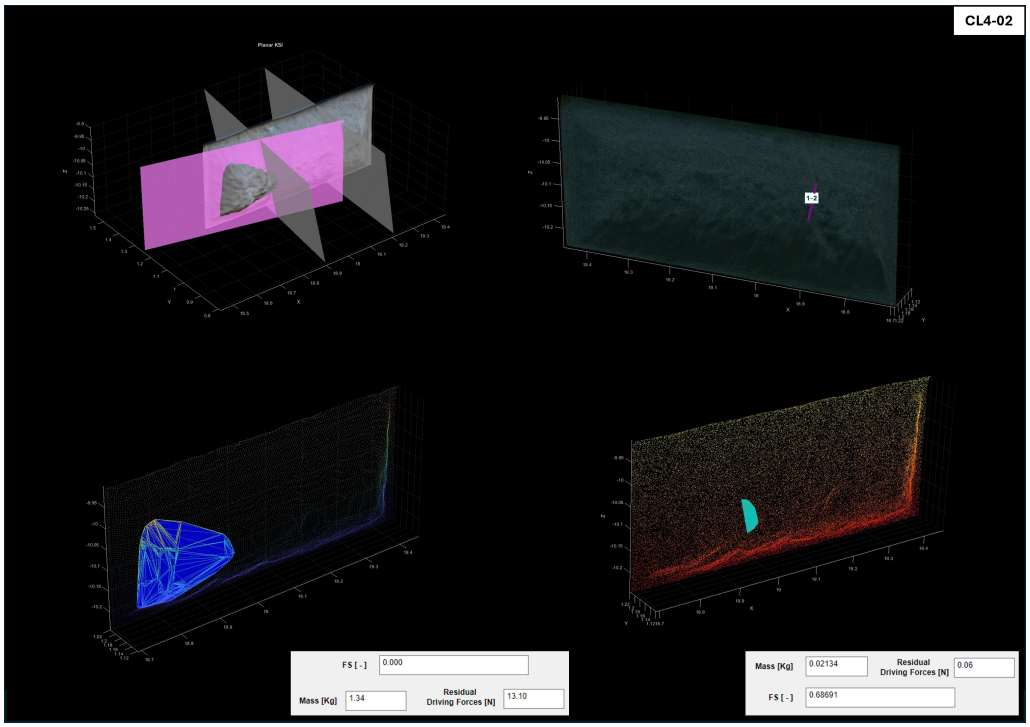

CL4-02
FS [-]
0.000
Mass [Kg]
1.34
Residual
Driving Forces [N]
13.10
Mass [Kg]
0.02134
Residual
Driving Forces [N]
0.05
FS [-]
0.68691

Figure 214

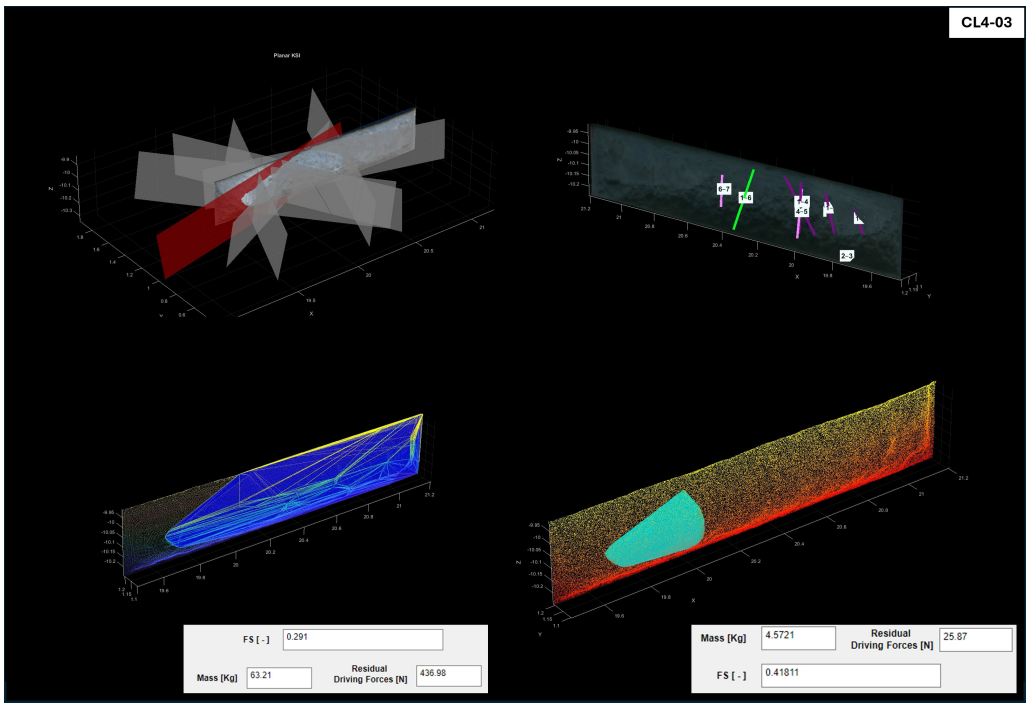

CL4-03
FS [-]
0.291
Mass [Kg]
63.21
Residual Driving Forces [N]
436.98
Mass [Kg]
4.5721
Residual Driving Forces [N]
25.87
FS [-]
0.41811

Figure 215

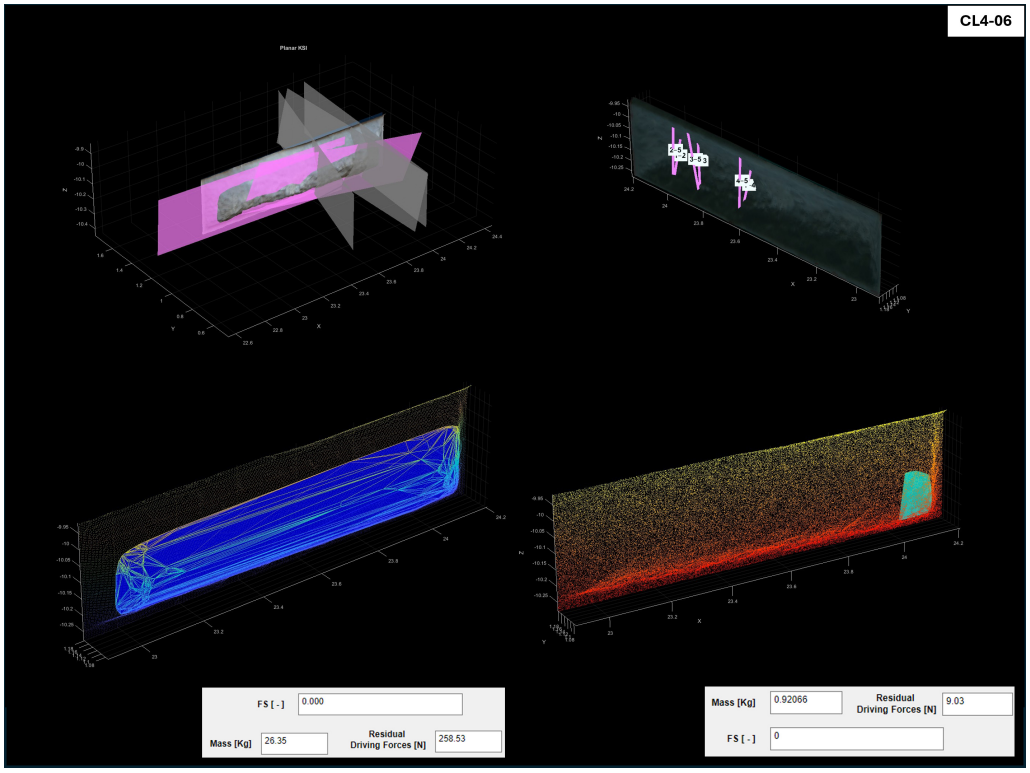

CL4-06
Planar KSI
FS [-]
0.000
Mass [Kg]
26.35
Residual
Driving Forces [N]
258.53
Mass [Kg]
0.92066
Residual
Driving Forces [N]
9.03
FS [-]
0

Figure 216

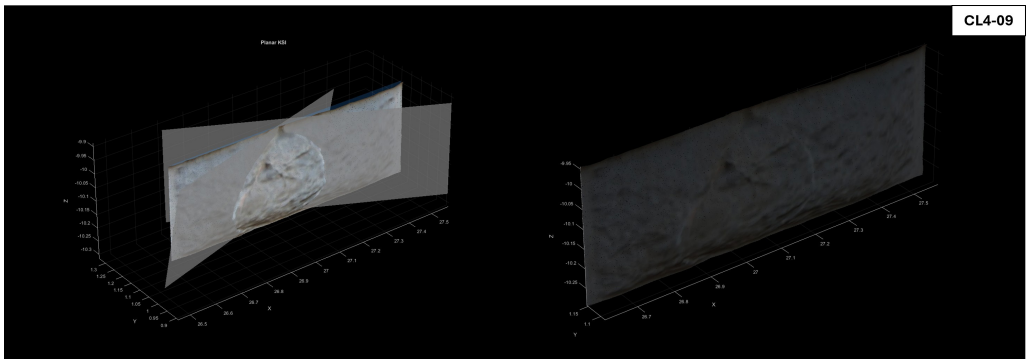


Figure 217

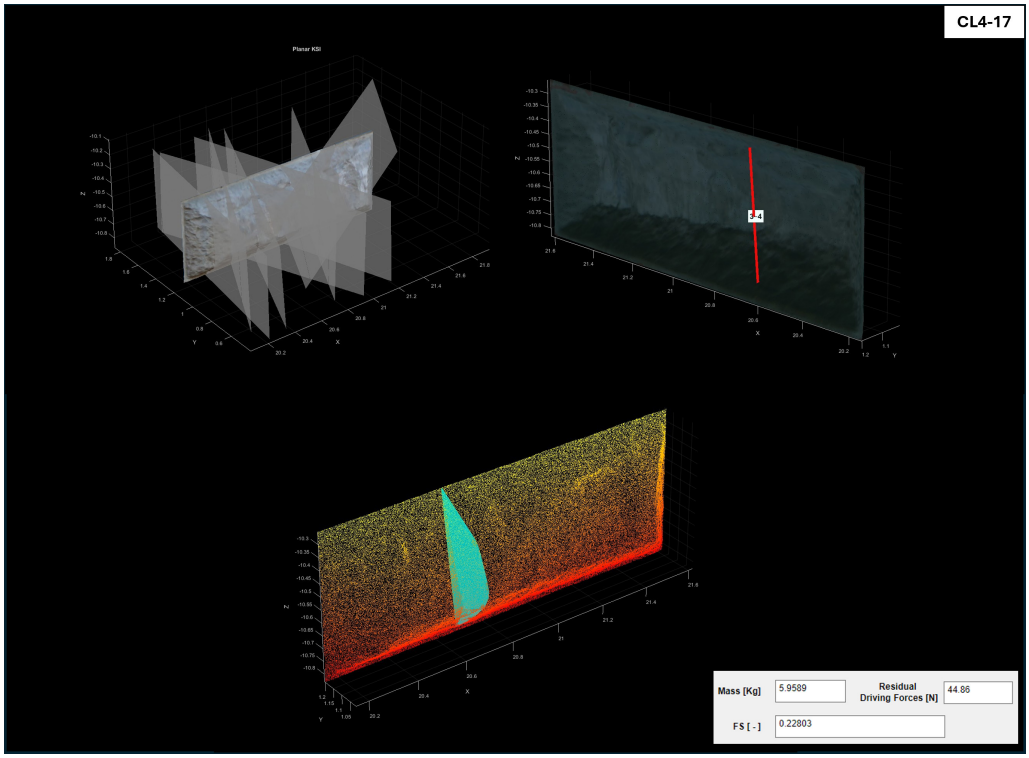


Figure 218

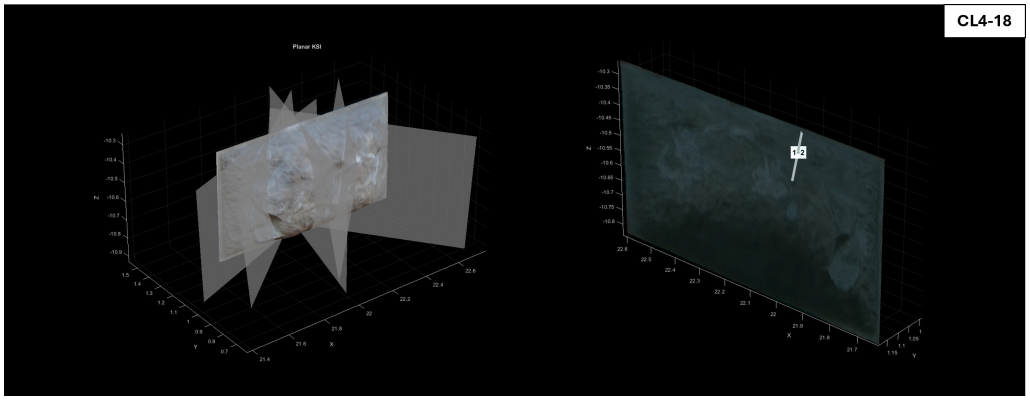


Figure 219

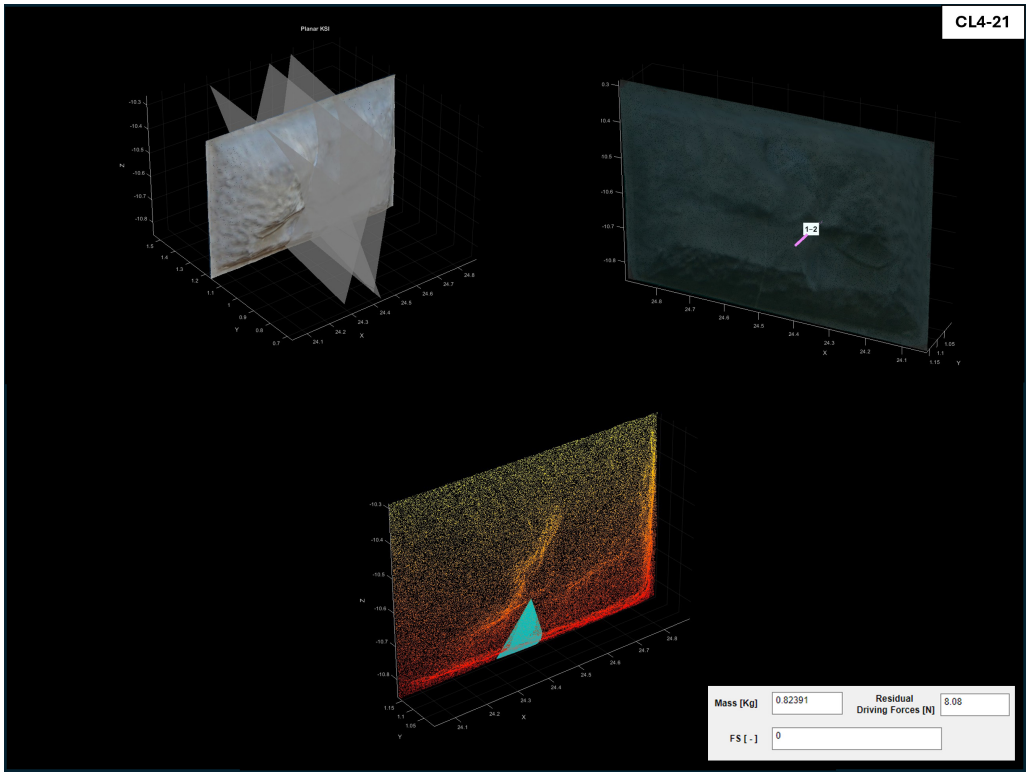


Figure 220

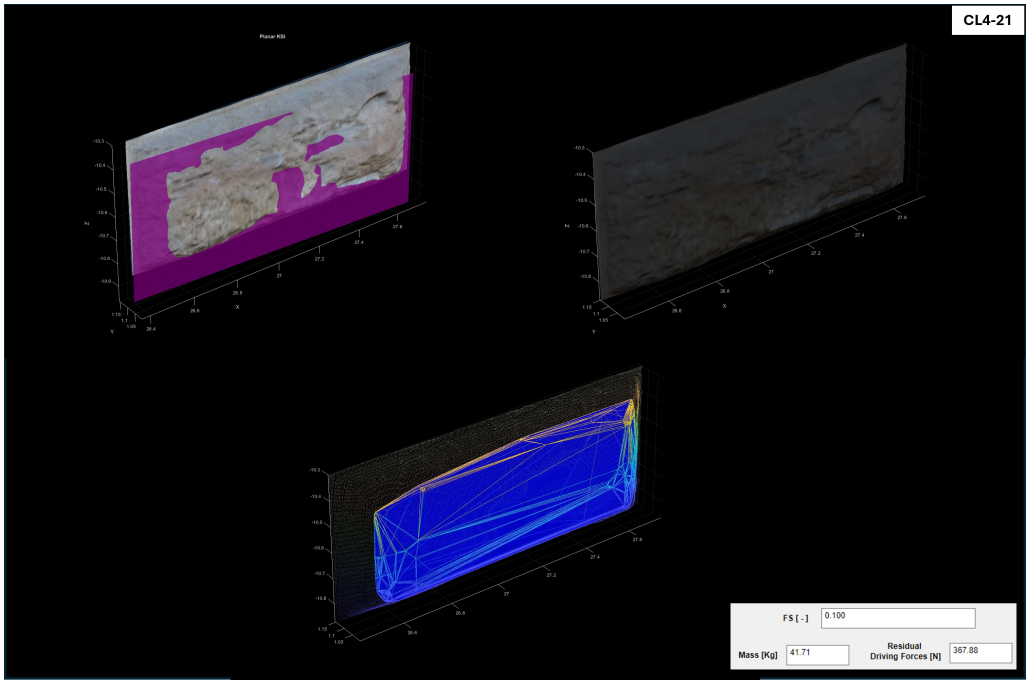

CL4-21
Planar KSI
FS [-]
0.100
Mass [Kg]
41.71
Residual
Driving Forces [N]
367.88

Figure 221

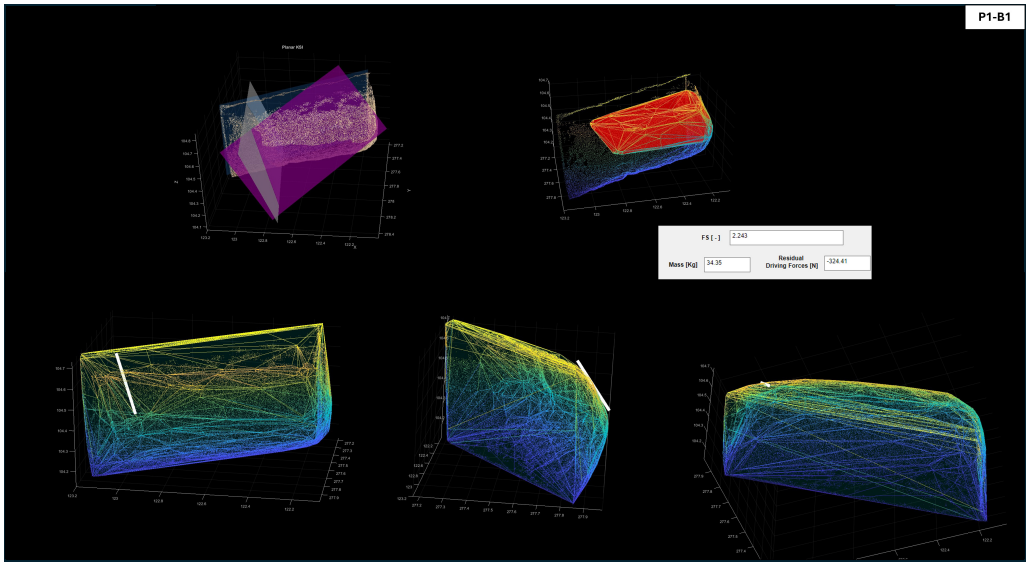


Figure 222

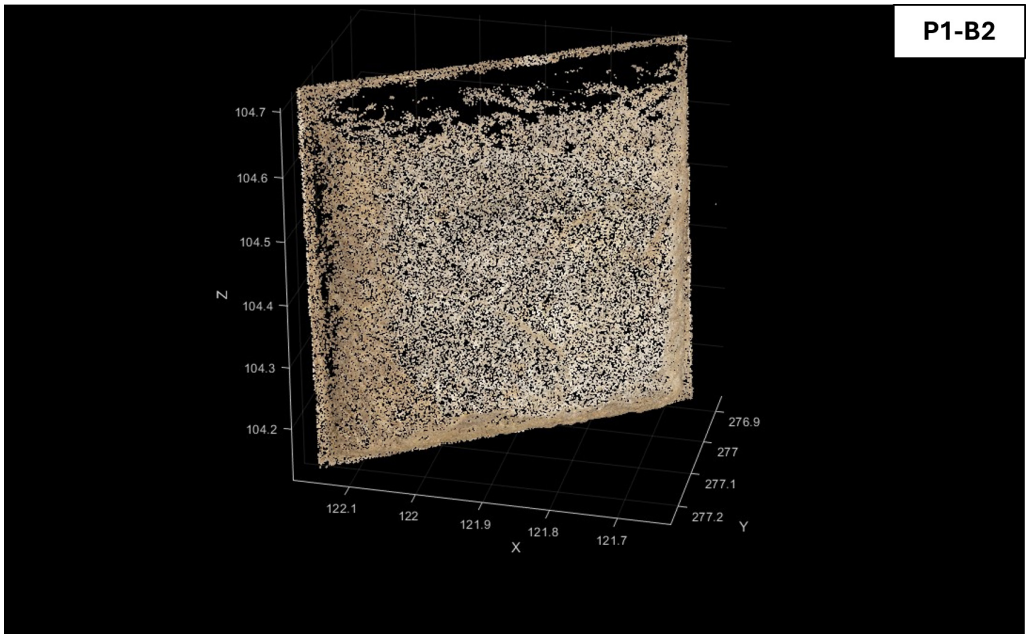


Figure 223

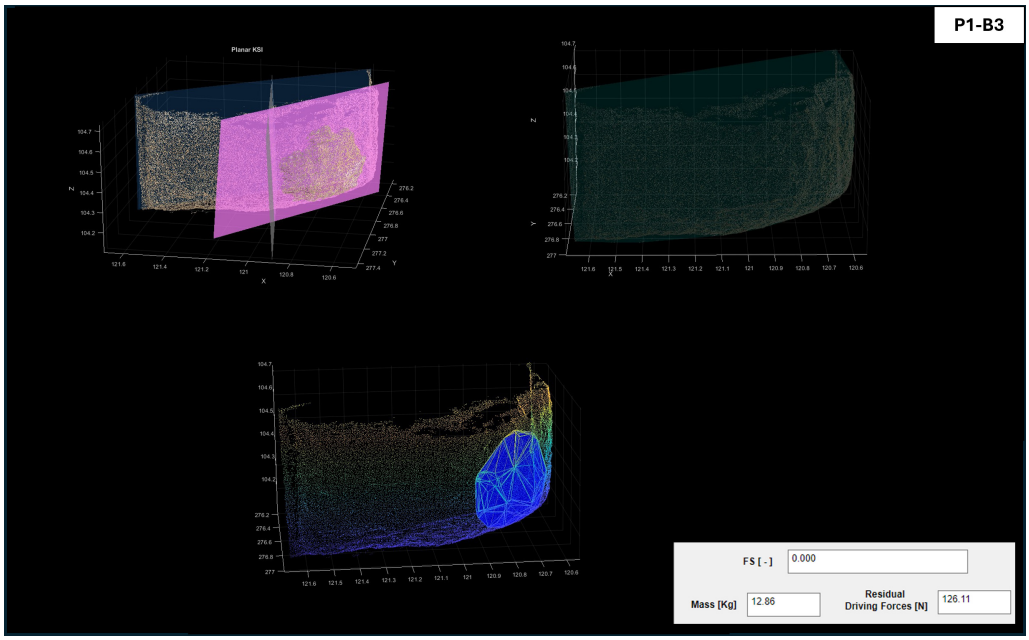


Figure 224

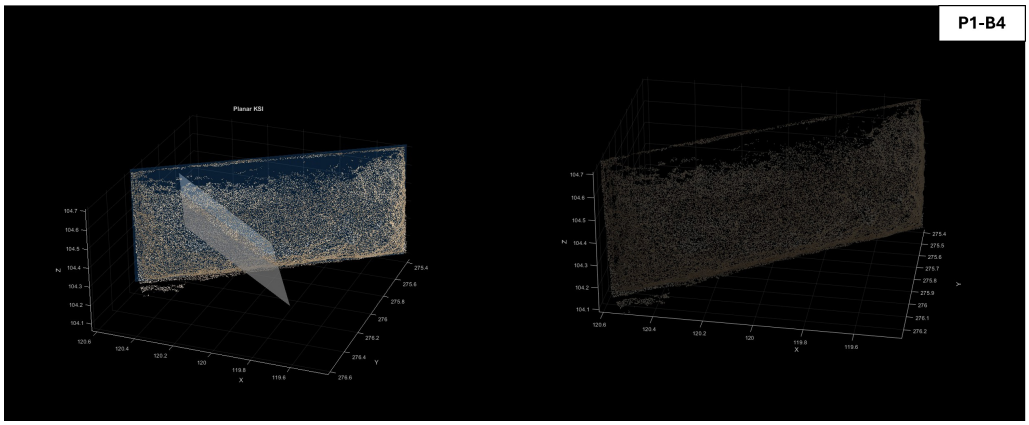


Figure 225

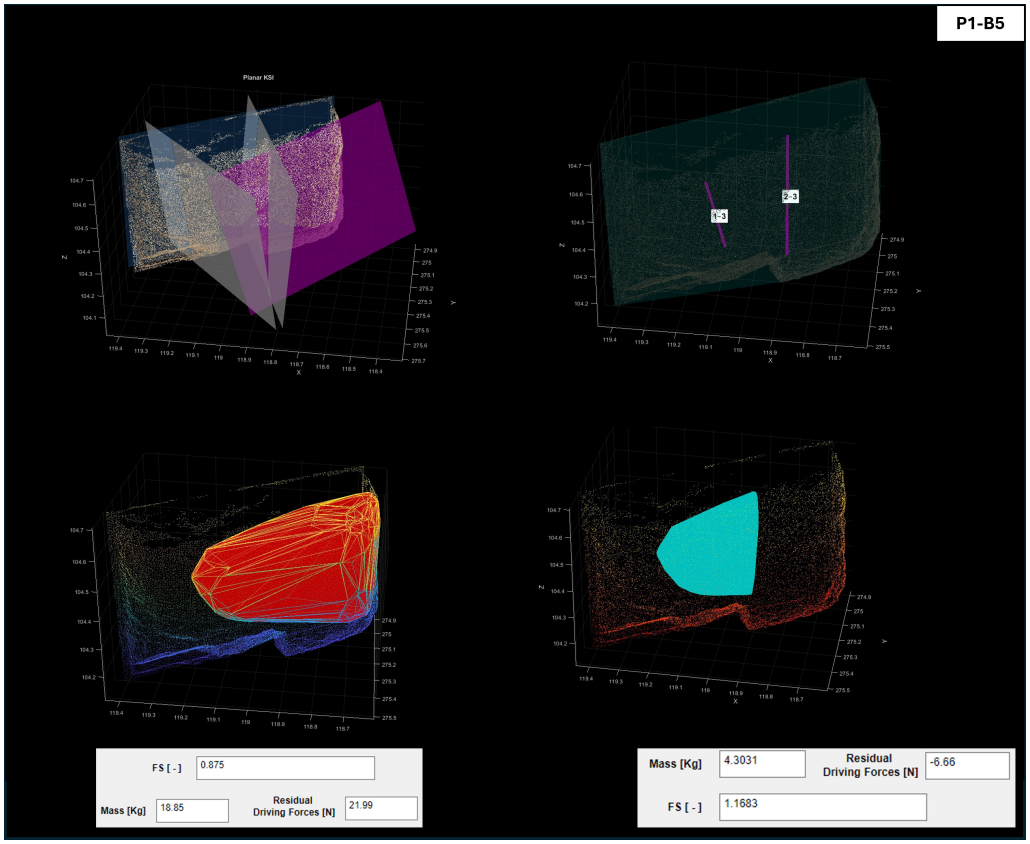

P1-B5
Planar KSI
1-3
2-3
FS [-]
0.875
Mass [Kg]
18.85
Residual
Driving Forces [N]
21.99
Mass [Kg]
4.3031
Residual
Driving Forces [N]
-6.66
FS [-]
1.1683

Figure 226

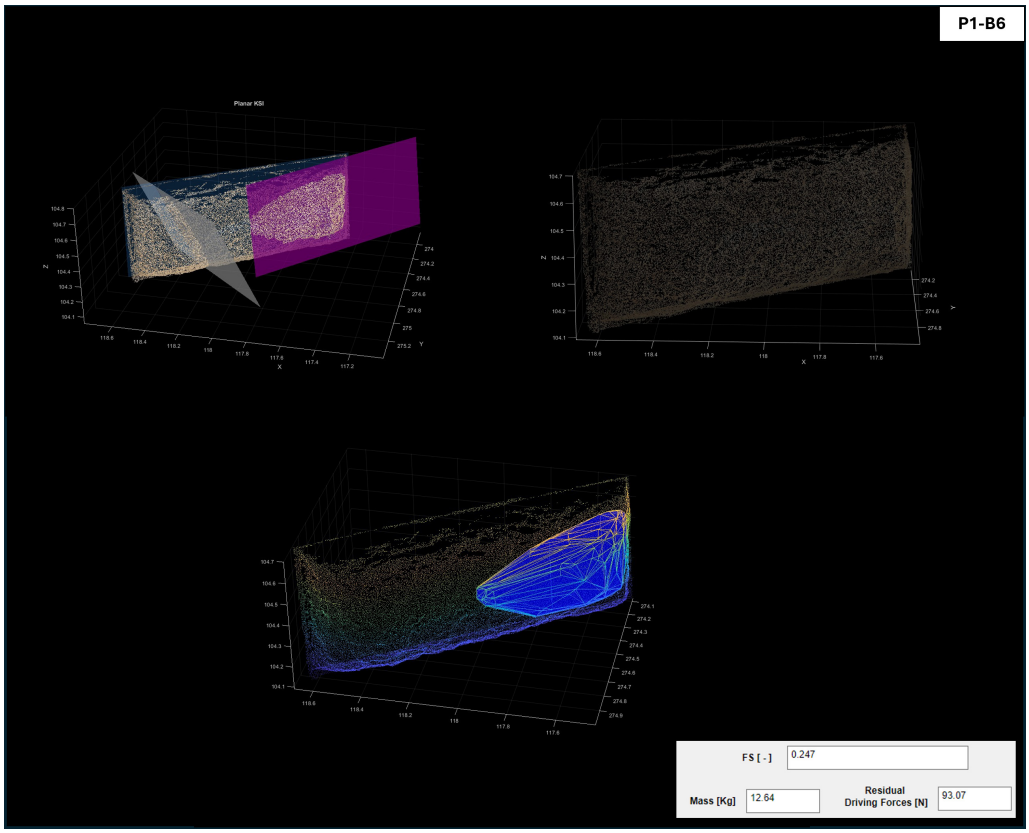

P1-B6
Planar KSI
FS [-]
0.247
Mass [Kg]
12.64
Residual
Driving Forces [N]
93.07

Figure 227

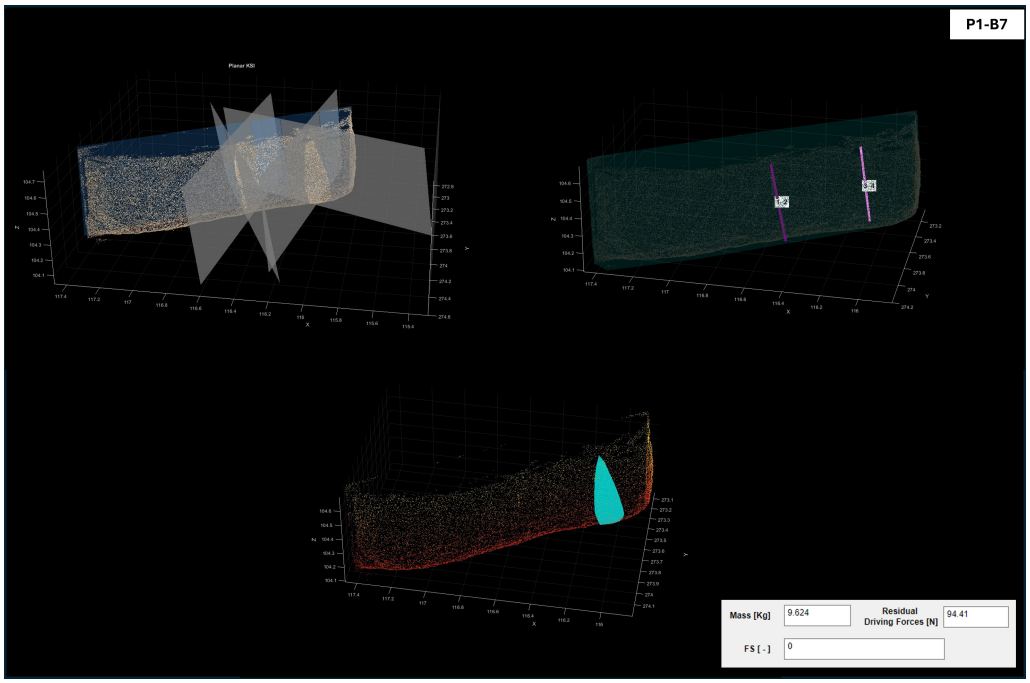


Figure 228

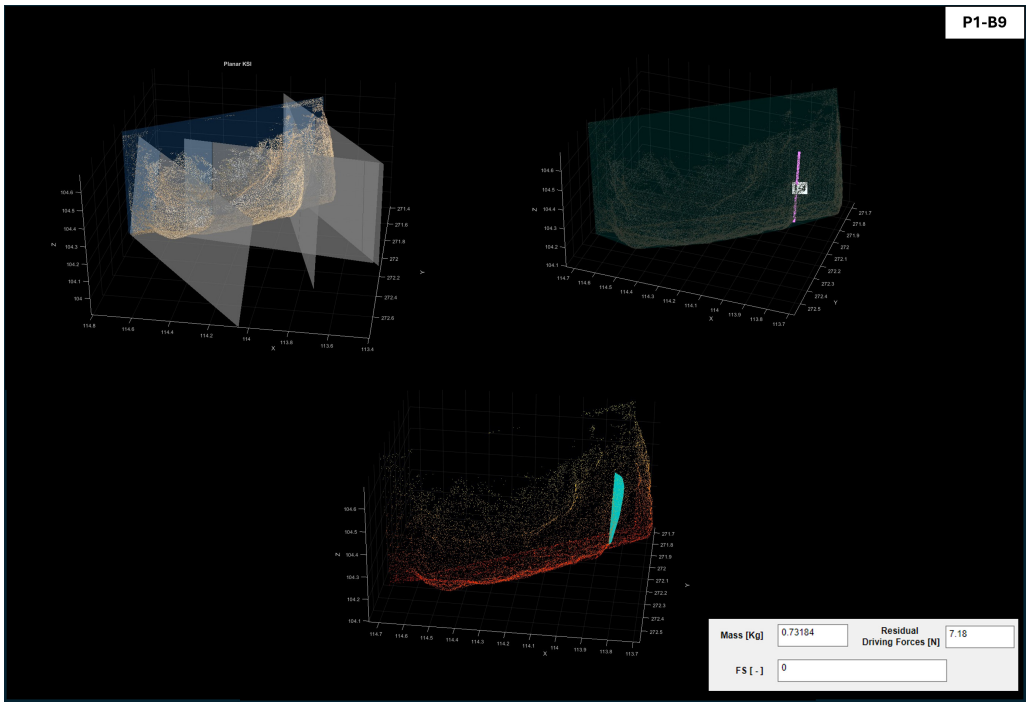


Figure 229

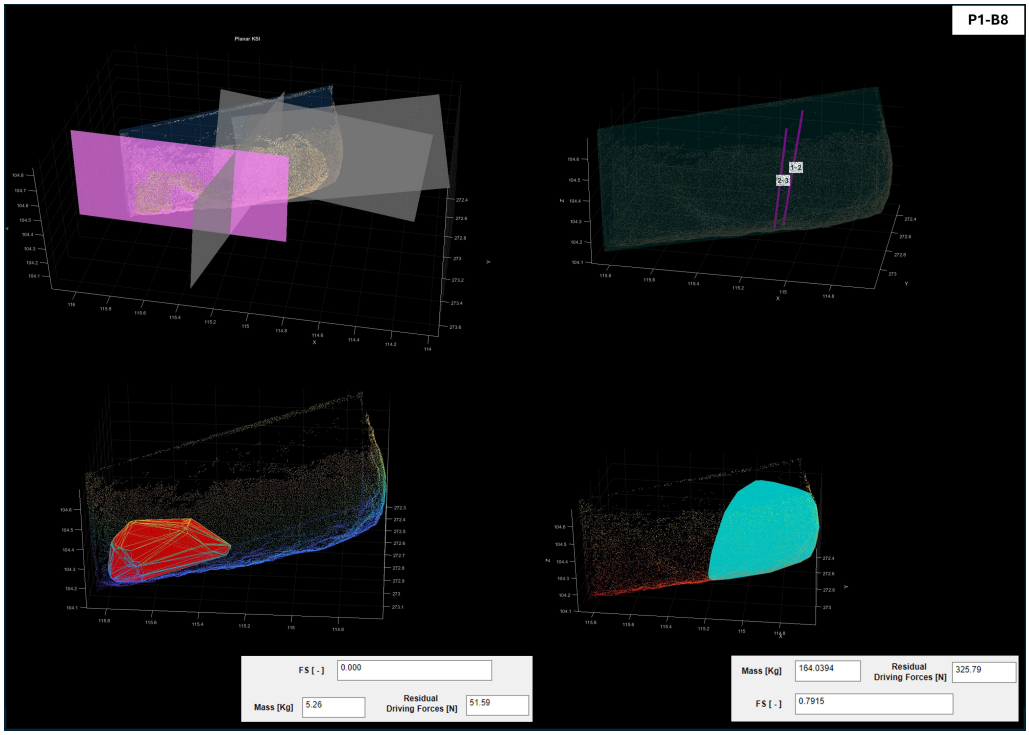

P1-B8
FS [-] 0.000
Mass [Kg] 5.26
Residual Driving Forces [N] 51.59
Mass [Kg] 164.0394
Residual Driving Forces [N] 325.79
FS [-] 0.7915

Figure 230

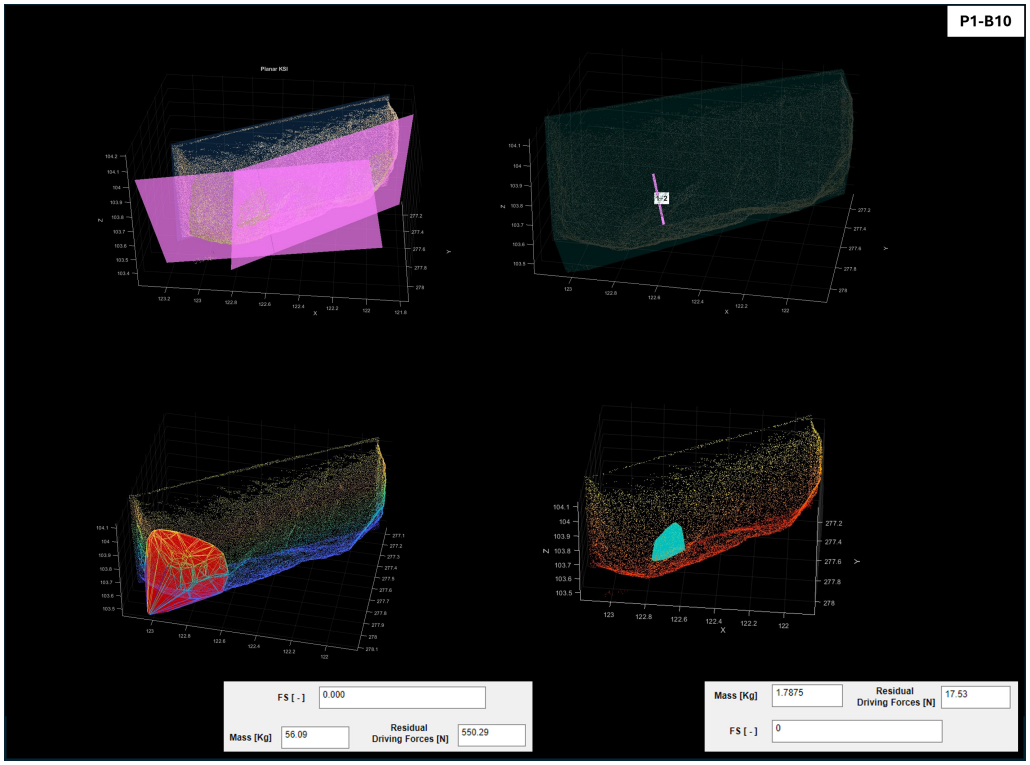

P1-B10
Planar KSI
FS [-]
0.000
Mass [Kg]
56.09
Residual Driving Forces [N]
550.29
Mass [Kg]
1.7875
Residual Driving Forces [N]
17.53
FS [-]
0

Figure 231

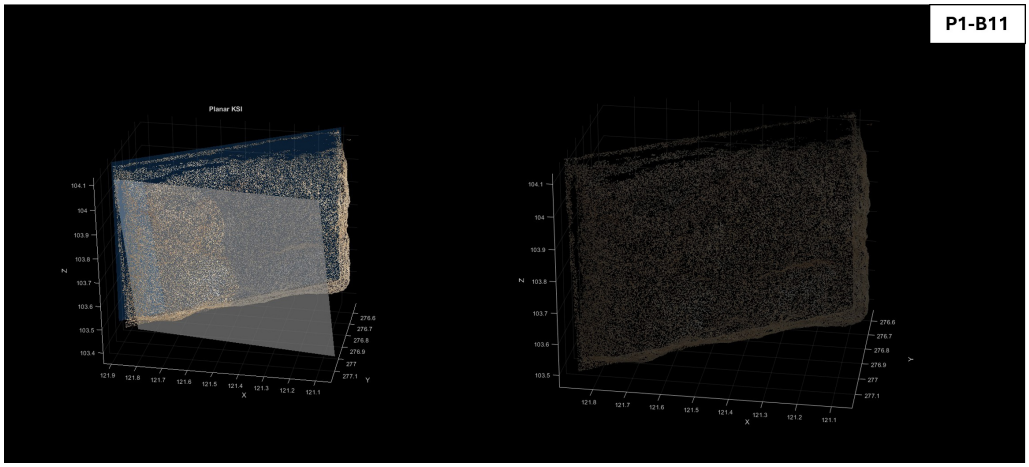


Figure 232

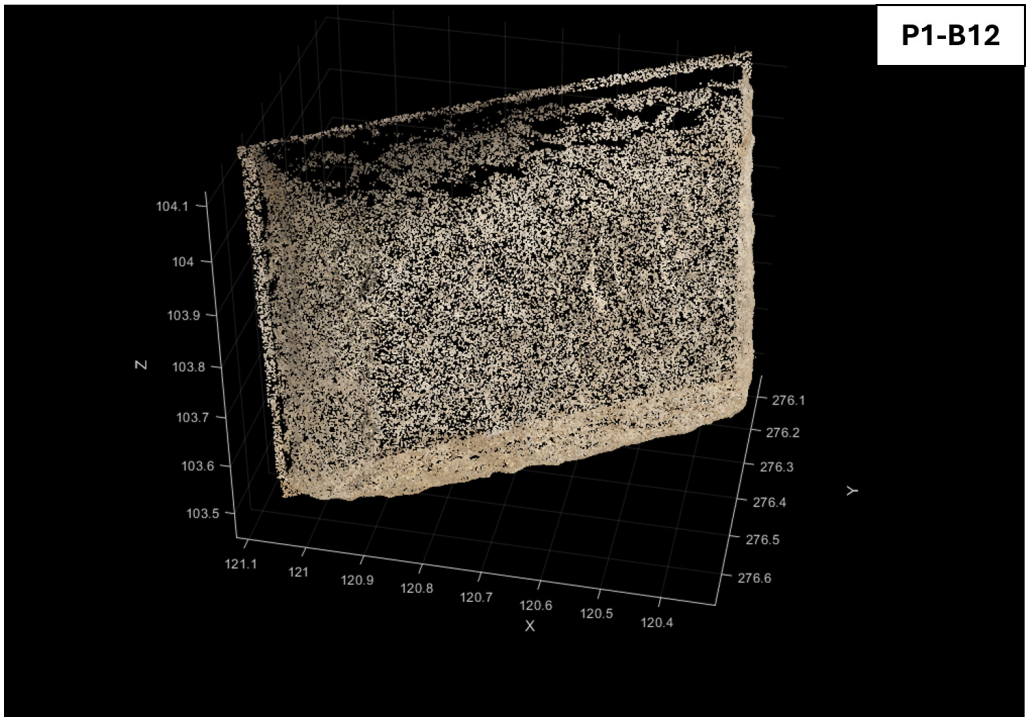


Figure 233

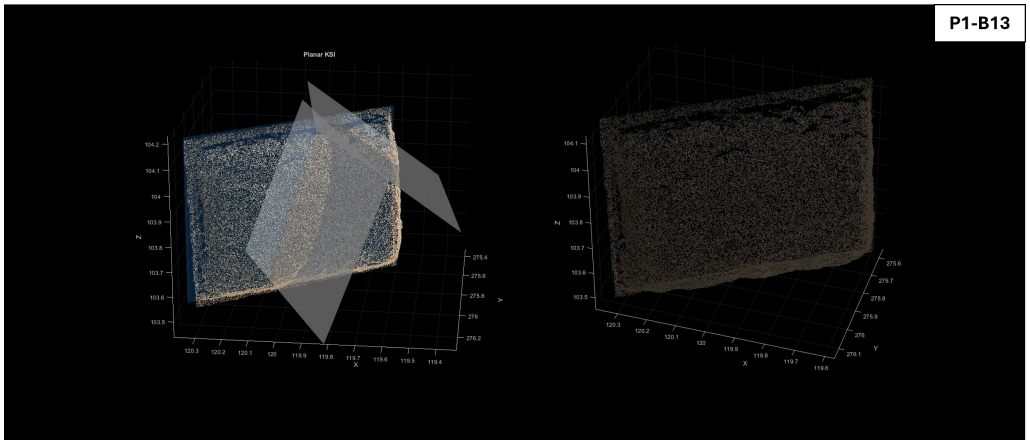


Figure 234

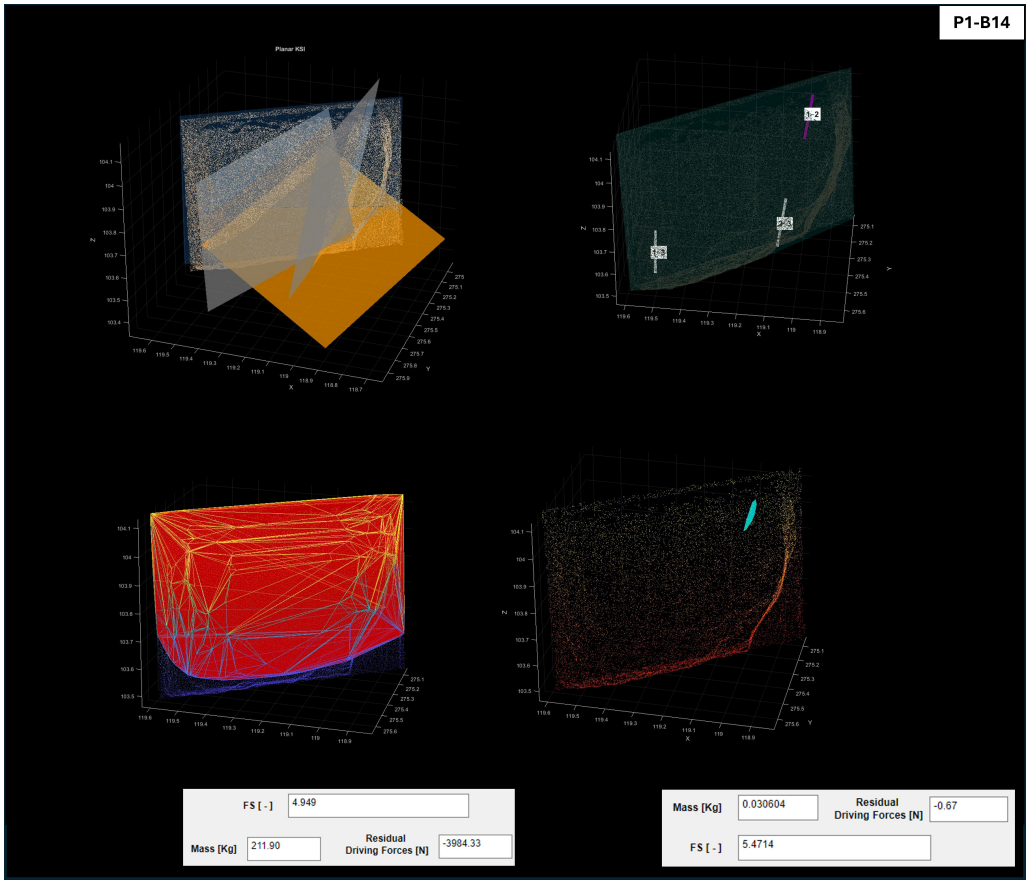


Figure 235

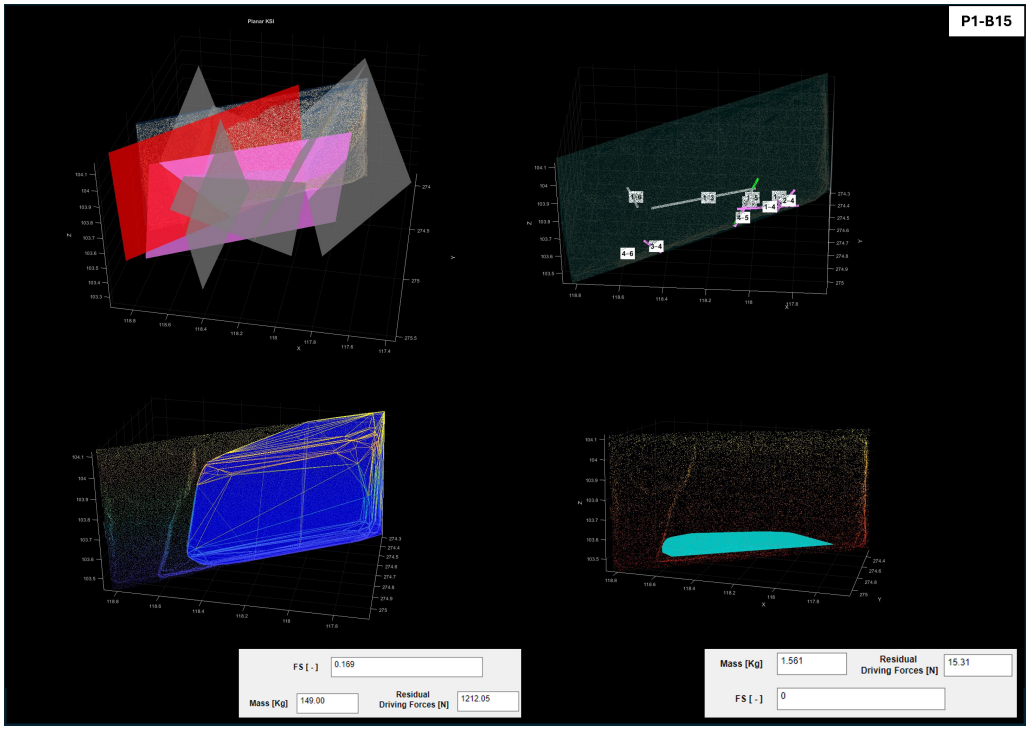

P1-B15
Planar KSI
FS [-]
0.169
Mass [Kg]
149.00
Residual Driving Forces [N]
1212.05
Mass [Kg]
1.561
Residual Driving Forces [N]
15.31
FS [-]
0

Figure 236

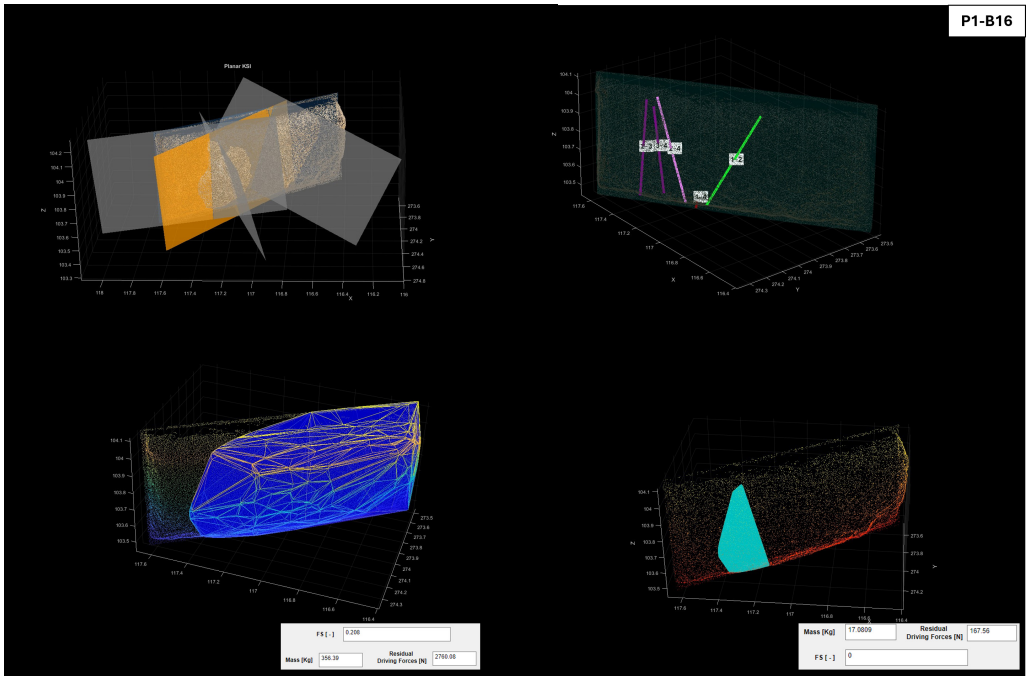

P1-B16
Planar KSI
FS [-]
0.206
Mass [Kg]
356.39
Residual Driving Forces [N]
2760.08
Mass [Kg]
17.0809
Residual Driving Forces [N]
167.56
FS [-]
0

Figure 237

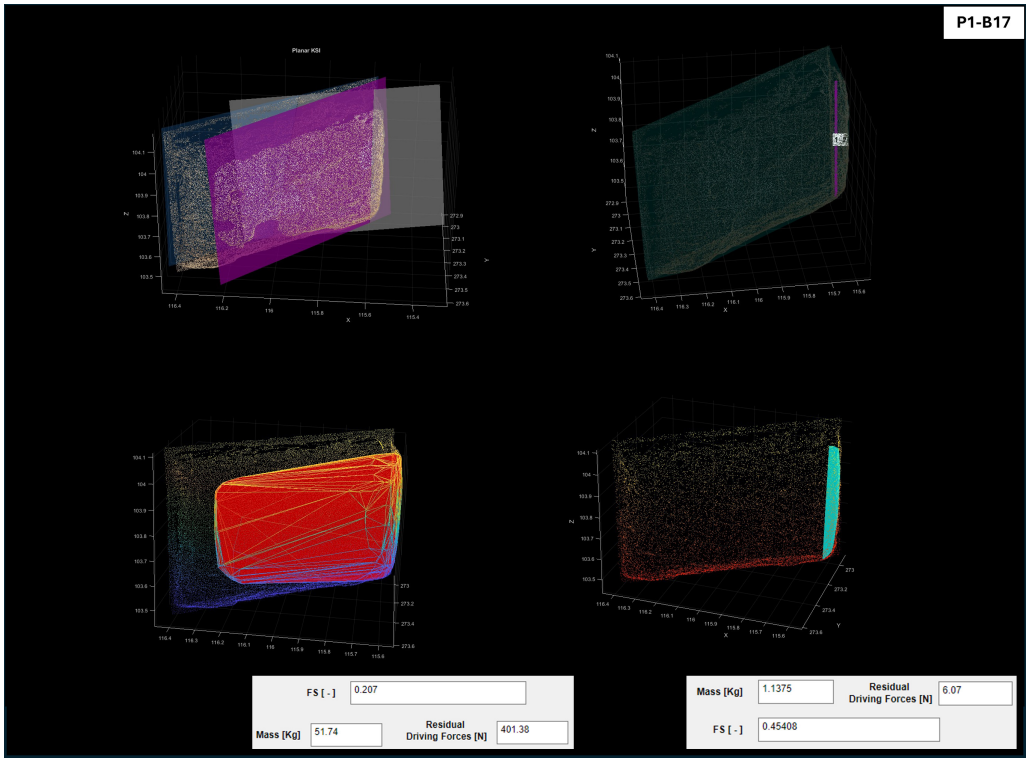

P1-B17
FS [-]
0.207
Mass [Kg]
51.74
Residual
Driving Forces [N]
401.38
Mass [Kg]
1.1375
Residual
Driving Forces [N]
6.07
FS [-]
0.45408

Figure 238

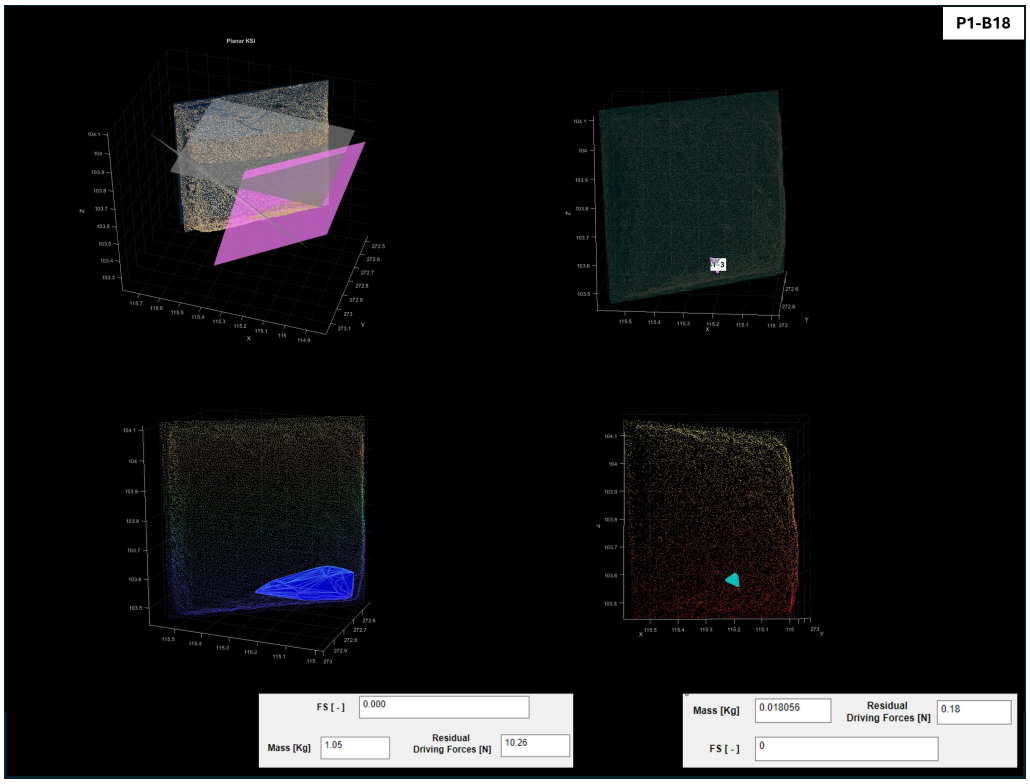


Figure 239

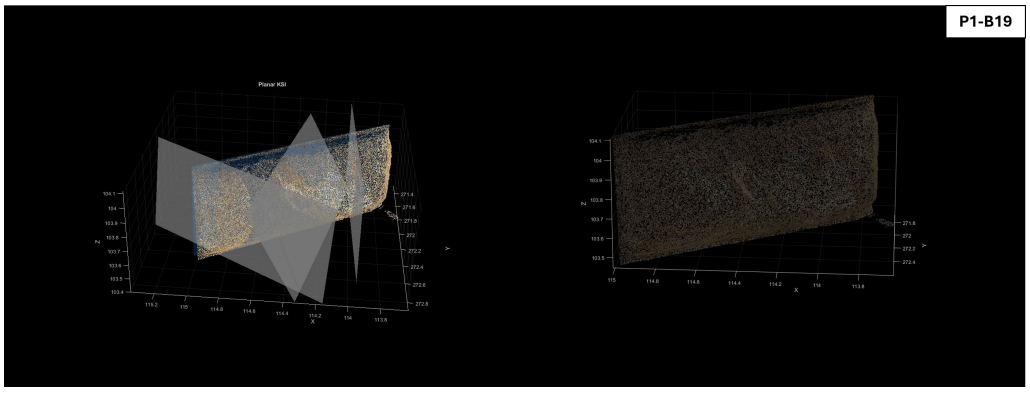


Figure 240

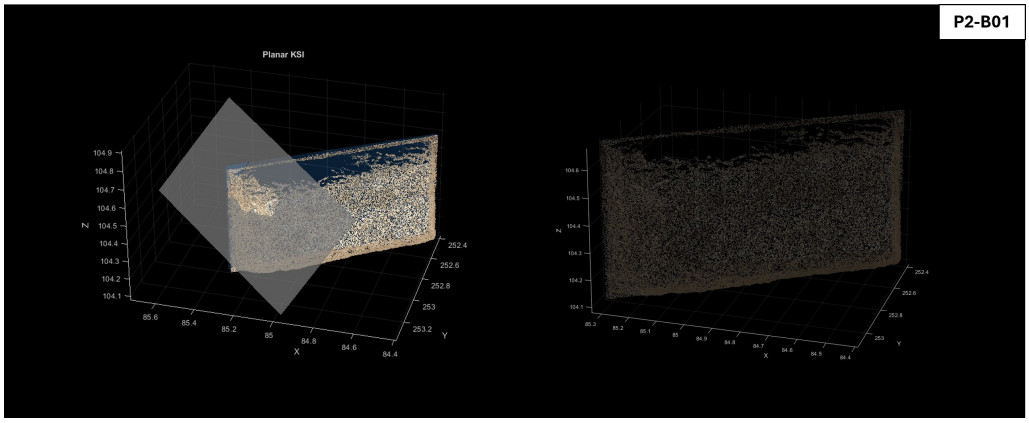

P2-B01
Planar KSI
104.9
104.8
104.7
104.6
104.5
104.4
104.3
104.2
104.1
Z
85.6
85.4
85.2
85
84.8
84.6
84.4
X
252.4
252.6
252.8
253
253.2
Y

Figure 241

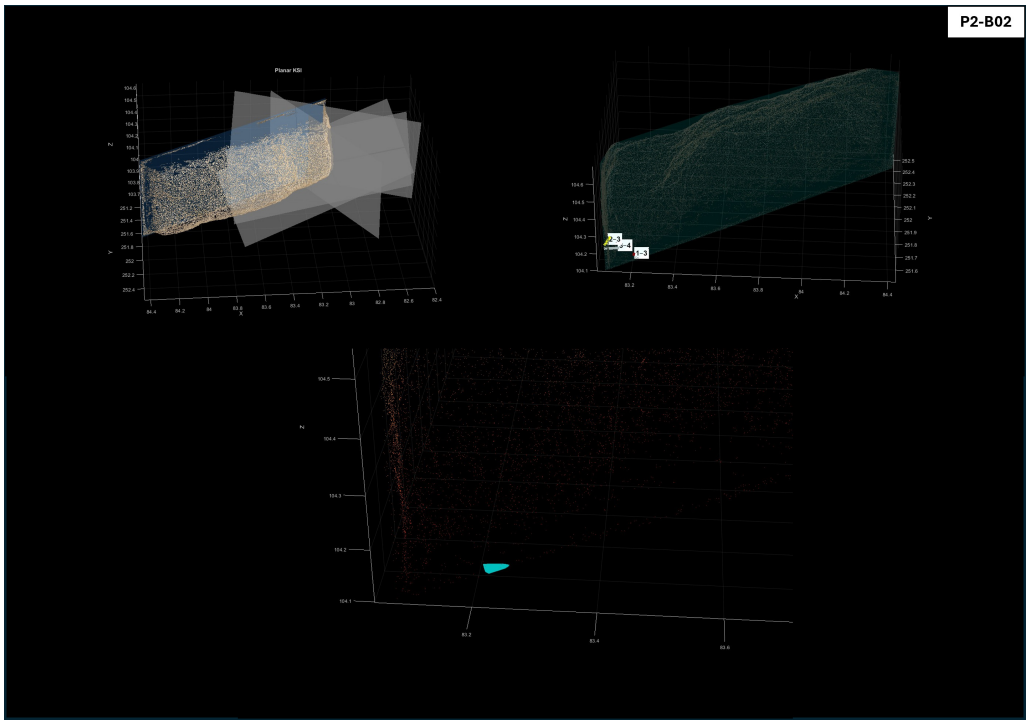


Figure 242

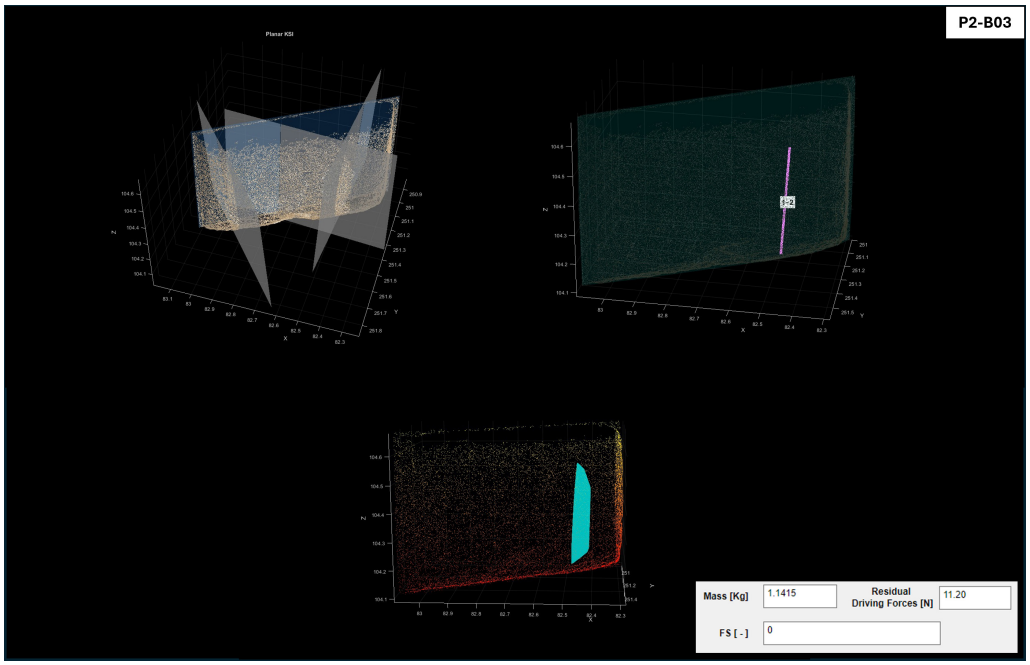


Figure 243

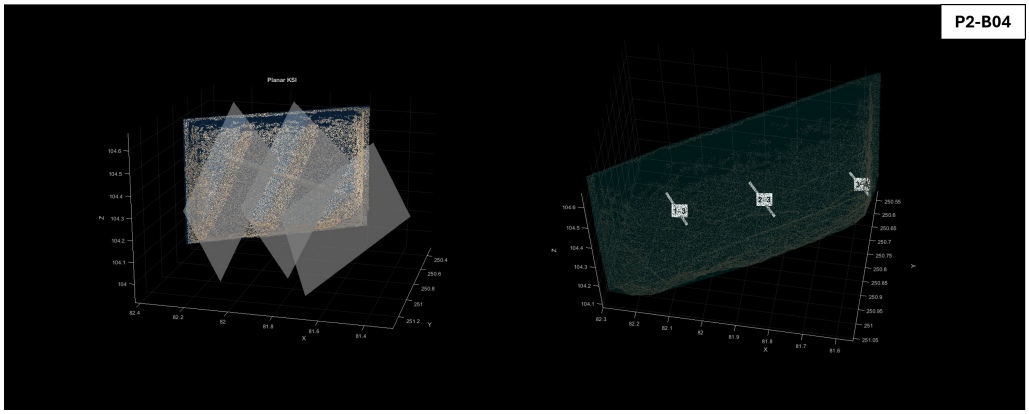


Figure 244

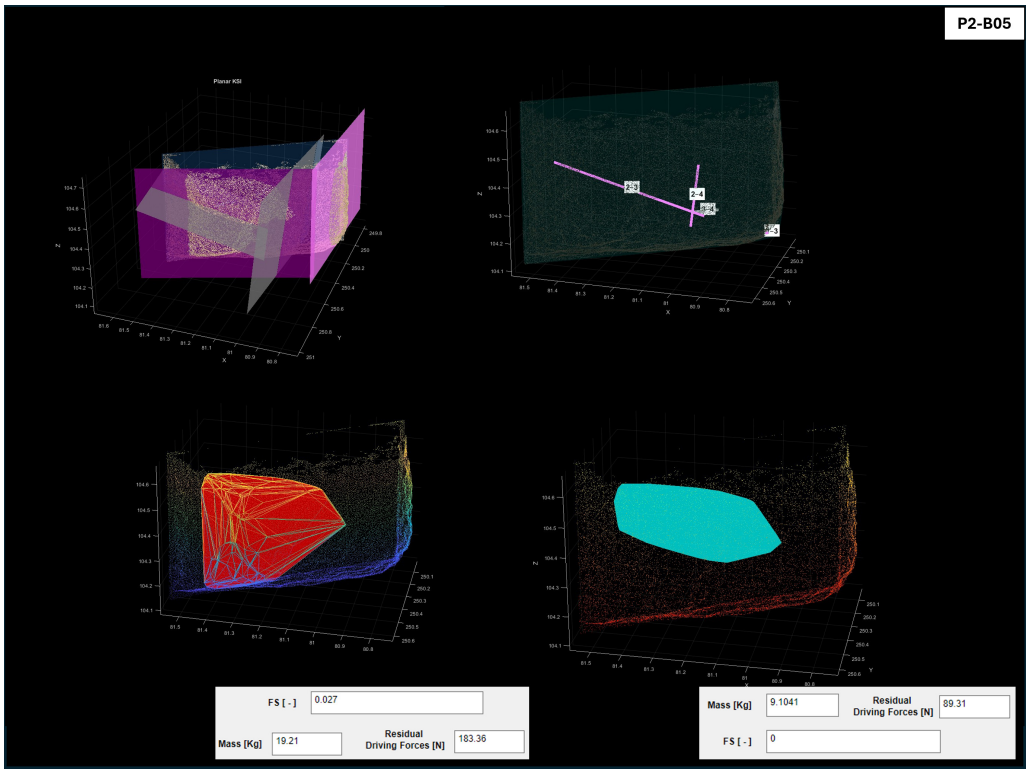


Figure 245

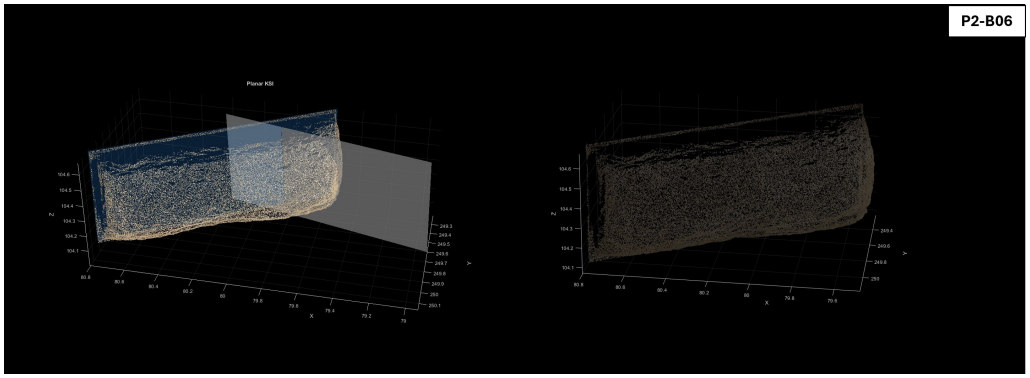


Figure 246

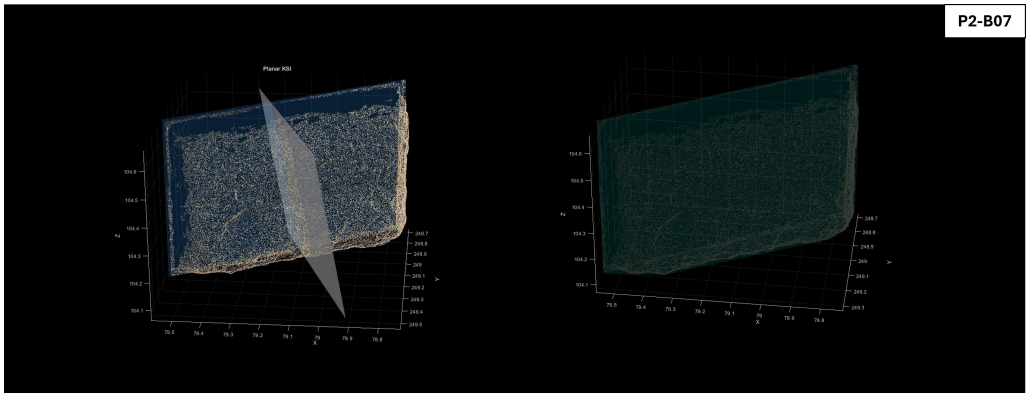


Figure 247

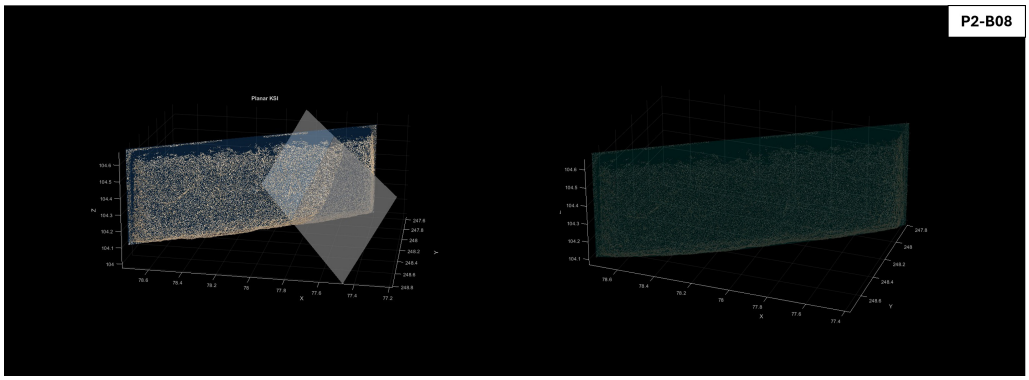


Figure 248

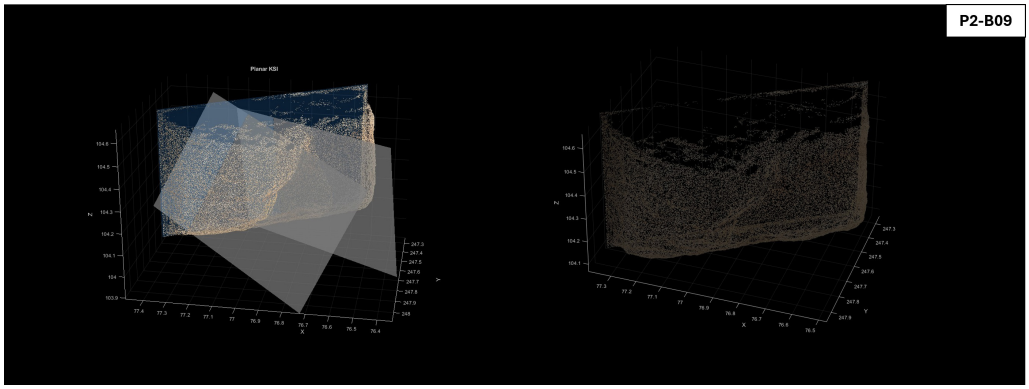


Figure 249

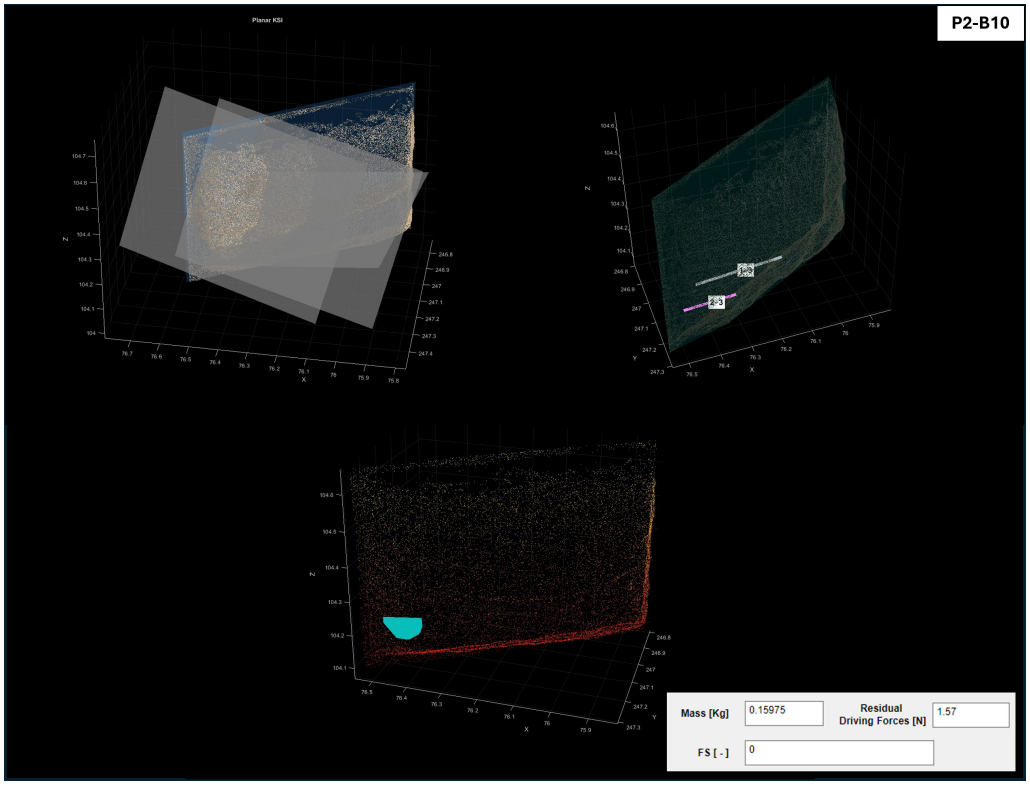

Planar KSI
P2-B10
Mass [Kg]
0.15975
Residual Driving Forces [N]
1.57
FS [-]
0

Figure 250

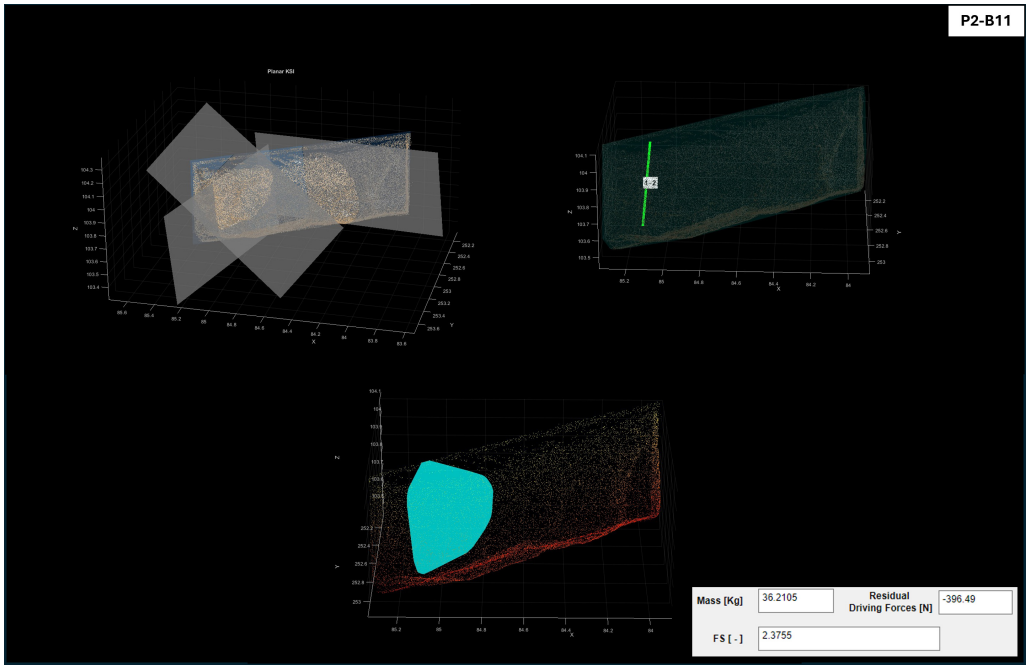

P2-B11
Planar KSI
Mass [Kg]
36.2105
Residual Driving Forces [N]
-396.49
FS [-]
2.3755

Figure 251

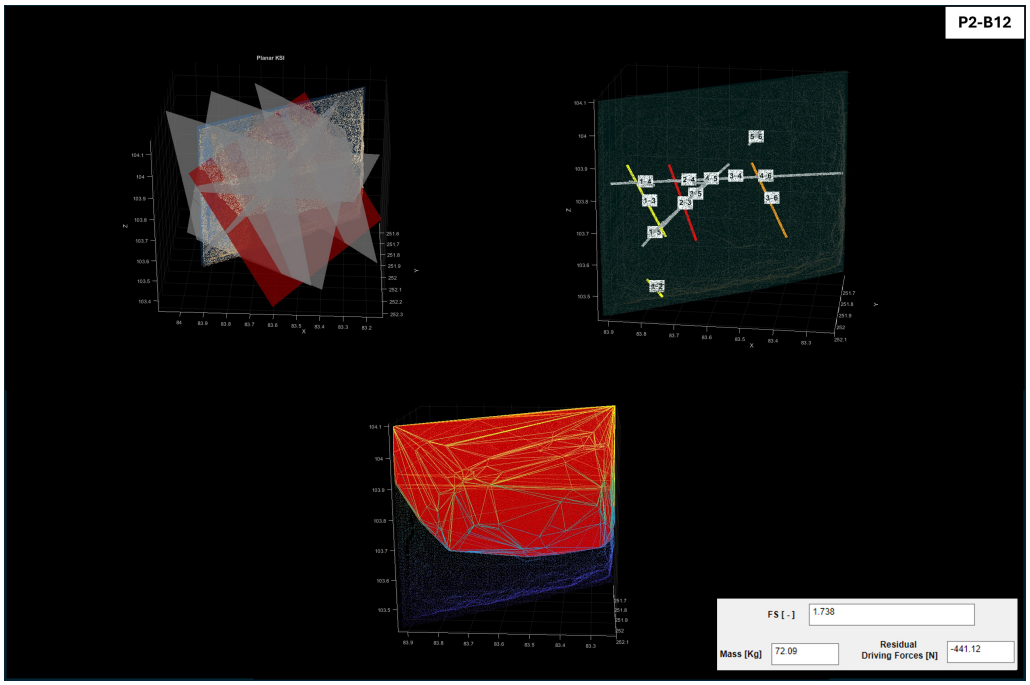

P2-B12
Planar KSI
FS [-] 1.738
Mass [Kg] 72.09
Residual Driving Forces [N] -441.12

Figure 252

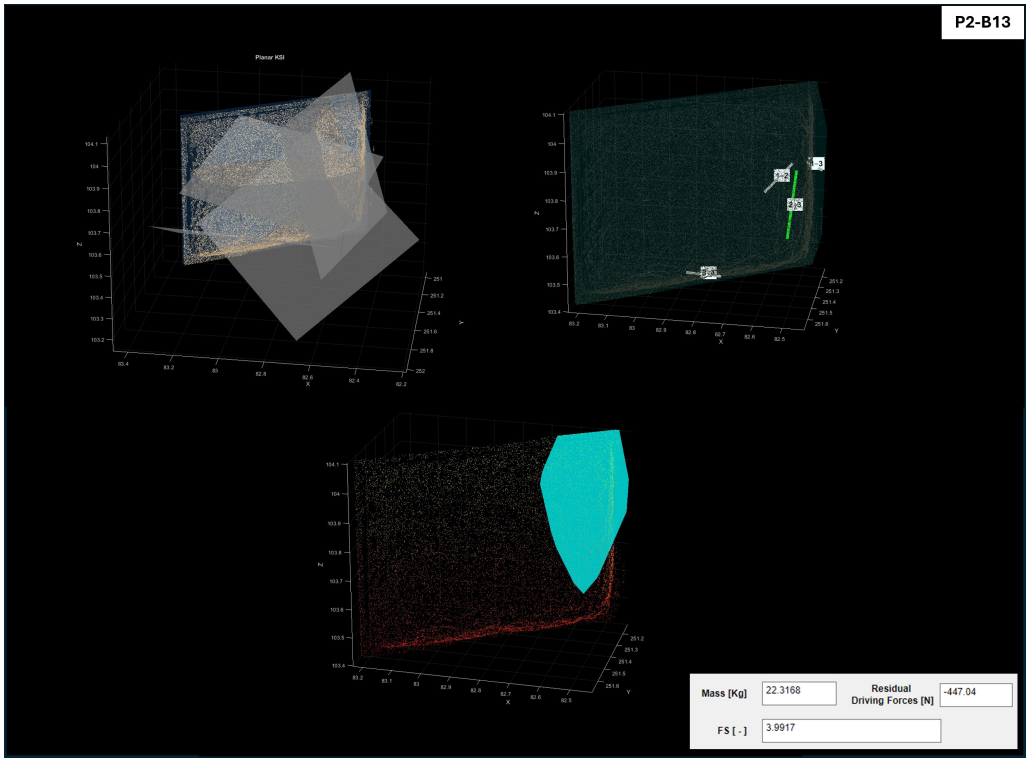


Figure 253

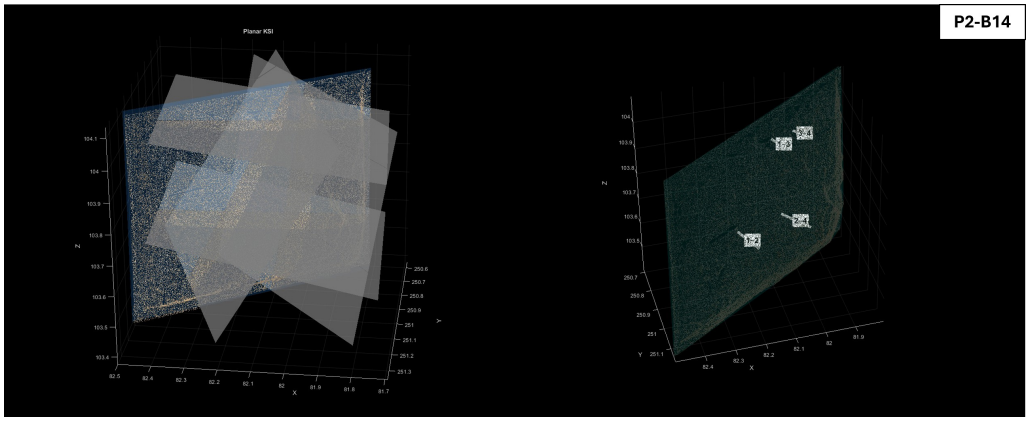


Figure 254

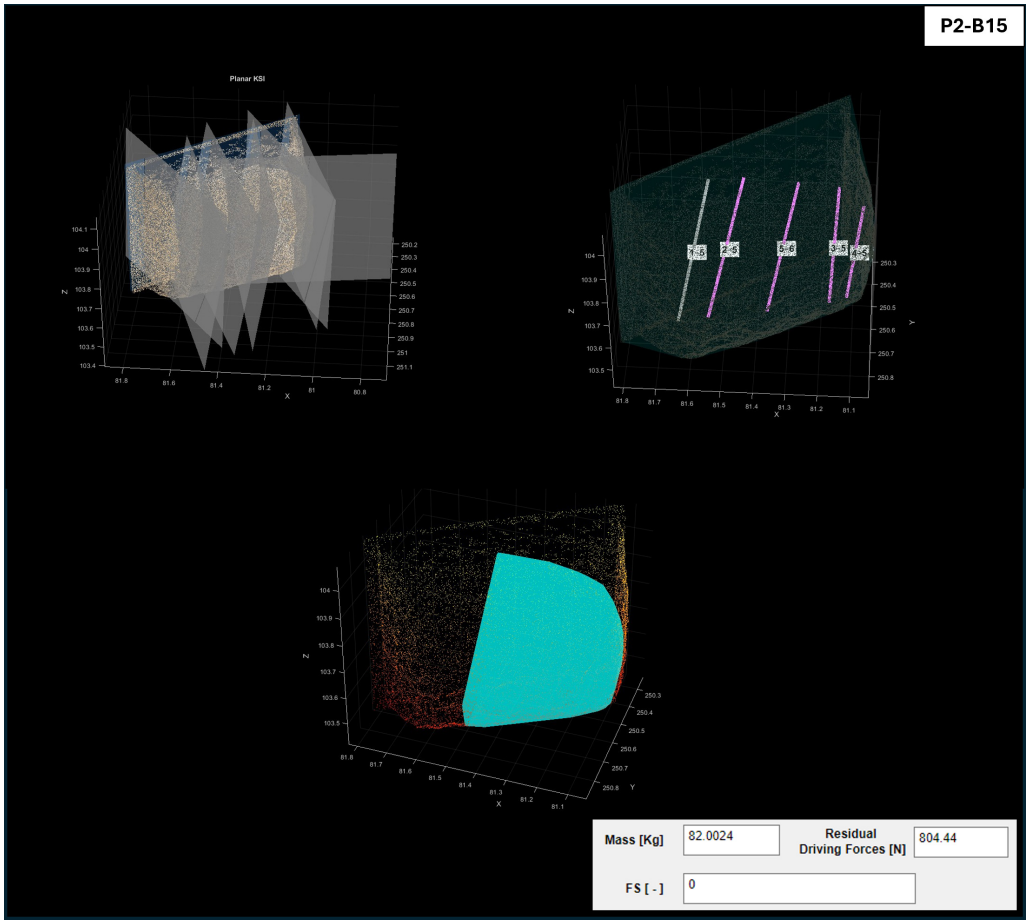

P2-B15
Planar KSI
Mass [Kg]
82.0024
Residual Driving Forces [N]
804.44
FS [-]
0

Figure 255

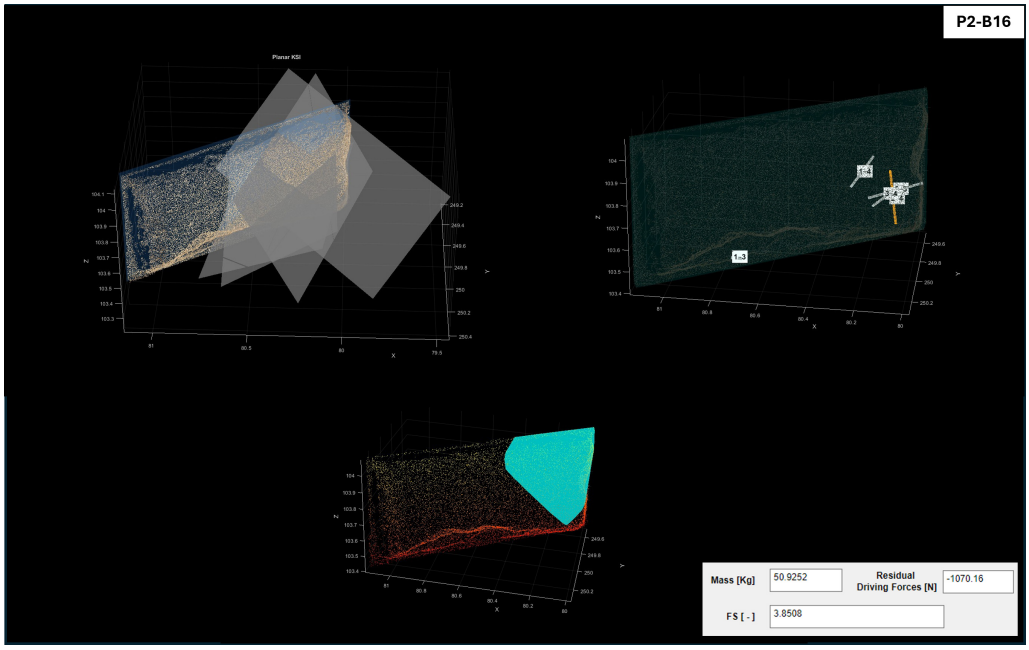

P2-B16
Planar KSI
Mass [Kg]
50.9252
Residual Driving Forces [N]
-1070.16
FS [-]
3.8508

Figure 256

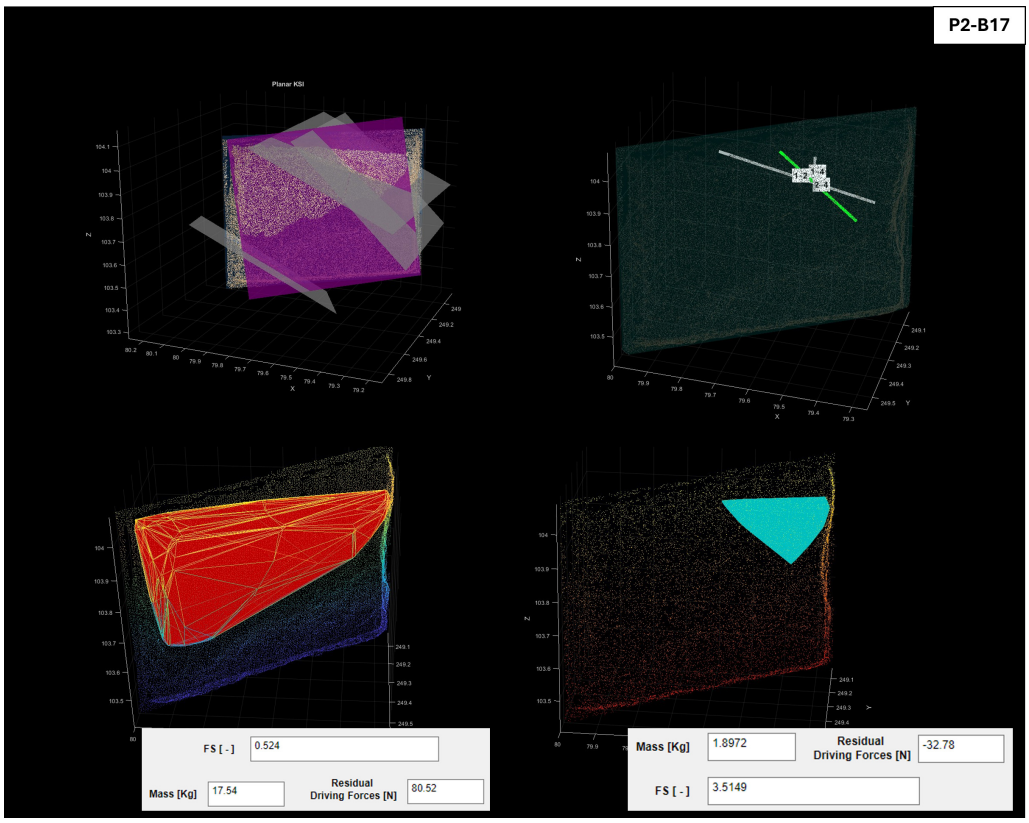


Figure 257

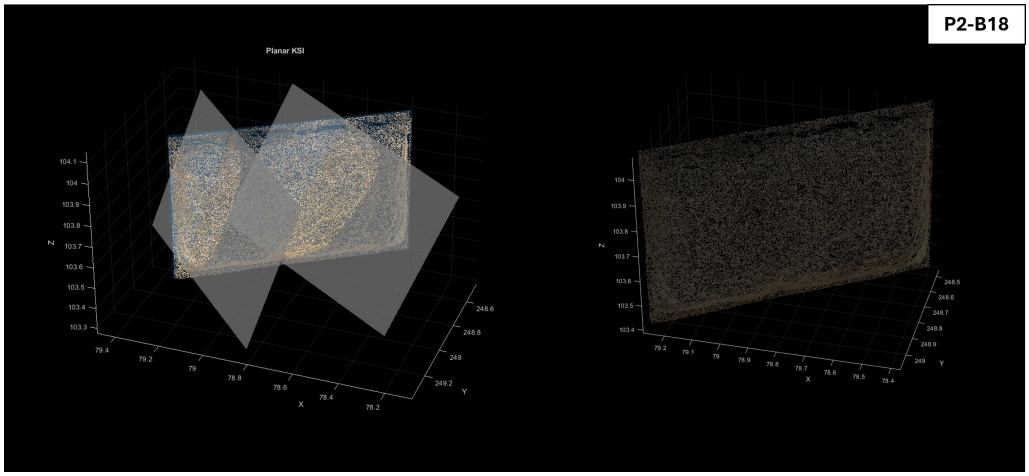


Figure 258

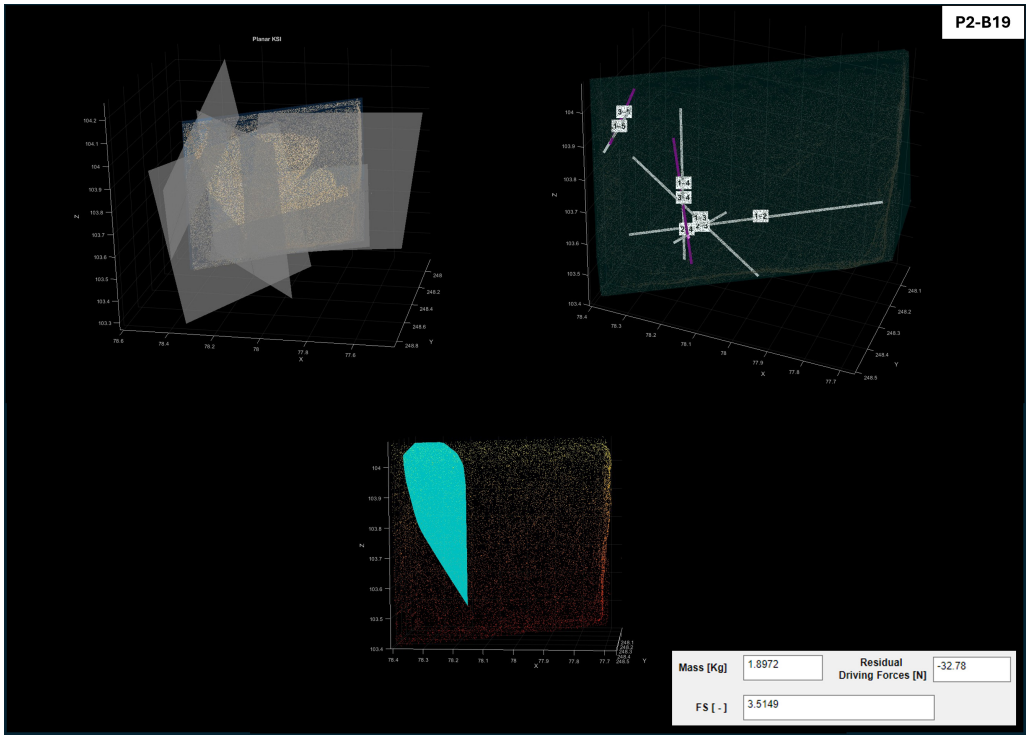


Figure 259

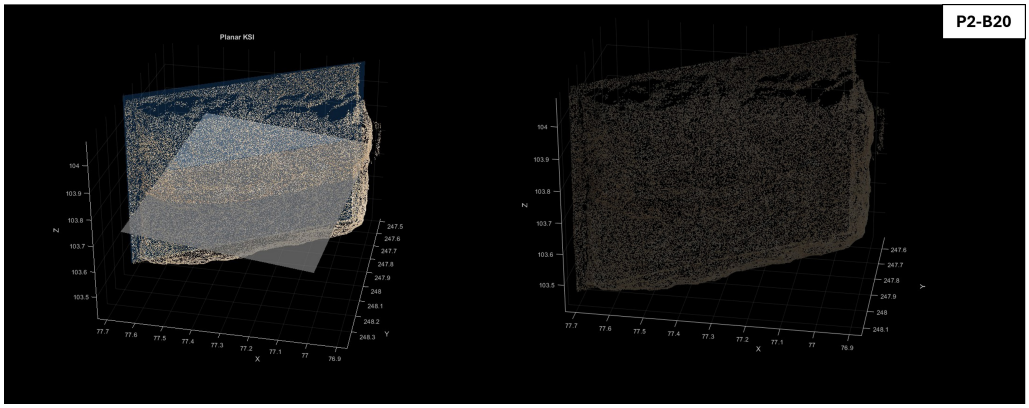


Figure 260

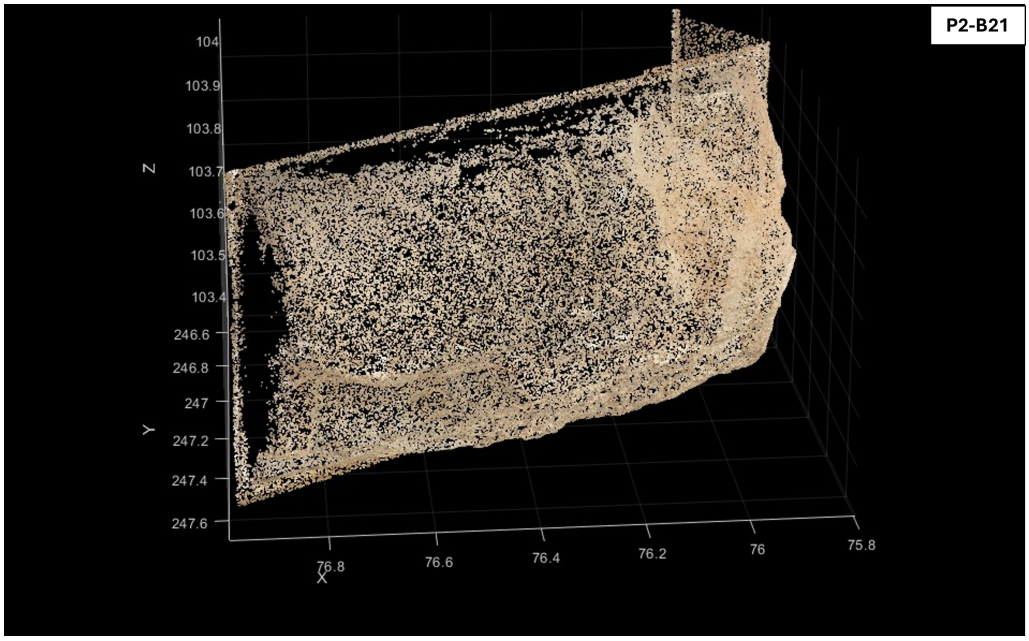

P2-B21
104
103.9
103.8
103.7
103.6
103.5
103.4
Z
246.6
246.8
247
247.2
247.4
247.6
Y
76.8
76.6
76.4
76.2
76
75.8
X

Figure 261

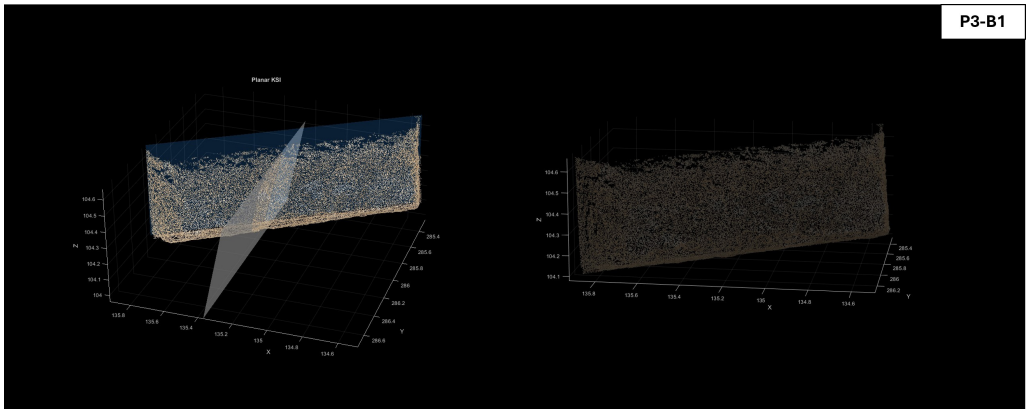


Figure 262

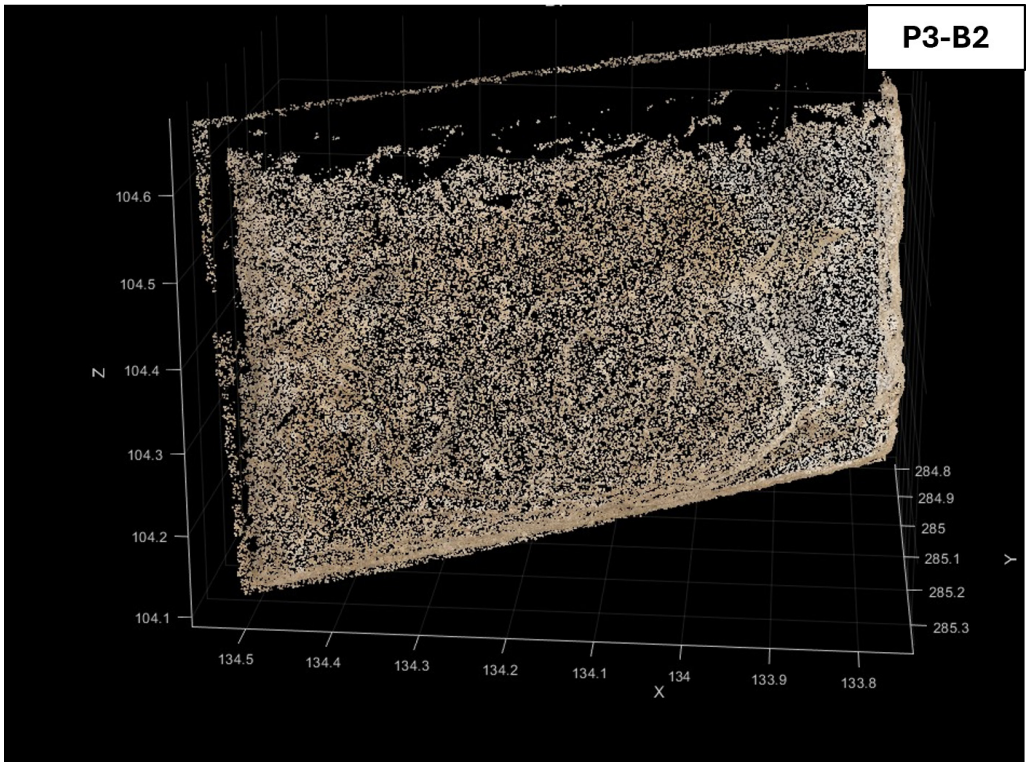

P3-B2
104.6
104.5
104.4
104.3
104.2
104.1
Z
134.5
134.4
134.3
134.2
134.1
134
133.9
133.8
X
284.8
284.9
285
285.1
285.2
285.3
Y

Figure 263

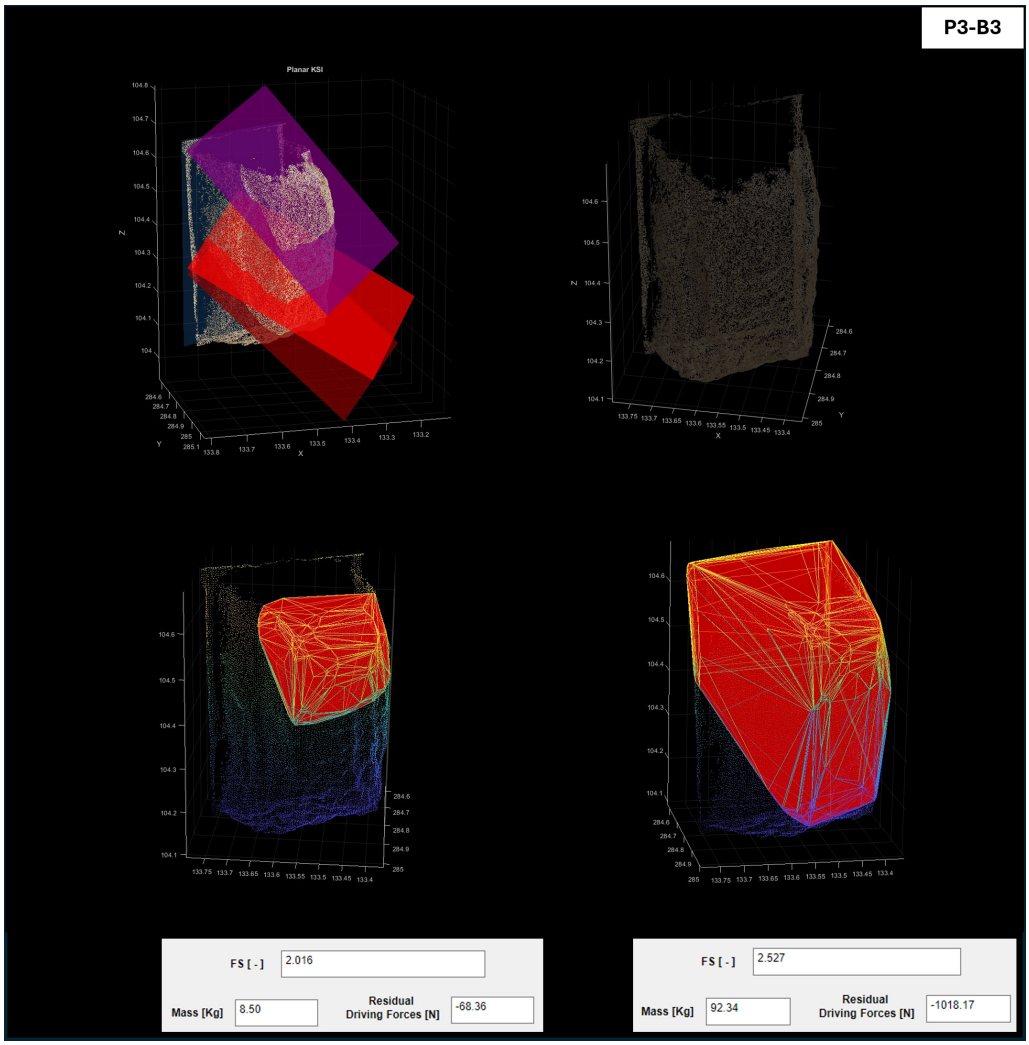

P3-B3
Planar KSI
FS [-]
2.016
Mass [Kg]
8.50
Residual Driving Forces [N]
-68.36
FS [-]
2.527
Mass [Kg]
92.34
Residual Driving Forces [N]
-1018.17

Figure 264

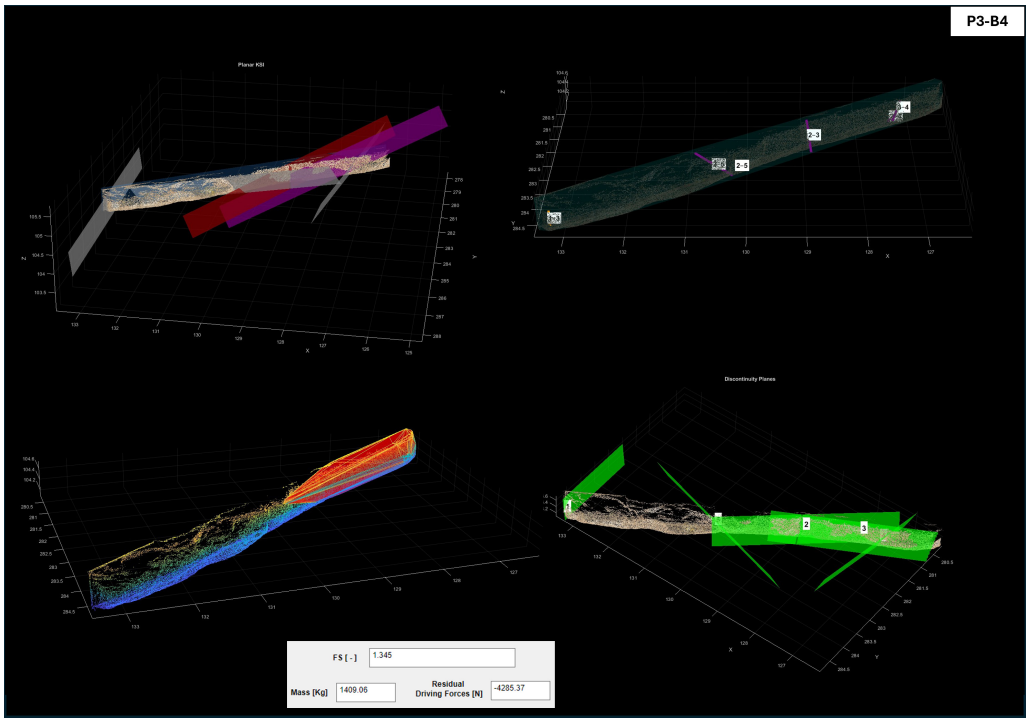


Figure 265

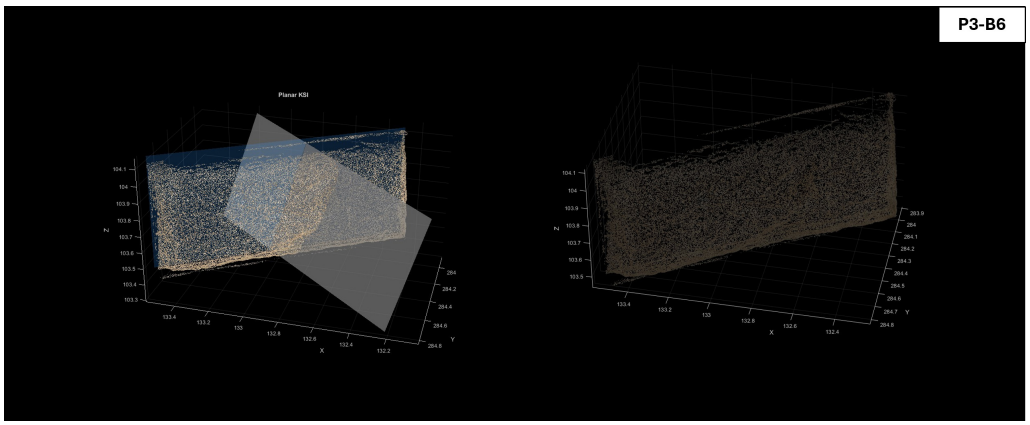


Figure 266

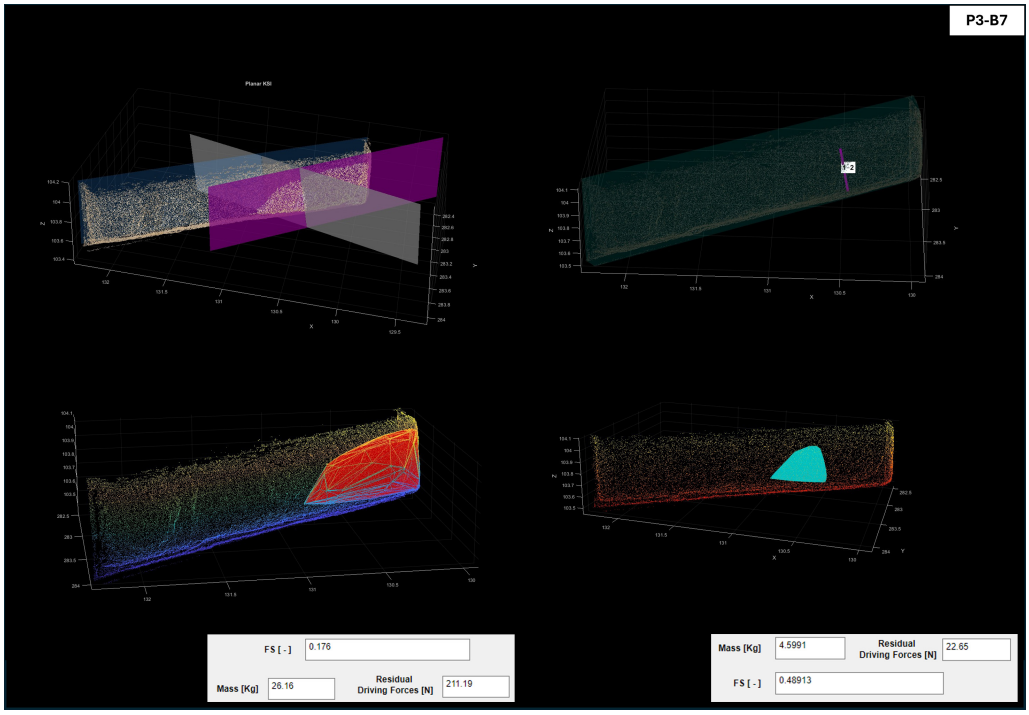

P3-B7
Planar KSI
FS [-] 0.176
Mass [Kg] 26.16
Residual Driving Forces [N] 211.19
Mass [Kg] 4.5991
Residual Driving Forces [N] 22.65
FS [-] 0.48913

Figure 267

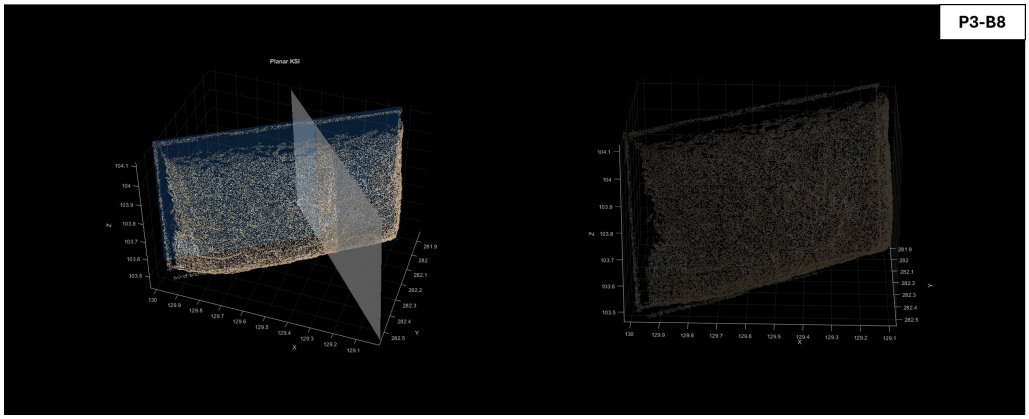


Figure 268

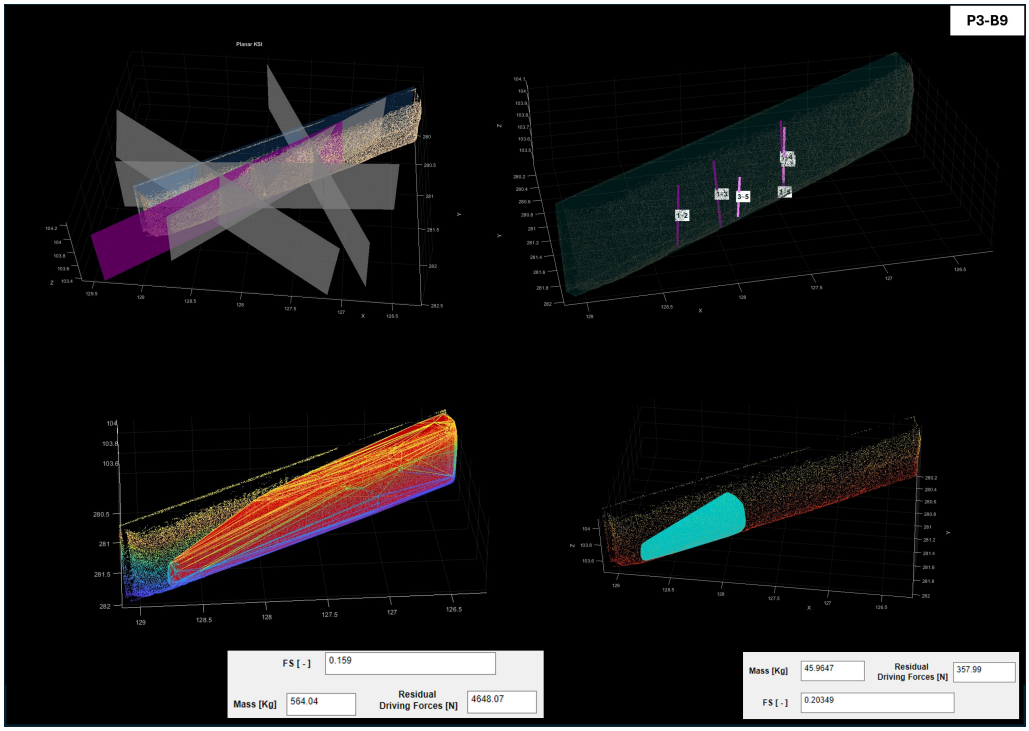

P3-B9
FS [-]
0.159
Mass [Kg]
564.04
Residual
Driving Forces [N]
4648.07
Mass [Kg]
45.9647
Residual
Driving Forces [N]
357.99
FS [-]
0.20349

Figure 269

La borsa di dottorato cofinanziata con risorse dell'Unione europea-*NextGeneration EU*
Piano Nazionale di Ripresa e Resilienza Missione 4 – Componente 1 – "Potenziamento dell'offerta dei servizi di istruzione: dagli asili nido all'Università"– Inv. 4.1 Borse PNRR patrimonio Culturale – *CUP B12B22000390007*